Statistical optics for synchrotron emission : numerical calculation of coherent modes

Mark Glass

To cite this version:

Mark Glass. Statistical optics for synchrotron emission : numerical calculation of coherent modes. Other [cond-mat.other]. Université Grenoble Alpes, 2017. English. NNT : 2017GREAY024 . tel-01664052

HAL Id: tel-01664052

https://theses.hal.science/tel-01664052

Submitted on 14 Dec 2017

Communauté
UNIVERSITÉ Grenoble Alpes

THÈSE

Pour obtenir le grade de

DOCTEUR DE LA COMMUNAUTÉ UNIVERSITÉ GRENOBLE ALPES

Spécialité : **Physique de la Matière Condensée et du Rayonnement**

Arrêté ministériel : 25 mai 2016

Présentée par

Mark GLASS

Thèse dirigée par **Manuel SANCHEZ DEL RIO**

préparée au sein du **Laboratoire European Synchrotron Radiation Facility**
dans **l'École Doctorale Physique**

Optique statistique pour l'émission synchrotron : calcul numérique en modes de cohérence

Thèse soutenue publiquement le **21 juin 2017**,
devant le jury composé de :

Monsieur ALEXANDRE SIMIONOVICI
PROFESSEUR, UNIVERSITE GRENOBLE ALPES, Président
Monsieur FRANK WYROWSKI
PROFESSEUR, UNIVERSITE F. SCHILLER, D'IENA ALLEMAGNE, Rapporteur
Monsieur GIANLUCA GELONI
CHEF DE GROUPE, EUROPEAN XFEL - ALLEMAGNE, Rapporteur
Monsieur VINCENT FAVRE-NICOLIN
MAITRE DE CONFERENCE, UNIVERSITE GRENOBLE ALPES, Membre

THÈSE

presenté par
Mark Glass

Pour obtenir le titre de

Docteur de l'Université Grenobles Alpes
Physique de la matière condensée et du rayonnement

Statistical optics for synchrotron emission : numerical calculation of coherent modes

Soutenance publique le 21 juin 2017

UNIVERSITÉ
Grenoble
Alpes

ESRF
The European Synchrotron

Directeur de thèse :

M. Sanchez del Rio

Composition du Jury :

A. Simionovici	Président de jury
G. Geloni	Rapporteur
F. Wyrowski	Rapporteur
V. Favre-Nicolin	Examinateur

Acknowledgements

I would like to express my sincere gratitude to Manuel Sanchez Del Rio who was *always* available for me, who *always* offered me his help and who *always* supported me.

I am grateful to Anna for her continuous encouragement and endless positivity.

I would like to thank Boaz Nash for his help with the electron beam aspects of this thesis.

My sincere thanks go to Kwang-Je Kim, Gianluca Geloni and his coworkers for fruitful discussions and their fundamental theoretical works.

I would also like to thank Alvaro Martin Ortega for being a cool office-mate and for helping me with all the organizational stuff, Oleg Chubar for the development of SRW, Sophie Thery for stimulating discussions about undulator radiation and her help with my French, our colleagues from APS Xianbo Shi, Ruben Reininger, Kwang-Je Kim and Ryan Lindberg for helpful discussions and hints, Julio Da Silva for discussions about ptychography and my parents for their encouragement.

Finally, I would like to thank the rapporteurs Gianluca Geloni and Frank Wyrowski for taking the time to review this thesis.

Contents

1. Introduction

In this thesis I discuss the application of statistical optics to radiation produced at synchrotrons. We focus on second order coherence phenomena. Second order coherence allows us to *calculate* coherence properties and the mean intensity.

Synchrotron radiation (SR) has witnessed an enormous growth in the last decades because of its applicability to multidisciplinary applied science. The history of SR goes through several generations of synchrotron radiation sources. The first generation in the 1960's used storage rings dedicated to high energy physics and produced the SR in parasitic mode. Many experimental techniques started to be used and the popularity of this new method to produce radiation grew in the scientific community. The high impact in applied science drove the community to build storage rings dedicated exclusively to the production and use of SR. This is the second generation, characterised by a high brilliance or brightness (emitted power per unit solid angle and source size). A new way of increasing the brilliance was implemented: the insertion device, or magnets that make the electrons oscillate strongly, thus boosting their acceleration and therefore their emission. A next generation of machines (third generation) were built incorporating large straight sections necessary to install multiple insertion devices. The ESRF was the first of the three largest third generation sources in the world (ESRF, APS and Spring8). A high increase in brilliance was provided by combining the high flux emitted by the insertion devices and by reducing the source size and divergence by limiting the electron emittance. The small vertical emittance (4 pm at ESRF) as compared with the 1000 times larger horizontal emittance lead to relatively high coherence of the radiation that was at the origin of many experimental techniques that are standard today. Examples of this techniques are X-ray photon correlation spectroscopy(XPCS)[1], coherent diffraction imaging (CDI)[2, 3] and ptychography[4, 5]. The current third generation of synchrotrons is now continued in two different new facilities: X-ray free electron lasers (XFELs), based on linear accelerator technology, and the so-called "diffraction limited storage rings", circular storage rings where the electron horizontal emittance is lowered to a level comparable to the present vertical emittance. These new facilities target experiments that exploit the X-ray beam coherence, like X-ray photon correlation spectroscopy, coherent diffraction imaging, or ptychography. In all new facilities or upgrades of the existing ones, the keyword "coherence" is omnipresent. We look to the upgrade of the existing facilities, like the EBS (Extremely Brilliant Source) at the ESRF, aiming at building a storage ring of 150 pm emittance (as compared with the present one of 4 nm) that will boost the X-ray brilliance and the coherence properties.

In this context of the ESRF upgrade and the construction of the new storage ring EBS it is important to perform accurate calculations and quantitative evaluation of the parameters related to X-ray coherence in new storage rings. These parameters can be extracted from the cross spectral density (CSD), a complex function of costly evaluation but containing most of the information we need about coherence. It is not only necessary to evaluate this function for the source, but to propagate it along the optical elements of the beamline. This thesis proposes a new practical and manageable way to compute the CSD and to propagate it along the beamline using standard wave optics methods. The key point is the decomposition of the CSD in its coherent modes. Although the idea is well known in statistical optics, this thesis shows how to do this calculation numerically for synchrotron sources. Once the CSD is decomposed one can propagate each mode like any coherent field along the beamline and construct the CSD at any point of the beamline. From this CSD one can extract the usual parameters like coherence lengths, spectral degree of coherence, spectral density (mean intensity in frequency representation), etc. But not only: the decomposition into coherent modes gives more practical information that is not directly visible even if the CSD is known. It permits the accurate calculation of the mode spectrum, or how the radiation is distributed into the different coherent modes. In this way, it will be shown that a fully coherent source contains only one mode, a quite coherent source like the EBS has most of its radiation distributed along few modes (that can be a few hundreds) and a quite incoherent source will typically have an almost flat mode spectrum. The study of how the mode spectrum is changed by the beamline is fundamental for designing new beamlines. We will show quantitatively, for example, how coherence increases when closing a pinhole, a well known method to improve the beam characteristics in experiments exploiting coherence. The maximisation of the intensity fraction carried by the first coherent mode, using optical elements, is the main task of the designer of a beamline for coherent applications. The method presented here will allow for quantitative practical studies that may impact in the design and constructions of more efficient beamlines. Moreover, the numerical description of the undulator cross spectral density in terms of its coherent modes opens a new door for theoretical and practical investigations of how partial coherent X-ray beams interact with samples.

In the second chapter of this thesis we review fundamental concepts of statistical optics like the mutual coherence function, the cross spectral density, the fundamental relation between source fluctuation, the Wolf equation and the propagation of the cross spectral density through optical elements. These statistical phenomena are rooted in the physics of deterministic optics and we review those concepts needed for the understanding of this thesis. Additionally, we present some parts of accelerator physics and insertion devices needed for the understanding of coherence in synchrotrons. It is precisely the statistical fluctuations of the electrons in the synchrotron storage ring that determines the coherence properties of the X-ray radiation.

We will derive in Chapter 3 the significant fundamental theoretical results for statistical optics applied to synchrotron radiation. These are the brightness convolution theorem by Kim[7] and the theory developed by Geloni *et al.*[8]. Our derivation is slightly different from the originals and more verbose. In particular we will put strong emphases on explaining the underlying physical ideas behind the formulas. This will lead to a discussion regarding the position of the straight section at which the brightness convolution can be performed and what kind of requirements the electron beam and undulator should fulfill to be valid for the convolution theorem in the given form.

The main goal of this thesis is the development of a practical algorithm to calculate and propagate the cross spectral density. Additionally we want to emphasize an awareness on electron beam parameters that enter in the calculation of X-ray emission calculations. For today's computers the storage of the cross spectral density in a naive way is very memory demanding because it is a four-dimensional function. The memory requirements can easily attain several terabytes which in consequence requires a big computer cluster. It is for this reason that I decided to perform a coherent mode decomposition that results in a comparably small number of coherent modes. These modes can be stored and propagated much more efficiently. The assumption that a small number of modes are sufficient to accurately calculate all coherence properties was motivated by the Gaussian Schell-model approximation.

After having established the theoretical description we present an algorithm to numerically determine the cross spectral density under not too restrictive assumptions. Several coherent mode decompositions for synchrotron undulators are performed. The decompositions result in a relatively small number of coherent modes for ESRF-EBS settings. The total memory requirement is reduced to a few gigabytes. Finally these modes are propagated using standard wavefront propagation methods.

We present (Chapter 5) some applications like source studies for varying electron parameters such as the transverse electron beam settings, the energy spread and a comparison of a model imaging beamline of the current ESRF storage ring and the upgraded ESRF-EBS for varying aperture sizes. We made a compatibility study with a Gaussian Schell-model approximation and an analytical approximation[8] and what we call a separation approximation.

We close this thesis with some ideas for future research and a summary.

The thesis is accompanied by the *Coherent Modes for Synchrotron Light (comsyl)*[9] open source software package.

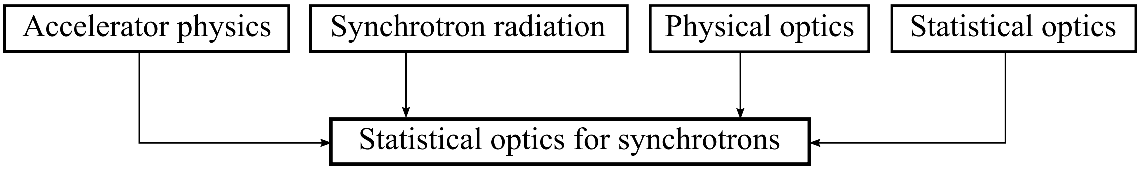

Figure 2.1.: Overview of the theory discussion.

2. Fundamental theory

In this chapter we develop the theory relevant for this thesis. We review briefly concepts from electron storage ring physics, some synchrotron radiation emission physics, concepts of physical optics and the basics of statistical optics. We combine these theories in chapter 3 to develop the theory of statistical optics for synchrotrons. There we follow Kim's ideas for his brightness convolution theorem[7] and the theoretical considerations of Geloni *et al.* for emission in storage rings[8].

2.1. Beam dynamics in storage rings

This section is meant to give a brief overview of accelerator physics for synchrotron storage rings. In calculations of the synchrotron emission the description of the electron beam is often oversimplified even though it is essential to completely describe the statistical character of the emission. We will present the electron beam parameters related to our synchrotron emission calculations in some detail.

2.1.1. Functional principle of synchrotrons

A synchrotron consists of an accelerating part and a storage ring. The accelerating part is usually the combination of a linear accelerator and a booster ring (see Fig. 2.2).

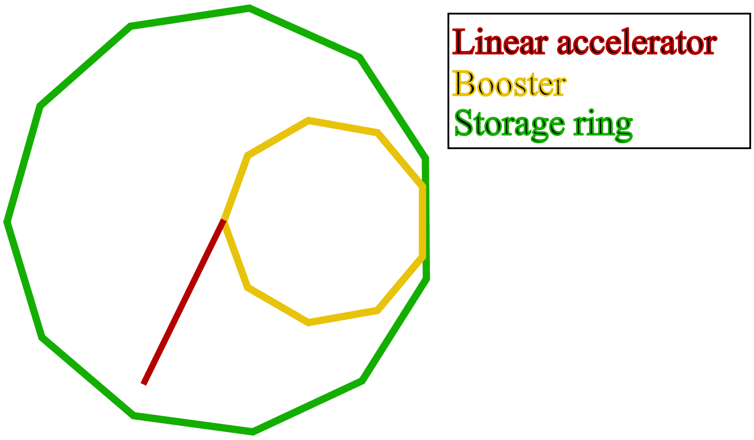

Figure 2.2.: Schematic sketch of a typical synchrotron design.

The underlying physical force for the acceleration and deflection of the electrons is the Lorentz-Force. The equation of motion for a free electron is:

$$\dot{\boldsymbol{p}} = -e\left(\boldsymbol{E} + \frac{\boldsymbol{p}}{\gamma m_0} \times \boldsymbol{B}\right), \tag{2.1}$$

here $\boldsymbol{p}$ is the electron's momentum, $\boldsymbol{E}$ is the external electric field, γ is the Lorentz factor, m_0 is the electron mass and $\boldsymbol{B}$ is the external magnetic field. An electron gun creates bunches of free electrons. Inside the linear accelerator (LINAC) these electrons are accelerated by pulsed electric fields (traveling waves) to a few hundred MeV. The linear geometry is useful to minimize the energy losses due to synchrotron radiation. To create high flux hard X-ray emission an electron energy of a few GeV is desirable. In order to attain this electron energy the electrons are injected into the booster. The booster is a circularlike shaped accelerator and the electrons now follow a circularlike trajectory. To change the direction of propagation of the electrons the so called bending magnets are used. Deflection of highly relativistic electrons is normally performed with magnetic fields because for comparable electric and magnetic field strengths the second term in the Lorentz force (Eq. 2.1) becomes much bigger due to the high velocity of the electrons. Often the bending magnet is a dipole magnet. The mathematical description of dipole magnets is comparably simple and additionally it is possible to fabricate real dipole magnets that reproduce these ideal theoretical values to a high precision. Highly relativistic electrons passing through a dipole magnet change their trajectory roughly by a deflection angle θ:

$$\theta = 0.3 \cdot l_m[m] \frac{|B[T]|}{E[GeV]}, \tag{2.2}$$

where l_m is the length of the bending magnet, B is the magnetic field, E is the electron's energy. The deflection angle depends on the electron energy and less energetic electrons will be bent stronger than electrons with higher energy. This effect results in a phenomenon called dispersion, in which the orbit depends on the energy. Additionally, because of the finite length of the bending magnets there is focusing due to edge fringe fields.

To keep the electrons focused around a design orbit quadrupole magnets are installed. Again, quadrupoles can be produced to a high degree of precision in reality. They have a scalar potential:

$$V(x, y) = -gxy, \tag{2.3}$$

where x and y are the horizontal and vertical spatial coordinate, respectively and g is the so called field gradient. Their magnetic field is therefore

$$B_x = gy; B_y = gx. \tag{2.4}$$

The effect of a quadrupole can be understood in analogy to lenses in ray optics. A lens in ray optics deflects a ray proportional to its distance from its optical axis. This results in a focusing of a bundle of parallel rays into a single point. The magnetic field of quadruples has the same effect on electrons, i.e. a deflection proportional to the distance of the electron to the quadrupole axis. Because the Lorentz force is the cross product of the electron direction and the magnetic field, the electrons are focused in either the horizontal or vertical plane and defocused in the other plane. The sign of the field gradient g determines in which plane the quadrupole will focus. For electrons $g < 0$ focuses in the horizontal plane and $g > 0$ focuses in the vertical plane. The former is called a focusing quadrupole and the latter a defocusing quadrupole. To arrive at a net focusing in both planes one can put a focusing quadrupole followed by a defocusing quadrupole in some distance. This principle of alternating gradient focusing is called strong focusing. The concept is similar to the focusing with a Kirkpatrick-Baez mirror in optics. The simplest magnetic cell employing this concept is the FODO cell which starts with half a focusing quadrupole followed by free space of length l, a defocusing quadrupole followed by another free space of length l and ending with half a focusing quadrupole. The FODO cell is easy to implement. In a ring these magnetic cells are usually repeated to form a lattice. The FODO lattice is the starting point for many accelerator lattices, including booster rings, synchrotron storage rings and particularly for particle colliders.

Electrons moving through an accelerator ring constantly lose energy because of synchrotron radiation. In the bending magnets the electrons are accelerated and according to Maxwell's equations they will radiate emission. If an electron loses too much energy its trajectory will end in the vacuum chamber wall. In the so called radio frequency cavities the electrons are accelerated and energy loss is compensated. The RF-cavities create strong oscillating electric fields. The idea is to create an accelerating electric field in the exact moment an electron passes the cavity. If an electron does not arrive in the right moment it may even be deaccelerated. This timing creates a *RF-bucket* structure. Only electrons that arrive at the correct RF phase get accelerated. This distribution has the form of moving buckets which explains the name RF-buckets.

Over time the electrons gain energy in the booster and therefore the fields of the magnets and the RF-cavity must be constantly adjusted. Once the target energy of a few GeV is reached the electrons are injected into the storage ring.

In the storage ring the electrons are no longer accelerated and the electron energy is not further increased. In the storage ring the RF-cavity serves for *recharging* the energy lost due to synchrotron radiation and also to provide longitudinal focusing which gives rise to synchrotron oscillations. The electrons remain in the storage ring for several hours. Their lifetime is determined by scattering with residual gas atoms, vacuum chamber interactions and intrabunch electron scattering (mainly by, i.e. Touschek effect). Over time more and more electrons get lost. New electrons are then injected from the booster to replace the lost electrons and a continuous operation over several days of the synchrotron is achieved. Extra straight sections are added which serve mainly to supply space for RF cavities or for insertion devices. The insertion devices are specially designed successions of magnets and serve in synchrotrons mainly for the creation of intense X-ray radiation. At the positions of the bending magnets and of the insertion devices the *beamlines* can be installed. Optical elements in the beamlines transport the emission to the sample position where the experiments are performed.

A consequence of the emission of the synchrotron radiation is the damping of the spatial electron distribution inside the RF-bucket's acceptance. Due to emission the electrons tend to lose transverse momentum but they regain energy only in the longitudinal channel because the acceleration of the RF-cavity is in the longitudinal direction. This process is called *radiation damping*. On the other hand emission of a photon is a stochastic effect. Combined with dispersion this leads to longitudinally and transverse growth. In synchrotrons this leads to a tendency to widen the transverse distribution of the electrons. This effect is called *quantum excitation*.

Assuming the orbit is stable an equilibrium between radiation damping and quantum excitation will be achieved. This process can be modelled as a stochastic diffusion using the Fokker-Planck equation for the electron distribution or the Langevin equation for single electrons. Its solution is a six dimensional Gaussian electron phase space density. The phase space density describes the spatial and divergence distribution of the electrons as well as the deviation for the ideal momentum and the longitudinal distribution.

The phase space density can be calculated numerically using software such as Accelerator Toolkit(AT)[10] or Strategic Accelerator and Design(SAD)[11] to name only two. We point out that for our work the stochastic behavior described by *this distribution is of fundamental importance*. It is this fluctuation that leads to the phenomena of partial coherence. It is therefore justified to spend some words on it on the following pages.

2.1.2. Single electron dynamics

In classical mechanics an electron is completely described by its three spatial components and its three momenta. In beam dynamics this is expressed slightly different. One defines the ideal orbit of an electron. In this definition some non-ideal phenomena such as scattering on residual gas atom and electron energy fluctuations are neglected. The description of the electron is then in terms of horizontal x and vertical y transverse spatial, horizontal x' and vertical y' transverse divergence, particle momentum deviation δ and the longitudinal position s. The particle momentum deviation is defined as $\delta = (p - p_0)/p_0$ where p_0 is the ideal particle momentum. The six-dimensional phase space of the electrons describes the transverse coordinates of an electron having a momentum deviation δ from the ideal momentum and a longitudinal displacement s from its longitudinal origin. The longitudinal origin lies on some point of the ideal orbit. A six-dimensional *phase space vector* is given by:

$$\boldsymbol{u} = \begin{bmatrix} x \\ x' \\ y \\ y' \\ \delta \\ s \end{bmatrix}. \tag{2.5}$$

In linear beam dynamics the change of the phase space state of an electron in a storage ring within one turn can be described with the one-turn transfer matrix $\mathcal{M}$:

$$\boldsymbol{u}(l + C) = \mathcal{M}(l)\boldsymbol{u}(l) \tag{2.6}$$

here l is the evolution variable and C is the circumference of the ring. For simple or idealized beam optics, such as combinations of ideal dipoles and quadrupoles, analytical forms for $\mathcal{M}$ are known[27]. In practical cases $\mathcal{M}$ is calculated more accurately numerically with computer codes like AT or SAD. These calculations can simulate RF-cavities and can therefore account for radiation damping.

We can calculate the particle energy γ in units of m_0c^2 from the ideal particle momentum p_0 and the particle momentum deviation δ:

$$\gamma = \sqrt{1 + (p/(m_0c))^2} \approx \frac{p_0(1+\delta)}{m_0c} = \gamma_0(1+\delta) = \gamma_0\delta + \gamma_0 \tag{2.7}$$

where we used the fact that the electrons are ultra relativistic.

The full statistical description of the electrons in the beam is given by a distribution around the ideal orbit which we discuss in the next section.

2.1.3. Electron phase space distribution

The electron phase space distribution is the probability density describing an electron in the electron beam. It is of *central importance* for our statistical optics theory for synchrotrons. We may consider different distributions whose s-origin lies on different points of the ideal orbit. Whenever we speak about density in this section we mean the electron phase space density.

Let ρ denote the density. The probability P to find an electron inside a region T in the transverse $x - y$ plane having longitudinal variation smaller than s_0, divergence smaller than D and momentum deviation smaller than δ_0 is given by the integral of the density:

$$P = \int_T dxdy \int_{[-s_0,s_0]} ds \int_D dx'dy' \int_{[-\delta_0,\delta_0]} d\delta \; \rho(x, x', y, y', \delta, s). \tag{2.8}$$

Like every multidimensional probability density the integral over the full configuration is equal to 1. Physically this means that the electron is somewhere having some momentum.

We may also consider marginals. If we want to know if the electron is in some spatial region $T \times [-s_0, s_0]$ having any momentum deviation and any divergence we integrate Eq. 2.8 over the three-dimensional divergence and momentum deviation subspace. Because we integrate over an entire subspace this integral must be 1 and the probability is:

$$P = \int_T dxdy \int_{[-s_0,s_0]} ds \; \rho(x, y, s). \tag{2.9}$$

For synchrotron storage rings to a good approximation the density can be described as a six-dimensional Gaussian:

$$\rho(\boldsymbol{u}) = \frac{1}{(2\pi)^3\sqrt{\det \Sigma}} \exp\left(-\frac{1}{2}\boldsymbol{u}^T\Sigma^{-1}\boldsymbol{u}\right), \tag{2.10}$$

here Σ is the second order covariance matrix. The covariance matrix depends on the longitudinal position s. The elements of the covariance matrix σ_{ij} are the covariances of the random variables

$$i, j \in \{x, x', y, y', \delta, s\} : \sigma_{ij} = \mathrm{Cov}(i, j). \tag{2.11}$$

and we define

$$i \in \{x, x', y, y', \delta, s\} : \sigma_i = \sqrt{\sigma_{ii}}. \tag{2.12}$$

The covariance matrix Σ is the solution[12] of:

$$\mathcal{M}(l)\Sigma(l)\mathcal{M}(l)^T + B(l) = \Sigma(l) \tag{2.13}$$

here B is the diffusion matrix that models the quantum excitation and $\mathcal{M}$ should account for radiation damping.

For the calculations in this thesis we are mainly interested in the elements of the *inverse* of the covariance matrix M. We will denote its elements by m_{ij} or in matrix notation:

$$M = \Sigma^{-1} = \begin{bmatrix} m_{xx} & m_{xx'} & m_{xy} & m_{xy'} & m_{x\delta} & m_{xs} \\ m_{x'x} & m_{x'x'} & m_{x'y} & m_{x'y'} & m_{x'\delta} & m_{x's} \\ m_{yx} & m_{yx'} & m_{yy} & m_{yy'} & m_{y\delta} & m_{ys} \\ m_{y'x} & m_{y'x'} & m_{y'y} & m_{y'y'} & m_{y'\delta} & m_{y's} \\ m_{\delta x} & m_{\delta x'} & m_{\delta y} & m_{\delta y'} & m_{\delta\delta} & m_{\delta s} \\ m_{sx} & m_{sx'} & m_{sy} & m_{sy'} & m_{s\delta} & m_{ss} \end{bmatrix}. \tag{2.14}$$

The Σ matrix is always positive definite and symmetric. The surfaces of constant density are ellipsoids (see Fig. 2.3).

Synchrotron storage rings are often designed to have small couplings between longitudinal and transverse degrees of freedom. These couplings can not be completely eliminated everywhere but regions with very low couplings can be designed in which we consider the coupling negligible.

In what follows we establish a notation we will use throughout this thesis for the approximations we may use.
If there are negligible couplings between the longitudinal bunch size and the other beam param-

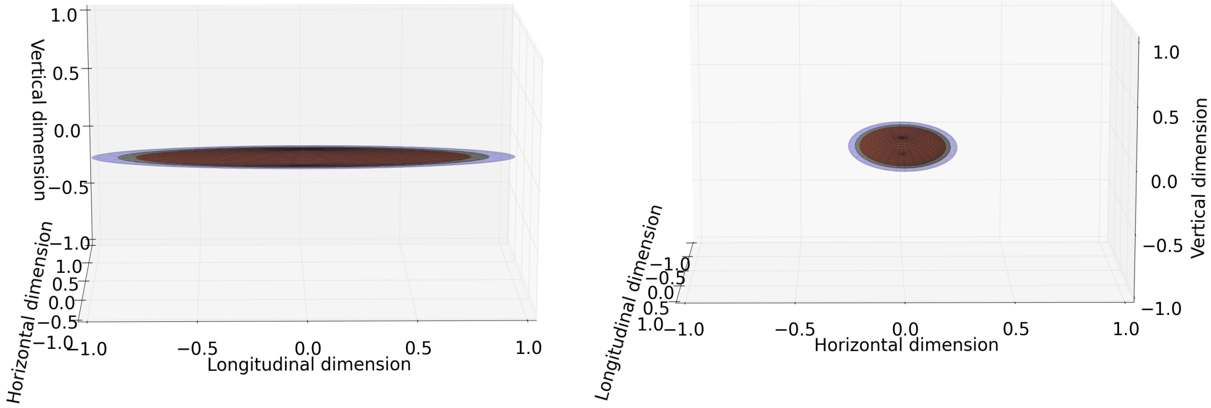

Figure 2.3.: Side view(left) and front view(right) of three constant density surfaces (red, yellow, blue) for a three dimensional Gaussian. Exemplary depicted is the 3D spatial subspace of the full 6D Gaussian density. We want to stress the fact that the spatial electron beam distributions for electron bunches is often much smaller in the vertical than in horizontal direction. The horizontal direction is usually much smaller than the longitudinal direction.

eters one may define the 5 × 5 matrix:

$$\boxed{M_5 = \begin{bmatrix} m_{xx} & m_{xx'} & m_{xy} & m_{xy'} & m_{x\delta} \\ m_{x'x} & m_{x'x'} & m_{x'y} & m_{x'y'} & m_{x'\delta} \\ m_{yx} & m_{yx'} & m_{yy} & m_{yy'} & m_{y\delta} \\ m_{y'x} & m_{y'x'} & m_{y'y} & m_{y'y'} & m_{y'\delta} \\ m_{x\delta} & m_{x'\delta} & m_{y\delta} & m_{y'\delta} & m_{\delta\delta} \end{bmatrix}} \tag{2.15}$$

Together with the reduced phase space vector $\tilde{\boldsymbol{u}}$:

$$\boxed{\tilde{\boldsymbol{u}} = \begin{bmatrix} x \\ x' \\ y \\ y' \\ \delta \end{bmatrix}} \tag{2.16}$$

we may define the five-dimensional phase space density:

$$\boxed{\rho_5(\tilde{\boldsymbol{u}}) = \frac{1}{(2\pi)^{\frac{5}{2}}\sqrt{\det M_5^{-1}}} \exp\left(-\frac{1}{2}\tilde{\boldsymbol{u}}^T M_5 \tilde{\boldsymbol{u}}\right).} \tag{2.17}$$

The five-dimensional phase space density ρ_5 will be important in our discussion of statistical optics of synchrotron emission in storage rings in chapter 3. The total electron phase space density is then approximately:

$$\rho(\boldsymbol{u}) \approx \rho_5(\tilde{\boldsymbol{u}}) \frac{1}{\sqrt{2\pi\sigma_s^2}} \exp\left(-\frac{s^2}{2\sigma_s^2}\right) \tag{2.18}$$

with $\sigma_s^{-2} = m_{ss}$.

We note that the dispersion function η is a transverse to longitudinal coupling. The approximation is good for achromatic lattices, in which the dispersion is minimized.

If there are no couplings of transverse and longitudinal dimension the M matrix takes a simpler form:

$$M = \begin{bmatrix} m_{xx} & m_{xx'} & m_{xy} & m_{xy'} & 0 & 0 \\ m_{x'x} & m_{x'x'} & m_{x'y} & m_{x'y'} & 0 & 0 \\ m_{yx} & m_{yx'} & m_{yy} & m_{yy'} & 0 & 0 \\ m_{y'x} & m_{y'x'} & m_{y'y} & m_{y'y'} & 0 & 0 \\ 0 & 0 & 0 & 0 & m_{\delta\delta} & m_{\delta s} \\ 0 & 0 & 0 & 0 & m_{s\delta} & m_{ss} \end{bmatrix}. \tag{2.19}$$

This form can be decoupled into a transverse part $M_\perp$ and longitudinal part $M_{||}$

$$M_\perp = \begin{bmatrix} m_{xx} & m_{xx'} & m_{xy} & m_{xy'} \\ m_{x'x} & m_{x'x'} & m_{x'y} & m_{x'y'} \\ m_{yx} & m_{yx'} & m_{yy} & m_{yy'} \\ m_{y'x} & m_{y'x'} & m_{y'y} & m_{y'y'} \end{bmatrix}; M_{||} = \begin{bmatrix} m_{\delta\delta} & m_{\delta s} \\ m_{s\delta} & m_{ss} \end{bmatrix} \tag{2.20}$$

and M is the direct sum of the transverse and longitudinal part:

$$M = M_\perp \oplus M_{||}. \tag{2.21}$$

If additionally the coupling between horizontal direction x and vertical direction y can be neglected Eq. 2.20 becomes:

$$M_\perp = \begin{bmatrix} m_{xx} & m_{xx'} & 0 & 0 \\ m_{x'x} & m_{x'x'} & 0 & 0 \\ 0 & 0 & m_{yy} & m_{yy'} \\ 0 & 0 & m_{y'y} & m_{y'y'} \end{bmatrix}. \tag{2.22}$$

In this case we may further separate the transverse M matrix into a horizontal and a vertical M matrix:

$$M_x = \begin{bmatrix} m_{xx} & m_{xx'} \\ m_{x'x} & m_{x'x'} \end{bmatrix} = \Sigma_x^{-1}; M_y = \begin{bmatrix} m_{yy} & m_{yy'} \\ m_{y'y} & m_{y'y'} \end{bmatrix} = \Sigma_y^{-1} \tag{2.23}$$

and

$$M_\perp = M_x \oplus M_y. \tag{2.24}$$

In this approximation we may define horizontal and vertical emittances by:

$$\begin{aligned} \epsilon_x &= \sqrt{\det \Sigma_x} = \sqrt{\sigma_x^2 \sigma_{x'}^2 - \sigma_{xx'}^2}, \\ \epsilon_y &= \sqrt{\det \Sigma_y} = \sqrt{\sigma_y^2 \sigma_{y'}^2 - \sigma_{yy'}^2}. \end{aligned} \tag{2.25}$$

We remark that this separation is in general not true everywhere and may be correct only approximately at some special positions of the ring. Some of these points are discussed in section 2.1.6.

A more general definition of the emittances for coupled dynamics is given by $\epsilon_\alpha = \frac{1}{2}\mathrm{tr}(G_\alpha \Sigma)$ with $\alpha \in \{1, 2, 3\}$ whereby tr denotes the trace and G_α are the so called invariants that depend on the eigenfunctions of the one-turn transfer matrix $\mathcal{M}$. The presentation of this formalism is, however, out of the scope of this thesis but can be found in [13].

2.1.4. Twiss parameters

When the dynamics are horizontally and vertically uncoupled and in the absence of dispersion it is possible to express the three independent elements of the symmetric 2x2 in terms of the so called *Twiss parameters* γ, α, β. The emittance is related to the Twiss parameters as follows:

$$i \in \{x, y\} : \epsilon_i = \left\langle \gamma_i i^2 + 2\alpha_i i i' + \beta_i i'^2 \right\rangle \tag{2.26}$$

where the average value is taken over the electron beam distribution. Theoretically the vertical emittance may be as small as $10^{-13}m$ but in reality it is about one percent of the horizontal emittance due to couplings between horizontal and vertical degrees of freedom. The relation between the Twiss parameters and the reduced Σ_i matrices are:

$$\Sigma_i = \epsilon_i^2 \begin{bmatrix} \beta_i & -\alpha_i \\ -\alpha_i & \gamma_i \end{bmatrix}. \tag{2.27}$$

In this formalism the beam size of an assumed Gaussian beam is calculated as

$$\sigma_b^{(i)}(s) = \sqrt{\epsilon_i \beta_i(s)}. \tag{2.28}$$

The β-functions can be numerically calculated from the one-turn transfer matrix $\mathcal{M}$. Let $\mathcal{M}_i$ be the one-turn transfer matrix for dimension i at longitudinal position s:

$$\mathcal{M}_i = \begin{bmatrix} C_i & S_i \\ C_i' & S_i' \end{bmatrix}. \tag{2.29}$$

The β-functions at position s are given by the solution of:

$$\left(\begin{bmatrix} C_i^2 & -2S_iC_i & S_i^2 \\ -C_iC_i' & S_iC_i' + C_iS_i' & -S_iS_i' \\ C_i'^2 & -2S_i'C_i' & S_i'^2 \end{bmatrix} - \mathcal{I} \right) \begin{bmatrix} \beta_i \\ \alpha_i \\ \gamma_i \end{bmatrix} = 0 \tag{2.30}$$

here $\mathcal{I}$ denotes the identity matrix.

The β-functions are often plotted like in Fig. 2.4. For the Twiss parameters one has always:

$$\beta_i \gamma_i - \alpha_i^2 = 1. \tag{2.31}$$

The α-function is the derivative of the β-function: $\alpha_i = -\frac{d}{ds}\beta_i(s)$.

2.1.5. Deformation of the phase space density

In a free drift, i.e. in the absence of magnetic fields, the Twiss parameters change as a function of the longitudinal coordinate s as follows:

$$\begin{aligned} \beta(s) &= \beta_0 - 2s\alpha_0 + \gamma_0 s^2, \\ \alpha(s) &= \alpha_0 - s\gamma_0, \\ \gamma(s) &= \gamma_0, \end{aligned} \tag{2.32}$$

where $\beta_0, \alpha_0, \gamma_0$ are the Twiss parameters at the beginning of the drift space, i.e. $s = 0$. In a free drift the velocities of the electrons do not change. This is seen from the constancy of γ. The linear change of α reflects a uniform rotation of the phase space ellipse. The reasoning is that slower and faster electrons are separated during the drift. Some examples of phase space density ellipse transformations are illustrated in Fig. 2.5.

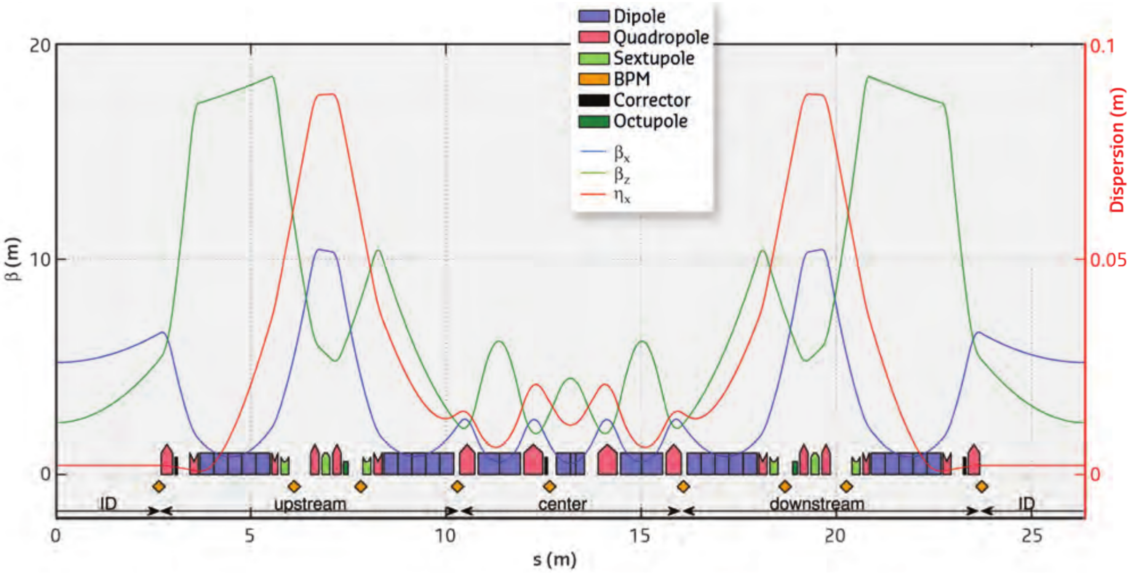

Figure 2.4.: Lattice plot for the EBS-ESRF standard cell taken from the Orange-Book[6].

The Eq. 2.28 describes the relation between the beam size and the β-function. The position of minimum beam size in a free drift section is called the *beam waist* (in a drift section). The size of the beam envelope decreases first until it reaches its minimum size at the waist position and increases afterwards. Since α is the derivative of the β-function the waist can only be located at positions where α vanishes. It follows from Eq. 2.32 that the waist is located at:

$$s_{\text{waist}} = \frac{\alpha_0}{\gamma_0}. \tag{2.33}$$

2.1.6. Distinguished points for undulator calculations

Usually synchrotrons have straight sections between FODO like cells. These sections provide place for insertion devices or diagnostics tools. In the middle of the straight section a symmetry point can be found in which the beta functions acquire their minimum value and α vanishes. This implies $\sigma_{xx'} = \sigma_{yy'} = 0$. Furthermore we assume that there is no coupling between the vertical and horizontal dimensions due to the storage ring design and that the longitudinal and transverse couplings vanish[1] because of low dispersion in the straight section. The transverse density ρ_{sp} at the symmetry point takes then the simple form:

$$\rho_{sp}(x, x', y, y') = \prod_{i \in \{x, x' y, y'\}} \frac{1}{\sqrt{2\pi\sigma_i^2}} \exp\left(-\frac{i^2}{2\sigma_i^2}\right) \tag{2.34}$$

with $\sigma_i^{-2} = m_{ii}$ because $M_\perp$ is a pure diagonal matrix. This position is interesting because under additional approximations and if an undulator is placed with its center at the symmetry point two theoretical simplifications fall together: one for the electron beam and one for the radiation produced by an undulator (see [8]).

In reality, however, this will often not be the case; if for instance several undulators are placed in a single straight section. Depending on the number and the length of the undulator, none of

---

[1] We will later discuss that weak couplings of the longitudinal spatial coordinate to the transverse coordinates do not change the result.

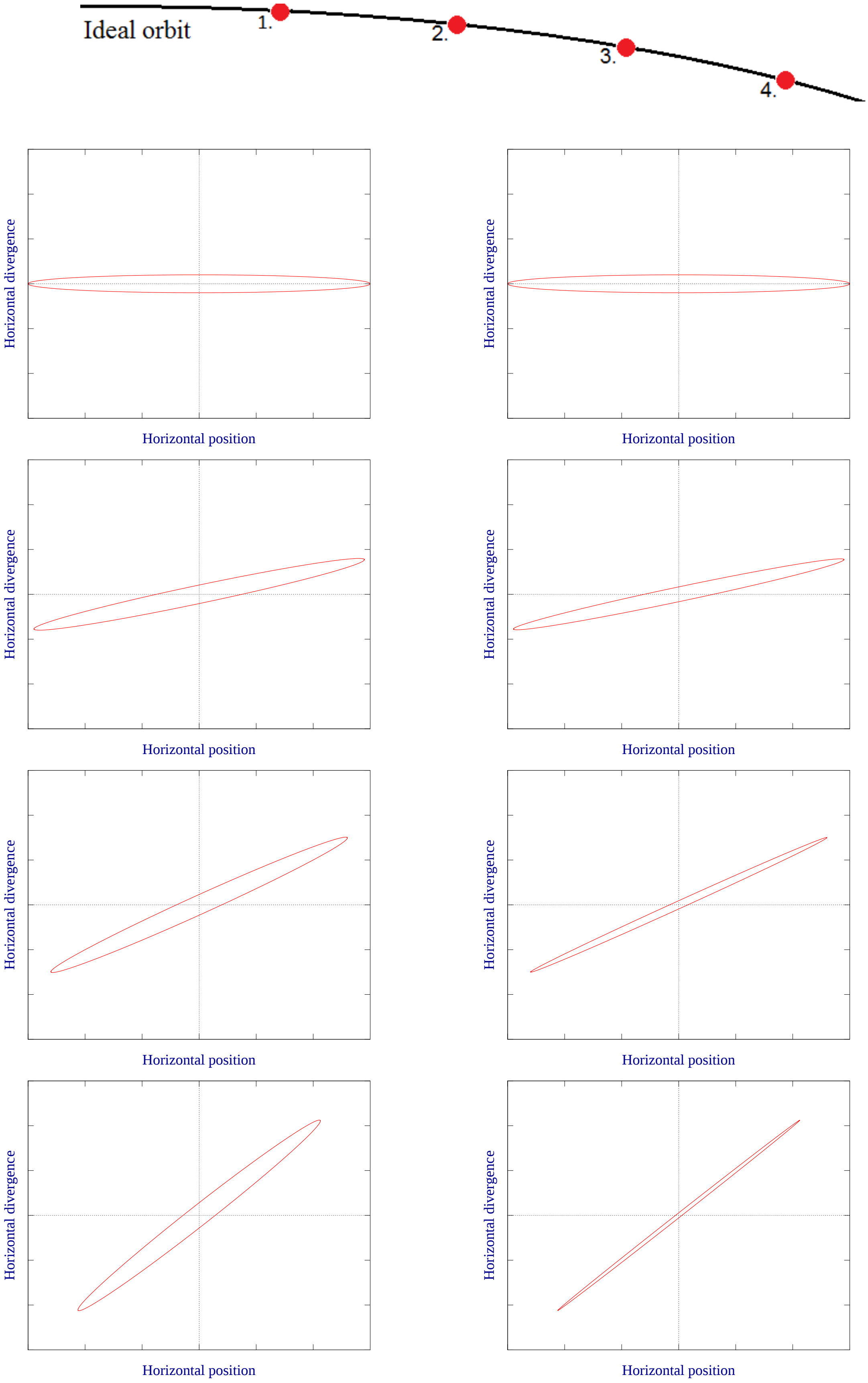

Figure 2.5.: Two examples of possible changes of the surface of constant density for a 2D Gaussian in dependence of the longitudinal position in the ring. Depicted are the rotation of the ellipse(left) and rotation and simultaneous shrinking of one dimension(right).

them may be centered at the symmetry point.
As a first correction we may therefore assume couplings between position and momentum in each dimension. In this case the transverse density $\rho_\perp$ takes the form

$$\rho_\perp(x,x',y,y') = \frac{1}{(2\pi)^2\sqrt{\det M_x^{-1}\det M_y^{-1}}}\exp\left(-\frac{1}{2}[x,x']M_x\begin{bmatrix}x\\x'\end{bmatrix}-\frac{1}{2}[y,y']M_y\begin{bmatrix}y\\y'\end{bmatrix}\right). \tag{2.35}$$

2.1.7. The ESRF-EBS upgrade

The ESRF Extremely Brilliant Source(EBS) is the on-going source upgrade of the ESRF lattice. In different stages the upgrade is planned to last until 2022. One of the main objectives is to reduce the horizontal emittance by at least a factor of 30[6]. The new lattice will have vertical emittance and energy spread comparable to the current lattice. The aim is to create brighter synchrotron radiation with improved coherence properties. This will allow smaller photon beam foci, thus coherence-based techniques like CDI, ptychography and XPCS will profit from increased flux. From the technical point of the view the bending magnets in the current double bend achromats lattice will be replaced by multiple but less strong bending magnetics. These kinds of lattices are called multi-bend achromats[14]. The splitting of the bending magnet into smaller magnets will reduce the total dispersion of the storage ring which in consequence leads to the desired reduction of emittance.

The aim of this thesis is the development of an algorithm that allows the simulation of the statistical properties of the synchrotron emission for the purpose of beamline design. In order to be applicable to beamline design studies, this algorithm has to run on modern computers in reasonable computation time. This algorithm can help beamline designers in the conception of their beamlines and it allows the usage of the shutdown time during the physical upgrade of the storage ring for the plannings of the beamline such that they are conceptually ready once the upgrade is finished.

2.1.8. The beam settings used throughout this thesis

The electron beam settings used within this thesis are tabulated in Table. 2.1

Symmetry point:

Name	$\sigma_x[\mu m]$	$\sigma'_x[\mu\text{rad}]$	$\sigma_y[\mu m]$	$\sigma'_y[\mu\text{rad}]$	Energy spread σ_δ
ESRF-EBS	27.2	5.2	3.4	1.4	$0.95\cdot10^{-3}$
High beta	387.8	10.3	3.5	1.2	$1.06\cdot10^{-3}$
Low beta	37.4	106.9	3.5	1.2	$1.06\cdot10^{-3}$

Finite alpha:

$\sigma_x[\mu m]$	$\sigma'_x[\mu\text{rad}]$	$\sigma_{xx'}$[pmrad]	$\sigma_y[\mu m]$	$\sigma'_y[\mu\text{rad}]$	$\sigma_{yy'}$[prad]	Energy spread σ_δ
30.6	4.4	-14.2	3.8	1.4	-1.4	$0.95\cdot10^{-3}$

Table 2.1.: Electron beam settings used for the calculations in this thesis. The symmetry point settings are given in terms of the standard deviations[6]. The finite alpha settings for the ESRF-EBS lattice are given in terms of the standard deviations and the elements of the covariance matrix that were extracted from internal data provided by the Accelerator Source Division of the ESRF.

2.2. Synchrotron radiation

This section describes the main characteristics of the synchrotron radiation (power, spectral and angular distribution) starting from basic concepts. We review the physics of some of the most important devices for synchrotrons: bending magnets and insertion devices. Both are used to produce X-ray radiation. While the main role of bending magnets is to keep the electrons on their orbit; the insertion devices are specifically dedicated to produce high flux.

2.2.1. Power emitted by accelerated charged particles

Synchrotron radiation is the electromagnetic radiation emitted by accelerated charged particles. In circular accelerators, the particles are moving in a non-rectilinear trajectory (cf Fig. 2.2), therefore they are centripetally accelerated. Most of practical results of the synchrotron radiation can be obtained using classical electrodynamics (see for instance [17]).

The power radiated by a *non-relativistic* accelerated charge is given by the Larmor formula. For an electron, the power emitted is [17]:

$$P = \frac{1}{6\pi}\frac{e^2}{c^3\epsilon_0}\left\|\dot{\boldsymbol{v}}\right\|^2 \tag{2.36}$$

where e is the electron charge, c is the speed of light, and $\dot{\boldsymbol{v}}$ is the acceleration. The direction distribution of the radiation is given by:

$$\frac{dP}{d\Omega} = \frac{e^2}{(4\pi)^2c^3\epsilon_0}\left\|\dot{\boldsymbol{v}}\right\|^2\sin^2\theta \tag{2.37}$$

where Ω is the solid angle and θ is the angle between the acceleration vector and the observation direction. If the particle moves along a circular trajectory with curvature radius R ($\left\|\dot{\boldsymbol{v}}\right\|^2 = (v^2/R)^2 = R^2\omega^4$), there is no radiation along the radial direction, and the directional map of radiated power looks like a donut with axis in the radius of curvature and no hole inside. The radiation of a non-relativistic electron has a dipole nature, and the power emitted looks like a torus (see figure 2.6a).

The Larmor formula is not invariant under Lorentz transformation, which preserves the constancy of the speed of light when changing from one reference system to another. Therefore, the Larmor formula is not valid for relativistic particles, in particular for ultrarelativistic particles like electrons circulating in storage rings at velocities close to that of the light.

A generalized Larmor formula can be obtained from the Maxwell equations using covariance arguments. This generalized formula shows[17] that the contribution to the total radiation of the linear component of the particle acceleration (i.e., in the direction of $\boldsymbol{v}$) is negligible compared to the contribution of the normal (centripetal) component (due to the curved trajectory). For a relativistic charge moving in a circular trajectory with the radiated power is:

$$P = \frac{1}{6\pi}\frac{e^2c}{\epsilon_0}\frac{\beta^4\gamma^4}{R^2} \tag{2.38}$$

where β is v/c and γ is the Lorentz factor for the electron ($\gamma = (1-\beta^2)^{-1/2}$. In practical units $\gamma \approx 1957E[GeV]$).

An uniform magnetic field B in a circular electron storage ring forces an electron to describe a circular trajectory. The radius of curvature is:

$$R = \frac{p}{eB} = \frac{m_0\beta\gamma c}{eB} \tag{2.39}$$

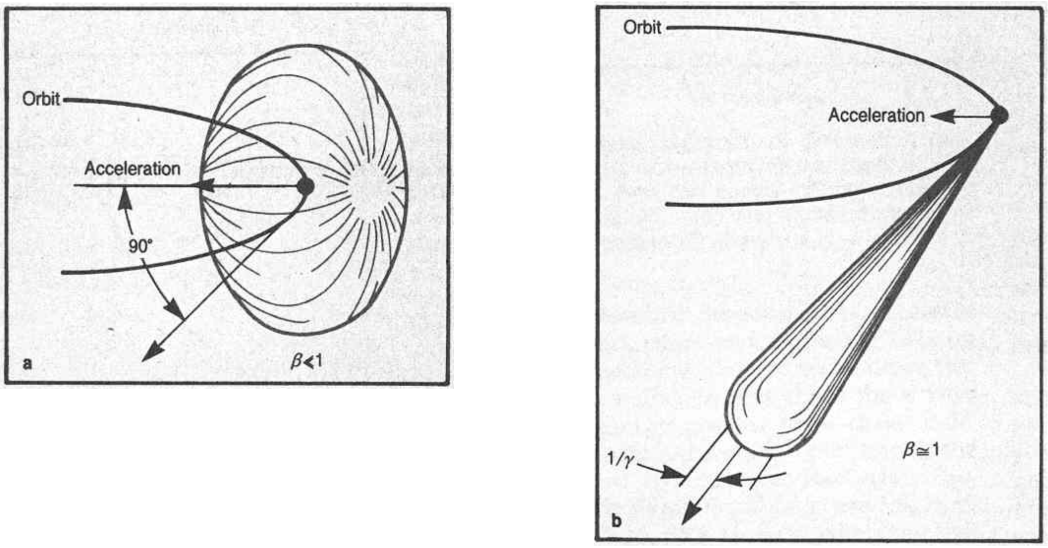

Figure 2.6.: Radiation pattern of electrons in a circular orbit. The left diagram shows the pattern for non-relativistic electrons predicted by Joseph Larmor. The left diagram shows the pattern for highly relativistic electrons: the radiation is concentrated in a narrow cone; the spectrum also extends to very high frequencies. Pictures taken from [18].

which is expressed in practical units as:

$$R[m] \approx 3.3356 E[GeV]/B[T]. \tag{2.40}$$

The energy radiated by an electron in a storage ring along one turn is the product of the radiated power multiplied by the time the electron takes for performing a complete revolution. We obtain:

$$\delta E = \frac{e^2 \beta^3}{3\epsilon_0} \frac{\gamma^4}{R}. \tag{2.41}$$

In circular accelerators, this is the lost energy that has to be supplied by the RF-cavity in order to keep the electron energy constant. We remark the fast growth of losses when the electron energy increases. It is proportional to the fourth power of the energy. The radiation power depends strongly on the mass of the radiating particle which scales like $1/m^4$ at a given total energy $\gamma = mc^2$. For protons, the emitted power compared to electrons of the same energy is $P_p/P_e = (m_e/m_p)^4 = (1/1834)^4 = 8.8 \cdot 10^{-14}$.

This equation can be written in practical units for ultra-relativistic electrons $\beta \approx 1$:

$$\delta E[keV] = 88.4715 \frac{E[GeV]^4}{R[m]}. \tag{2.42}$$

This result describes a single electron. When multiplied by the storage ring current I one obtains the total radiated power in a single turn:

$$P[kW] = \delta E[keV] I[A]. \tag{2.43}$$

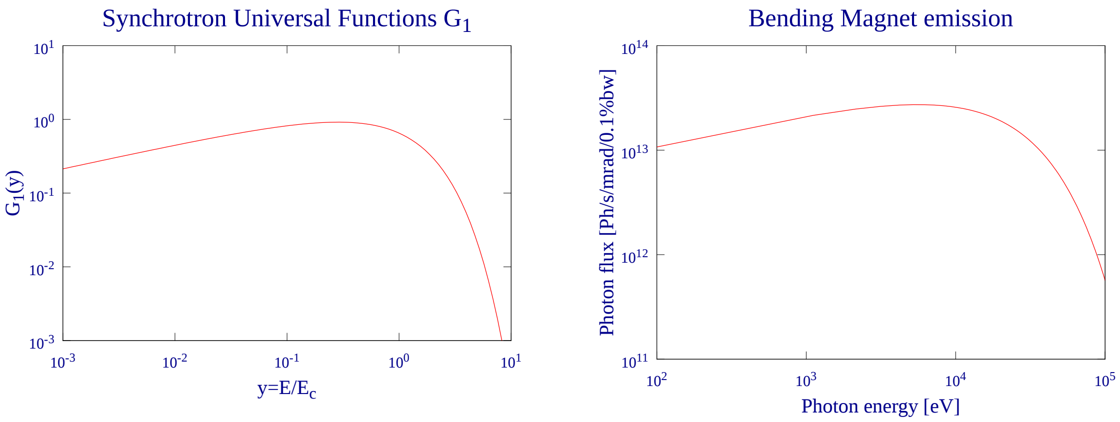

Figure 2.7.: Left: Universal G_1 function for bending magnet spectrum (Eq. 2.47). Right: Spectrum of the ESRF bending magnet (Eq. 2.48).

2.2.2. Spectral distribution of synchrotron radiation emitted by ultra-relativistic electrons

The power radiated by a charged particle moving in a circular path was obtained by Schott[19] before synchrotron radiation was known. The equation is known as *Schott formula* and is valid for all values of particle velocity, thus including relativistic electrons. Following [20] the differential radiation in a solid angle $d\Omega = \sin\theta d\theta d\phi$ is given by a sum of harmonics with the form:

$$dP(\nu,\theta) = \frac{ce^2\beta^2}{2\pi R^2}\nu^2 \left\{\cot^2\theta J_\nu^2(\nu\beta\sin\theta)\beta^2 J_\nu'^2(\nu\beta\sin\theta)\right\} d\Omega, \tag{2.44}$$

where θ is the radiation angle and ν is the harmonic number ($\nu = \omega/\omega_0$ with ω the radiation frequency and ω_0 the electron frequency of rotation) and J and J' the Bessel functions.

In the case of ultra-relativistic electrons[20], the Bessel functions can be replaced by their asymptotic form so the radiated power by a singular electron in a circular orbit is approximately:

$$dP(\nu,\theta) = \frac{ce^2}{6\pi^3 R^2}\nu^2 \left\{\epsilon^2 K_{2/3}^2\left(\frac{\nu}{3}\epsilon^{3/2}\right) + \epsilon\cos^2\theta K_{1/3}^2\left(\frac{\nu}{3}\epsilon^{3/2}\right)\right\} d\Omega, \tag{2.45}$$

where $\epsilon = 1 - \beta^2\sin^2\theta$ and K are the Bessel functions of the third kind. This can be integrated over the 4π solid angle into the well known equation:

$$P(\nu) = \frac{2ce^2\gamma^3}{3R^2}\frac{9\sqrt{(3)}}{8\pi}G_1(y), \tag{2.46}$$

where

$$G_1(y) = y\int_y^\infty K_{\frac{5}{3}}(x)dx \tag{2.47}$$

and y is the ratio of the emitted radiation frequency ω over the *critical frequency* $\omega_c = (3/2)\gamma^3\omega_0 = 3\gamma^3 c/(2R)$ thus $y = \omega/\omega_c = \nu\omega_0/\omega_c$. This function is shown in Fig. 2.7. In practical units, the photon critical energy is $\epsilon_c[keV] = 2.2183E[GeV]^3/R[m]$.

Converting power in number of photons per second in a given energy bandwidth (typically 0.1% of the photon energy), considering the emission of an electron over an given arc (typically 1 *mrad*) and multiplying by the total number of electrons given by the electron current we obtain:

$$N[\text{photons/s/0.1\%bw/mrad}] = 9\sqrt{3}\ 10^{12}\frac{e^2}{hmc^3}E[GeV]I[A]G_1(\omega/\omega_c) \approx \\ 2.4605\ 10^{13}E[GeV]I[A]G_1(\omega/\omega_c) \tag{2.48}$$

Fig. 2.7b shows the spectrum for the ESRF bending magnet. The critical frequency ω_c divides the power spectrum in two parts each one with one half of the total power. Numerical calculations show that the maximum in the spectrum $G(y)$ is attained at $y \approx 1/3$.

2.2.3. Polarization properties

The asymptotic version of the Schott's formula including polarization components (Eq. 2.45) can be written[20]:

$$dP(\nu,\theta) = \frac{ce^2}{6\pi^3R^2}\nu^2\left\{l_2\epsilon^2K^2_{2/3}\left(\frac{\nu}{3}\epsilon^{3/2}\right) + l_3\epsilon\cos^2\theta K^2_{1/3}\left(\frac{\nu}{3}\epsilon^{3/2}\right)\right\}d\Omega, \tag{2.49}$$

where l_2 and l_3 are the parameters describing polarization (horizontal linear polarization or σ-polarization: $l_2 = 1; l_3 = 0$, vertical linear polarization or π-polarization: $l_2 = 0; l_3 = 1$, circular polarization: $l_2 = \pm l_3 = 1/\sqrt(2))$.

The integration over the angles and frequencies leads to:

$$W_i = W\left(\frac{7}{8}l_2^2 + \frac{1}{8}l_2^3\right). \tag{2.50}$$

That means that 7/8 of the total power is σ-polarized (i.e. the electric vector lies in the orbit plane) and 1/8 of the total intensity is π-polarized (electric vector is perpendicular to the orbit plane). This proportion varies with the wavelength.

2.2.4. Angular distribution

The angular dependence of the radiations at a particular photon frequency is given by Eq. 2.49. For a given photon energy, the radiation is symmetrical with respect of the ψ angle (measured with respect to the plane of the orbit, the complementary of θ in Eq. 2.49). The width of this distribution reduces when the photon energy increases.

Integration over the frequency of Eq. 2.49 results in [20]:

$$dW(\psi) = \frac{ce^2\gamma^{5/2}}{2\pi R^2}f(\xi)d\Omega, \tag{2.51}$$

where we used a reduced angle $\xi = \gamma\cos\theta \approx \gamma\psi$, and the function:

$$f(\xi) = \frac{7}{16(1+\xi^2)^{5/2}}l_2^2 + \frac{5\xi^2}{16(1+\xi^2)^{7/2}}l_3^2 + \frac{4\xi}{\pi\sqrt{3}(1+\xi^2)^3}l_2l_3 \tag{2.52}$$

from where the angular distribution for all polarization states can be obtained. The total power can be calculated adding the σ $(l_2 = 1, l_3 = 0)$ plus the π-polarization components $(l_2 = 0, l_3 = 1)$. Fig. 2.8 shows the f function for σ and π polarization. The result looks similar to a Gaussian with standard deviation $\sigma_\xi = 0.608$ [21].

To understand qualitatively the synchrotron radiation emission we may use basic concepts of the Lorentz transformation. The radiation emitted by non-relativistic electrons has dipole nature. The spatial distribution of the radiation emitted from ultra-relativistic electrons is of different

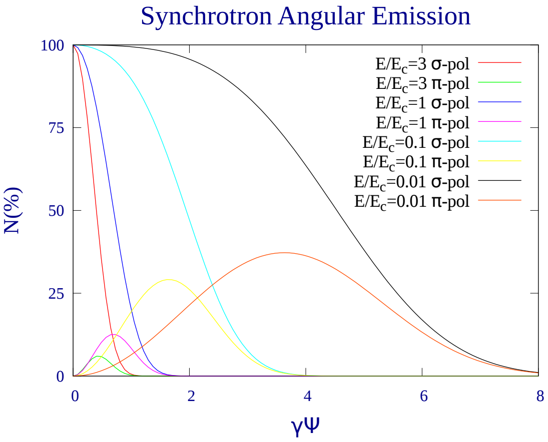

Figure 2.8.: The f function (Eq. 2.52) for σ and π polarization (results have been normalized to the total value at $\gamma\Psi = 0$)

nature. We showed the quantitative calculations in the frame of the classical electrodynamics. Basic relativistic principles motivate that the radiation by ultra-relativistic electrons is confined in a narrow cone. In fact, if we assume that the radiation is observed at an angle ψ' respect to the direction of the velocity of the electron in a reference frame where the observer is at rest then the angle ψ at which the radiation is observed in the laboratory frame can be found from the law of velocity addition:

$$\sin(\psi) = \frac{\sqrt{1-\beta^2}\sin\psi'}{1+\beta\cos\psi'}. \tag{2.53}$$

Considering that the maximum power associated with dipolar radiation is at $\psi' = \pi/2$, we obtain

$$\sin\psi \approx \delta\Psi \approx \sqrt{1-\beta^2} = \frac{m_0c^2}{E} = \gamma^{-1}. \tag{2.54}$$

The synchrotron radiation for photon energies around the critical energy E_c from an electron moving at a relativistic speed is concentrated within a narrow cone centred in the instantaneous direction of electron motion, and forward directed as shown in Fig. 2.6b.

2.3. Synchrotron radiation devices

In the following sections we give a brief overview of the devices used in a synchrotron to create X-ray emission. The presentation is largely based on [22, 23].

2.3.1. Electron trajectories

We present the geometries and the electron trajectories of the devices for the production of emission in synchrotrons.

2.3.1.1. Bending magnets

The simplest and most common realization of bending magnets is the dipole magnet. Idealized a dipole magnet has a constant vertical magnetic field

$$\boldsymbol{B} = (0, B_y, 0). \tag{2.55}$$

The general equation of motion for an electron in a magnetic field is:

$$\frac{d\boldsymbol{p}}{dt} = -e(\boldsymbol{v} \times \boldsymbol{B}). \tag{2.56}$$

here $\boldsymbol{p}$ is the electron momentum, $\boldsymbol{v}$ its velocity and $\boldsymbol{B}$ the magnetic field. For a dipole magnet we therefore have:

$$\dot{\boldsymbol{p}} = eB_y \begin{pmatrix} -v_s \\ 0 \\ v_x \end{pmatrix} \tag{2.57}$$

with

$$\boldsymbol{v} = \begin{pmatrix} v_x \\ v_y \\ v_s \end{pmatrix}. \tag{2.58}$$

Ideally the electron enters the dipole magnet without initial transverse velocity. With this assumption the trajectory is given by:

$$\boldsymbol{r}(t) = \begin{pmatrix} \rho\cos(\omega_b(t-t_0)) + x_0 \\ 0 \\ \rho\sin(\omega_b(t-t_0)) + s_0 \end{pmatrix} \tag{2.59}$$

with $\omega_b = \frac{eB_y}{\gamma m_e}$ and $\rho = \frac{\beta c}{\omega_b}$. The trajectory describes a circle in the x-s plane. During the motion the electron radiates and the radiation follows the general characteristics discussed in the previous section, i.e. it is very collimated and highly polarized.

2.3.1.2. Insertion devices: wigglers and undulators

Modern synchrotrons use wigglers and undulators to create particular intense X-ray radiation. The name insertion device stems from the fact that the first devices of these kinds where used in particle colliders and these devices could be inserted or removed when they where needed to create synchrotron radiation. Ideally an insertion device for the purpose of synchrotron radiation creation should have negligible influence on the beam dynamics, i.e. it should not introduce extra deviations of the particle trajectory or velocity outside the insertion device. In equations this is approximately expressed as $\int ds' B(s') = 0$ and $\int ds \int^s ds' B(s') = 0$. Theoretically the description of wigglers and undulators are rather similar. Undulator are wigglers with many oscillations and

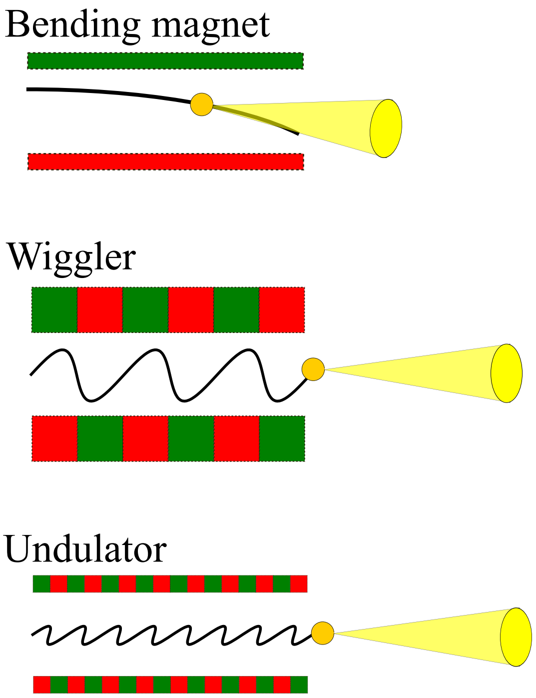

Figure 2.9.: Schematic illustration of a bending magnet, a wiggler and an undulator.

generally shorter period length. We restrict our discussion to planar vertical insertion device, i.e. the magnetic field vector lies in a vertical plane.

The schematic view of a planar wiggler and a planar undulator is depicted in Fig. 2.9. We will restrict our presentation to the idealized cases of an arrangement of alternating magnets that create a perfect sinusoidal magnetic field in the vertical direction. This magnetic field leads to a sinusoidal trajectory in the horizontal plane. In the derivation that follows, we follow strongly the ideas given in [22, 23]. For a vertical planar wiggler the magnetic field is ideally given by:

$$\boldsymbol{B} = \left(0, \hat{B}\cos\left(2\pi\frac{s}{\lambda_u}\right), 0\right) \tag{2.60}$$

where λ_u is the insertion device period length. With this magnetic field the transverse velocities are given by:

$$v_x(s) = \frac{e}{\gamma mc}\int_{-\infty}^{s} ds' B_y(s'), \tag{2.61}$$

$$v_y(s) = \frac{e}{\gamma mc}\int_{-\infty}^{s} ds' B_x(s'). \tag{2.62}$$

The trajectory can then be derived from the integral over the velocity.

In the case at hand we arrive at the velocity:

$$\begin{aligned} v_x &\approx \frac{Kc}{\gamma}\sin\left(2\pi\frac{s}{\lambda_u}\right), \\ v_y &= 0. \end{aligned} \tag{2.63}$$

with the *deflection parameter* or **undulator number** K:

$$K = \frac{e\hat{B}\lambda_0}{2\pi mc} \approx 93.3729 B[T]\lambda_u[m]. \tag{2.64}$$

The undulator number can be viewed as the amplitude of transverse velocity oscillations in units of $1/\gamma$.

The trajectory is then a sine:

$$x(s) = -\frac{Kc\lambda_u}{2\pi\gamma}\cos\left(2\pi\frac{s}{\lambda_u}\right). \tag{2.65}$$

We remark that the given magnetic field is an idealization and that field error inhomogeneities and edge effects are totally ignored[27]. Computer codes like the Synchrotron Radiation Workshop (*SRW*)[24] may include this effects numerically either from theoretical models or experimentally measured data.

2.3.2. Emission by an electron following an arbitrary trajectory

Single electron radiation can be calculated using the Lienard-Wiechert potentials[17]:

$$\begin{aligned} \Phi(\boldsymbol{r},t) &= \left.\frac{e}{4\pi\epsilon_0\left\|\boldsymbol{r}-\boldsymbol{R}(\tau)\right\|}\right|_{ret} \\ A(\boldsymbol{r},t) &= \left.\frac{e\boldsymbol{v}(\tau)}{4\pi\epsilon_0\left\|\boldsymbol{r}-\boldsymbol{R}(\tau)\right\|}\right|_{ret} \end{aligned} \tag{2.66}$$

with the retarded time τ:

$$\tau = t - \frac{\boldsymbol{r}-\boldsymbol{R}(\tau)}{c} \tag{2.67}$$

where $\boldsymbol{r}$ is the observation point and $\boldsymbol{R}$ is the electron position.
In the frequency domain the potentials become:

$$\begin{aligned} \hat{\Phi}(\boldsymbol{r},\omega) &= \frac{e}{4\pi\epsilon_0}\int_{-\infty}^{\infty} d\tau\frac{\exp(i\omega(\tau+\left\|\boldsymbol{r}-\boldsymbol{R}(\tau)\right\|/c))}{\left\|\boldsymbol{r}-\boldsymbol{R}(\tau)\right\|}, \\ \hat{A}(\boldsymbol{r},\omega) &= \frac{e}{4\pi\epsilon_0 c}\int_{-\infty}^{\infty} d\tau\boldsymbol{v}\frac{\exp(i\omega(\tau+\left\|\boldsymbol{r}-\boldsymbol{R}(\tau)\right\|/c))}{\left\|\boldsymbol{r}-\boldsymbol{R}(\tau)\right\|}. \end{aligned} \tag{2.68}$$

The electric field in frequency domain can be derived from the potentials:

$$\boldsymbol{E}(\boldsymbol{r},\omega) = -\nabla\Phi(\boldsymbol{r},\omega) + i\omega\boldsymbol{A}(\boldsymbol{r},\omega). \tag{2.69}$$

The electric field becomes:

$$\boldsymbol{E}(\boldsymbol{R},\omega) = \frac{ie\omega}{4\pi c\epsilon_0}\int\left[\frac{\boldsymbol{n}\times[(\boldsymbol{n}-\dot{\boldsymbol{r}})\times\ddot{\boldsymbol{r}}]}{(1-\dot{\boldsymbol{r}}\boldsymbol{n})^2} + \frac{c}{\gamma^2 R}\frac{(\boldsymbol{n}-\dot{\boldsymbol{r}})}{(1-\dot{\boldsymbol{r}}\boldsymbol{n})^2}\right]e^{i\omega(t-\boldsymbol{n}\boldsymbol{r}/c)}dt \tag{2.70}$$

where $\boldsymbol{r}(t)$ is the electron trajectory and $\boldsymbol{n}(t) = \boldsymbol{R}-\boldsymbol{r}(t)/\left\|\boldsymbol{R}-\boldsymbol{r}(t)\right\|$ is the unit vector pointing from the particle to the observation point. In the ultra-relativistic limit the second term is usually negligible and one arrives at:

$$\boldsymbol{E}(\boldsymbol{R},\omega) = \frac{ie\omega}{4\pi c\epsilon_0}\int\left[\frac{\boldsymbol{n}\times[(\boldsymbol{n}-\dot{\boldsymbol{r}})\times\ddot{\boldsymbol{r}}]}{(1-\dot{\boldsymbol{r}}\boldsymbol{n})^2}\right]e^{i\omega(t-\boldsymbol{n}\boldsymbol{r}/c)}dt. \tag{2.71}$$

We remark that far field approximations to this formula are known which make the integral significant easier. Additionally, for undulators the big number of periods allow further approximations[8]. These analytical approximations lead to rather complicated expressions that involve integrals which can not be solved in closed form. Additionally, they impose extra constraints, e.g. on the

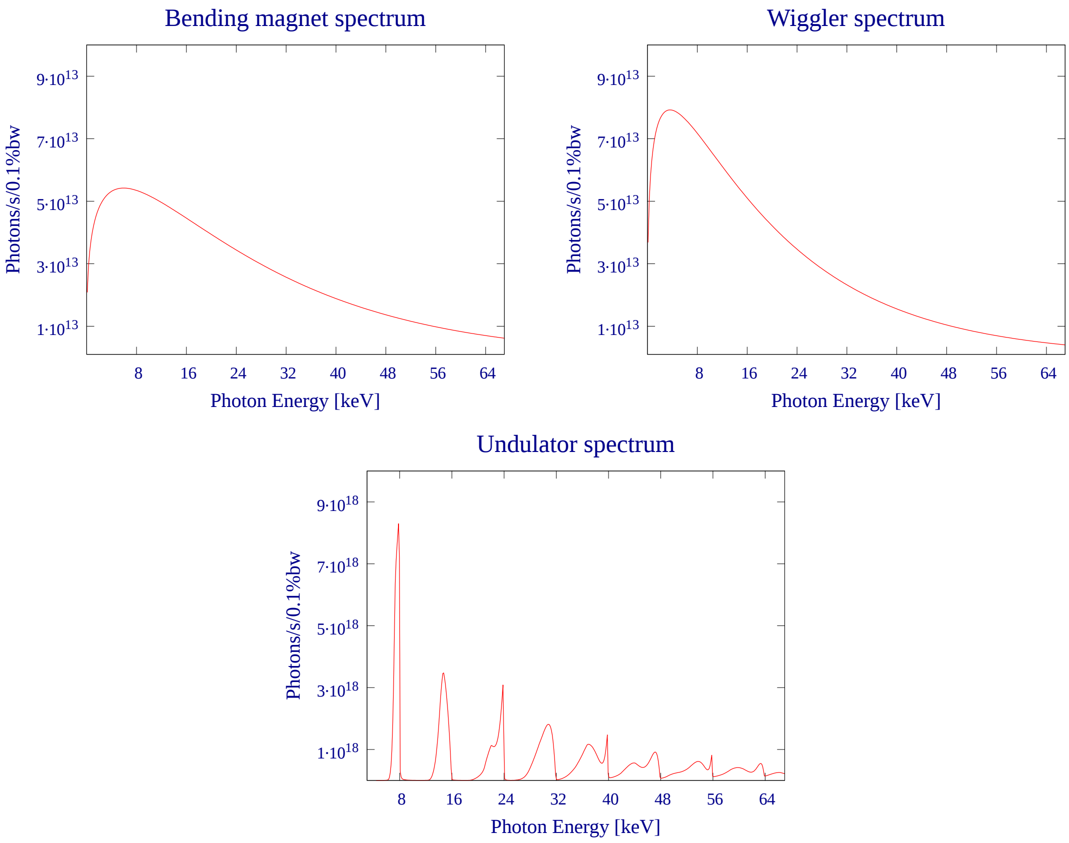

Figure 2.10.: Typical emission spectra of a bending magnet(left), a wiggler(right) and an undulator(bottom). For the undulator at about every multiple of 8keV one can see the spectral peaks at the energies of the harmonics of this undulator.

form of the magnetic field or the distance of the observer. On the other hand, computer codes like SRW[24] or pySRU[25] can solve Eq. 2.70 and Eq. 2.71 directly without particular computational difficulties. In the scope of this thesis we decided therefore to calculate the radiation directly by Eq. 2.71 because from the numerical perspective the approximations mentioned before do not add notable computational benefit but add unnecessary constraints.

2.3.3. Emission spectra

The emission spectra of a bending magnet and a wiggler look rather similar. They consist of one bump that reaches its maximum and decrease afterwards (see Fig. 2.10 top). For an undulator instead the spectrum has several peaks that correspond to the *undulator harmonics* (see Fig. 2.10 bottom). The peaks are approximately equidistant. The peaks of the undulator emission can be understood from the harmonics of the electron motion in the undulator[26]. Because of the Lorentz space time transform the electron moving through the undulator experiences in its reference frame a periodic electromagnetic field with a period $\lambda'_u = \lambda_u/\gamma$ and therefore radiates at a frequency $\omega'_0 = 2\pi c\gamma/\lambda_u$. In the laboratory frame the frequency transforms as:

$$\omega_0 = 2\frac{\omega'_0}{1+\gamma^2\theta^2} \tag{2.72}$$

where θ is the angle of emission measured from the undulator axis. Higher harmonics of the electron motion result in a frequency multiplication n in the rest frame and equally in the laboratory

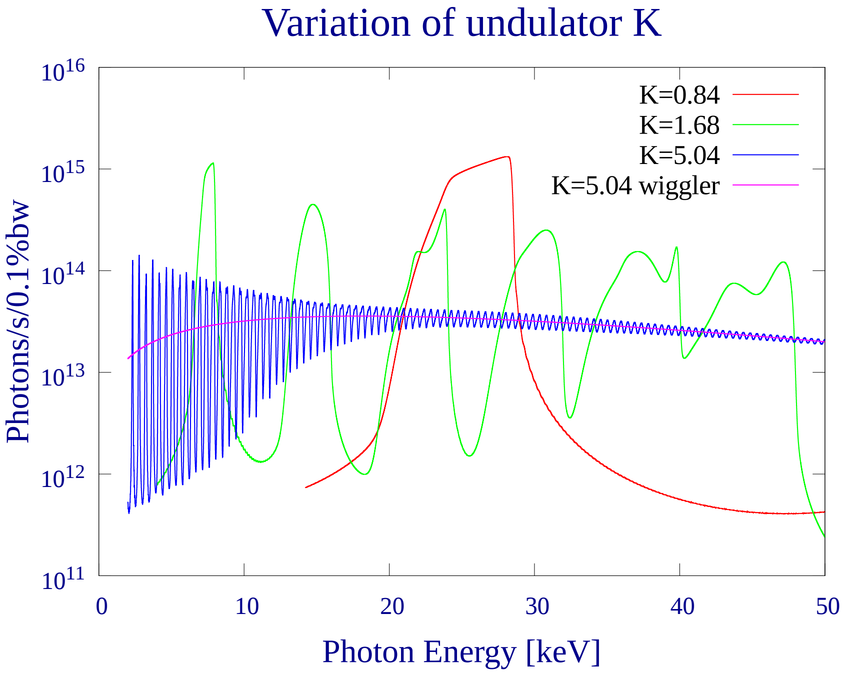

Figure 2.11.: Variation of the 2m long ESRF u18 undulator radiation for different K numbers. For large K the undulator spectrum approaches the wiggler spectrum.

frame:

$$\omega_n = 2\frac{n\omega_0'}{1+\gamma^2\theta^2}. \tag{2.73}$$

This result can be corrected for the decrease of the mean electron velocity along the undulator axis and results in:

$$\omega_n = n\frac{4\pi c\gamma^2}{\lambda_u}\frac{1}{1+\frac{K^2}{2}+\gamma^2\theta^2}. \tag{2.74}$$

For large undulator numbers K the undulator spectrum approaches a wiggler spectrum (see Fig. 2.11). For fixed undulator number K and variation of the primary slit size, i.e. the acceptance, the spectrum changes. The sharp spectral peaks smear out and other spectral maxima close to the harmonic energies are found. We will call these maxima *flux maxima* (see Fig. 2.12).

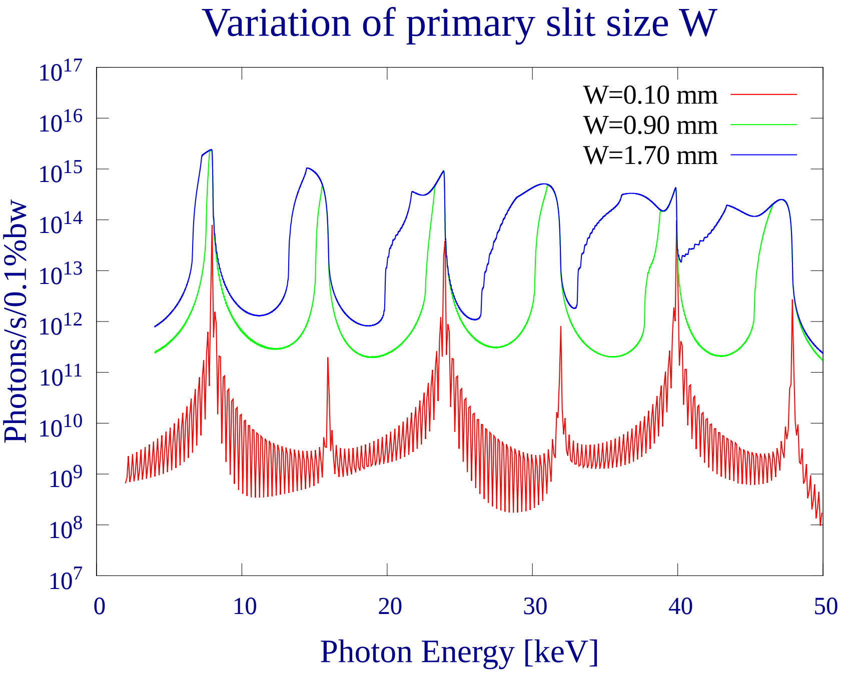

Figure 2.12.: Emission spectrum of a 2m long ESRF u18 undulator with $K = 1.68$. The quadratic shaped primary slit is varied in size W. With increasing slit size the spectral peaks are smeared out. For large slit sizes the maximum of the integrated flux does not coincide with the resonance energy.

2.3.4. The undulator settings used throughout this thesis

The undulators used throughout this thesis are tabulated in Table. 2.2. All the undulators are planar undulators with their magnetic fields directed along the vertical direction. We use always an electron beam energy of $E = 6.04\ GeV$[1]. The first harmonic of all the undulators lies at $E_0 = 7982\ eV$. The energy of the n-th harmonic is then $E_{n-1} = n \cdot E_0$. In practice one uses only the odd harmonics (1, 3, 5, . . .) because the even harmonics (2, 4, 6, . . .) have impractical intensity distribution, i.e. no on-axis radiation, and more complicated polarization properties.

Close to each harmonic one finds an energy of maximum flux which does not coincide with the harmonic energy. We use $E_{0\max} = 7920\ eV$ for the first maximum of the flux and $E_{2\max} = 23893\ eV$ for the third maximum of the flux.

Name	vertical K	period length [mm]	length [m]
ESRF u18 1m	1.68	18	1
ESRF u18 2m	1.68	18	2
ESRF u18 4m	1.68	18	4

Table 2.2.: Undulator settings used for calculations in this thesis. All the undulators are planar vertical undulators.

---

[1] Strictly for the ESRF-EBS it would be $E = 6.00GeV$.

2.4. Optics for synchrotron beamlines

In the previous section we established the equations to calculate the single electron emission for wiggler and undulator radiation. Because of the linearity of the Maxwell equations we may construct the electric field created by an electron bunch using these formulas and summing up the single electron emissions. Hence, we are able to theoretically calculate the emission of a bunch at some distance from the undulator exit plane. For practical purposes we would now be interested to model the free space propagation of the electric field of the radiation, i.e. how the synchrotron emission is transported from a plane to another in vacuum. Additionally, we are interested in the effect of apertures and the effect of focusing elements of a synchrotron beamline. These elements already allow to model in a simplified way the most important optical elements of a beamline.

We will review the underlying theory to model the before mentioned effects and present the techniques used in practise.

2.4.1. Wave optics

We restate briefly the derivation of the Fresnel and Fraunhofer diffraction equations. We follow the ideas given in [35, 36].

2.4.1.1. Propagation of radiation in free space

Let $E(\boldsymbol{r},\omega)$ be the electric field that satisfies the Helmholtz equation:

$$(\Delta + k^2)E(\boldsymbol{r},\omega) = 0. \tag{2.75}$$

here k is the wavenumber and ω is the frequency. In general the propagation of $E(\boldsymbol{r},\omega)$ in vacuum can be described with the knowledge of the Green's function G for the wave equation

$$\left(\Delta + k^2\right) G(\boldsymbol{r},\boldsymbol{r}_0) = -4\pi\delta(\boldsymbol{r}-\boldsymbol{r}_0). \tag{2.76}$$

For any Green's function G that satisfies the same continuity requirements as $E(\boldsymbol{r},\omega)$ the Green's identity

$$\int_V \phi\Delta\psi - \psi\Delta\phi = -\int_S dS\left(\phi\frac{\partial\psi}{\partial n} - \psi\frac{\partial\phi}{\partial n}\right) \tag{2.77}$$

where V is a continuous volume, S its closed surface, $\frac{\partial}{\partial n}$ is the differentiation along the inward normal, states:

$$\int_V dV\left(E(\boldsymbol{r},\omega)\Delta G - G\Delta E(\boldsymbol{r},\omega)\right) = -\int_S dS\left(E(\boldsymbol{r},\omega)\frac{\partial G}{\partial n} - G\frac{E(\boldsymbol{r},\omega)}{\partial n}\right). \tag{2.78}$$

The left hand side of Eq. 2.78 can be evaluated using the Helmholtz equation Eq. 2.75 and the defining property of a Green's function Eq. 2.76:

$$\int_V dV\left(E(\boldsymbol{r},\omega)\Delta G - G\Delta E(\boldsymbol{r},\omega)\right) = \int_V dV\left(E(\boldsymbol{r},\omega)(-4\pi)\delta(\boldsymbol{r}-\boldsymbol{r}_0)\right) = -4\pi E(\boldsymbol{r}_0,\omega) \tag{2.79}$$

Together with Eq. 2.78 this leads to the final propagation formula:

$$E(\boldsymbol{r}_0,\omega) = \frac{1}{4\pi}\int_S dS\left(E(\boldsymbol{r},\omega)\frac{\partial G}{\partial n} - G\frac{E(\boldsymbol{r},\omega)}{\partial n}\right). \tag{2.80}$$

Theoretically the evolution of the electric field for every optical element could be modeled if an appropriate Green's function can be found. In practice the Green's function is unknown. We

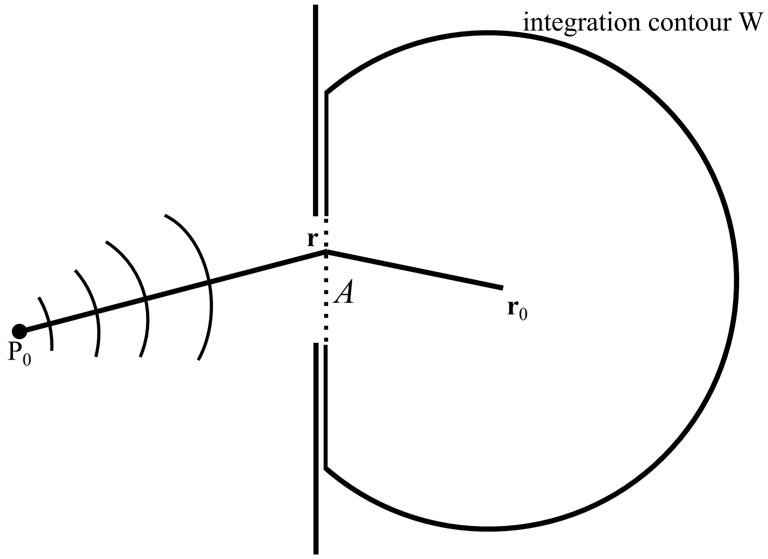

Figure 2.13.: Illustration of the contour integration for the Fresnel Kirchhoff diffraction theory. The contour consists of the opening $\mathcal{A}$, the part of the sphere W and the area of the aperture that connect $\mathcal{A}$ and W.

will however apply this formalism to the propagation in free space and derive with its help the Fresnel and Fraunhofer diffraction formulas.

With the special choice of a Green's function:

$$G(s) = \frac{e^{iks}}{s} \tag{2.81}$$

one arrives at the *integral theorem of Helmholtz and Kirchhoff*:

$$E(\boldsymbol{r}_0, \omega) = \frac{1}{4\pi} \int_S dS \left\{ E(\boldsymbol{r}, \omega) \frac{\partial}{\partial n} \left(\frac{e^{iks}}{s} \right) - \frac{e^{iks}}{s} \frac{\partial E(\boldsymbol{r}, \omega)}{\partial n} \right\} \tag{2.82}$$

where $\boldsymbol{r}_0$ is any point within S. This theorem expresses $E(\boldsymbol{r}_0, \omega)$ through the values of $E(\boldsymbol{r}, \omega)$ and its derivation of its inward normal $\partial_n E(\boldsymbol{r}_0, \omega)$ on the surface S. The choice of G can be motivated by the Huygens-Fresnel principle, i.e. every point of a wave-front may be seen as the source of a spherical wave and these spherical waves interfere mutually. This general integral theorem is however more complicated then Fresnel assumed.

We can apply the integral theorem to the case of a monochromatic wave from a point source:

$$E(\boldsymbol{r}, \omega) = A \frac{e^{ikr}}{r} \tag{2.83}$$

at point $\boldsymbol{r}_0$ that gets diffracted at an opening $\mathcal{A}$ whereas the opening size is considered large compared to the wavelength but small compared to the distance between opening and $\boldsymbol{r}_0$ (see Fig. 2.13). We want to know $E(\boldsymbol{r}_0, \omega)$ for points that have a much larger distance than the opening size of the aperture. Additionally, we assume that in the opening $\mathcal{A}$ the wave and its directional derivation are unchanged by the present of the aperture around the opening, i.e. they are the same as if there was no aperture. Furthermore we assume that both the wave and its directional derivation are zero on the aperture. These are reasonable assumptions but nonetheless assumptions. The integration surface is then closed with an infinitely extended sphere W in forward direction. The contributions from the infinitely large surface W go to zero and we are lead to the *Fresnel-Kirchhoff diffraction formula*:

$$E(\boldsymbol{r}_0,\omega) = -\frac{iA}{2\lambda}\int_{\mathcal{A}} dS \left\{ \frac{e^{ik(r+s)}}{rs} \left[\cos\langle \boldsymbol{n},\boldsymbol{r}\rangle - \cos\langle \boldsymbol{n},\boldsymbol{r}_0\rangle\right] \right\}. \tag{2.84}$$

where $\langle\cdot,\cdot\rangle$ denotes the scalar product and $\boldsymbol{n}$ is the normal vector of the integration surface. The integration surface S reduced to the part of the aperture $\mathcal{A}$.

For all the used arguments it is not necessary to chose $\mathcal{A}$ as a plane. If $\mathcal{A}$ is chosen to be a spherical surface of very large radius of curvature then one can approximate $\cos\langle \boldsymbol{n},\boldsymbol{r}\rangle = 1$ and arrives at:

$$E(\boldsymbol{r}_0,\omega) = -\frac{iA}{2\lambda}\int_{\mathcal{A}} dS \left\{ \frac{e^{ik(r+s)}}{rs} (1+\cos(\chi)) \right\} \tag{2.85}$$

with

$$\chi = \pi - \langle \boldsymbol{n},\boldsymbol{r}_0\rangle. \tag{2.86}$$

This formula corresponds to the Huygens-Fresnel principle, where each point of the aperture $\mathcal{A}$ becomes a source of a spherical wave. The formula allows us to identify the inclination factor of Fresnel's theory:

$$K(\chi) = -\frac{i}{2\lambda}(1+\cos(\chi)) \tag{2.87}$$

For $\chi = 0$ the inclination factor resembles the result of Fresnel's theory. However in general $\chi \neq 0$ and the results differ. In particular $K(\frac{\pi}{2}) \neq 0$. The non-monochromatic case can be derived from this monochromatic result by means of Fourier analysis.

To model an extended source we use in Eq. 2.82 the special choice of $E(\boldsymbol{r},\omega)$:

$$E(\boldsymbol{r},\omega) = A(\boldsymbol{r})e^{-i\boldsymbol{k}\boldsymbol{r}}, \tag{2.88}$$

with a magnitude function A in the opening $\mathcal{A}$. This choice has a well-defined direction at every point in the aperture: $\partial_n E(\boldsymbol{r},\omega) = -ikA(\boldsymbol{r})\cos\langle \boldsymbol{n},\boldsymbol{r}\rangle$ and it may be applied if an extended source is significantly further away than the wavelength. The only real difference to the previously given derivation is that $A(\boldsymbol{r})$ was constant. We may therefore follow similar mathematical manipulations and we arrive at:

$$E(\boldsymbol{r}_0,\omega) = -\frac{i}{2\lambda}\int_{\mathcal{A}} dS \left\{ A(\boldsymbol{r})\frac{e^{iks}}{s} (\cos\langle \boldsymbol{n},\boldsymbol{r}\rangle - \cos\langle \boldsymbol{n},\boldsymbol{r}_0\rangle) \right\}. \tag{2.89}$$

We point out that in the close vicinity of the opening $\mathcal{A}$ these formulas are in general invalid and the pure boundary value problem must be solved.

If, additionally the extended source and the point at $\boldsymbol{r}_0$ are both much further away from the opening $\mathcal{A}$ than the size of the opening $\mathcal{A}$ then the scalar products in Eq. 2.89 will always give a very small angle and the cosines in Eq. 2.89 can be approximated by 1 and -1, respectively and we rewrite Eq. 2.89 as:

$$E(\boldsymbol{r}_0,\omega) = -\frac{i}{z\lambda}\int_{\mathcal{A}} dS A(\boldsymbol{r}) e^{iks} \tag{2.90}$$

with

$$s^2 = (x-a_x)^2 + (y-a_y)^2 + z^2 \tag{2.91}$$

here x, y, z are the coordinates of $\boldsymbol{r}_0$ and a_x, a_y are the coordinates in the opening. The distance s practically equals z for all changes over the opening. We could therefore safely replace the factor $1/s$ in the integrand by $1/z$ and may pull it out from the integral. The complex phase factor on the other hand is much more sensitive and in its argument we can not simply replace s by z. We therefore rewrite s as:

$$s = z\sqrt{1 + \frac{(x-a_x)^2 + (y-a_y)^2}{z^2}}. \tag{2.92}$$

The square root can be expanded into a Taylor series:

$$\sqrt{1+v} = 1 + \frac{v}{2} - \frac{v^2}{8} + \frac{v^3}{16} - \dots \tag{2.93}$$

Depending on the highest order used of this expansion one arrives at the Fresnel diffraction equation or the Fraunhofer diffraction equation.

2.4.1.2. Fresnel diffraction equation

The expansion of Eq. 2.92 to first order is:

$$s = z + \frac{(x-a_x)^2 + (y-a_y)^2}{2z}. \tag{2.94}$$

And Eq. 2.89 takes the form of the *Fresnel diffraction equation*:

$$E(\boldsymbol{r}_0, \omega) = \frac{e^{ikz}}{i\lambda z} \int_{\mathcal{A}} da_x da_y \; A(\boldsymbol{r}) e^{\frac{ik}{2z}((x-a_x)^2+(y-a_y)^2)}, \tag{2.95}$$

or in vector notation with $\tilde{\boldsymbol{r}} = [x, y]^T$:

$$\boxed{E(\tilde{\boldsymbol{r}}, z, \omega) = \frac{e^{ikz}}{i\lambda z} \int_{\mathcal{A}} d\boldsymbol{r}' A(\boldsymbol{r}') e^{\frac{ik}{2z}(\tilde{\boldsymbol{r}}-\boldsymbol{r}')^2}.} \tag{2.96}$$

This approximation is often referred to as near field approximation.

2.4.1.3. Fraunhofer diffraction equation

If linear terms in Eq. 2.94 are sufficient one arrives at:

$$s = z - \frac{xa_x + ya_y}{z} \tag{2.97}$$

and the *Fraunhofer diffraction equation*:

$$E(\tilde{\boldsymbol{r}}, z, \omega) = \frac{e^{ikz}}{i\lambda z} \int_{\mathcal{A}} d\boldsymbol{r}' A(\boldsymbol{r}') e^{-\frac{ik}{z}\tilde{\boldsymbol{r}}\boldsymbol{r}'}. \tag{2.98}$$

This regime is often called far field approximation.

The *Fresnel number*:

$$F = \frac{A}{d\lambda} \tag{2.99}$$

where A is the area of the aperture and d is the distance of the screen from the aperture, can give an indication whether to use the near field or the far field approximation. For cases with $F \gg 1$ the Fresnel formula should be used while for $F \ll 1$ the Fraunhofer formula should be sufficient.

We point out that even in 30 m distance from the undulator the emission may often still require treatment in the near field approximation because the wavelength of X-rays is several orders of magnitude smaller than for visible light.

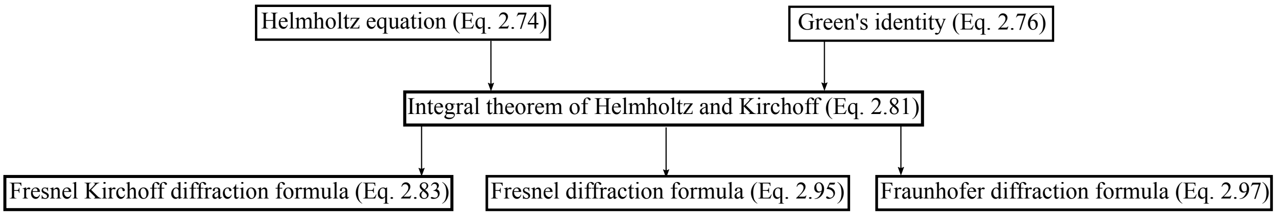

Figure 2.14.: Overview of the diffraction formulas

2.4.1.4. Summary of this section

In this section we derive the Fresnel diffraction formula Eq. 2.96 and the Fraunhofer diffraction formula Eq. 2.98 (see also Fig. 2.14 for a schematic overview).

The Helmholtz equation together with Green's identity and an appropriate Green's function lead to the integral theorem of Helmholtz and Kirchhoff (Eq. 2.82). From the integral theorem with the special choice $E(\boldsymbol{r},\omega) = A(\boldsymbol{r})e^{-ik\boldsymbol{r}}$ (Eq. 2.88) we can derive the two diffraction formulas by a Taylor expansion of the distance s between the aperture coordinates and the observation point $\boldsymbol{r}_0$ in Eq. 2.90. The Fresnel diffraction formula keeps quadratic terms in the spatial coordinates $\boldsymbol{r}_0$. It can be used in the near-field and far-field region. The Fraunhofer diffraction formula keeps only linear terms in the spatial coordinates $\boldsymbol{r}_0$ and is valid only in the far-field. For X-ray radiation the namings of near- and far-field can be a bit misleading. The names stem from visible light wavelengths but the wavelengths of X-rays are much shorter such that a distance of several meters can still be in the near-field region for hard X-ray radiation. An indication whether to use the Fresnel diffraction formula or the Fraunhofer diffraction formula is given by the wavelength dependent Fresnel number F given by Eq. 2.99.

2.4.2. Optical elements in thin elements approximation

In practice many X-ray optical elements are modeled in thin element approximation. The effect of an optical element on the electric field is considered by multiplication with a complex transfer function T:

$$E'(\boldsymbol{r},\omega) = T(\omega)E(\boldsymbol{r},\omega). \tag{2.100}$$

The transfer function has the general form:

$$T(\omega) = A(\omega)e^{i\Phi(\omega)} \tag{2.101}$$

where A is a real function called the amplitude transfer function and Φ is the phase transfer function. The amplitude transfer function models the absorption of the element and the phase transfer function the change of optical path length. The name of this approximation stems from the fact that light rays that enter an optical element exit the optical element at the same position in this approximation.

In this approximation an ideal lens is given by $A(\omega) = 1$ and $\Phi(\omega) = -\frac{k}{2}(x^2/f_x + y^2/f_y)$. Here f_x and f_y are the horizontal and vertical focal lengths. An ideal absorber is modelled with $\Phi(\omega) = 0$ and $A(\omega) < 1$. In particular an aperture is a an ideal absorber with $A(\omega) = 0$.

2.4.3. Numerical propagation and computational limitations

In principle wave optics is a very accurate theory. In practice, computational limitations arise. It is not clear how to practically calculate arbitrary thick elements in the near field. The formula for the Fresnel propagation Eq. 2.96 can be read as a convolution with the Fresnel kernel. The convolution theorem states that a convolution becomes a simple multiplication in Fourier space.

One of the most sophisticated numerical algorithm is the Cooley-Tukey Fast Fourier Transform (FFT) algorithm[28]. The Cooley-Tukey FFT algorithm is the basis of many other algorithms which are often simply referred to as FFT. All the FFT algorithms have in common that they can perform numerically very efficiently the discrete Fourier transform which can be used to approximate the continuous Fourier transform. The convolution of the Fresnel kernel can therefore be very efficiently calculated using FFT-based convolutions. If a convolution is performed on the basis of the Fourier transform which itself is approximated by a discrete Fourier transform one very important pitfall has to be considered: the discrete Fourier transform is inherently periodic and the convolution may be accidentally approximated numerically by a circular convolution. A circular convolution may mix effects from the boundary into the result. This can lead to completely wrong results. It depends a bit on the implementation of the convolution algorithm but in most cases it must be guaranteed that the input factors of the calculation are given on a grid that is large enough to not mix in boundary effects. This is often accomplished by the so called *zero-padding*, which means that the input factor is just extended by zeros outside its support. Effects of optical elements like apertures and ideal lenses can be approximated by thin elements, which among other elements, are available in SRW. We will adopt the notion of **wavefront** used in SRW[29]. The wavefront is the electric field in a given plane along the beamline or at a virtual position before the beamline. Throughout this thesis we only use the Fresnel propagation, apertures and ideal lenses. In SRW for every optical element of a beamline the numerical grid must be specified. This is a rather time consuming part because at least for the inexperienced user all these grid settings have to be converged. The grid settings include the grid size in meters and the step width of the grid. For instance, if the optical element is a slit often a lot of grid points must be used. The same is true if the wavefront is strongly focused. Sometimes the grid size must be increased to account for zero padding and to allow for sufficient low frequency contributions. Keeping the grid size constant and decreasing the step width, i.e. increasing the number of grid points, will account for higher frequencies contributions.

Furthermore the memory demand can become significant. A single ultra-relativistic electron creates an electric field that can be treated in paraxial approximation[30]. As a consequence a term

$$e^{\frac{ikz\theta^2}{2}} \tag{2.102}$$

appears in the angular representation of the created electric field. With increasing z this term leads to fast phase oscillations in dependence of θ because $k \gg 1$ for X-rays[31]. In view of numerical wavefront calculations this requires in general a tight sampling grid to store the fast phase oscillations. We stress the fact that phase information are very important for wave optics. One illustrative example is the phase retrieval algorithm[33]. Some strategies[29, 32] are known to factor out this fast oscillating term with radius of curvature R which leads to a smoothed factor that can be stored more easily (see Fig. 2.15). Further propagation can then be performed partially analytical and partially numerical. Successive propagation along a beamline must eventually update the radius of curvature of the phase function. This, however, only works if the wavefront was not significantly distorted from its initial spherical/parabolic shape. To relax the memory restrictions at least a bit one could implement a parallelized convolution algorithm and distribute the required memory for the wavefront propagation over many computers. Unfortunately, SRW does not possess a parallelization for the purpose of wavefront propagation.

In practice mirror errors become more and more important. When mirrors are illuminated partially coherent their height errors can lead to speckles.

By date, accurate simulations for these effects are actively researched.

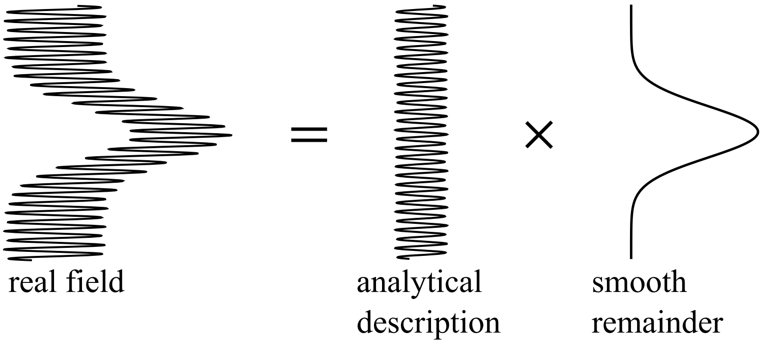

Figure 2.15.: Illustration of a strategy to reduce the memory consumption of wavefronts created by ultrarelativistic electrons.

2.5. Statistical optics

We have seen in the chapter of insertion devices that we can calculate the electric field created by an electron given its trajectory. Furthermore once we know it in a plane we may propagate it through optical elements, e.g. a slit, and we will see the diffraction of a slit. Where does *incoherence* enter in this description? There is none because everything is deterministic. What happens if we had two electrons? Let the second electron position at the entrance of the insertion device be shifted transverse relative to the position of the first electron. What is the radiation in this case? Well, because of the superposition principle we would, under the assumption of no magnetic field variation in the insertion device, get just the sum of the initial field plus the shifted field (see Fig. 2.16). Again, no stochastic. Everything is deterministic. We still see something like an interference pattern. We may repeat this process many times for electrons distributed following a Gaussian distribution and we get a single well defined *deterministic* electric field. Now, let us imagine we do not know the exact position of the electron but only probabilities of an electron being there. As an example let us consider that an electron with probability 0.9 enters on the ideal orbit and that with a probability of 0.1 an electron electron enters shifted laterally. What is the electric field in this experiment? Is there a deterministic electric field? In fact the uncertainty in the knowledge of the electron position transfers to the uncertainty of the electric field. The electric field became a so called random function, i.e. we can only say with a probability of 0.9 the field looks like this and with a probability of 0.1 like that. The situation described is actually quite close to synchrotron reality. In Fig. 2.17 we illustrate in each plot the radiation created by a sample of two-hundred electrons. For the creation of these plots we used SRW, a realistic Gaussian distribution (ESRF-EBS at the symmetry point) and a realistic undulator (ESRF u18 2m). The very small sampling was chosen intentionally to highlight the statistical nature of the electron emission created by an electron bunch. In these plots the statistical nature is manifested in the different shape of the emission in each plot. A typical bunch has of the order 10^{10} electrons and some statistical convergence is expected, such that the emission of every bunch should look alike. On the other hand in the most general case the sampling follows a six-dimensional distribution. If the convergence is reached in every dimension equally “fast” there are $10^{\frac{10}{6}} \approx 50$ samples per dimension. We saw in the previous chapter that the electrons are statistically distributed following a Gaussian distribution. It is exactly this statistics that leads to stochastics in the radiation. In general finding the random function of the electric field is a very difficult task. However, in many situations the knowledge of the mean intensity is interesting in its own right. We will review here some results of second order coherence theory that can be used to describe the evolution of the mean intensity along a synchrotron beamline.

A single spatial shift:

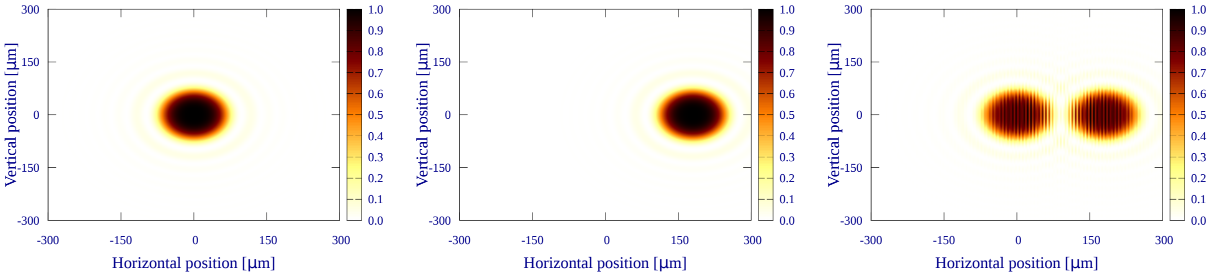

Two spatially shifted electrons:

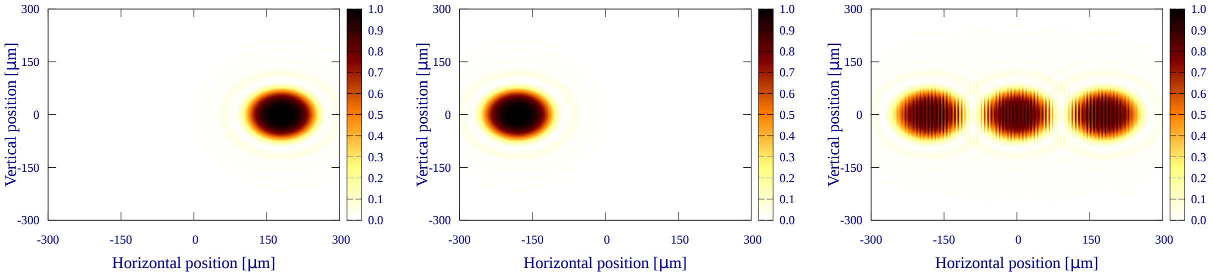

A single inclination:

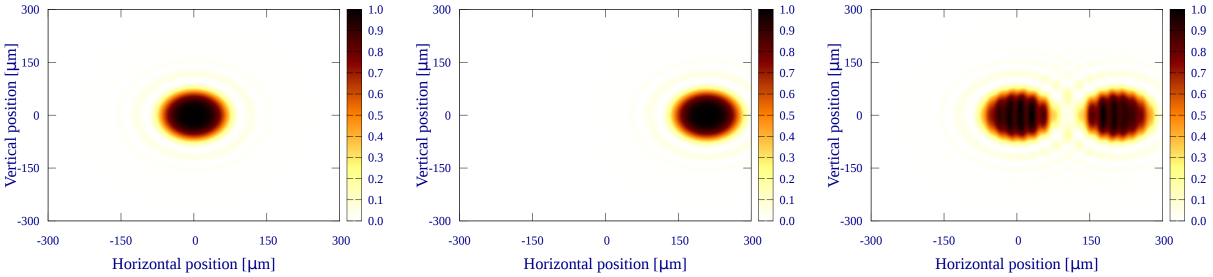

Two inclinations:

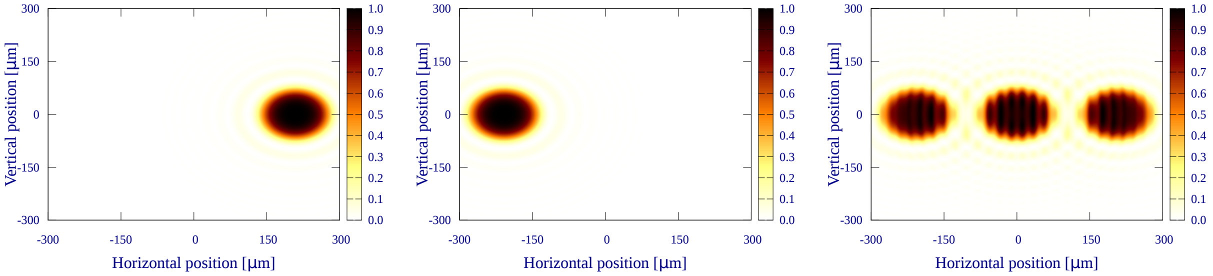

Figure 2.16.: Deterministic addition of single electron emissions of the 2m long ESRF u18 undulator at 7m from the undulator exit plane. The ideal on-axis emission is summed with single or double initial shifts or inclinations. The resulting intensity is depicted right. Interference effects are visible.

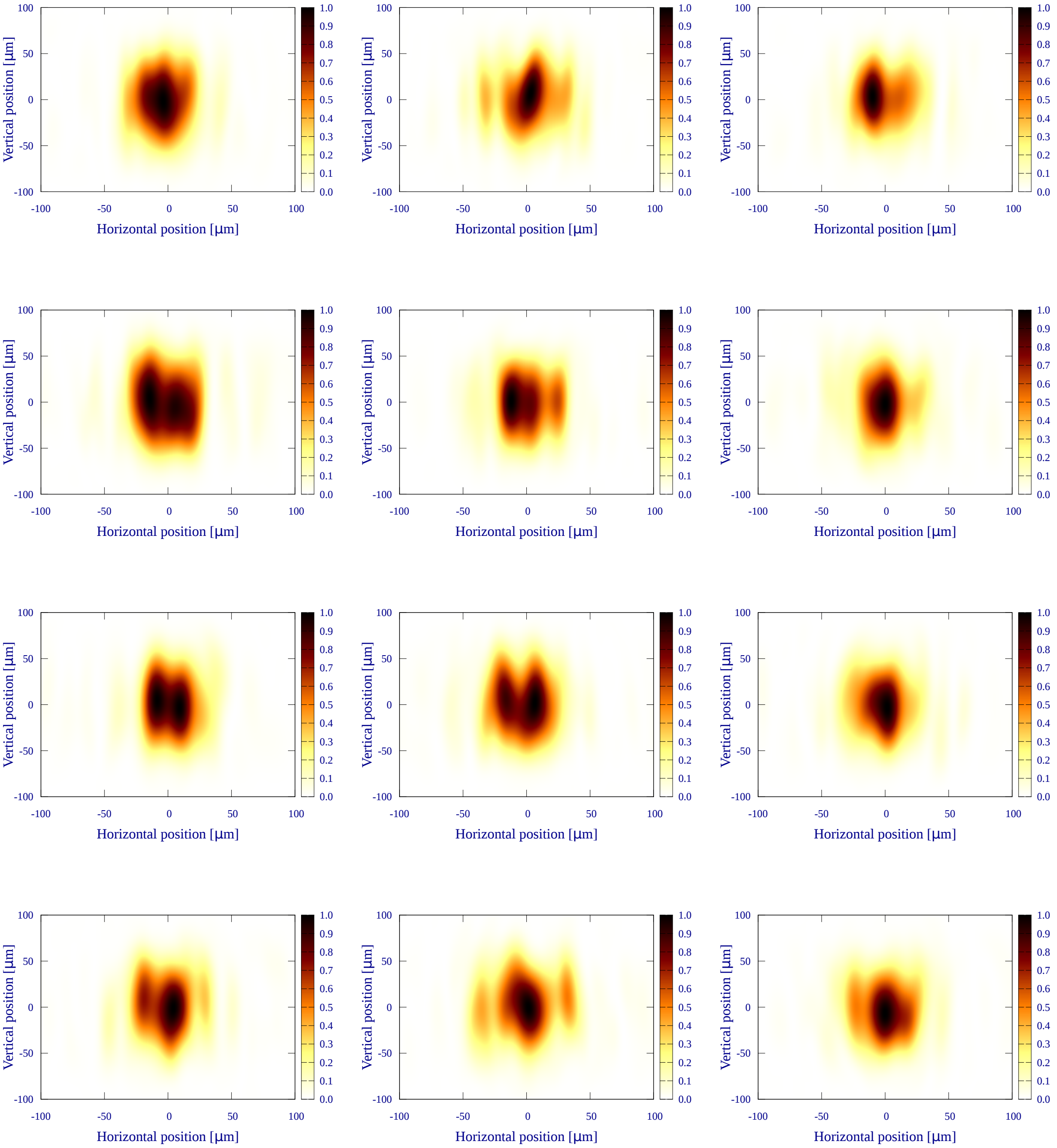

Figure 2.17.: Very small sample(200 electrons) of a synchrotron radiation bunch from a 2m long ESRF u18 undulator at 7m from the undulator exit plane. Every sample looks different. This sampling is intentionally chosen a way too small to illustrate the random idea. A full sampling of all the electrons in the bunch would not show any visible change in these intensity plots.

2.5.1. Second order coherence

In practice one is often interested in the mean intensity of some statistically fluctuating intensity distribution. The intensity can be deduced from the electric field by

$$I(\boldsymbol{r},t) = E^*(\boldsymbol{r},t)E(\boldsymbol{r},t) \tag{2.103}$$

the mean intensity $\bar{I}$ is the average value of all *fluctuations*, *realizations* or what is usually called an *ensemble*:

$$\bar{I}(\boldsymbol{r},t) = \langle E^*(\boldsymbol{r},t)E(\boldsymbol{r},t)\rangle_{ens} \tag{2.104}$$

where $(\cdot)^*$ indicates complex conjugation. In the process of determining the intensity the phase is lost. The laws that describe the propagation of radiation rely on the knowledge of the phase and they can in general not be applied without it. We know therefore no direct way to propagate the mean intensity further through a beamline. If we however define the *mutual coherence function*:

$$\Gamma(\boldsymbol{r}_1,t_1,\boldsymbol{r}_2,t_2) = \langle E^*(\boldsymbol{r}_1,t_1)E(\boldsymbol{r}_2,t_2)\rangle_{ens}\,, \tag{2.105}$$

phase information are kept and we explain later how this quantity can be propagated on the grounding of the laws of wave optics. Furthermore the mean intensity is included in Γ:

$$\bar{I}(\boldsymbol{r},t) = \Gamma(\boldsymbol{r},t,\boldsymbol{r},t). \tag{2.106}$$

The theory is called second order coherence because we consider only second order correlations of the electric fields. A phenomenological description of coherence is often the manifestation of interference pattern. We point out that the knowledge of Γ describes second order coherence completely. In particular as long as we are only interested in the mean intensity of a radiation ensemble the knowledge of Γ is sufficient for a full description.

A process is called *wide-sense stationary* if its average value is time independent and its mutual coherence function depends not on two time variables t_1, t_2 but only on the difference τ of the two time variables.

If the fluctuation ensemble is stationary, at least in the wide sense, we may define the **cross spectral density** W as the frequency-time Fourier transform of the mutual coherence function:

$$\boxed{W(\boldsymbol{r}_1,\boldsymbol{r}_2,\omega) = \int_0^\infty d\tau\ \Gamma(\boldsymbol{r}_1,\boldsymbol{r}_2,\tau)e^{i\omega\tau}.} \tag{2.107}$$

For $\boldsymbol{r}_1 = \boldsymbol{r}_2$ one defines the **spectral density** as:

$$\boxed{S(\boldsymbol{r},\omega) = W(\boldsymbol{r},\boldsymbol{r},\omega).} \tag{2.108}$$

The spectral density is the energy per unit time[34].

Additionally we define the equal time correlation function J:

$$J = \Gamma(\boldsymbol{r}_1,\boldsymbol{r}_2,\tau = 0) \tag{2.109}$$

which is also called the *mutual intensity function*.

2.5.2. Second order source fluctuations

In this section we will highlight the origin of the radiation ensemble. If we look at the inhomogeneous wave equations for the electric field we find that we have to solve

$$\left(\Delta - \frac{1}{c^2}\frac{\partial^2}{\partial t^2}\right) E(\boldsymbol{r}, t) = -4\pi Q(\boldsymbol{r}, t) \tag{2.110}$$

where Q is some charge density. Whatever physically meaningful choice of Q may be, as long as Q is a deterministic function, i.e. not a random function, the solution E will be a deterministic function as well.

But how does the situation change if the source density is a random function? We will not address the general question to determine the random functions of the electric field but restrict our discussion to second order source fluctuations from which we will be able to derive the mutual coherence function Γ. For mathematical simplicity we take E, Q to be analytical signals, i.e. their real and imaginary parts are related by a Hilbert transform and hence they are also analytic functions. Following [15], we may then look at the complex conjugate of Eq. 2.110:

$$\left(\Delta - \frac{1}{c^2}\frac{\partial^2}{\partial t^2}\right) E^*(\boldsymbol{r}, t) = -4\pi Q^*(\boldsymbol{r}, t) \tag{2.111}$$

so we arrived at a differential equation for the complex conjugate of E and of Q. We therefore have two independent differential equation that we can combine:

$$\left(\Delta_{\boldsymbol{r}_1} - \frac{1}{c^2}\frac{\partial^2}{\partial t_1^2}\right)\left(\Delta_{\boldsymbol{r}_2} - \frac{1}{c^2}\frac{\partial^2}{\partial t_2^2}\right) E^*(\boldsymbol{r}_1, t_1)E(\boldsymbol{r}_2, t_2) = (4\pi)^2 Q^*(\boldsymbol{r}_1, t_1)Q(\boldsymbol{r}_2, t_2). \tag{2.112}$$

For every choice of Q and Q^* one obtains a solution to this partial differential equation. Taking the ensemble average on the right hand side therefore induces an ensemble average on the left side:

$$\left(\Delta_{\boldsymbol{r}_1} - \frac{1}{c^2}\frac{\partial^2}{\partial t_1^2}\right)\left(\Delta_{\boldsymbol{r}_2} - \frac{1}{c^2}\frac{\partial^2}{\partial t_2^2}\right) \Gamma(\boldsymbol{r}_1, t_1, \boldsymbol{r}_2, t_2) = (4\pi)^2 \Gamma_Q(\boldsymbol{r}_1, t_1, \boldsymbol{r}_2, t_2) \tag{2.113}$$

with

$$\Gamma_Q(\boldsymbol{r}_1, t_1, \boldsymbol{r}_2, t_2) = \langle Q^*(\boldsymbol{r}_1, t_1)Q(\boldsymbol{r}_2, t_2)\rangle_{ens}\,. \tag{2.114}$$

If the source is stationary, at least in the wide sense, then only the time difference τ is relevant:

$$\left(\Delta_{\boldsymbol{r}_1} - \frac{1}{c^2}\frac{\partial^2}{\partial \tau^2}\right)\left(\Delta_{\boldsymbol{r}_2} - \frac{1}{c^2}\frac{\partial^2}{\partial \tau^2}\right) \Gamma(\boldsymbol{r}_1, \boldsymbol{r}_2, \tau) = (4\pi)^2 \Gamma_Q(\boldsymbol{r}_1, \boldsymbol{r}_2, \tau). \tag{2.115}$$

Similar as in the derivation of the Helmholtz equation from the wave equation we can make a Fourier transform to the frequency representation and we arrive at the *Wolf equation*:

$$(\Delta_1 + k^2)(\Delta_2 + k^2)W(\boldsymbol{r}_1, \boldsymbol{r}_2, \omega) = (4\pi)^2 W_Q(\boldsymbol{r}_1, \boldsymbol{r}_2). \tag{2.116}$$

The Wolf equation may, similar to the Helmholtz equation in the deterministic case, be taken as the starting point for studies of fields generate by a steady-state primary source in vacuum.

Because of the similarity in the formulas, the Wolf equation is basically the tensor product of the Helmholtz equation, one may expect similar formulas for the propagation of the electric field in wave optics and the propagation of the cross spectral density in statistical optics. This is indeed true and we will see this in the next section.

2.5.3. Propagation formulas

The knowledge of the mutual coherence function or the cross spectral density allows us to determine the average intensity or the spectral density, respectively. We would however like to propagate the ensemble as a whole through a beamline, very much like we can do with electric fields. Since the Wolf equations take the form of a tensor product version of the Helmholtz equations one expects for the propagation something like a tensor product of the electric field propagators. We will see that this is indeed the case. As discussed in section 2.4 given the appropriate Greens function G a known electric field E may be propagated through an arbitrary optical system. This includes cases of free space propagation and possible transmission through thick optical elements according to Eq. 2.80. The integral operator in Eq. 2.80 may also be rewritten as an *integral operator with kernel*:

$$E'(\boldsymbol{r}) = \int d\boldsymbol{r}' h(\boldsymbol{r},\boldsymbol{r}')E(\boldsymbol{r}') \tag{2.117}$$

where E' is the propagated electric field and the kernel h is the so called *impulse response function*.

If the kernel h is a deterministic function we may use the same argumentation of bringing in the ensemble average as we used when we discussed the source. This leads to

$$\Gamma'(\boldsymbol{r}_1,t_1,\boldsymbol{r}_2,t_2) = \int d\boldsymbol{r}'_1 d\boldsymbol{r}'_2\ h^*(\boldsymbol{r}_1,\boldsymbol{r}'_1)h(\boldsymbol{r}_2,\boldsymbol{r}'_2)\Gamma(\boldsymbol{r}'_1,t_1,\boldsymbol{r}'_2,t_2) \tag{2.118}$$

here Γ' is the propagated mutual coherence function.

If the field is at least wide sense stationary we get similarly for the cross spectral density:

$$\boxed{W'(\boldsymbol{r}_1,\boldsymbol{r}_2,\omega) = \int d\boldsymbol{r}'_1 d\boldsymbol{r}'_2\ h^*(\boldsymbol{r}_1,\boldsymbol{r}'_1)h(\boldsymbol{r}_2,\boldsymbol{r}'_2)W(\boldsymbol{r}'_1,\boldsymbol{r}'_2,\omega).} \tag{2.119}$$

In conclusion, in contrast to the mere mean intensity the mutual coherence function or the cross spectral density can be propagated through an optical set up. Phase information necessary for the propagation of the mean intensity or the spectral density are present.

To deduce the propagated intensity we derive the equation:

$$I'(\boldsymbol{r},t) = \int d\boldsymbol{r}'_1 d\boldsymbol{r}'_2\ h^*(\boldsymbol{r},\boldsymbol{r}'_1)h(\boldsymbol{r},\boldsymbol{r}'_2)\Gamma(\boldsymbol{r}'_1,t,\boldsymbol{r}'_2,t). \tag{2.120}$$

In Fresnel approximation Eq. 2.96 the propagation formula for the cross spectral density takes the form:

$$W'(\boldsymbol{r}_1,\boldsymbol{r}_2,\omega) = \frac{1}{\lambda^2 z^2}\int_{\mathcal{A}} d\boldsymbol{r}'_1 d\boldsymbol{r}'_2\ W(\boldsymbol{r}_1,\boldsymbol{r}_2,\omega)e^{\frac{ik}{2z}\left(\|\boldsymbol{r}_1-\boldsymbol{r}'_1\|^2-\|\boldsymbol{r}_2-\boldsymbol{r}'_2\|^2\right)}. \tag{2.121}$$

We stress the fact that both formulas Eq. 2.118 and Eq. 2.120 *sum up all possible pairs* of $\boldsymbol{r}_1$ and $\boldsymbol{r}_2$ (see Fig. 2.18). In general it is not sufficient to sum up only a subset, i.e. to keep one of the $\boldsymbol{r}$ fixed.

2.5.4. Complex degree of coherence and longitudinal coherence length

We introduce the notion of complex degree of coherence and of longitudinal coherence length with the help of two examples.

The general formalism of statistical optics can be used to describe the interference of two waves

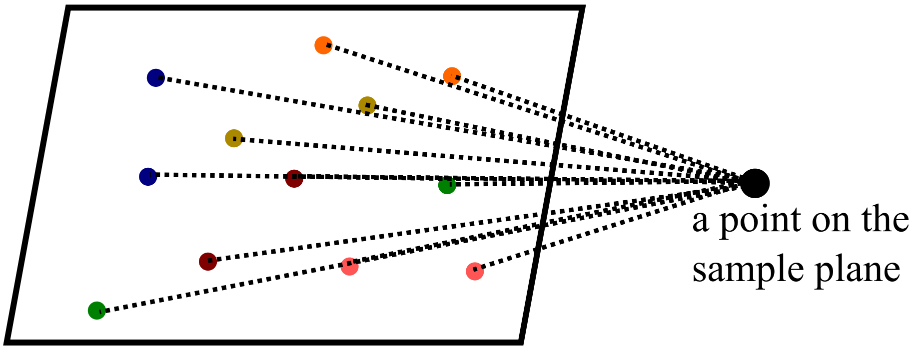

Figure 2.18.: Every point on the image plane is the superposition of all possible two points pairings on the source plane.

E_1 and E_2. The average intensity of the sum of the two waves is:

$$\begin{aligned} I &= \left\langle |E_1 + E_2|^2 \right\rangle_{ens} \\ &= \left\langle |E_1|^2 \right\rangle_{ens} + \left\langle |E_2|^2 \right\rangle_{ens} + \langle E_1^* E_2 \rangle_{ens} + \langle E_1 E_2^* \rangle_{ens} . \\ &= \bar{I}_1 + \bar{I}_2 + 2\mathrm{Re} \langle E_1^* E_2 \rangle_{ens} . \end{aligned} \tag{2.122}$$

Let us apply the interference equation Eq. 2.122 to the case of a partially coherent wide-sense stationary optical wave E that illuminates two pinholes at position $\boldsymbol{r}_1$ and $\boldsymbol{r}_2$ on an opaque screen (see Fig. 2.19). Let a be half the distance between the two holes. Because of the wide-sense stationarity the mutual coherence function takes the form: $\Gamma(\boldsymbol{r}_1, \boldsymbol{r}_2, \tau) = \langle E_1(t)^* E_2(t+\tau) \rangle$. From the two pinholes the light is diffracted in the form of spherical waves. The interference of these two spherical waves is observed on a plane in distance d. The observation plane is placed sufficiently far away to allow the application of the Fresnel approximation. The two diffracted waves are then proportional to:

$$\begin{aligned} E_1(\boldsymbol{r}, t) &\propto E\left(\boldsymbol{r}_1, t - \frac{d + (x+a)^2}{2dc}\right) \\ E_2(\boldsymbol{r}, t) &\propto E\left(\boldsymbol{r}_2, t - \frac{d + (x-a)^2}{2dc}\right) \end{aligned} \tag{2.123}$$

with $\boldsymbol{r} = [x, y, d]^T$. The difference in time delays encountered by the two waves is:

$$\tau_x = \frac{(x+a)^2 - (x-a)^2}{2dc} = \frac{2ax}{dc}. \tag{2.124}$$

Let us further assume that the intensity at the two pinholes is approximately equal to I_0. The interference equation Eq. 2.122 takes the form:

$$I(\boldsymbol{r}) = 2I_0 \left(1 + |\gamma(\boldsymbol{r}_1, \boldsymbol{r}_2, \tau_x)| \cos \phi_x\right) \tag{2.125}$$

where

$$\gamma(\boldsymbol{r}_1, \boldsymbol{r}_2, \tau) = \frac{\Gamma(\boldsymbol{r}_1, \boldsymbol{r}_2, \tau)}{\sqrt{\Gamma(\boldsymbol{r}_1, \boldsymbol{r}_1, \tau)\Gamma(\boldsymbol{r}_2, \boldsymbol{r}_2, \tau)}} \tag{2.126}$$

is the *complex degree of coherence* and $\phi_x = \arg\left(\gamma(\boldsymbol{r}_1, \boldsymbol{r}_2, \tau_x)\right)$ its phase. This formula describes the famous Young's experiment (see Fig. 2.19).

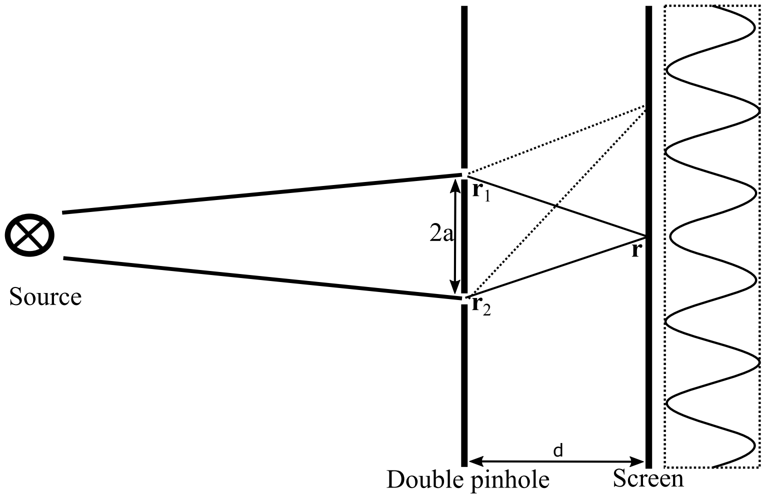

Figure 2.19.: Illustration of Youngs experiment to probe the mutual coherence function.

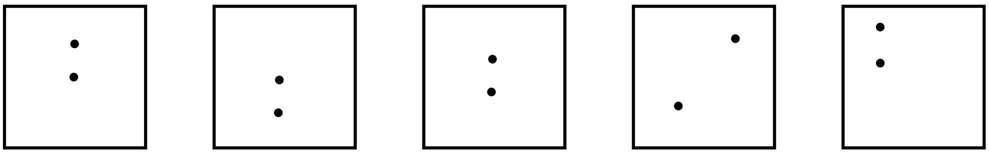

Figure 2.20.: Illustration of a very small subset of possible locations of two holes. The position of any of the hole can be chosen independent of the other.

The complex degree of coherence γ has the property

$$0 \leq |\gamma(\boldsymbol{r}_1, \boldsymbol{r}_2, \tau)| \leq 1. \tag{2.127}$$

One defines

$$\begin{cases} \textit{complete coherence} \text{ for } |\gamma| = 1 \\ \textit{partial coherence} \text{ for } 0 < |\gamma| < 1 \\ \textit{complete incoherence} \text{ for } |\gamma| = 0 \end{cases} \tag{2.128}$$

for the pair of points $\boldsymbol{r}_1, \boldsymbol{r}_2$.

Let us consider another case. We add a partially coherent wide-sense stationary wave to a replica of itself delayed by the time τ. From the interference equation Eq. 2.122 we derive:

$$I(\boldsymbol{r}) = 2I_0 \left(1 + \mathrm{Re}\gamma(\boldsymbol{r}, \boldsymbol{r}, \tau)\right). \tag{2.129}$$

This set up can be realized with the help of a Michelson interferometer (see Fig. 2.21) or a Mach-Zehnder Interferometer.

Traditionally one can define the *longitudinal coherence time for quasi-monochromatic light* with bandwidth $\Delta\omega$ by:

$$\Delta\tau_c \Delta\omega \leq 1 \tag{2.130}$$

respectively

$$\Delta\tau_c \approx \frac{1}{\Delta\omega}. \tag{2.131}$$

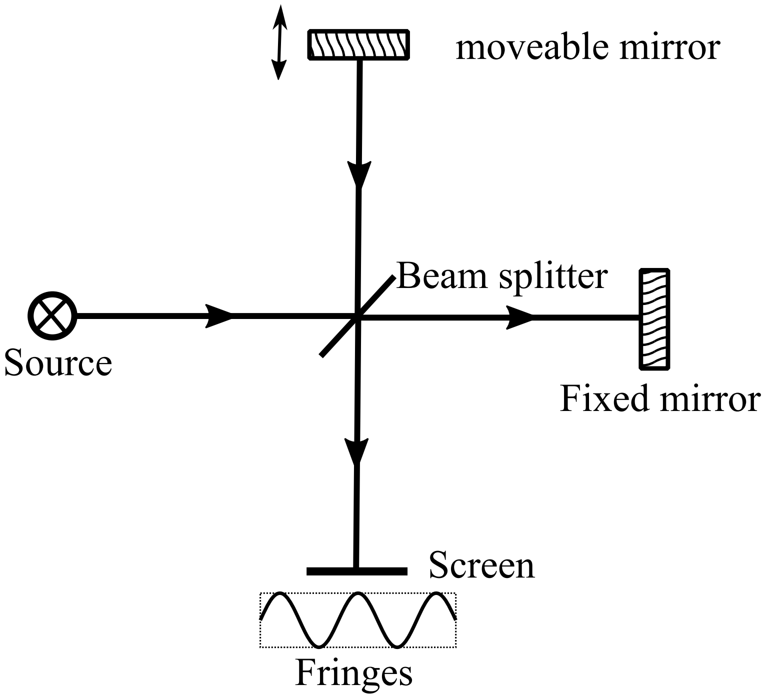

Figure 2.21.: Illustration of Michelson interferometry.

This gives rise to a *longitudinal coherence length*

$$l_c = c\Delta\tau_c. \tag{2.132}$$

It is an experimental fact that in a Michelson interferometer fringes are visible as long as the time delay τ is smaller than about the coherence time, or equivalently, the optical path length difference is smaller than the coherence length. This can be explained with the superposition of fringes/rings with different periodicity that wash out each other if the period length differences approach the coherence length. Note, however, that in the general case of non monochromatic light other phenomena may appear (cf. the chapter on "Effects of spatial coherence on the spectrum of radiated fields" in [15]).

One alternative definition[15] is based on the mutual coherence function Γ. More precisely it is the normalized root mean square of the self-coherence function, i.e. $\boldsymbol{r}_1 = \boldsymbol{r}_2$:

$$(\Delta\tau(\boldsymbol{r}))^2 = \frac{\int \tau^2 \Gamma(\boldsymbol{r}, \boldsymbol{r}, \tau) d\tau}{\int \Gamma(\boldsymbol{r}, \boldsymbol{r}, \tau) d\tau}. \tag{2.133}$$

We stress the fact, that unless the mutual coherence function can be factorized in a spatial and a temporal part, this defines a coherence time that depends on the spatial position.

2.5.5. Coherent mode decomposition

In this section we present the theoretical motivation behind the numerical algorithm developed in this thesis.

It can be shown[15] that for fixed frequency ω the cross spectral density W is bounded

$$\int d\boldsymbol{r}_1 d\boldsymbol{r}_2 \; |W(\boldsymbol{r}_1, \boldsymbol{r}_2, \omega)|^2 < \infty \tag{2.134}$$

Hermitian:

$$W(\boldsymbol{r}_2, \boldsymbol{r}_1, \omega) = W^*(\boldsymbol{r}_1, \boldsymbol{r}_2, \omega) \tag{2.135}$$

and non negative definite:

$$\int d\boldsymbol{r}_1 d\boldsymbol{r}_2 \; W(\boldsymbol{r}_1, \boldsymbol{r}_2, \omega) f^*(\boldsymbol{r}_1) f(\boldsymbol{r}_2) \geq 0 \tag{2.136}$$

for every square integrable function f. In other words W is a non-negative, Hermitian Hilbert-Schmidt kernel according to Mercer's theorem W can always be expressed in the form of:

$$\boxed{W(\boldsymbol{r}_1, \boldsymbol{r}_2, \omega) = \sum_n \lambda_n(\omega) \Phi_n^*(\boldsymbol{r}_1, \omega) \Phi_n(\boldsymbol{r}_2, \omega)} \tag{2.137}$$

here λ_n are eigenvalues and $\Phi_n(\boldsymbol{r}, \omega)$ eigenvectors of the Fredholm integral operator that is defined by the homogeneous Fredholm integral equation of the second kind:

$$A_W(f) = \lambda f \tag{2.138}$$

with

$$\boxed{A_W(f) = \int d\boldsymbol{r}_1 \; W(\boldsymbol{r}_1, \boldsymbol{r}_2, \omega) f(\boldsymbol{r}_1).} \tag{2.139}$$

We want to call A_W the **cross spectral density operator** (associated to W). The eigenvalues λ_n are non-negative because W is non-negative definite. And the Hermiticity ensure that there is at least one non-zero eigenvalue. Without loss of generality the eigenvalues can be assumed to be in decreasing order and the eigenvectors can be assumed to be orthonormal.

We will call the eigenvectors Φ of the cross spectral density operator **coherent modes**. Following the naming convention of the spectral theory in mathematics we will call the set of eigenvalues **spectrum of the cross spectral density**, **mode spectrum** or simply **spectrum**.

An important remark is that the coherent mode decomposition is not a four-dimensional basis set expansion but a decomposition into a tensor product of two-dimensional factors. In this context we want to mention that in view of the Moore-Aronszajn theorem[37] the cross spectral density W can be seen as the reproducing kernel of the Hilbert space $\mathcal{H}$:

$$\mathcal{H} = \left\{ f \in L^2 \middle| \sum_n \frac{|\langle f, \Phi_n \rangle|^2}{\lambda_n} < \infty \right\} \tag{2.140}$$

here $\langle \cdot, \cdot \rangle$ denotes the canonical scalar product.

It can be shown that the coherent modes satisfy the Helmholtz equation[15]. In view of this analogy we will speak of **mode intensity** as the intensity of the coherent mode if this mode was an electric field. The eigenvalues of the expansion can be seen as the part of the spectral density carried by the associated coherent mode.

2.5.6. Optimal spectral density approximation in terms of coherent modes

In the following we want to show that the coherent mode decomposition can be used to construct an optimal finite dimensional approximations in view of the spectral density. With an n-dimensional approximation we mean an approximation F of the cross spectral density W such that:

- F has all the properties of W, i.e. Hermiticity, non-negativity, boundness.

- the associated integral operator A_F has rank n.
- the operators A_W and A_F are equal for all vectors of the range of A_F.

Let us define $W^{(m)}$ as the the *m-dimensional truncation of W* by:

$$W^{(m)} = \sum_{n=0}^{m-1} \lambda_n(\omega)\Phi_n^*(\boldsymbol{r}_1,\omega)\Phi_n(\boldsymbol{r}_2,\omega). \tag{2.141}$$

We claim that there is no m-dimensional approximation A such that:

$$\mathrm{tr}(A) > \mathrm{tr}\Big(W^{(m)}\Big). \tag{2.142}$$

Physically the trace of the cross spectral density is the spectral density. Because F fulfils the requirements of Mercer's theorem it may be represented in terms of its eigenvalues β_n and eigenfunctions f_n. Because of $A_F(x) = A_W(x)$ the function f_n is eigenfunction of A_W with eigenvalue $\lambda_{a(n)}$. The trace of a finite dimensional Hermitian operator is the sum of its eigenvalues and it follows:

$$\mathrm{tr}(A) = \sum_{n=0}^{m-1} \lambda_{a(n)} \leq \sum_{n=0}^{m-1} \lambda_n = \mathrm{tr}\Big(W^{(m)}\Big) \tag{2.143}$$

by construction of $W^{(m)}$ because $\{\lambda_0, \ldots, \lambda_{m-1}\}$ are positive and the largest eigenvalues in magnitude. That proves that there is no m-dimensional approximation with trace larger than the trace of the m-dimensional truncation $W^{(m)}$ of the cross spectral density.[1]

2.5.7. Complete spatial coherence in terms of coherent modes

In [15] it is stated that for a given frequency ω an ensemble is completely coherent if and only if the cross spectral density is of the form:

$$W(\boldsymbol{r}_1,\boldsymbol{r}_2,\omega) = U^*(\boldsymbol{r}_1,\omega)U(\boldsymbol{r}_2,\omega) \tag{2.144}$$

with

$$U(\boldsymbol{r},\omega) = \sqrt{S(\boldsymbol{r},\omega)}e^{i\beta(\boldsymbol{r},\omega)} \tag{2.145}$$

here β is a real phase factor. Furthermore U is a solution of the Helmholtz equation.

Contrary to the presentation in [15] the description of the cross spectral density in this thesis will be mainly based on coherent modes. We derive therefore a complete coherence characterisation in terms of coherent modes: For a given frequency ω **an ensemble is completely coherent if and only if the cross spectral density consists of a single coherent mode**. The implication a single coherent mode has the form of a completely coherent cross spectral density is readily seen with $U = \sqrt{\lambda_0}\Phi_0$. For the other implication we use the Fredholm integral equation:

$$A_W(\Phi) = \lambda\Phi. \tag{2.146}$$

Since the ensemble is fully coherent we can make use the form of W given by Eq. 2.144:

$$\int d\boldsymbol{r}_1\; U^*(\boldsymbol{r}_1,\omega)U(\boldsymbol{r}_2,\omega)\Phi(\boldsymbol{r}_1,\omega) = \lambda\Phi(\boldsymbol{r}_2,\omega) \tag{2.147}$$

---

[1] Condition 2.142 could be the link between coherent modes and the modes recovered from ptychography experiments in [4] because the coherent modes are orthogonal and minimize the total spectral density and these are the constraints of the ptychography reconstruction algorithms.

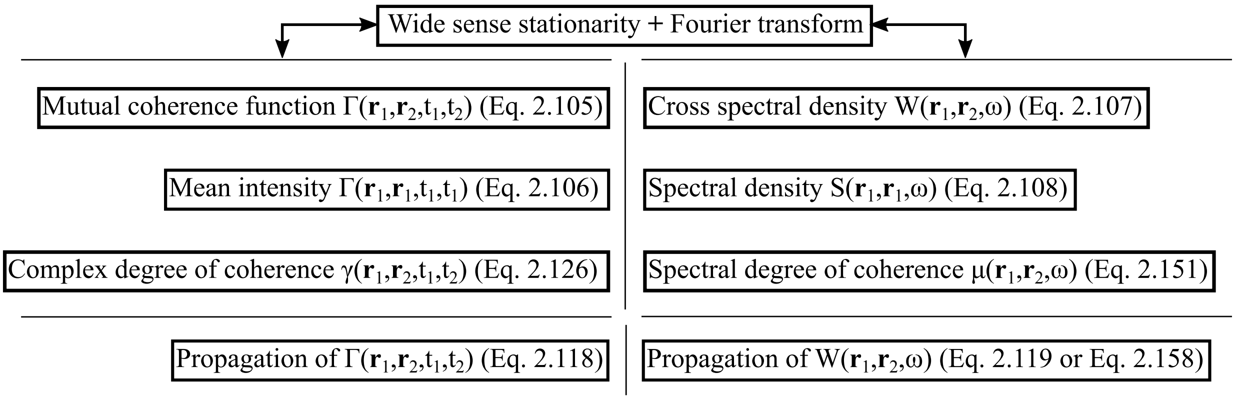

Figure 2.22.: Overview of the second order correlation theory quantities in time and in frequency representation.

which can be rewritten as:

$$U(\boldsymbol{r}_2,\omega)\langle U,\Phi\rangle = \lambda\Phi(\boldsymbol{r}_2,\omega). \tag{2.148}$$

Since λ and the scalar product are scalars every possible coherent mode must equal U up to a scalar. Hence the sole coherent mode is

$$\Phi = \frac{U}{\|U\|} \tag{2.149}$$

and a single mode is always orthogonal.

The sum of all eigenvalues equals the total spectral density S. We use this observation to define **mode occupations** d_n:

$$\boxed{d_n = \frac{\lambda_n}{\sum_m \lambda_m}.} \tag{2.150}$$

In the complete coherent case only $d_0 = 1$ and all other d_i equal zero. The sum of the mode occupations always equals 1. We want to call the so normalized mode spectrum **mode distribution**.

2.5.8. Spectral degree of coherence

The **spectral degree of coherence** μ is defined as the normalization of the cross spectral density W:

$$\boxed{\mu(\boldsymbol{r}_1,\boldsymbol{r}_2,\omega) = \frac{W(\boldsymbol{r}_1,\boldsymbol{r}_2,\omega)}{\sqrt{W(\boldsymbol{r}_1,\boldsymbol{r}_1,\omega)W(\boldsymbol{r}_2,\boldsymbol{r}_2,\omega)}}.} \tag{2.151}$$

From Young's experiment the definition in Eq. 2.128 were motivated.

We show that complete coherence and complete incoherence can also be expressed in terms of the spectral degree of coherence. The partially coherent case is then situated between these two limits.

Similar to Eq. 2.128 a field is completely coherent if and only if the absolute value of the spectral degree of coherence μ assumes its maximum value 1 for all $\boldsymbol{r}_1$ and $\boldsymbol{r}_2$. To see this we assume first that the field is completely coherent. The cross spectral density consists then of one mode only:

$$W = \lambda\Phi^*(\boldsymbol{r}_1)\Phi(\boldsymbol{r}_2). \tag{2.152}$$

We insert this form into the definition:

$$|\mu(\boldsymbol{r}_1, \boldsymbol{r}_2, \omega)| = \left| \frac{\lambda \Phi^*(\boldsymbol{r}_1)\Phi(\boldsymbol{r}_2)}{\lambda\,|\Phi(\boldsymbol{r}_1)|\,|\Phi(\boldsymbol{r}_2)|} \right| = \left| \frac{\Phi^*(\boldsymbol{r}_1)}{|\Phi(\boldsymbol{r}_1)|} \cdot \frac{\Phi(\boldsymbol{r}_2)}{|\Phi(\boldsymbol{r}_2)|} \right| = 1. \tag{2.153}$$

Controversy, if the spectral degree of coherence takes only values of magnitude 1 we see from the definition:

$$W(\boldsymbol{r}_1, \boldsymbol{r}_1, \omega) W(\boldsymbol{r}_2, \boldsymbol{r}_2, \omega) = |W(\boldsymbol{r}_1, \boldsymbol{r}_2, \omega)|^2 . \tag{2.154}$$

Using the coherent mode representation this is rewritten as:

$$\left(\sum_n \lambda_n |\Phi_n(\boldsymbol{r}_1)|^2 \right) \left(\sum_m \lambda_m |\Phi_n(\boldsymbol{r}_2)|^2 \right) = \sum_{n,m} \lambda_n \lambda_m \Phi_n^*(\boldsymbol{r}_1)\Phi_n(\boldsymbol{r}_2)\Phi_m(\boldsymbol{r}_1)\Phi_m^*(\boldsymbol{r}_2). \tag{2.155}$$

Because of the orthonormality of the modes the integration of this equation over $\boldsymbol{r}_1$ and $\boldsymbol{r}_2$ gives:

$$\left(\sum_n \lambda_n \right)^2 = \sum_n \lambda_n^2 . \tag{2.156}$$

Since the eigenvalues λ are non-negative the equality can only hold if there is only a single coherent mode. This implies that the field is completely coherent. The Eq. 2.156 can be seen in analogy to the criteria in quantum statistics that for a pure state the trace of the density operator squared must equal to one. Because the left hand side which corresponds to the trace of the density operator equals always one.

The case of complete incoherence can be seen directly from the definition of the cross spectral density (Eq. 2.107) because the mutual coherence function and the cross spectral density are Fourier conjugated. If the mutual coherence function Γ is zero for all time delays τ so will be the cross spectral density for all frequencies ω and vice versa.

2.5.9. Propagation of the cross spectral density in terms of coherent modes

The propagation of the cross spectral density can be accomplished by the propagation of its coherent modes. The modes are propagated just like ordinary electric fields. From the *practical point of view this property is probably the most advantageous* in particular if the source is rather coherent and consists therefore only of a few modes.

With the decomposition given by Eq. 2.137 the propagation formula Eq. 2.119 takes the form:

$$W'(\boldsymbol{r}_1, \boldsymbol{r}_2, \omega) = \sum_n \lambda_n(\omega) \int d\boldsymbol{r}_1' d\boldsymbol{r}_2' \; h^*(\boldsymbol{r}_1, \boldsymbol{r}_1')\Phi_n^*(\boldsymbol{r}_1, \omega) h(\boldsymbol{r}_2, \boldsymbol{r}_2')\Phi_n(\boldsymbol{r}_2, \omega) \tag{2.157}$$

which can be rewritten as:

$$\boxed{W'(\boldsymbol{r}_1, \boldsymbol{r}_2, \omega) = \sum_n \lambda_n(\omega) \left(\Phi_n'(\boldsymbol{r}_1, \omega) \right)^* \Phi_n'(\boldsymbol{r}_2, \omega)} \tag{2.158}$$

with

$$\boxed{\Phi_n'(\boldsymbol{r}, \omega) = \int d\boldsymbol{r}' \; h(\boldsymbol{r}, \boldsymbol{r}')\Phi_n(\boldsymbol{r}, \omega).} \tag{2.159}$$

The coherent mode is propagated like an electric field in Eq. 2.117.

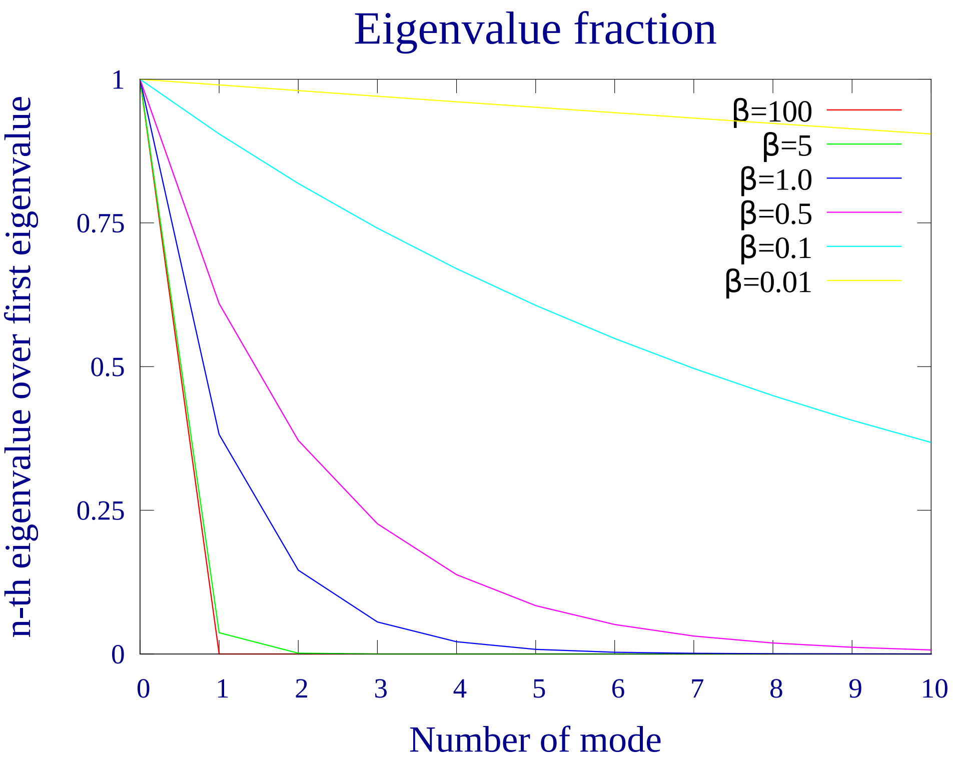

Figure 2.23.: Plot of the fraction of the eigenvalues λ_0/λ_n for a Gaussian Schell-model with different fractions $\beta = \sigma_g/\sigma_s$.

2.5.10. Gaussian Schell-model

In this section we present one of the few known models for a cross spectral density that possesses an analytically known coherent mode decomposition.

A *Schell-model*[15] is given in terms of the cross spectral density:

$$W(x_1, x_2, \omega) = \sqrt{S(x_1, \omega)}\sqrt{S(x_2, \omega)}g(x_2 - x_1, \omega) \tag{2.160}$$

where S is the spectral density.

A **Gaussian Schell-model** is a Schell-model with spectral density S:

$$S(x, \omega) = A^2(\omega) \exp\left(-\frac{x^2}{2\sigma_s^2(\omega)}\right) \tag{2.161}$$

and spectral degree of coherence g:

$$g(x, \omega) = \exp\left(-\frac{x^2}{2\sigma_g^2(\omega)}\right). \tag{2.162}$$

In a Gaussian Schell-model, like in every Schell-model, only the difference between two points is relevant for the spectral degree of coherence.

The eigenvalues and coherent modes are given by [38, 39]:

$$\lambda_n(\omega) = S(0, \omega)\left(\frac{\pi}{a(\omega) + b(\omega) + c(\omega)}\right)^{1/2}\left(\frac{b(\omega)}{a(\omega) + b(\omega) + c(\omega)}\right)^n \tag{2.163}$$

and

$$\Phi_n(x,\omega) = \frac{1}{\sqrt{2^n n!}} \left(\frac{2c(\omega)}{\pi}\right)^{1/4} \exp\left(-c(\omega)x^2\right) H_n(x\sqrt{2c(\omega)}). \tag{2.164}$$

Here, H_n is the physicists' Hermite polynomial of order n, $a(\omega) = 1/(4\sigma_s^2(\omega))$, $b(\omega) = 1/(2\sigma_g^2(\omega))$, and $c(\omega) = [a_x(\omega)^2 + 2a_x(\omega)b_x(\omega)]^{1/2}$. The functions Φ_n of Eq. 2.164 are also known as **Hermite functions** of order n with argument $x\sqrt{2c}$ [38]. Some coherent modes are depicted in Fig. 2.24.

The fraction of the first eigenvalue with the n-th eigenvalue is:

$$\frac{\lambda_n}{\lambda_0} = \left(\frac{1}{1 + \frac{\beta(\omega)^2}{2} + \beta(\omega)\sqrt{1 + \frac{\beta(\omega)^2}{4}}}\right)^n, \tag{2.165}$$

with

$$\beta(\omega) = \frac{\sigma_g(\omega)}{\sigma_s(\omega)}. \tag{2.166}$$

In our numerical setting we are more interested in the number of modes needed to find a good representation of the cross spectral density with a few coherent modes. A good description will incorporate almost the entire spectral density. Therefore we derive with the help of the geometrical series the fraction of spectral density incorporated by the first N modes:

$$F_N(\omega) = \frac{\sum_{n=0}^{N-1} \lambda_n}{\sum_{n=0}^{\infty} \lambda_n} = 1 - \left(\frac{1}{1 + \frac{\beta(\omega)^2}{2} + \beta(\omega)\sqrt{1 + \frac{\beta(\omega)^2}{4}}}\right)^N = 1 - \left(\frac{\lambda_1}{\lambda_0}\right)^N, \tag{2.167}$$

The spectral density fraction F can be solved for the number of modes N to incorporate that fraction:

$$N = \frac{\log(1-F)}{\log\left(\frac{\lambda_1}{\lambda_0}\right)}. \tag{2.168}$$

From the spectral density fraction F we can also derive the mode occupation:

$$d_n = F_{n+1} - F_n. \tag{2.169}$$

A two-dimensional model can be constructed as the product of a horizontal model x and vertical model y, with $W(\boldsymbol{r}_1, \boldsymbol{r}_2, \omega) = W_x(x_1, x_2, \omega)W_y(y_1, y_2, \omega)$, $\lambda_{lm}(\omega) = \lambda_l^x(\omega)\lambda_m^y(\omega)$, $\Phi_{lm}(\boldsymbol{r}, \omega) = \Phi_l^x(x,\omega)\Phi_m^y(y,\omega)$, and $F = F_x F_y$.

For the sake of readability we may define for a fixed frequency the cross spectral density:

$$\boxed{W(x_1, x_2) = A^2 \exp\left(-\frac{x_1^2}{4\sigma_s^2}\right) \exp\left(-\frac{x_2^2}{4\sigma_s^2}\right) \exp\left(-\frac{(x_2 - x_1)^2}{2\sigma_g^2}\right).} \tag{2.170}$$

A special class of Schell-models are the *quasi-homogeneous sources*. Quasi-homogeneous sources are characterised by a slowly varying spectral density $S(\boldsymbol{r}, \omega)$ and a fast varying function $g(\boldsymbol{r}, \omega)$, i.e. on the scale on which g varies significantly the spectral density is almost constant. A Gaussian Schell-model is quasi-homogeneous if $\sigma_s \gg \sigma_g$.

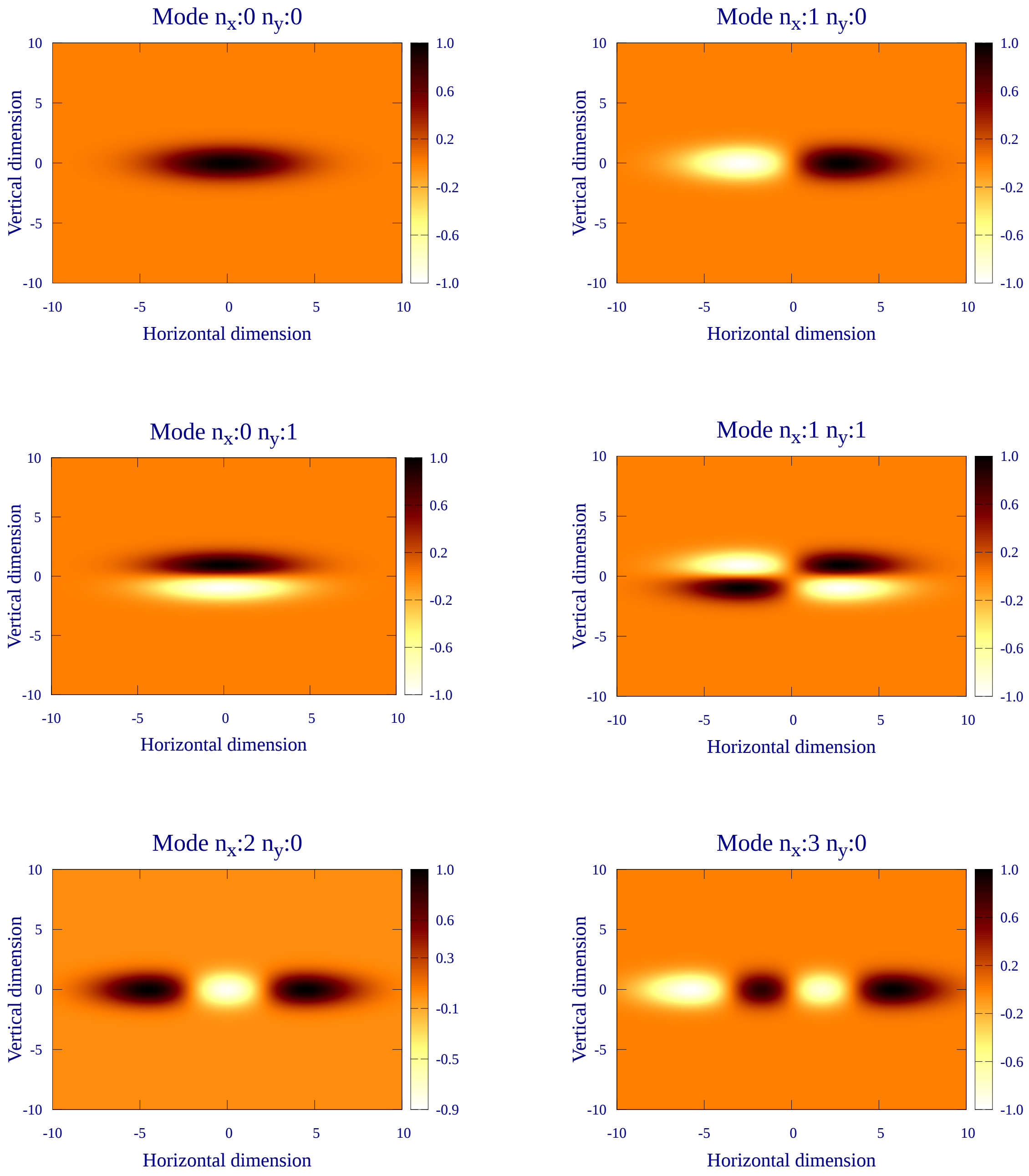

Figure 2.24.: First normalized coherent modes of the Gaussian Schell model with larger horizontal parameters $\sigma_s^{(x)} = \sigma_s^{(y)} = 3$ than vertical parameters: $\sigma_s^{(y)} = \sigma_s^{(y)} = 1$.

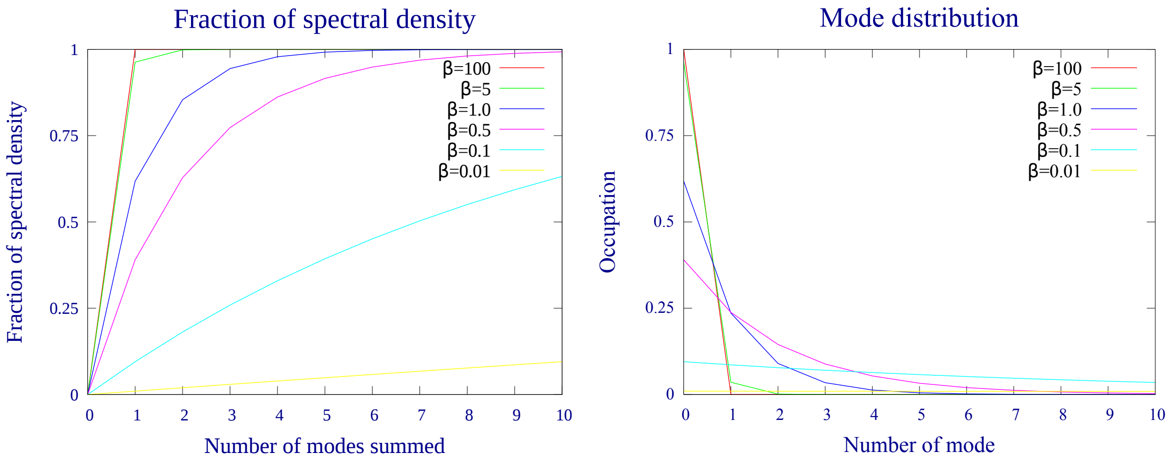

Figure 2.25.: Fraction of the spectral density incorporated by the first n modes(left) and mode distribution(right) for a Gaussian Schell-model with varying $\beta = \sigma_g/\sigma_s$.

2.5.11. Gaussian processes

We present here an important class of stochastic processes. Although the theory of stochastic processes is underlying many phenomena in statistical optics we could until this point avoid mentioning it. So far, the only knowledge we needed from the field of statistics was the ensemble average, which is implicitly based on stochastic processes. It is outside of the scope of this thesis to give a complete introduction of the theory of stochastic processes. Nevertheless the theory is well established and can lead to interesting interpretations as we will see in the next section.

Here we just restate some definitions and try to motivate their consequences.
A continuous stochastic process is Gaussian if for every finite set of indices $t_1, \ldots, t_n$ the random variable

$$X_{t_1,\ldots,t_n} = (X_1, \ldots, X_n) \tag{2.171}$$

is a multivariant Gaussian random variable.
This definition is suited for problems that do not need the description of complex variables. In our case we work with electric fields that are usually described with complex variables. The transition from a real Gaussian process to a complex stochastic process is straightforward: a complex Gaussian stochastic process is a complex random process whose real and imaginary part is a jointly Gaussian random process. In general, however, complex Gaussian processes can have very different behavior than a real Gaussian process.

By contrast the next class of complex random processes we present has very close analogies to real Gaussian processes[40]. For its definition we need to define one of its building blocks first:

An n-dimensional *circularly-symmetric Gaussian* Z is an n-dimensional complex Gaussian with the property that for all phase angles $\Phi \in \mathbb{R}$ the distribution of Z and $Ze^{i\Phi}$ are the same. For a zero mean complex Gaussian, an alternative characterisation of circularly symmetry is that the pseudo-covariance matrix:

$$M = \langle ZZ \rangle \tag{2.172}$$

is equal to zero.

The important consequence of this definition is that similar to the case of a real Gaussian the probability density function of Z is described solely in terms of its mean value and its covariance matrix:

$$\Sigma = \langle ZZ^* \rangle \, . \tag{2.173}$$

The probability density function of a n-dimensional circularly-symmetric Gaussian is given by:

$$f_Z(z) = \frac{1}{\pi^n \det(\Sigma)} e^{-(z-\mu)^* \Sigma^{-1} (z-\mu)}. \tag{2.174}$$

This is *a simpler form than for a general complex Gaussian* and *a consequence of the vanishing of the pseudo-covariance M* for a circular symmetric random variable.

We come now to the stochastic process we are interested in most in view of storage ring undulator radiation:
A circularly-symmetric Gaussian process is a complex Gaussian stochastic process with the property that for every finite set of indices $t_1, \ldots, t_n$ the random variable

$$Z_{t_1,\ldots,t_n} = (Z_1, \ldots, Z_n) \tag{2.175}$$

is a multivariant circularly-symmetric Gaussian random variable.

2.5.12. Interpretation of the coherence length for zero mean circularly-symmetric Gaussian processes

In this section we establish a clear physical interpretation of the spectral degree of coherence and the complex degree of coherence for a circularly-symmetric Gaussian random process. To the best of the authors' knowledge, a similar interpretation has not been published elsewhere. Let us consider an ensemble that is a complex zero mean circularly-symmetric Gaussian process. Let us further assume we know it in a plane. Like in Young's experiment we would like to know the correlation between two pinholes at $\boldsymbol{r}_1$ and at $\boldsymbol{r}_2$. Now, because the process is circularly-symmetric and Gaussian the induced random variable $Z = (Z_{\boldsymbol{r}_1}, Z_{\boldsymbol{r}_2})$ from the index set $T = \{\boldsymbol{r}_1, \boldsymbol{r}_2\}$ is a two-dimensional circularly-symmetric Gaussian random variable. The covariance of the two random variables equals the cross spectral density at these points[40]:

$$\mathrm{Cov}(Z_{\boldsymbol{r}_1}, Z_{\boldsymbol{r}_2}) = \langle E^*(\boldsymbol{r}_1, \omega) E(\boldsymbol{r}_2, \omega) \rangle = W(\boldsymbol{r}_1, \boldsymbol{r}_2, \omega). \tag{2.176}$$

Because the process has zero mean, is circularly-symmetric and Gaussian its probability density function is Gaussian and given by Eq. 2.174. The covariance matrix Σ is a Hermitian 2×2 matrix. Its elements are the cross spectral density W at $\boldsymbol{r}_1$ and $\boldsymbol{r}_2$[40]:

$$\Sigma = \begin{pmatrix} W(\boldsymbol{r}_1, \boldsymbol{r}_1, \omega) & W(\boldsymbol{r}_1, \boldsymbol{r}_2, \omega) \\ W(\boldsymbol{r}_2, \boldsymbol{r}_1, \omega) & W(\boldsymbol{r}_2, \boldsymbol{r}_2, \omega) \end{pmatrix}. \tag{2.177}$$

For a circularly-symmetric Gaussian the conditional probability $r_2|r_1$ of measuring a value y at $\boldsymbol{r}_2$ given a value x at $\boldsymbol{r}_1$ is[40]:

$$\boxed{f_{r_2|r_1}(y|x) = \frac{1}{2\pi\sigma^2_{r_2|r_1}} \exp\left(- \frac{\left| y - \sqrt{\frac{W(\boldsymbol{r}_2, \boldsymbol{r}_2, \omega)}{W(\boldsymbol{r}_1, \boldsymbol{r}_1, \omega)}} \mu(\boldsymbol{r}_2, \boldsymbol{r}_1, \omega) x \right|^2}{2\sigma^2_{r_2|r_1}} \right)} \tag{2.178}$$

with

$$\boxed{\sigma^2_{r_2|r_1} = \frac{1}{2} W(\boldsymbol{r}_2, \boldsymbol{r}_2, \omega) \left(1 - |\mu(\boldsymbol{r}_1, \boldsymbol{r}_2, \omega)|^2\right)} \tag{2.179}$$

here μ is the spectral degree of coherence.
In the derivation of this equation we used the fact that $W(\boldsymbol{r}_1, \boldsymbol{r}_2, \omega)$ can be expressed in terms of

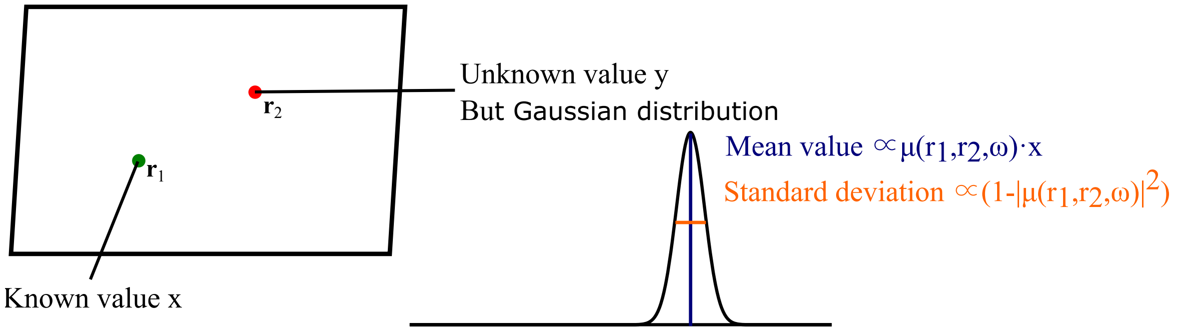

Figure 2.26.: Illustration of a thought experiment. Similar to Young's experiment two pinholes are located in a plane. The value x at the pinhole at $\boldsymbol{r}_1$ is known, for instance due to a measurement. The conditional probability distribution for the value y at the hole at $\boldsymbol{r}_2$ is sketched.

the spectral degree of coherence:

$$W(\boldsymbol{r}_1, \boldsymbol{r}_2, \omega) = \mu(\boldsymbol{r}_1, \boldsymbol{r}_2, \omega)\sqrt{W(\boldsymbol{r}_1, \boldsymbol{r}_1, \omega) W(\boldsymbol{r}_2, \boldsymbol{r}_2, \omega)}. \tag{2.180}$$

The equation 2.178 allows the *interpretation of the spectral degree of coherence* μ *as a quadratic scaling factor of the standard deviation of the conditional probability* (see Fig. 2.26).

One can do analog for the degree of coherence. To write the same in words: given the value x at pinhole $\boldsymbol{r}_1$ the distribution of $\boldsymbol{r}_2$ is Gaussian. Its standard deviation depends quadratically on the magnitude of the spectral degree of coherence. Its expectation value depends linearly on the value x, the spectral degree of coherence and the ratio between the spectral densities at the two points.

In the case of complete coherence the Gaussian degrades and no fluctuation exist at $\boldsymbol{r}_2$, i.e. given the value at $\boldsymbol{r}_1$ the value is surely determined at $\boldsymbol{r}_2$.

In the case of complete incoherence the value fluctuates independently with the width of the spectral density at $\boldsymbol{r}_2$. In between the Gaussian is narrowed from complete incoherence to complete coherence.

In conclusion in the case of a zero mean circularly-symmetric Gaussian process the spectral degree of coherence determines the standard deviation of the conditional probability between two positions. It allows therefore a physical clear interpretation. The knowledge of the value at hole $\boldsymbol{r}_1$ restricts the fluctuation at other holes depending on their correlation with the hole at $\boldsymbol{r}_1$. Note that these arguments can equally be applied to the mutual coherence function Γ to get analog results in the time domain.

2.6. Summary

In this chapter we discuss the comprehensive theory necessary for this thesis.

We start with some accelerator physics and explain the principle functioning of electron storage rings. The statistics of the electrons in the storage ring can be described by a Gaussian electron phase space distribution Eq. 2.10 with the covariance matrix Σ. The covariance matrix can be calculated numerically with accelerator physics software codes. In the calculations in this thesis we are mainly interested in *the elements* m_{ij} of the inverse of the covariance matrix M as we define in Eq. 2.14. In section 2.1.6 we introduce the two points in the straight section at which we will perform calculations in this thesis: the *symmetry point* and the *finite alpha* position. We define the *electron beam settings* used in this thesis in section 2.1.8.

We discuss general synchrotron radiation characteristics and special devices for the production of intense X-ray radiation, the so called insertion devices, in section 2.2 and 2.3. In this thesis we will use only undulator insertion devices. We describe how their emission can be calculated from the electron trajectory which in turn is related to the magnetic field of the insertion device. In this thesis we will calculate the undulator emission numerically with SRW[24]. We define the notions of *resonance energy*, *flux maxima* as well as *the undulator settings we will use in this thesis* in section 2.3.4.

We review the theory of physical optics in view of synchrotron applications in section 2.4. We derive the Fresnel diffraction formula from the Helmholtz equation and the Green's identity and we discuss how optical elements in thin element approximation affect the electric field. In section 2.4.3 we mention how the Fresnel propagation can be implemented numerically in terms of FFT based convolutions and some difficulties arising in combination with these implementations. We introduced the notion of *wavefront* that is used by SRW and which means the electric field in a plane along or before the beamline.

In section 2.5 we introduce the statistical optics concept of second order coherence theory. We point out that the source fluctuations are *fundamental* for the coherence properties of the emission. We define several important quantities of second order coherence theory. An overview of these quantities is depicted in Fig. 2.22. For the rest of this thesis the most important of them are: the *cross spectral density* W (Eq. 2.107), the *cross spectral density operator* A_W (Eq. 2.139), the *spectral degree of coherence* μ (Eq. 2.151) and the *spectral density* S (Eq. 2.108). We introduced the coherent mode decomposition of the cross spectral density in Eq. 2.137 which gives a representation of the cross spectral density in terms of *eigenvalues* λ_n and *coherent modes* Φ_n. The coherent mode decomposition is the theoretical basis of the algorithm we present in chapter 4. We define the *mode spectrum* of the cross spectral density as the set of its eigenvalues; the *mode occupation* d_n in Eq. 2.150 as the n-th eigenvalue normalized by the sum of all the eigenvalues; *mode distribution* as the set of all mode occupations and the *mode intensity* as the intensity of a coherent mode if it was an electric field. In section 2.5.6 we show that there is no finite dimensional representation of the cross spectral density that incorporates more spectral density than a coherent mode representation of the same dimension. We discuss that the emission is completely coherent if and only if the cross spectral density consists of a single mode in section 2.5.7. We mention how the cross spectral density can be propagated along a synchrotron beamline. Given a propagation kernel h the propagation of the cross spectral density can be described by Eq. 2.119 or in terms of its coherent modes (Eq. 2.157). We introduce the *Gaussian Schell-model* in Eq. 2.170 that possesses an analytical decomposition into coherent modes and we discuss properties of its mode spectrum. The Gaussian Schell-model will serve as an important test case for the algorithm in chapter 4.

Finally, we discuss in section 2.5.12 that for a circularly-symmetric Gaussian random process the spectral degree of coherence μ can be interpreted as a quadratic scaling factor of the standard deviation of the conditional probability.

3. Statistical optics for synchrotrons

In the previous chapter we reviewed the fundamentals of statistical optics in a general fashion. In this chapter we apply it to the radiation of synchrotrons. We restrict our discussion mainly to undulator radiation because undulators are nowadays the most used source for experiments exploiting high coherence. We present a formula to calculate the cross spectral density under non restrictive assumptions. We follow Kim's idea of the brightness convolution theorem[7] and the theoretical considerations of Geloni *et al.*[8]. During the derivations we try to be verbose and to highlight the most important underlying physical ideas.

3.1. The brightness convolution theorem

As stated in the previous section the cross spectral density W describes second order coherence completely. Its knowledge would allow us to describe the spectral density of the radiation ensemble and its propagation through a beamline. The **brightness convolution theorem** states: Let E_0 be the electric field produced by a reference electron that traveled some trajectory (see Fig. 3.1), let the electrons be statistically independent and let the magnetic field variations over the electron beamsize be negligible. The cross spectral density is then given by:

$$\boxed{W(\boldsymbol{r}_1, \boldsymbol{r}_2, \omega) = N_e \int d\boldsymbol{r} d\boldsymbol{\theta}\ \rho(\boldsymbol{r}, \boldsymbol{\theta}) e^{ik\boldsymbol{\theta}(\boldsymbol{r}_2 - \boldsymbol{r}_1)} {E_0}^*(\boldsymbol{r}_1 - \boldsymbol{r}, \omega) E_0(\boldsymbol{r}_2 - \boldsymbol{r}, \omega)} \tag{3.1}$$

here N_e is the number of electrons per bunch, ρ is the electron phase space electron density, k is the wavenumber, θ the angle of the electrons.

The theorem is called brightness convolution theorem because the initial paper is mainly interested in the Wigner function, which is also called *brightness* or *brilliance* in the synchrotron community. On the other hand some authors prefer to define the brightness as a single number extracted from the Wigner function[16]. The Wigner function in frequency representation and the cross spectral density are related by a spatial Fourier transform and what we state here is basically the real-space representation of the last line of the derivation of the brightness convolution theorem given in the original paper[7]. The theorem allows us to actually calculate the cross spectral density from which the entire second order correlations of the system are derived.

The reference electric field E_0 can be calculated numerically or approximated with analytical formulas[8]. Usual analytical formulas for undulators will, however, only work for undulators

Figure 3.1.: Illustration of an electron entering the undulator on axis. It follows a reference trajectory and creates a reference emission E_0.

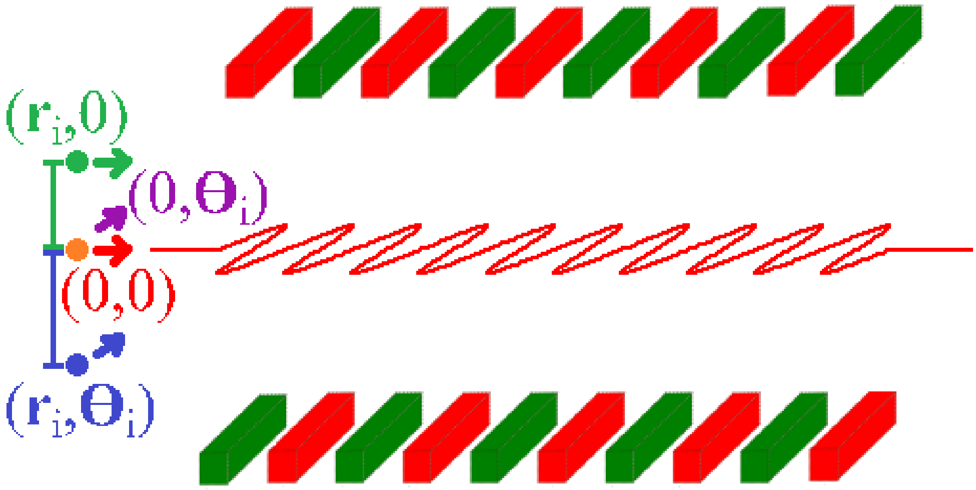

Figure 3.2.: The reference electron (red arrow) enters the undulator and follows a reference trajectory. Electrons can enter relative to the reference electron with a spatial shift $(\boldsymbol{r}_i, 0)$ (green), with an initial angle $(0, \boldsymbol{\theta}_i)$ (violet) or with an initial shift and an angle $(\boldsymbol{r}_i, \boldsymbol{\theta}_i)$ (blue). The on-axis electron is colored orange because the red and violet arrow start from it.

with a large number of periods $N \gg 1$ and may neglect some effects like edge effects. Statistical independence of the electron is naturally given in today's synchrotron storage rings in which electron-electron and electron-photon interaction is practically none existing. In free electron lasers this condition is seriously violated due to the SASE microbunching of the electrons. The last condition of negligible magnetic field variations over the electron beamsize can be fulfilled to a good accuracy in real undulators. If, however, focusing elements are used inside the undulator this assumption can no longer be held.

Because of the theorem's central importance for our algorithm and also for the physical understanding of coherence properties of storage ring radiation we redo the derivation of the theorem in a different way and add some enlightening comments. Additionally we will discuss at which positions of the storage ring the theorem can be applied.

The underlying idea of the theorem is a simple analytical relation between **the reference electric field E_0** and **the electric field produced by the i-th electron in the bunch E_i** in particular planes in the storage ring. One of these planes is called the virtual source and is often assumed to be in the middle of the undulator. The mentioned relation is then integrated over all electrons in the bunch and leads to Eq. 3.1. Even though it is complicated to solve the integral given in Eq. 3.1 the problem becomes much easier than the calculation of every single electron emission. This is particularly true for numerical approaches, which we want to follow in this thesis. Instead of the computational expensive need to calculate the trajectory and the emission of every electron in the bunch, only a single reference emission E_0 has to be calculated numerically and the remaining single electron emissions are deduced in a simple fashion.

In what follows we will discuss this relation between the emission of the reference electron E_0 and the emission of the i-th electron E_i in all detail. In the original paper[7] equation (22) relates the reference emission and the emission of the i-th electron in angular representation:

$$\hat{E}_i(\boldsymbol{\theta}) = e^{ik(ct_i - \boldsymbol{\theta}\boldsymbol{r}_i)}\hat{E}_0(\boldsymbol{\theta} - \boldsymbol{\theta}_i) \tag{3.2}$$

here k is the wavenumber, $\boldsymbol{r}_i$ is the relative shift of the i-th electron to the reference electron, $\boldsymbol{\theta}_i$ is the relative angle at the virtual source plane of the i-th electron (see Fig. 3.2) and t_i is the arrival time at the virtual source.

The implication of Eq. 3.2 may become clearer if we state it equivalently in real-space:

$$\boxed{E_i(\boldsymbol{r}) = e^{ik(ct_i+\boldsymbol{\theta}_i(\boldsymbol{r}-\boldsymbol{r}_i))}E_0(\boldsymbol{r}-\boldsymbol{r}_i).} \tag{3.3}$$

The physical meaning of this relation can be understood if we propagate E_i in free space by a distance z with the Fresnel propagator (Eq. 2.96):

$$\begin{aligned} E_i'(\boldsymbol{r}) &= \frac{e^{ikz}}{i\lambda z}\int e^{ik(ct_i+\boldsymbol{\theta}_i(\boldsymbol{r}'-\boldsymbol{r}_i))}E_0(\boldsymbol{r}'-\boldsymbol{r}_i)\exp\left(\frac{ik}{2z}(\boldsymbol{r}-\boldsymbol{r}')^2\right)d\boldsymbol{r}' \\ &= \frac{e^{ik(z+ct_i)}}{i\lambda z}\int E_0(\boldsymbol{u})\exp\left(\frac{ik}{2z}[(\boldsymbol{r}-\boldsymbol{r}_i-\boldsymbol{u})^2+2z\boldsymbol{\theta}_i\boldsymbol{u}]\right)d\boldsymbol{u} \\ &= \frac{e^{ik(z+ct_i)}}{i\lambda z}\exp\left(\frac{ik}{2z}[2z\boldsymbol{\theta}_i(\boldsymbol{r}-\boldsymbol{r}_i)]\right)\int E_0(\boldsymbol{u})\exp\left(\frac{ik}{2z}[(\boldsymbol{r}-\boldsymbol{r}_i-\boldsymbol{u})^2-2z\boldsymbol{\theta}_i(\boldsymbol{r}-\boldsymbol{r}_i-\boldsymbol{u})]\right)d\boldsymbol{u} \\ &= \frac{e^{ik(z+ct_i+\boldsymbol{\theta}_i(\boldsymbol{r}-\boldsymbol{r}_i))}}{i\lambda z}\exp\left(-\frac{ik}{2z}z^2\boldsymbol{\theta}_i^2\right)\int E_0(\boldsymbol{u})\exp\left(\frac{ik}{2z}(\boldsymbol{r}-\boldsymbol{r}_i-\boldsymbol{u}-z\boldsymbol{\theta}_i)^2\right)d\boldsymbol{u} \\ &= \frac{e^{ik(z+ct_i+\boldsymbol{\theta}_i(\boldsymbol{r}-\boldsymbol{r}_i)-\frac{z}{2}\boldsymbol{\theta}_i^2)}}{i\lambda z}\int E_0(\boldsymbol{u})\exp\left(\frac{ik}{2z}(\boldsymbol{r}-\boldsymbol{r}_i-\boldsymbol{u}-z\boldsymbol{\theta}_i)^2\right)d\boldsymbol{u} \end{aligned} \tag{3.4}$$

where we substituted: $\boldsymbol{u} = \boldsymbol{r}' - \boldsymbol{r}_i$.
This can be rewritten as:

$$E_i'(\boldsymbol{r}) = e^{i\Phi_i(\boldsymbol{r})}{E_0}'(\boldsymbol{r}-(\boldsymbol{r}_i+z\boldsymbol{\theta}_i)) \tag{3.5}$$

with a real phase function $\Phi_i(\boldsymbol{r})$:

$$\Phi_i(\boldsymbol{r}) = k\left(ct_i+\boldsymbol{\theta}_i(\boldsymbol{r}-\boldsymbol{r}_i)-\frac{z}{2}\boldsymbol{\theta}_i^2\right). \tag{3.6}$$

We conclude that according to the relation given in Eq. 3.3 the propagated reference field ${E_0}'$ and the propagated field of the i-th electron E_i' is relatively shifted by the sum of the spatial shift $\boldsymbol{r}_i$ and the inclination $z\boldsymbol{\theta}_i$ multiplied by a complex factor that depends on the specific electron. For our purposes we will only we interested in *correlation expressions* of the form $E_i^*(\boldsymbol{r}_1)E_i(\boldsymbol{r}_2)$ for which the situation becomes even more handy:

$$(E_i^*(\boldsymbol{r}_1))'E_i'(\boldsymbol{r}_2) = e^{ik\boldsymbol{\theta}_i(\boldsymbol{r}_2-\boldsymbol{r}_1)}\left({E_0}^*(\boldsymbol{r}_1-(\boldsymbol{r}_i+z\boldsymbol{\theta}_i))\right)'{E_0}'(\boldsymbol{r}_2-(\boldsymbol{r}_i+z\boldsymbol{\theta}_i)). \tag{3.7}$$

In view of these correlation expressions the emissions of the reference electron and of the i-th electron are related due to the sum of a shift and an inclination as well as a plane wave phase factor that depends on the i-th electron angle and the coordinates $\boldsymbol{r}_1$, $\boldsymbol{r}_2$ at which the correlation is evaluated.

At no point we imposed the non negativity of z and we may define **virtual sources** with the property that a virtual electric field from a virtual sources propagated by z reproduces the real electric field.

So far we have discussed the consequences of Eq. 3.2 we will now present why this formula reflects the storage ring situation. First we will discuss how the trajectories of the reference electron and the i-th electron are related. Afterwards we will discuss how the relation of their trajectories reflects in the relation of their emissions. Finally we will conclude that Eq. 3.7

describes the resulting correlation expression.

We consider first the situation for an electron entering the undulator with a finite spatial shift $\boldsymbol{r}_i \neq 0$ but zero relative angle $\boldsymbol{\theta}_i = 0$. The requirements of the brightness convolution theorem guarantees that the electron is subjected to the same magnetic field as the reference electron. In consequence the trajectory of the i-th electron will be the same trajectory as the trajectory of the reference electron but globally shifted by $\boldsymbol{r}_i$ (see Fig. 3.3 top).

For an electron with zero relative shift $\boldsymbol{r}_i = 0$ but finite relative angle $\boldsymbol{\theta}_i \neq 0$ the trajectory of the i-th electron will essentially be the reference trajectory on top of an uniform motion with slope $\boldsymbol{\theta}_i$ in units of the speed of light (see Fig. 3.3 bottom). This is again due to the condition that the magnetic field variation over the electron beamsize is negligible. A constant drift of the electron is added to the trajectory of the reference electron. This can be seen from the equation of motion (Eq. 2.56). For simplicity we assume the magnetic field is directed only along the vertical axis y:

$$\frac{d\boldsymbol{p}}{dt} = -eB_y(\boldsymbol{v} \times \hat{e}_y). \tag{3.8}$$

here $\hat{e}_y$ is the unit vector pointing in the vertical direction. This is rewritten as:

$$\frac{d\boldsymbol{p}}{dt} = -eB_y(v_x\hat{e}_s - v_s\hat{e}_x) = eB_y v_s\hat{e}_x - eB_y v_x\hat{e}_s. \tag{3.9}$$

with the unit vectors $\hat{e}_x$ and $\hat{e}_s$ along the x and s direction, respectively. The first term is identically to the one of the reference electron whose velocity is directed purely along the s direction. The second term is due to the extra initial velocity in the horizontal x direction at the entrance plane of the undulator. The second term produces a force along the longitudinal s direction. This force is very small on the scale of the momentum in s direction because $v_x/c \approx 10^{-6} \ll v_s/c \approx 1$. Hence the motion of the electron that enters with an initial inclination is essentially the motion of the reference electron on top of the initial uniform motion in the transverse direction $\boldsymbol{r}_\perp(t) = (v_x\hat{e}_x + v_y\hat{e}_y)t$.

A combination of finite relative shift $\boldsymbol{r}_i \neq 0$ and finite relative angle $\boldsymbol{\theta}_i \neq 0$ results in a trajectory that is shifted relative to the reference trajectory and superimposed with a constant drift.

Let us now discuss how these shifts and drifts translate to the emission of the i-th electron.

From Eq. 2.71 one can conclude that a trajectory shifted by $\boldsymbol{r}_i$ simply produces an emission that is shifted by $\boldsymbol{r}_i$:

$$E_i(\boldsymbol{r}) = E_0(\boldsymbol{r} - \boldsymbol{r}_i). \tag{3.10}$$

In the case of an extra constant drift the trajectory gets an extra uniform linear motion $\boldsymbol{r}_\perp(t) = c\boldsymbol{\theta}_i t$ with $\ddot{\boldsymbol{r}}_\perp = 0$. The angular representation of Eq. 2.71, i.e. its Fourier transform from real-space to angle representation, reveals that due to the extra constant drift relative to the reference field there is an extra plane wave phase factor in the real-space representation of the emission of the i-th electron. Because the axis of inclination lies at the origin of the undulator entrance plane we arrive due to geometric consideration at the inclination $z\boldsymbol{\theta}_i$ of the emission on an observation screen in distance z from the undulator entrance. The emission of an electron with finite angle is therefore:

$$E_i(\boldsymbol{r}) = e^{ik\boldsymbol{\theta}_i\boldsymbol{r}} E_0(\boldsymbol{r} - z\boldsymbol{\theta}_i). \tag{3.11}$$

Combining the two cases one arrives at:

$$E_i(\boldsymbol{r}) = e^{ik\boldsymbol{\theta}_i\boldsymbol{r}} E_0(\boldsymbol{r} - \boldsymbol{r}_i - z\boldsymbol{\theta}_i) \tag{3.12}$$

and correlation expressions take exactly the form of Eq. 3.7.

Summarizing we have seen that an electron entering the undulator with a spatial offset $\boldsymbol{r}_i$ and an angle $\boldsymbol{\theta}_i$ creates on a screen in distance z the field E_i as given in Eq. 3.12. Hereby z is the

Shifted incoming electron:

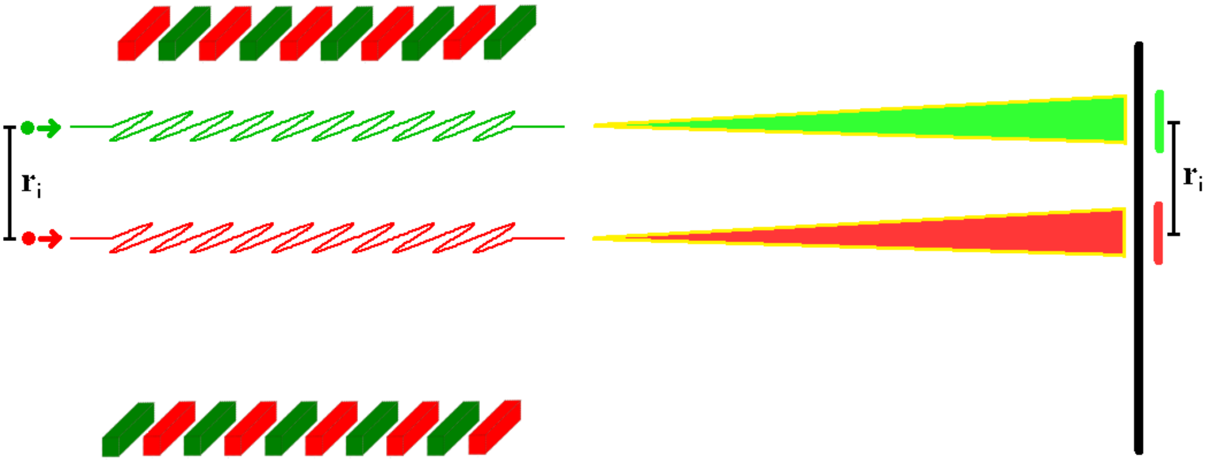

Inclined incoming electron:

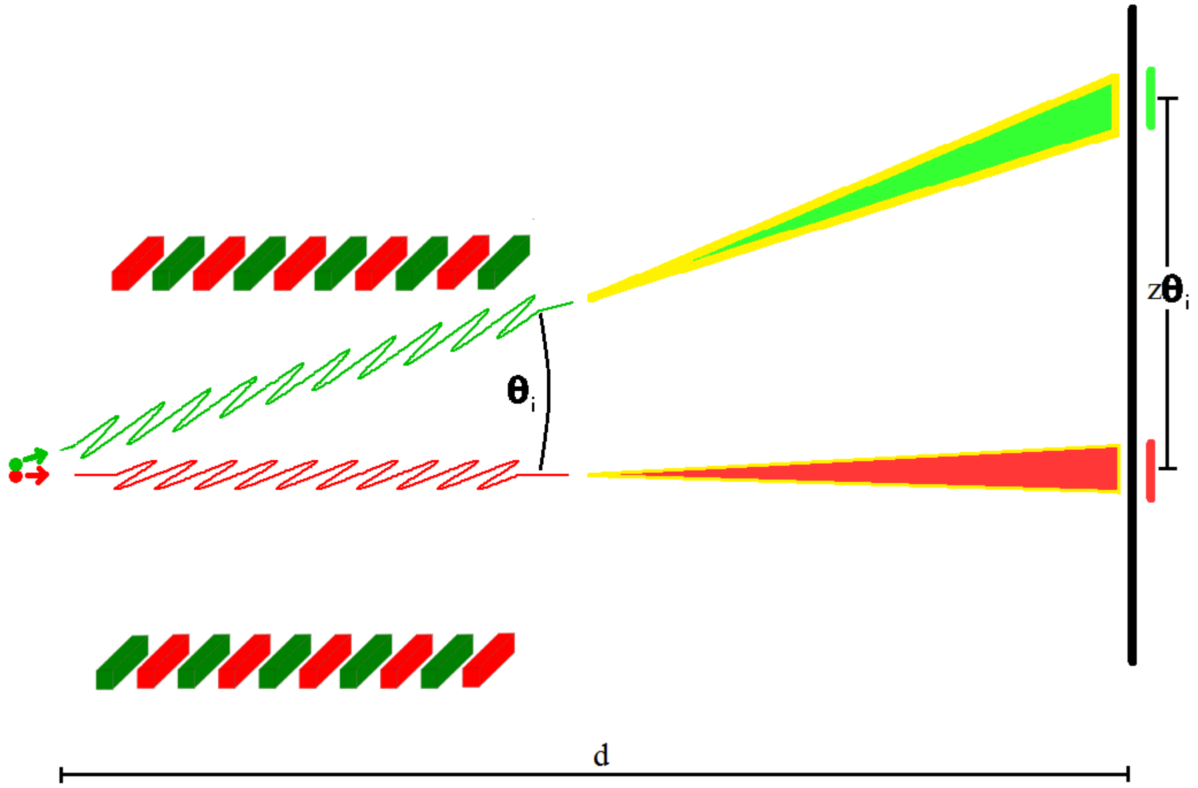

Figure 3.3.: Schematic illustration of the effect of an initial spatial offset or an initial inclination of an electron at the entrance plane of the undulator. The red electron is the reference electron. The green electron enters with a spatial shift $\boldsymbol{r}_i$ (top) or an inclination $\boldsymbol{\theta}_i$ (bottom). The produced radiation is shifted transverse by $\boldsymbol{r}_i$ and $z\boldsymbol{\theta}_i$, respectively. It turns out that $z = d$. Additionally, in the case with initial inclination (bottom), one has an extra phase factor relative to the reference emission and the emission in that case is the same as the reference emission if the screen is rotated. This concept is the root of the convolution theorem.

distance from the undulator entrance plane to the observation plane. We may bring Eq. 3.12 in the form of Eq. 3.5 because in view of correlation expression they are identical. Reading Eq. 3.4 in the inverse direction we can define a virtual source. In this virtual source Eq. 3.3 holds. The virtual source has no direct physical meaning but after propagation by z it describes the real situation. In what follows the usage of the virtual source, in which $z = 0$, makes the resulting integral much simpler. We exploit hereby that the summation of single electron emission and free space propagation of the emission commute.

We have established how the initial condition of the i-th electron reflect in the description of its emission in terms of the reference emission E_0. The total electric field of the electron bunch at the virtual source will be the summation of the electrons in the bunch:

$$E(\boldsymbol{r}) = \sum_{i \in \text{bunch}} E_i(\boldsymbol{r}_i). \tag{3.13}$$

The cross spectral density at the virtual source is then

$$\begin{aligned} \langle E^*(\boldsymbol{r}_1)E(\boldsymbol{r}_2)\rangle_{ens} &= \sum_{i,j \in \text{ens}} E_i^*(\boldsymbol{r}_1)E_j(\boldsymbol{r}_2) \\ &= N_e \int d\boldsymbol{r} d\boldsymbol{\theta} e^{ik\boldsymbol{\theta}(\boldsymbol{r}_2-\boldsymbol{r}_1)} \rho(\boldsymbol{r},\boldsymbol{\theta}) {E_0}^*(\boldsymbol{r}_1-\boldsymbol{r})E_0(\boldsymbol{r}_2-\boldsymbol{r}). \end{aligned} \tag{3.14}$$

The summation of the cross terms $i \neq j$ averages to zero for most synchrotron applications. Geloni *et al.*[8] dedicated a long discussion based on electron beam statistics to this summation. For now we will just state the result and we will follow and slightly modify their argumentation in the next section. With Eq. 3.14 we arrived at the brightness convolution theorem Eq. 3.1.

Earlier we said that the choice $z = 0$ makes the calculation much simpler. Let us now discuss why this is the case. For $z = 0$ the dependence of $\boldsymbol{\theta}$ is only found in the electron phase space density ρ and in the complex exponential in Eq. 3.14 while for any choice $z \neq 0$ an extra $\boldsymbol{\theta}$ dependence appears inside the arguments of the reference electric fields E_0. The choice $z = 0$ makes further analytical work with numerically given reference electric fields E_0 possible. It will reduce the four-dimensional integral to a two-dimensional integral for all practical cases. It is this analytical reduction of two dimensions of integration that allows us to think of practical numerical applications based on the brightness convolution theorem.

So far we neglected the energy spread of the electron, i.e. electrons arriving at the undulator entrance have a statistically distributed energy. From Eq. 2.63, Eq. 2.65 together with Eq. 2.71 it can be seen that the emission depends on the electron energy. On the other hand all the arguments used in the discussion of the relation between a reference field E_0 and the field of the i-th electron E_i, that both have the same electron energy, were free of any energy dependence. In a more general discussion in the next section we will see that the summation Eq. 3.14 additionally averages to zero cross terms arising from electrons with different kinetic energies. The brightness convolution theorem can there be enhanced to account for energy spread:

$$\boxed{W(\boldsymbol{r}_1,\boldsymbol{r}_2,\omega) = N_e \int d\delta d\boldsymbol{r} d\boldsymbol{\theta}\ \rho(\boldsymbol{r},\boldsymbol{\theta},\delta) e^{ik\boldsymbol{\theta}(\boldsymbol{r}_2-\boldsymbol{r}_1)} {E_0}^*(\boldsymbol{r}_1-\boldsymbol{r},\omega,\delta)E_0(\boldsymbol{r}_2-\boldsymbol{r},\omega,\delta).} \tag{3.15}$$

Here we adopted the notion used in electron beam dynamics to express the electron phase space density in terms of the momentum deviation δ which is related to the energy γ by Eq. 2.7.

From the nature of the convolution theorem, i.e. it imitates spatial offsets and initial inclinations of an electron entering the undulator, follows that **the electron phase space density of the undulator entrance plane is a natural choice for the convolution, i.e. for the definition of the virtual source position.** This can be deduced from a thought experiment.

Imagine we put a screen in some distance d from the undulator entrance plane. The emission intensity of an electron entering the undulator on-axis with an initial angle $\boldsymbol{\theta}_i$ will we shifted by $z\boldsymbol{\theta}_i$ relative to the reference electron's emission intensity. The value of z is considered to be unknown (see Fig. 3.3 bottom). We may determine z by a linear regression because the shift of the emission intensity $z\boldsymbol{\theta}_i$ is a linear function of $\boldsymbol{\theta}_i$ and z is its *slope*. The so obtained z will define the position of the virtual source. According to our earlier discussion we expect $z = d$. This prediction is numerically simulated and verified in section 4.2.1 for the undulators we use in this thesis.

In other works, however, the virtual source is often chosen too lie in the middle of the undulator. In this case the analytical expressions for the undulator radiation in resonance approximation become simpler and the field at the center of the undulator is real [8]. The phase space distribution is then taken from the unperturbed ring, i.e. it is assumed that the undulator has no significant effect on the electron beam dynamics inside the undulator [41]. Due to the design of undulators the electron phase space distribution outside the undulator will certainly not be changed significantly by the presence of the undulator (not the case for damping wigglers). Inside the undulator, locally, there could however be changes of the electron phase space distribution. This local deviation of the electron's phase space configuration from its free space propagation is numerically investigated and discussed in section 4.2.5 for the undulators used in this thesis.

3.2. Statistical considerations for emission from electron bunches

In this section we will discuss some statistical properties of undulator radiation in synchrotron storage rings. One of our main observations will be the validity of the summation in Eq. 3.14 for all photon frequencies of practical interest. Geloni *et al.* show in [8] that for storage ring undulator radiation the second-order field correlation function in frequency domain can be separated into two functions. One function depends only on a frequency difference and the other one depends only on the spatial coordinates and one frequency coordinate. In order to do this they assume an electron density that can be separated into a purely transverse and purely longitudinal part. In practice this may only be approximately possible. In general the electron beam does not obey a separation in transverse and longitudinal parts. Borrowing largely the same arguments we show that the before mentioned separation remains possible for a Gaussian shaped electron phase distribution (see section 2.1.3) that has weak couplings between the longitudinal bunch size and the other beam parameters.

Implicitly the following discussion describes on a more concrete level that even though two electrons, and therefore their emissions, are independent their *sum* is correlated. To see this we calculate the covariance. Let E_1 and E_2 be the emissions of two single electrons and let their emission be uncorrelated, i.e. $\mathrm{Cov}(E_1, E_2) = 0$. Their *sum* however is correlated:

$$\mathrm{Cov}(E_1 + E_2, E_1 + E_2) = \mathrm{Cov}(E_1, E_1) + \mathrm{Cov}(E_2, E_2) + 2\mathrm{Cov}(E_1, E_2) \neq 0. \tag{3.16}$$

The second-order field correlation function in frequency representation of the electric field of an electron bunch describes the second order statistics. It is given by:

$$\Gamma_\omega(z, \boldsymbol{r}_1, \boldsymbol{r}_2, \omega_1, \omega_2) = \langle E_b^*(\boldsymbol{r}_1, \omega_1) E_b(\boldsymbol{r}_2, \omega_2) \rangle_{ens} \tag{3.17}$$

where E_b is the electric field of a bunch and the average has to be taken over the ensemble. The ensemble average over a function w is given by:

$$\langle w(\boldsymbol{u}) \rangle_{ens} = \int d\boldsymbol{u}\ \rho_6(\boldsymbol{u}) w(\boldsymbol{u}) \tag{3.18}$$

here ρ_6 is the six dimensional electron phase space density and $\boldsymbol{u} = (x, x', y, y', \delta, s)$ is a vector of the phase space. As discussed in section 2.1.3 for many cases a multivariant Gaussian is a good approximation for the phase space density. The random variables x, x', y, y', δ, s follow the electron beam phase space distribution. In general they can not be considered independent. While storage rings are usually designed such that vertical and horizontal coupling in the straight section should be very small the coupling between position and momenta away from a symmetry point is non zero due to finite derivatives of the beta functions.

The total electric field of a bunch can be written as:

$$E_b(\boldsymbol{r}, \omega) = \sum_n^{N_b} E(\tilde{\boldsymbol{u}}_n, \boldsymbol{r}, \omega) \exp(i\omega t_n) \tag{3.19}$$

where N_b is the number of electrons in the bunch, t_n is the arrival time at some fixed position of the undulator and $\tilde{\boldsymbol{u}}$ is the reduced phase space vector defined in Eq. 2.16.

We insert Eq. 3.19 into Eq. 3.17 and arrive at:

$$\Gamma_\omega(\boldsymbol{r}_1, \boldsymbol{r}_2, \omega_1, \omega_2) = \sum_{n,m}^{N_b} \langle E^*(\tilde{\boldsymbol{u}}_n, \boldsymbol{r}_1, \omega_1) E(\tilde{\boldsymbol{u}}_m, \boldsymbol{r}_2, \omega_2) \exp(i(\omega_2 t_m - \omega_1 t_n)) \rangle_{ens} . \tag{3.20}$$

This can be written as a diagonal and off-diagonal summation:

$$\begin{aligned}\Gamma_\omega(\boldsymbol{r}_1, \boldsymbol{r}_2, \omega_1, \omega_2) = &\sum_{n}^{N_b} \left\langle E^*(\tilde{\boldsymbol{u}}_n, \boldsymbol{r}_1, \omega_1) E(\tilde{\boldsymbol{u}}_n, \boldsymbol{r}_2, \omega_2) \exp(i t_n(\omega_2 - \omega_1)) \right\rangle_{ens} \\ &+ \sum_{n \neq m}^{N_b} \left\langle E^*(\tilde{\boldsymbol{u}}_n, \boldsymbol{r}_1, \omega_1) \exp(-i\omega_1 t_n) \right\rangle_{ens} \left\langle E(\tilde{\boldsymbol{u}}_m, \boldsymbol{r}_2, \omega_2) \exp(i\omega_2 t_m) \right\rangle_{ens} .\end{aligned} \tag{3.21}$$

In the last cross term summation we used the fact that electrons in storage rings are independent of each other. That allows us to write the mean of the product as a product of means. If the electrons are correlated the cross term summation may become dominant with respect to the diagonal summation because it scales with the number of particles squared[1].

For brevity, let us define the function T:

$$T(\tilde{\boldsymbol{u}}, \omega_1, \omega_2) = E^*(\tilde{\boldsymbol{u}}, \boldsymbol{r}_1, \omega_1) E(\tilde{\boldsymbol{u}}, \boldsymbol{r}_2, \omega_2) \tag{3.22}$$

as well as

$$\Delta\omega = \omega_2 - \omega_1 \tag{3.23}$$

and

$$j(\tilde{\boldsymbol{u}}) = \sum_{\beta \neq s} m_{s\beta} \beta \tag{3.24}$$

with $\beta \in \{x, x', y, y', \delta\}$.

In the following we perform only the time average of the first term of Eq. 3.21. The time average is equivalent to the longitudinal average because the relative arrival time of ultra-relativistic electrons in the bunch is $t = s/c$ with s being the longitudinal deviation of the electron from the ideal electron:

$$\begin{aligned}&\left\langle T \exp\left(i t_n(\omega_2 - \omega_1)\right)\right\rangle_{ens} \\ &\quad = \frac{1}{c} \int d\tilde{\boldsymbol{u}}\; T(\tilde{\boldsymbol{u}}, \omega_1, \omega_2) \int ds\; \rho_6(\tilde{\boldsymbol{u}}, s) \exp\left(i \frac{s}{c} \Delta\omega\right) \\ &\quad = \frac{\mathcal{C}}{\sqrt{2\pi}\sigma_s} \int d\tilde{\boldsymbol{u}}\; T(\tilde{\boldsymbol{u}}, \omega_1, \omega_2) \rho_5(\tilde{\boldsymbol{u}}) \int ds\; \exp\left(-\frac{s^2}{2\sigma_s^2}\right) \exp\left(\left(-j(\tilde{\boldsymbol{u}}) + i\frac{\Delta\omega}{c}\right) s\right) \\ &\quad = \mathcal{C} \exp\left(-\frac{\sigma_s^2}{2c^2}\Delta\omega^2\right) \int d\tilde{\boldsymbol{u}}\; T(\tilde{\boldsymbol{u}}, \omega_1, \omega_2) \rho_5(\tilde{\boldsymbol{u}}) \exp\left(j(\tilde{\boldsymbol{u}})^2 \frac{\sigma_s^2}{2} + i \frac{\sigma_s^2}{2c} \Delta\omega\; j(\tilde{\boldsymbol{u}})\right)\end{aligned} \tag{3.25}$$

with a constant $\mathcal{C} = c^{-1}(\sigma_s \det M_5^{-1} / \det M_6^{-1})$ and with $\sigma_s^{-2} = m_{ss}$.

For many practical purposes the Gaussian with argument $\Delta\omega$ can be approximated by a delta function. With a typical bunch length σ_s of a few millimeters the Gaussian will limit the difference wavevector Δk to $3 \cdot 10^3 m^{-1}$. At a photon energy of $E = 8\ keV$ the wavenumber is about $4 \cdot 10^{10} m^{-1}$. That means radiations with energy differences below $\Delta E = 8\ meV$ are considered equal. For experiments with an energy resolution larger than 10^{-6} the exponential in front of the integral may become relevant. We *restrict our following discussions to those cases where the radiation frequencies in questions and the resolution of the used monochromator are much larger than* c/σ_s. One example would be a 8 keV emission, a silicon (111) monochromator ($\Delta\omega/\omega \approx 10^{-4}$) with a bunch length of 1 mm.

---

[1] This is the situation in X-ray free electron lasers (XFEL) where the electrons in a XFEL are correlated because they are coordinated by the emission and the cross term summation leads to coherent synchrotron radiation.

The term:

$$\exp\left((j(\tilde{\boldsymbol{u}})^2\frac{\sigma_s^2}{2} + i\frac{\sigma_s^2}{c}\Delta\omega\; j(\tilde{\boldsymbol{u}})\right) \tag{3.26}$$

can be rewritten as:

$$\exp\left(\frac{1}{2}\tilde{\boldsymbol{u}}^T\widetilde{M_s}\tilde{\boldsymbol{u}}\right)\exp\left(i\frac{\sigma_s^2}{c}\Delta\omega\; j(\tilde{\boldsymbol{u}})\right) \tag{3.27}$$

with:

$$\widetilde{M_s} = \sigma_s^2\begin{pmatrix} m_{xs}^2 & m_{xs}m_{x's} & m_{xs}m_{ys} & m_{xs}m_{y's} & m_{xs}m_{\delta s} \\ m_{x's}m_{xs} & m_{x's}^2 & m_{x's}m_{ys} & m_{x's}m_{y's} & m_{x's}m_{\delta s} \\ m_{ys}m_{xs} & m_{ys}m_{x's} & m_{ys}^2 & m_{ys}m_{y's} & m_{ys}m_{\delta s} \\ m_{y's}m_{xs} & m_{y's}m_{y's} & m_{y's}m_{ys} & m_{y's}^2 & m_{y's}m_{\delta s} \\ m_{\delta s}m_{xs} & m_{\delta s}m_{y's} & m_{\delta s}m_{ys} & m_{\delta s}m_{y's} & m_{\delta s}^2 \end{pmatrix}. \tag{3.28}$$

As discussed, $\Delta\omega$ is limited by $3c/\sigma_s$. This implies that as long as $3\sigma_s \cdot j(\tilde{\boldsymbol{u}}) \ll 1$ the exponential phase factor may be approximated with 1. The typical horizontal bunch size, for instance, is smaller than 1 mm. If the vertical coupling m_{sx} is much smaller than 10^6 the approximation is surely justified in the horizontal direction.

In what follows we want *always assume that the s-coupling is sufficiently weak* to approximate the complex phase function by one.

The integral over $\tilde{\boldsymbol{u}}$ in Eq. 3.25 can then be interpreted as the ensemble average of the effective electron phase space distribution:

$$\tilde{\rho}_5(\tilde{\boldsymbol{u}}) = \rho_5(\tilde{\boldsymbol{u}})\exp\left(\tilde{\boldsymbol{u}}^T\widetilde{M_s}\tilde{\boldsymbol{u}}\right) = \exp\left(\tilde{\boldsymbol{u}}^T(M_5 + \widetilde{M_s})\tilde{\boldsymbol{u}}\right). \tag{3.29}$$

Similarly we can evaluate the mean value of E:

$$\begin{aligned} &\langle E(\tilde{\boldsymbol{u}}_n,\omega)\exp(i\omega t_n)\rangle_{ens} \\ &= \frac{1}{c}\int d\tilde{\boldsymbol{u}}\; E(\tilde{\boldsymbol{u}},\omega)\int ds\; \rho_6(\tilde{\boldsymbol{u}},s)\exp\left(i\frac{s}{c}\omega\right) \\ &= \mathcal{C}\exp\left(-\frac{\sigma_s^2}{2}\left(\frac{\omega}{c}\right)^2\right)\int d\tilde{\boldsymbol{u}}\; E(\tilde{\boldsymbol{u}},\omega)\rho_5(\tilde{\boldsymbol{u}})\exp\left(j(\tilde{\boldsymbol{u}})^2\sigma_s^2 + i\sigma_s\left(\frac{\omega}{c}\right)j(\tilde{\boldsymbol{u}})\right). \end{aligned} \tag{3.30}$$

The mean value is zero unless:

$$\omega \leq 3\frac{c}{\sigma_s}. \tag{3.31}$$

For a bunch length in the millimeter length scale all frequencies larger than $10^{12}Hz$, i.e. infrared emission, lead to a suppression of the mean value. If the bunch length becomes significant smaller, like in XFEL microbunches, the term may become significant. For all frequencies that are higher than infrared frequencies the random process of the electric field is a zero mean process. The ensemble average over the off-diagonal summation in Eq. 3.21 therefore becomes zero for synchrotron storage rings.

We assume that for all electron energies[1] γ_n in the electron bunch and for all relevant frequencies ω the emission at frequency ω is approximately equal to the emission at $\omega + \Delta\omega$ because $\Delta\omega$ is relatively small. In formulas we assume that for all $\delta\omega \in [\omega - \Delta\omega, \omega + \Delta\omega]$ the condition:

$$E(\boldsymbol{r},\omega,\gamma_n) \approx E(\boldsymbol{r},\omega + \delta\omega,\gamma_n) \tag{3.32}$$

is fulfilled.

Under this assumption together with the condition of sufficiently weak coupling of the lon-

---

[1] Electron energy γ and electron momentum deviation δ are related by Eq. 2.7.

gitudinal bunch position to the other random variables the equation Eq. 3.21 takes the simple form:

$$\boxed{\Gamma_\omega(\boldsymbol{r}_1, \boldsymbol{r}_2, \omega) := \Gamma_\omega(\boldsymbol{r}_1, \boldsymbol{r}_2, \omega, \omega) = N_b \left\langle T(\tilde{\boldsymbol{u}}, \omega, \omega)\right\rangle_{\widetilde{\mathrm{ens}}}} \tag{3.33}$$

In the limit of the viewpoint of a monochromator with a resolution below:

$$\frac{\Delta\omega}{\omega} \approx \frac{3c}{\sigma_s \omega} \tag{3.34}$$

the function Γ_ω can be interpreted as the cross spectral density W of the undulator radiation of one bunch.

In this approximation the bunch length does not influence the coherence properties apart from making the process wide sense stationary.

In [8] Geloni *et al.* show that under an assumption to the statistics of the electron beam the synchrotron undulator radiation is a Gaussian random process. Their assumption is that the arrival time t_n of the electron is statistically independent of the spatial offset $\boldsymbol{r}_n$ and divergence $\boldsymbol{r}'_n$. They do not discuss the energy spread but the generalization to energy spread is straightforward, i.e. t_n must additionally be independent of the electron energy γ_n or momentum deviation δ_n, respectively. In general this assumption is not true for a Gaussian electron beam. Two Gaussian random variables are independent if and only if they are uncorrelated. But the elements $\sigma_{s\beta}$ with $\beta \in \{x, x', y, y', \delta\}$ of the covariance matrix Σ are in general not all zero. This implies that there is a correlation between the arrival time t_n and the other random variables of the electron beam.

If the bunch length is sufficiently long the condition of independence of the arrival time to the other electron beam parameters can, however, be relaxed. The total electric field of a bunch E_b is the sum of independent and identically distributed random variables E_n because in a synchrotron storage ring the electrons are all independent and identically distributes. From the central limit theorem in its complex version follows that $E_b(\tilde{\boldsymbol{u}}, \omega, t)$ is Gaussian distributed. In what follows we will show that E_b is a zero mean circularly-symmetric Gaussian for all frequencies of interest. We already showed that E_b has zero mean. According to section 2.5.11 it remains to show that the pseudo-covariance:

$$M(\boldsymbol{r}_1, \omega_1, \boldsymbol{r}_2, \omega_2) = \langle E(\boldsymbol{r}_1, \omega_1) E(\boldsymbol{r}_2, \omega_2)\rangle \tag{3.35}$$

vanishes for all frequencies of interest. We may basically do the same calculation as for the cross spectral density. The only significant changes are that T in Eq. 3.22 becomes:

$$T'(\tilde{\boldsymbol{u}}, \omega_1, \omega_2) = E(\tilde{\boldsymbol{u}}, \boldsymbol{r}_1, \omega_1) E(\tilde{\boldsymbol{u}}, \boldsymbol{r}_2, \omega_2) \tag{3.36}$$

and that expressions of the form $\omega_2 - \omega_1$ become $\omega_2 + \omega_1$. The Gaussian in front of the integral in Eq. 3.25 with $\Delta\omega' = \omega_1 + \omega_2$ will suppress the pseudo-covariance for all frequencies of interest.

We may conclude that for a Gaussian electron beam and for all frequencies of interest the undulator storage ring radiation is a zero mean circularly-symmetric Gaussian process. Our results from the discussion in section 2.5.12 may be applied to undulator storage ring radiation. The spectral degree of coherence can then be interpreted as a measure for the width of the conditional probability between two positions.

3.3. Calculation of the cross spectral density for undulators in storage rings

In this section we will calculate the cross spectral density with the Eq. 3.15 for a general electron phase space distribution in Gaussian approximation. We will exploit that certain Gaussian integrals can be solved analytically. A naive integration of Eq. 3.15 would be practically impossible even on modern computers. We exploit the *very important observation* that two dimensions of the four-dimensional integral can be performed analytically. The remaining two dimension of integration still pose a fair numerically problem but can be performed on today's computers and we present results of these integration later in this thesis. The general formula for a general five-dimensional Gaussian leads to rather unhandy expressions. We will therefore present two different levels of approximations with which we work throughout the thesis: the symmetry point, where the Twiss parameter alpha is zero, and the finite alpha approximation.

3.3.1. The general case

Let us start with the general case. We apply the brightness convolution theorem derived in section 3.1 using the storage ring electron phase space distribution ρ_5 as discussed in the previous section. Hereby, as long as the coupling between the longitudinal bunch extension and the other dimensions is not too strong it can be accounted for by an effective electron phase space density as defined in Eq. 3.29. We can insert the electron phase space distribution and rewrite Eq. 3.15:

$$W(\boldsymbol{r}_1, \boldsymbol{r}_2, \omega) = \frac{N_e}{(2\pi)^{\frac{5}{2}} \sqrt{\det(M_5^{-1})}} \int d\delta d\boldsymbol{r}\; E_0^*(\boldsymbol{r}_1 - \boldsymbol{r}, \omega) E_0(\boldsymbol{r}_2 - \boldsymbol{r}, \omega) f(\boldsymbol{r}, \boldsymbol{\Delta r}) \tag{3.37}$$

with:

$$\boldsymbol{\Delta r} = \boldsymbol{r}_2 - \boldsymbol{r}_1 \tag{3.38}$$

and

$$f(\boldsymbol{r}, \boldsymbol{\Delta r}) = \int d\boldsymbol{r'} \exp\left(-\frac{1}{2}[x, x', y, y', \delta] \bullet M_5 \bullet \begin{bmatrix} x \\ x' \\ y \\ y' \\ \delta \end{bmatrix} + ik\boldsymbol{r'}\boldsymbol{\Delta r} \right). \tag{3.39}$$

with $\boldsymbol{r} = [x, y]^T$ and $\boldsymbol{r'} = [x', y']^T$. Note that we adopted the $\boldsymbol{r'}$ notation for $\boldsymbol{\theta}$ which is commonly used in accelerator physics.

The observation is that $f(\boldsymbol{r}, \boldsymbol{\Delta r})$ can be *calculated analytically*. In order to do this we will use the central formula for calculations of Gaussian integrals occurring in quantum field theory. From [43] p.103 we know:

$$\int d\boldsymbol{v} \exp\left(-\frac{1}{2}\boldsymbol{v}^T A \boldsymbol{v} + \boldsymbol{j}^T \boldsymbol{v}\right) = (2\pi)^{N/2} \sqrt{\det(A^{-1})} \exp\left(\frac{1}{2}\boldsymbol{j}^T A^{-1} \boldsymbol{j}\right) \tag{3.40}$$

for any invertible symmetric matrix A and any vector $\boldsymbol{j}$.
We will perform the integral in Eq. 3.39 by treating x, y, δ as parameters and using Eq. 3.40 for the coordinates x', y'.
As a preparation we make some definitions:

- The M "projections" to the $x-y$ and $x'-y'$ spaces:

$$M_P = \begin{bmatrix} m_{xx} & m_{xy} \\ m_{yx} & m_{yy} \end{bmatrix}; \quad M_{P'} = \begin{bmatrix} m_{x'x'} & m_{x'y'} \\ m_{y'x'} & m_{y'y'} \end{bmatrix} \tag{3.41}$$

  and:

$$M_{P'}^{-1} = \frac{1}{m_{x'x'}m_{y'y'} - 2m_{x'y'}} \begin{bmatrix} m_{y'y'} & -m_{y'x'} \\ -m_{x'y'} & m_{x'x'} \end{bmatrix}. \tag{3.42}$$

- The simple shift vectors:

$$\boldsymbol{s}_{P'xy} = -\begin{bmatrix} m_{x'x}\cdot x + m_{x'y}\cdot y \\ m_{y'x}\cdot x + m_{y'y}\cdot y \end{bmatrix}; \boldsymbol{s}_{P_\delta} = -\begin{bmatrix} m_{x\delta}\cdot \delta \\ m_{y\delta}\cdot \delta \end{bmatrix}; \boldsymbol{s}_{P'\delta} = -\begin{bmatrix} m_{x'\delta}\cdot \delta \\ m_{y'\delta}\cdot \delta \end{bmatrix} \tag{3.43}$$

- The combined shift vectors:

$$\begin{aligned} \boldsymbol{s}_{P'} &= \boldsymbol{s}_{P'xy} + \boldsymbol{s}_{P'\delta} \\ \boldsymbol{s}_{P'\delta r} &= \boldsymbol{s}_{P'\delta} + ik\boldsymbol{\Delta r} \end{aligned} \tag{3.44}$$

- The shift matrix:

$$S_{P'} = -\begin{bmatrix} m_{x'x} & m_{x'y} \\ m_{y'x} & m_{y'y} \end{bmatrix} \quad \text{with: } S_{P'}\begin{bmatrix} x \\ y \end{bmatrix} = \boldsymbol{s}_{P'xy}. \tag{3.45}$$

With these definitions we can write Eq. 3.39 as:

$$\begin{aligned} f(\boldsymbol{r}, \boldsymbol{\Delta r}) =& \exp\left(-\frac{\sigma_{\delta\delta}}{2}\delta^2\right)\exp\left(-\frac{1}{2}\left[x, y\right] M_P \begin{bmatrix} x \\ y \end{bmatrix} + (\boldsymbol{s}_{P_\delta})^T \begin{bmatrix} x \\ y \end{bmatrix}\right) \\ & \int d\boldsymbol{r'} \exp\left(-\frac{1}{2}\left[x', y'\right] M_{P'} \begin{bmatrix} x' \\ y' \end{bmatrix} + (\boldsymbol{s}_{P'} + ik\boldsymbol{\Delta r})^T \begin{bmatrix} x' \\ y' \end{bmatrix}\right). \end{aligned} \tag{3.46}$$

The last integral can be calculated using Eq. 3.40:

$$\begin{aligned} f(\boldsymbol{r}, \boldsymbol{\Delta r}) =& 2\pi\sqrt{\det(M_{P'}^{-1})}\exp\left(-\frac{\sigma_{\delta\delta}}{2}\delta^2\right) \\ & \exp\left(-\frac{1}{2}\left[x, y\right] M_P \begin{bmatrix} x \\ y \end{bmatrix} + (\boldsymbol{s}_{P_\delta})^T \begin{bmatrix} x \\ y \end{bmatrix}\right) \\ & \exp\left(\frac{1}{2}(\boldsymbol{s}_{P'} + ik\boldsymbol{\Delta r})^T M_{P'}^{-1}(\boldsymbol{s}_{P'} + ik\boldsymbol{\Delta r})\right) \end{aligned} \tag{3.47}$$

Notice that the last exponential in Eq. 3.47 has a "hidden" x, y dependence through $\boldsymbol{s}_{P'}$. In our final step we factorize out the x, y dependence. For the moment let us only consider the argument of the last exponential in Eq. 3.47:

$$\begin{aligned} & \frac{1}{2}(\boldsymbol{s}_{P'} + ik\boldsymbol{\Delta r})^T M_{P'}^{-1}(\boldsymbol{s}_{P'} + ik\boldsymbol{\Delta r}) \\ &= \frac{1}{2}(\boldsymbol{s}_{P'xy} + \boldsymbol{s}_{P'\delta r})^T M_{P'}^{-1}(\boldsymbol{s}_{P'xy} + \boldsymbol{s}_{P'\delta r}) \\ &= \frac{1}{2}\left[(\boldsymbol{s}_{P'xy})^T M_{P'}^{-1}\boldsymbol{s}_{P'xy} + (\boldsymbol{s}_{P'xy})^T M_{P'}^{-1}\boldsymbol{s}_{P'\delta r} + (\boldsymbol{s}_{P'\delta r})^T M_{P'}^{-1}\boldsymbol{s}_{P'xy} + (\boldsymbol{s}_{P'\delta r})^T M_{P'}^{-1}\boldsymbol{s}_{P'\delta r}\right] \\ &= \frac{1}{2}\left[(\boldsymbol{s}_{P'xy})^T M_{P'}^{-1}\boldsymbol{s}_{P'xy} + (\boldsymbol{s}_{P'\delta r})^T \left(M_{P'}^{-1} + (M_{P'}^{-1})^T\right)\boldsymbol{s}_{P'xy} + (\boldsymbol{s}_{P'\delta r})^T M_{P'}^{-1}\boldsymbol{s}_{P'\delta r}\right]. \end{aligned} \tag{3.48}$$

Using the shift matrix Eq. 3.45 to rewrite $\boldsymbol{s}_{P'xy}$ the previous equation takes the form:

$$\begin{aligned}&\frac{1}{2}(\boldsymbol{s}_{P'}+ik\boldsymbol{\Delta r})^T M_{P'}^{-1}(\boldsymbol{s}_{P'}+ik\boldsymbol{\Delta r})\\ &=\frac{1}{2}\left[[x,y]\left((S_{P'})^T M_{P'}^{-1}S_{P'}\right)\begin{bmatrix}x\\y\end{bmatrix}+2(\boldsymbol{s}_{P'\delta r})^T\left(M_{P'}^{-1}S_{P'}\right)\begin{bmatrix}x\\y\end{bmatrix}+(\boldsymbol{s}_{P'\delta r})^T M_{P'}^{-1}\boldsymbol{s}_{P'\delta r}\right].\end{aligned} \tag{3.49}$$

This leads finally to:

$$\boxed{\begin{aligned}W(\boldsymbol{r}_1,\boldsymbol{r}_2,\omega)=&\frac{N_e\sqrt{\det(M)}}{(2\pi)^{\frac{3}{2}}\sqrt{\det(M_{P'})}}\int d\delta\ \exp\left(-\frac{m_{\delta\delta}}{2}\delta^2\right)\exp\left(\frac{1}{2}(\boldsymbol{s}_{P'\delta r})^T M_{P'}^{-1}\boldsymbol{s}_{P'\delta r}\right)\times\\ &\int d\boldsymbol{r}\exp\left(-\frac{1}{2}\boldsymbol{r}^T\left(M_P-(S_{P'})^T M_{P'}^{-1}S_{P'}\right)\boldsymbol{r}\right)\exp\left(\left((\boldsymbol{s}_{P_\delta})^T+(\boldsymbol{s}_{P'\delta r})^T M_{P'}^{-1}S_{P'}\right)\boldsymbol{r}\right)\\ &\times E_0^*\left(\boldsymbol{r}_1-\boldsymbol{r},\omega\right)E_0\left(\boldsymbol{r}_2-\boldsymbol{r},\omega\right).\end{aligned}} \tag{3.50}$$

Note that the $\boldsymbol{r}_1$ and $\boldsymbol{r}_2$ dependence is given through the electric field expressions $E_0^*(\boldsymbol{r}_1-\boldsymbol{r},\omega)$ and $E_0(\boldsymbol{r}_2-\boldsymbol{r},\omega)$ as well as the $\boldsymbol{\Delta r}$ dependence of $\boldsymbol{s}_{P'\delta r}$.

3.3.2. The approximations used in this thesis

The general formula 3.50 is rather unhandy and difficult to calculate numerically. For the rest of this thesis we will discuss only two approximations: the symmetry point case and the finite alpha case which have been defined in section 2.1.6.

3.3.2.1. Symmetry point of the straight section (Twiss alpha equals zero)

In this approximation Eq. 3.50 takes the much simpler form:

$$\begin{aligned}W(\boldsymbol{r}_1,\boldsymbol{r}_2,\omega)=&\frac{N_e\sqrt{m_{xx}m_{yy}m_{\delta\delta}}}{(2\pi)^{\frac{3}{2}}}\int d\delta\ \exp\left(-\frac{m_{\delta\delta}}{2}\delta^2\right)\exp\left(-\frac{k^2\Delta x^2}{2m_{x'x'}}-\frac{k^2\Delta y^2}{2m_{y'y'}}\right)\\ &\int d\boldsymbol{r}\ \exp\left(-\frac{m_{xx}}{2}x^2-\frac{m_{yy}}{2}y^2\right)E_0{}^*\left(\boldsymbol{r}_1-\boldsymbol{r},\omega\right)E_0\left(\boldsymbol{r}_2-\boldsymbol{r},\omega\right).\end{aligned} \tag{3.51}$$

Numerically it is much more favorable to write this formula in terms of convolutions: Set for every $\boldsymbol{r}_1$:

$$h_{\boldsymbol{r}_1}(\boldsymbol{r})=\exp\left(-\frac{m_{xx}}{2}x^2-\frac{m_{yy}}{2}y^2\right)E_0{}^*\left(\boldsymbol{r}_1-\boldsymbol{r},\omega\right). \tag{3.52}$$

Then Eq. 3.51 can be written as

$$\boxed{\begin{aligned}W(\boldsymbol{r}_1,\boldsymbol{r}_2,\omega)=&\frac{N_e\sqrt{m_{xx}m_{yy}m_{\delta\delta}}}{(2\pi)^{\frac{3}{2}}}\int d\delta\ \exp\left(-\frac{m_{\delta\delta}}{2}\delta^2\right)\exp\left(-\frac{k^2\Delta x^2}{2m_{x'x'}}-\frac{k^2\Delta y^2}{2m_{y'y'}}\right)\\ &\left\{h_{\boldsymbol{r}_1}\star E_0\right\}(\boldsymbol{r}_2).\end{aligned}} \tag{3.53}$$

here $\star$ denotes a convolution. To calculate the full cross spectral density one needs therefore number of grid points (all possible values of $\boldsymbol{r}_1$) two-dimensional convolutions.

3.3.2.2. Finite Twiss alpha

Additionally to the non zero parameters of the symmetry point case we will consider finite $\sigma_{xx'}$ and finite $\sigma_{yy'}$, i.e. couplings between the spatial coordinates and the divergence. This implies that $\boldsymbol{s}_{P_\delta} = \boldsymbol{s}_{P'\delta} = 0$ and $m_{x'y} = m_{y'x} = m_{x'y'} = m_{y'x'} = 0$.

$$\begin{aligned} W(\boldsymbol{r}_1, \boldsymbol{r}_2, \omega) = \mathcal{C} \int d\delta \; \exp\left(-\frac{m_{\delta\delta}}{2}\delta^2\right) \exp\left(-\frac{k^2 \Delta x^2}{2m_{x'x'}} - \frac{k^2 \Delta y^2}{2m_{y'y'}}\right) \times \\ \int d\boldsymbol{r} \; \exp\left(-\frac{N_x}{2}x^2 - \frac{N_y}{2}y^2 - ik\Delta\boldsymbol{r}\begin{bmatrix} \frac{m_{xx'}}{m_{x'x'}} x \\ \frac{m_{yy'}}{m_{y'y'}} y \end{bmatrix}\right) E_0{}^*\left(\boldsymbol{r}_1 - \boldsymbol{r}, \omega\right) E_0\left(\boldsymbol{r}_2 - \boldsymbol{r}, \omega\right) \end{aligned} \tag{3.54}$$

with

$$\mathcal{C} = \frac{N_e \sqrt{(m_{xx} m_{x'x'} - m_{xx'}{}^2)(m_{yy} m_{y'y'} - m_{yy'}{}^2) m_{\delta\delta}}}{(2\pi)^{\frac{3}{2}} \sqrt{m_{x'x'} m_{y'y'}}} \tag{3.55}$$

and

$$\begin{aligned} N_x &= m_{xx} - \frac{m_{xx'}{}^2}{m_{x'x'}} \\ N_y &= m_{yy} - \frac{m_{yy'}{}^2}{m_{y'y'}}. \end{aligned} \tag{3.56}$$

For later numerical application in this thesis, the following mathematically equivalent form will be more favorable:

$$\boxed{\begin{aligned} W(\boldsymbol{r}_1, \boldsymbol{r}_2, \omega) =& \mathcal{C} \int d\delta \; \exp\left(-\frac{m_{\delta\delta}}{2}\delta^2\right) \exp\left(-\frac{k^2 \Delta x^2}{2m_{x'x'}} - \frac{k^2 \Delta y^2}{2m_{y'y'}}\right) \\ & \int d\boldsymbol{r} \; h_{\boldsymbol{r}_1}\left(\boldsymbol{r}\right) E_0\left(\boldsymbol{r}_2 - \boldsymbol{r}, \omega\right) \exp\left(-ik\boldsymbol{r}_2 \begin{bmatrix} \frac{m_{xx'}}{m_{x'x'}} x \\ \frac{m_{yy'}}{m_{y'y'}} y \end{bmatrix}\right) \end{aligned}} \tag{3.57}$$

here

$$\boxed{h_{\boldsymbol{r}_1}(\boldsymbol{r}) = \exp\left(-\frac{N_x}{2}x^2 - \frac{N_y}{2}y^2\right) E_0{}^*\left(\boldsymbol{r}_1 - \boldsymbol{r}, \omega\right) \exp\left(ik\boldsymbol{r}_1 \begin{bmatrix} \frac{m_{xx'}}{m_{x'x'}} x \\ \frac{m_{yy'}}{m_{y'y'}} y \end{bmatrix}\right)} \tag{3.58}$$

is a function parametrized by $\boldsymbol{r}_1$. This no longer has the form of a convolution. We may conclude that in the limits $m_{xx'} \ll m_{x'x'}$ and $m_{yy'} \ll m_{y'y'}$ the symmetry point approximation is usable.

3.3.3. The case of a Gaussian wavefront

If we approximate the undulator electric field E_0 by a Gaussian wavefront:

$$E_0(\boldsymbol{r}) = A \exp\left(-\frac{x^2}{2s_x^2} - \frac{y^2}{2s_y^2}\right) \tag{3.59}$$

and if we neglect energy spread the integration in Eq. 3.50 can be performed analytically. The parameters s_x and s_y are often fitted to the central cone of a single electron emission. In our discussion we will restrict ourselves to the special cases of the symmetry point (Eq. 3.51) and the finite alpha case (Eq. 3.57). The first case will turn out to be Gaussian Schell-model the second will be a simple modification. For Gaussian Schell-models analytical solutions are known (see Eq. 2.164).

The Gaussian wavefront approximation will serve as an important test case for the algorithm in chapter 4.

3.3.3.1. At a symmetry point

Let us first focus only on the *spatial* part of Eq. 3.51, i.e. the part that is integrated. The *divergence* part will be considered afterwards.
For a Gaussian wavefront vertical dimension x and horizontal dimension y factorizes and it suffices to consider only the one dimensional case.
For the sake of readability let us define the difference coordinate and the sum coordinate:

$$\begin{aligned} \Delta x &= x_1 - x_2 \\ X &= x_1 + x_2 \end{aligned} \tag{3.60}$$

The horizontal part of $W(\boldsymbol{r}_1, \boldsymbol{r}_2, \omega)$ takes the form:

$$W_x = A^2 \int dx \exp\left(-\frac{x^2}{2\sigma_x^2}\right) \exp\left(-\frac{(x_1 - x)^2 + (x_2 - x)^2}{2s_x^2}\right) \tag{3.61}$$

with $\sigma_x^{-2} = m_{xx}$. The products can be rearranged:

$$\begin{aligned} W_x &= A^2 \int dx \exp\left(-\frac{x^2}{2\sigma_x^2}\right) \exp\left(-\frac{(x - \frac{1}{2}X)^2}{2(\frac{\sqrt{2}}{2})^2 s_x^2}\right) \exp\left(-\frac{\Delta x^2}{4s_x^2}\right) \\ &= A^2 \exp\left(-\frac{\Delta x^2}{4s_x^2}\right) \int dx \exp\left(-\frac{x^2}{2\sigma_x^2}\right) \exp\left(-\frac{(x - \frac{1}{2}X)^2}{2(\frac{\sqrt{2}}{2})^2 s_x^2}\right). \end{aligned} \tag{3.62}$$

This may be rewritten as:

$$W_x = A^2 \exp\left(-\frac{\Delta x^2}{4s_x^2}\right) \exp\left(-\frac{1}{8}\frac{X^2}{\sigma_x^2 + \frac{1}{2}s_x^2}\right) \int dx \exp\left(-\frac{(x - \mu_{\Sigma\sigma})^2}{2\sigma_{\Sigma\sigma}^2}\right) \tag{3.63}$$

with

$$\sigma_{\Sigma\sigma} = \sqrt{\frac{\sigma_x^2 \cdot \frac{1}{2}s_x^2}{\sigma_x^2 + \frac{1}{2}s_x^2}} \qquad \text{and} \qquad \mu_{\Sigma\sigma} = \frac{\frac{1}{2}X \cdot \sigma_x^2}{\sigma_x^2 + \frac{1}{2}s_x^2}. \tag{3.64}$$

The standard Gaussian integration of Eq. 3.63 gives:

$$W_x = \sqrt{2\pi\sigma_{\Sigma\sigma}^2}A^2 \exp\left(-\frac{\Delta x^2}{4s_x^2}\right) \exp\left(-\frac{1}{8}\frac{X^2}{\sigma_x^2 + \frac{1}{2}s_x^2}\right). \tag{3.65}$$

For the spectral width we therefore have:

$$\sigma_s^{(x)} = 2\sqrt{\sigma_x^2 + \frac{1}{2}s_x^2}. \tag{3.66}$$

The *divergence* part of Eq. 3.51 contributes an extra exponential factor

$$\exp\left(-\frac{\Delta x^2}{2m_{x'x'}}\right). \tag{3.67}$$

According to the addition rules for Gaussian sigmas this leads finally to a correlation sigma:

$$\sigma_g^{(x)} = \sqrt{\frac{2m_{x'x'}s_x^2}{m_{x'x'} + 2s_x^2}}. \tag{3.68}$$

One may do the same for the vertical direction y and the complete cross spectral density function in Gaussian wavefront approximation is

$$W(\boldsymbol{r}_1, \boldsymbol{r}_2) = W_x(x_1, x_2)W_y(y_1, y_2). \tag{3.69}$$

In order to relate Eq. 3.66 and Eq. 3.68 to the standard form of the Gaussian Schell-model Eq. 2.170, we can rewrite W_x in the form:

$$W_x(x_1, x_2) = \mathcal{C}\ \exp\left(-a(x_1 - x_2)^2\right) \exp\left(-b(x_1 + x_2)^2\right) \tag{3.70}$$

with some constant $\mathcal{C}$ and inverse standard deviations a, b. This can be rearranged to the standard form of a Gaussian Schell-model:

$$\begin{aligned} W_x(x_1, x_2) =& \mathcal{C}\ \exp\left(-ax_1^2 - ax_2^2 + 2ax_1x_2 - bx_1^2 - bx_2^2 - 2bx_1x_2\right) \\ =& \mathcal{C}\ \exp\left(-a(x_1^2 + x_2^2)\right) \exp\left(-b(x_1^2 + x_2^2)\right) \exp\left(-2x_1x_2(b - a)\right) \\ =& \mathcal{C}\ \exp\left(-(a - b)(x_1^2 + x_2^2 - 2x_1x_2)\right) \exp\left(-2b(x_1^2 + x_2^2)\right) \\ =& \mathcal{C}\ \exp\left(-(a - b)(x_1 - x_2)^2\right) \exp\left(-2b(x_1^2 + x_2^2)\right) \end{aligned} \tag{3.71}$$

which gives the correlation sigma $\sigma_g = (2(a - b))^{-1/2}$ and spectral sigma $\sigma_s = (4b)^{-1/2}$.

3.3.3.2. Modification for the finite α case

As seen in Eq. 3.54 the main difference on the level of the formulas between the finite alpha case to the symmetry point case Eq. 3.51 is the presence of an extra complex exponential. The integral in Eq. 3.63 becomes:

$$\int dx \exp\left(-\frac{(x - \mu_{\Sigma\sigma})^2}{2\sigma_{\Sigma\sigma}^2}\right) \exp\left(-i\nu x\right) \tag{3.72}$$

with

$$\nu = E_x\Delta x \tag{3.73}$$

here is $E_x = k(m_{xx'}/m_{x'x'})$. The integral yields:

$$\sqrt{2\pi\sigma_{\Sigma\sigma}^2}\exp\left(-\frac{\Delta x^2}{2\sigma_\alpha^2}\right)\exp\left(-iE_x\Delta x\mu_{\Sigma\sigma}\right) \tag{3.74}$$

with

$$\sigma_\alpha = \frac{1}{\sigma_{\Sigma\sigma}\left|E_x\right|}. \tag{3.75}$$

The resulting extra exponential with Δx in the argument can be account for with an adjustment of the correlation sigma:

$$(\sigma_g^{(x)})' = \sqrt{\frac{\sigma_\alpha^2(\sigma_g^{(x)})^2}{\sigma_\alpha^2 + (\sigma_g^{(x)})^2}}. \tag{3.76}$$

The spectral sigma $\sigma_s^{(x)}$ remains unchanged.
This is no longer a Gaussian Schell-model because of the extra complex phase (a Gaussian Schell-model is always real). However, the complex phase function depends on $(x_1-x_2)(x_1+x_2) = x_1^2+x_2^2$ only, i.e. there are no cross terms between x_1 and x_2. The coherent modes Φ_n' for the Gaussian Schell-model like model can therefore be expressed with the help of the coherent modes of the Gaussian Schell-model Φ_n given by Eq. 2.164:

$$\Phi_n'(x) = \exp(i(p_x x^2 + p_y y^2))\Phi_n(x) \tag{3.77}$$

with frequencies p_x:

$$p_x = \frac{\frac{1}{2}E_x \cdot \sigma_x^2}{\sigma_x^2 + \frac{1}{2}s_x^2}. \tag{3.78}$$

The vertical dimension is similar.

3.4. Complete coherence

We will show that a synchrotron undulator cross spectral density is complete coherent if and if the electron phase space density ρ is a delta function. Let us describe the cross spectral density in the form of Eq. 3.14:

$$W(\boldsymbol{r}_1, \boldsymbol{r}_2, \omega) = \sum_{\boldsymbol{u}_i} \rho_6(\boldsymbol{u}_i) {E_0}^*(\boldsymbol{u}_i, \boldsymbol{r}, \omega) E_0(\boldsymbol{u}_i, \boldsymbol{r}, \omega). \tag{3.79}$$

here $\boldsymbol{u}_i$ are the phase space vectors defined in Eq. 2.5. Clearly if the density is a delta function then the cross spectral density is single moded and therefore complete coherent. We will show now that if the electron phase space density is not a delta function then the cross spectral density is not single moded and hence not complete coherent. For mathematical simplicity we assumed that there are many but only a finite number of possible configurations for the electrons in the beam. Furthermore let us assume that all single electron emissions $E_0(\boldsymbol{u}_i, \omega)$ are linear independent from each other. This assumption is likely fulfilled because different electron configurations will produce different single electron emissions. If the fundamental relation of the brightness convolution theorem (3.3) holds, at least to a good approximation, this assumption is fulfilled. We show in the following that A_W is not single moded and hence not completely coherent. First we show that we can create nonzero vectors. Afterwards we show that every two of these vectors are linear independent. From this will follow that the range of A_W is at least two-dimensional and therefore A_W is not single moded. For brevity we will not explicitly write the frequency dependence.

We define for any configuration $\boldsymbol{u}_j$ with $\rho_6(\boldsymbol{u}_j) \neq 0$:

$$\begin{aligned} a_j := A_W(E_0(\boldsymbol{u}_j, \boldsymbol{r})) =& \rho_6(\boldsymbol{u}_j) E_0(\boldsymbol{u}_j, \boldsymbol{r}) \left\| E_0(\boldsymbol{u}_j) \right\|^2 + \\ & \sum_{i \neq j} \rho_6(\boldsymbol{u}_i) E_0(\boldsymbol{u}_i, \boldsymbol{r}) \langle E_0(\boldsymbol{u}_i), E_0(\boldsymbol{u}_j) \rangle \end{aligned} \tag{3.80}$$

which is not zero because $\rho_6(\boldsymbol{u}_j)$ and the norm are positive and it is a summation of linear independent vectors. For $j \neq k$ the vectors a_j and a_k are linear independent because there is no β such that

$$\begin{aligned} a_j - \beta a_k =& (\left\| E_0(\boldsymbol{u}_j) \right\|^2 - \beta \langle E_0(\boldsymbol{u}_j), E_0(\boldsymbol{u}_k) \rangle) \rho_6(\boldsymbol{u}_j) E_0(\boldsymbol{u}_j, \boldsymbol{r}) + \\ & (\langle E_0(\boldsymbol{u}_k), E_0(\boldsymbol{u}_j) \rangle - \beta \left\| E_0(\boldsymbol{u}_k) \right\|^2) \rho_6(\boldsymbol{u}_k) E_0(\boldsymbol{u}_k, \boldsymbol{r}) + \dots \end{aligned} \tag{3.81}$$

equals zero. The first coefficient determines $\beta = \left\| E_0(\boldsymbol{u}_j) \right\|^2 / \langle E_0(\boldsymbol{u}_j), E_0(\boldsymbol{u}_k) \rangle$. Which implies that the second coefficient is:

$$\frac{\left\| E_0(\boldsymbol{u}_j) \right\|^2 \left\| E_0(\boldsymbol{u}) \right\|^2}{\langle E_0(\boldsymbol{u}_j), E_0(\boldsymbol{u}_k) \rangle} - \langle E_0(\boldsymbol{u}_k), E_0(\boldsymbol{u}_j) \rangle. \tag{3.82}$$

After Cauchy-Schwarz the second coefficient is zero only for linear dependent E_j, E_k. But all E_j are linear independent and therefore the second coefficient is not zero. Thus there exists no β such that $a_j = \beta a_k$.

This proves that in the range of A_W there are at least two linear independent vectors which requires two coherent modes for its representation and the cross spectral density W does therefore not represent a completely coherent ensemble.

3.5. Summary

In this chapter we develop a theory for the calculation of the cross spectral density for emission devices in a storage ring.

We start with the *brightness convolution theorem* developed by Kim [7]. We derive the theorem in a different manner and add extra comments. The foundation of the theorem is the relation between initial conditions of the electrons at the *virtual source* and shifts of their produced emission relative to a reference emission E_0. The virtual source is a virtual plane in or before the undulator that reproduces the real electron emission outside the undulator if the electric field is propagated by a given distance. At the virtual source the relation between initial electron conditions and emission shift is given by Eq. 3.3. We identify the *natural position of the virtual source to be the undulator entrance plane*.

In the derivation of the brightness convolution theorem a summation over all possible second order correlations of the single electron emissions is performed in Eq. 3.14. In [8] Geloni *et al.* devoted a detailed study to this summation. In the original paper the arrival time of the electrons and the other beam parameters were assumed to be independent. In section 3.2 we slightly enhance their discussion and we show that for weak-couplings between longitudinal electron position s and the other electron beam parameters their result remains valid. Also in [8] it was mentioned that storage ring emission is a Gaussian random process. We add that the process is even circularly-symmetric and that the results from section 2.5.12 can be applied to storage ring emission, i.e. the spectral degree of coherence μ can be interpreted as a quadratic scaling factor of the standard deviation of the conditional probability between two positions.

In section 3.3 we derive from the brightness convolution theorem with the five-dimensional electron phase space density ρ_5 (see Eq. 2.17) and the assumption of weak couplings to the longitudinal electron position s the general equation for the calculation of the cross spectral density of storage ring emission (Eq. 3.50) in brightness convolution theorem approximation. We applied this formula to the special cases of the symmetry point (Eq. 3.51) and the finite alpha position (Eq. 3.54). In section 3.3.3 we applied these formulas to an initial Gaussian reference emission E_0 and we arrive at a Gaussian Schell-model source or Gaussian Schell-model like source, respectively. These cases will serve as important test cases for the algorithm developed in chapter 4.

Finally in section 3.4, we mention that in the brightness convolution theorem approximation the emission is completely coherent if and only if the electron phase space distribution ρ_6 is a delta function.

4. Numerical coherent mode decomposition algorithm

The application of second order coherence theory to the design of synchrotron beamlines requires the propagation of the cross spectral density W along the beamline. Because of the four-dimensional nature of the cross spectral density W this a computational heavy task. Alone the memory requirement of the full cross spectral density W can easily reach several terabytes for realistic problems. Additionally, to propagate the cross spectral density one has to perform a four-dimensional integral of the type of Eq. 2.119 which is computational rather difficult and may only be performed on large computer clusters.

In this chapter two different algorithms that I implemented are presented. These algorithms calculate numerically the cross spectral density for an synchrotron undulator source and its decomposition into coherent modes. In general for undulator emission a limitation to a small number of relevant modes is expected. In our applications the number of coherent modes is usually limited to a few hundred up to a few thousand. Storage and propagation of the cross spectral density can then be realized in terms of its coherent modes (see section 2.5.9) and the required computational power for these tasks is drastically reduced.

The first algorithm is a straightforward discretization of the full representing matrix of the cross spectral density operator A_W (Eq. 2.139). In the following we will call this method the **matrix method**. The drawback of the matrix method is that it needs a lot of memory. And basically all interesting applications become impractical to calculate.

To allow the calculation of real applications I developed another method that performs the decomposition much more memory-efficient in two steps. We will refer to this method as the **two-step method**. The two-step method exploits the Gaussian nature of the electron beam and can calculate the decomposition under some not too restrictive assumptions. The matrix method is simpler and therefore the likelihood of implementation errors is lower. In the beginning I developed the matrix method but because of its impractical nature I looked for a more practical solution. The experience and insight gained during the development of the matrix method allowed me to develop the two-step method. In this thesis we use the matrix method exclusively to test the two-step method. We start first with implementations without energy spread to keep the initial problem as simple as possible. We add the energy spread calculation in section 4.6. We discuss the possible change of the coherent modes and the mode spectrum due to propagation and the possibility to perform a second diagonalization after the propagation in section 4.3. The technical complexity of the algorithms makes it necessary to perform extensive tests. These tests include benchmarking against the Gaussian Schell-model, which has analytical solutions, and tests against the SRW multielectron sampling for the spectral density and selected points of the spectral degree of coherence.

4.1. Numerical eigendecompositon: the matrix method

In this section we describe the implementation of the numerical eigendecomposition of the cross spectral density into its coherent modes. We will calculate the full representing matrix of the cross spectral density operator A_W in an *unbiased* basis set, i.e. a basis set without prior assumptions. The drawback of this method is the high demand of memory and the connected limitation of applicability to practical problems. In section 4.4 an alternative method is presented that typically requires much less memory, such that interesting problems can be addressed.

4.1.1. Numerical representation of the cross spectral density operator

In chapter 3 we established expressions for the cross spectral density W. Here we want to numerically perform the coherent mode decomposition. As mentioned in section 2.5.5 there is a duality between the cross spectral density and its induced nuclear integral operator:

$$\begin{aligned} A_W &: \mathcal{H} \mapsto \mathcal{H} \\ A_W[f](\boldsymbol{r}) &= \int d\boldsymbol{r}_1 \; W(\boldsymbol{r}_1, \boldsymbol{r}_2, \omega) f(\boldsymbol{r}_1) \end{aligned} \tag{4.1}$$

here $\mathcal{H}$ is the W induced reproducing Hilbert space.

Standard eigensolver software take a matrix and numerically approximate its eigenvalues and eigenvectors. In order to use them we have to translate our integral operator to a matrix acting on $\mathbb{C}^n$. The usual technique to do this is to take some finite dimensional subspace $\mathcal{A}$ of $\mathcal{H}$ for which a basis $\{b_n\}$ is known and expand in $\mathcal{A}$ the restriction $\widetilde{A_W}$ of A_W on $\mathcal{A}$. The hope is then that if $\mathcal{A}$ approximates well $\mathcal{H}$ then $\widetilde{A_W}$ will approximate A_W well. For many problems reasonable basis sets can be suggested and the evaluation of the integral operator may be numerically cheap. In our case a priori no coercive basis set is known. The best candidate may be well scaled Hermite functions because they are the coherent modes of the Gaussian Schell-model. However, the expansion of A_W into a Hermite function basis set is still expensive to do and an additional parameter, the scaling parameter of the Hermite functions, is introduced. Let $\{b_n\}$ be a well approximating orthonormal basis of $\mathcal{H}$. To expand A_W in $\{b_n\}$ we have in general to perform $3n^2$ two dimensional integrals integrals:

$$A_{nm} = \int d\boldsymbol{r}_2 \; b_n^*(\boldsymbol{r}_2) \int d\boldsymbol{r}_1 \; W(\boldsymbol{r}_1, \boldsymbol{r}_2) b_m(\boldsymbol{r}_1) \tag{4.2}$$

which in Dirac notation is written:

$$A_{nm} = \langle b_n | \, A_W \, | b_m \rangle \, . \tag{4.3}$$

From this equation $2n^2$ integrations are evident and note that for the calculation of W (Eq. 3.50) without energy spread an additional two-dimensional integration must be performed.

Since a priori a good basis set is not securely known and we did not want to add any bias we decided to take a two-dimensional step function basis. In numerical calculations the functions are only known on a finite number of grid points. The distance between neighboring grid points is often equidistant but this is in general not necessary. Let $G = \{g_{ij}\}$ be some equidistant two-dimensional grid of $[-h, h] \times [-v, v]$ where h and c are non negative and supposed to cover horizontally and vertically the typical relevant range at the virtual source. Typical values for h and v range from a few microns to a few hundred microns and typical we choose a few hundred grid points N_h, N_v in each direction. A grid point g_{ij} has then horizontal position x_i and vertical position y_j. The collection of vectors $\boldsymbol{r}_{ij}$ are supposed to point to the grid point g_{ij}. Let $\mathcal{P}$

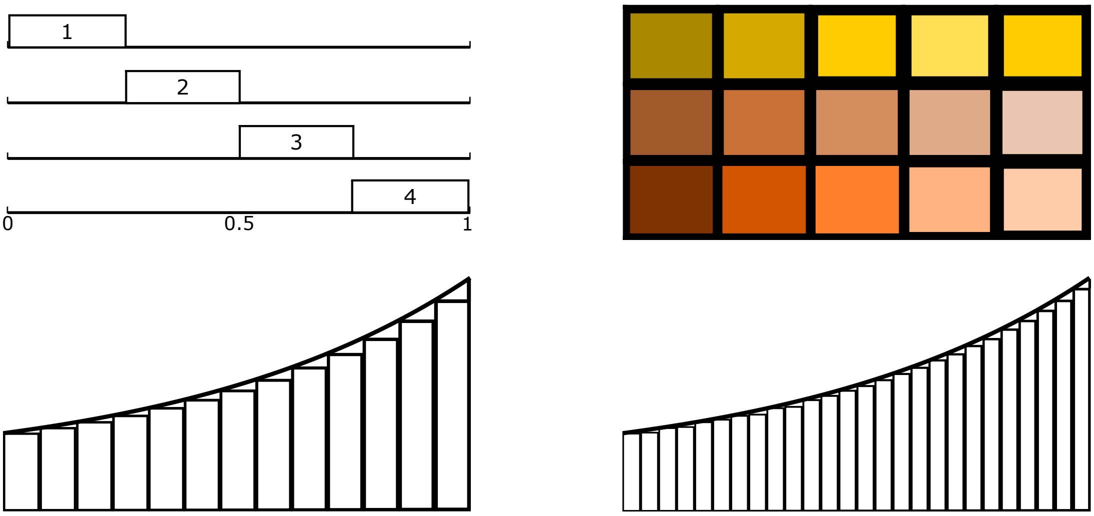

Figure 4.1.: Illustration of the basis set used for the expansion. Upper left: On the interval 0 to 1 four step function basis functions are depicted. They have no overlap and are therefore orthogonal. Furthermore they are normalized. The step functions are therefore orthonormal. Upper right: schematic illustration of two dimensional step functions. A two dimensional domain is covered with two dimensional step functions. Every color represents a different basis function. The functions take constant values on "their color" and are zero for all other colors. Their integral is normalized to 1. Bottom left: a function is expanded in a step function basis set. Bottom right: the same function is expanded in a refined basis set, i.e. more basis functions. The expansion is more accurate.

be a countable partition of the virtual source consisting of identical rectangles $\{\mathrm{rect}_n\}$ that are centered at the grid points g_{ij}. Furthermore let $I : \{1, \ldots, N_h \cdot N_v\} \mapsto \{1, \ldots, N_h\} \otimes \{1, \ldots, N_v\}$ be a bijective index mapping that maps a 1d partition index to an index pair of the grid G. A two-dimensional step function basis is then given by:

$$\boxed{b_n(\boldsymbol{r}) = \begin{cases} \frac{1}{h} & \text{if } \boldsymbol{r} \in \mathrm{rect}_n \\ 0 & \text{otherwise} \end{cases}} \tag{4.4}$$

where the normalization constant h is the same for all basis functions and is chosen such that b_n has norm one. This kind of basis sets are then orthonormal because if $n \neq m$ then $b_n b_m$ have no overlap and therefore the integral of their product is zero (see Fig. 4.1).

The quality of the approximation of this basis set depends on the fineness of the grid. The basis functions *sample* the function. If the grid would be infinitely fine the b_n would approximate delta functions. In that limit the described step function basis set is complete.

Let us introduce a single parameter to increase or decrease the number of grid points. We call this parameter the **sampling factor** s. It will be important throughout this thesis. Given an equidistant grid G a sampling factor of $s = 1$ means just the initial grid. A sampling factor of $s = 2$ means that in each of the two dimensions between every two points of the initial grid an extra point is added that lies in the middle of this two points (see also Fig. 4.1 bottom for the associated basis set refinement). For general values of s the size of the grid is kept but the number of equidistant grid points in each dimension is multiplied by s. The total number of grid points scales therefore quadratically with s. We will use the sampling factor to describe the increase of grid points and hence the quality of the approximation. In a physical picture one can imagine a plane with rectangular aperture that is moved to probe the plane like it is done in Young's experiment.

Why do we use this basis set? Other basis sets may need some proper numerical scaling. The Hermite functions for instance, must be adjusted for rapid convergence such that the support of the first Hermite functions coincides with relevant ranges of the function to expand. This gives raise to an extra scaling parameter we want to avoid. We find that the sampling factor is more straightforward to understand and to control. Furthermore the calculation and the expansion into high order Hermite functions may become numerically unstable or at least difficult because the evaluation of high order polynomials is necessary. Additionally, there are some claims that the Hermite functions are the coherent modes of our cross spectral density or, at least, are close to them. To avoid any bias to the numerical result we do not to start to start from these functions. And probably the most important reason to choose a step function basis is that it adapts rather natural to the equation for W (Eq. 3.51) or (Eq. 3.57) because:

$$A_{nm} = \int d\boldsymbol{r}_2\ b_n^*(\boldsymbol{r}_2) \int d\boldsymbol{r}_1\ W(\boldsymbol{r}_1, \boldsymbol{r}_2) b_m(\boldsymbol{r}_1) \approx W(\boldsymbol{r}_{I(m)}, \boldsymbol{r}_{I(n)}). \tag{4.5}$$

So the knowledge of W gives immediately rise to its **representing matrix** in the step function basis. The symmetry point case Eq. 3.51 allows the usage of convolutions for the calculation of A_{nm} which can be implemented efficiently on computers with FFT based methods. A disadvantage of this basis set is its scaling. If high precision is needed the grid must be refined. To refine the grid we increase the sampling factor s. As already mentioned the grid scales quadratically with s. The representing matrix scales quadratically with the basis set size. In consequence *the representing matrix scales to the fourth power with the sampling factor s.* This explains the vast memory exhaustion with increase of the sampling factor in this method.

The most difficult technical part is the recasting of the equations on the paper into a form that is compatible with the interface of standard eigensolver software. The *central role in this translation takes the index mapping I* that maps a two-dimensional domain to a one-dimensional enumeration of basis functions. The choice of the index mapping I is theoretically free in the limits of I being bijective. For performance reasons, however, the mapping should be as fast as possible and any expensive bookkeeping should be avoided. The canonical choice for I is therefore the same mapping used by the programming language to flatten two-dimensional arrays and the inverse I^{-1} is the ravel operation. On most modern computers two-dimensional arrays are flattened to and raveled from continuous chunks like it is illustrated in Fig. 4.2.

Being aware of this mapping the calculation of A can exploit vectorization and the calculation becomes sufficiently efficient.

Once the Hermitian representing matrix A is known we may find its eigenvalues and eigenvectors. The eigenvectors are the coefficient vectors of the eigenfunctions of W in the step function basis. By construction the coherent modes $\{\Phi_k\}$ of W are related to the eigenvectors $\{e_k\}$ of A by:

$$\Phi_k(\boldsymbol{r}_{ij}) = \frac{1}{h} e_k[I^{-1}(i,j)]. \tag{4.6}$$

here $[\cdot]$ indicates the component of the vector.

4.1.2. Numerical eigensolver

Once the representing matrix in a given basis is known we use numerical eigensolvers to approximate the eigenvectors of the matrix. In general normalized eigenfunctions are free up to a global phase. For our problem we use an iterative eigensolver. Iterative eigensolver in contrast to full diagonalization are designed to calculate only a few eigenvectors while full diagonalization

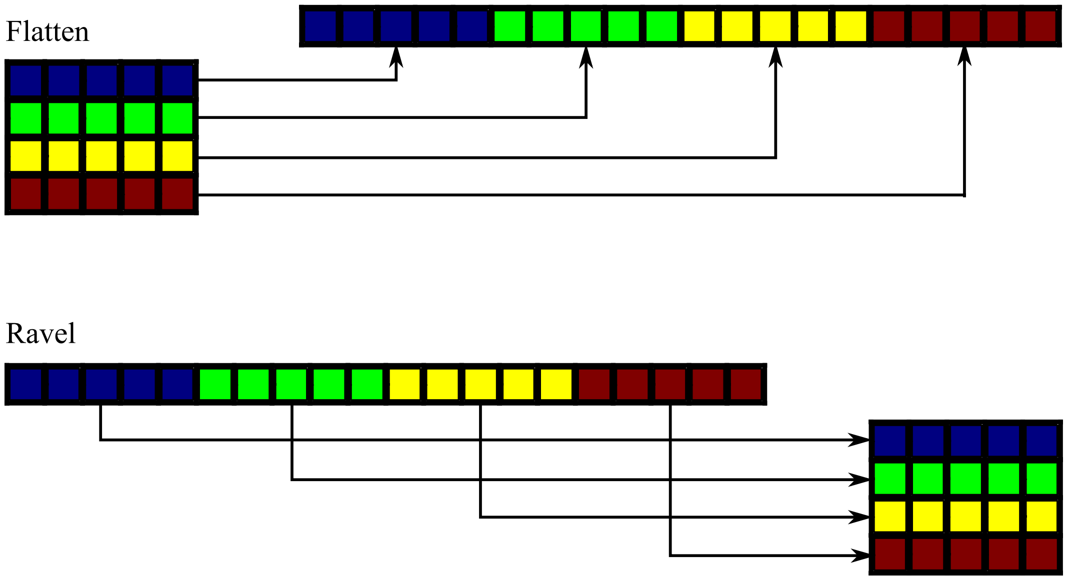

Figure 4.2.: Illustration of the memory mapping of a two-dimensional array. Each color symbolizes a different one-dimensional part of the full two-dimensional array. Top: a two-dimensional array is mapped to a continuous chunk. Bottom: a continuous chunk is mapped to a two-dimensional array.

techniques are optimised to calculate all eigenvectors. We know that the cross spectral density operator is positive and nuclear. Furthermore we know that for a Gaussian wavefront the operator takes the form of a Gaussian Schell-model whose eigenvalues decay exponentially. Additionally, we expect that there is only a small number of dominant coherent modes in the limit of high coherence. We are therefore not interested to calculate all eigenvectors and are satisfied with a small subset of all eigenvectors. Therefore we use an iterative eigensolver. Likewise to full diagonalization techniques, iterative techniques do not always converge. Prominent problems are ill conditioned matrices and in the case of iterative eigensolver matrices with rather uniform eigenvalue spectrum pose extra difficulties.

For our purpose we use the mature software package SLEPc [44, 45, 46] that is based on PETSc[47, 48, 49]. It provides an iterative solver optimized for sparse matrices and has a python interface. The package allows the definition of custom matrix-vector multiplications. In the SLEPc realm this is called **Shell-free form** and we will adopt this notion in the following. Later in section 4.4 when we discuss the two-step method we will see why an iterative solver with the possibility of user defined matrix-vector multiplication is even more useful.

By default we use the Krylov-Space based methods *krylov-schur* or *arnoldi* implemented in SLEPc. Roughly speaking the Arnoldi method creates a m-dimensional subspace of the range of the matrix and assumes that this subspace is a good approximation to the n dimensional eigenspace of the matrix. Here m is often of the order of $2n$. Once the Krylov-Space is created a basis of it is known which can be diagonalized using full diagonalization techniques like a QR decomposition. The last step is to apply the transformation matrix from the n-dimensional eigenspace back to the initial space. The *krylov-schur* method is based on the *arnoldi* method but advanced further and uses an effective and robust restarting scheme that reduces memory requirements.

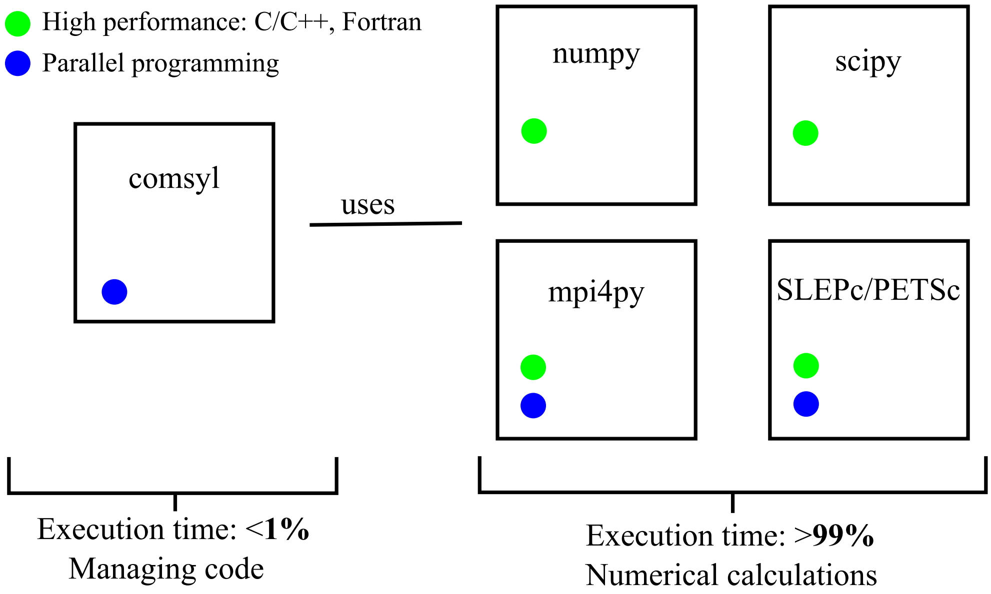

Figure 4.3.: Schema of the decomposition algorithm: Coherent modes for synchrotron light (comsyl). The algorithm itself is written in python. It delegates the computational expensive numerical work to software packages written in high performances languages.

4.1.3. The complexity of the implementation

The open source *Coherent modes for synchrotron light (comsyl)*[9] code implements the algorithms developed in this thesis.

The complexity of the implementation is rather high. For the matrix method the memory usage can quickly reach several hundreds gigabytes and a low number of terabytes of RAM. Already the memory requirement makes a pure parallel implementation necessary. Of course this amount of data must also be calculated and that requires equally a lot of CPU power and some level of performance optimized programming.

The code is written in python but in a way that only a small fraction of the execution time is actually spent in python routines. When using python the development time is often drastically reduced compared to the same development in high performance languages like C/C++. Calculations are wherever possible performed with numpy, scipy or SLEPc. Parallelization is based on MPI. All three codes are C or C++ based compiled codes and are only interfaced to python.

When doing numerical calculations on this scale the knowledge of memory layout and vectorization is very helpful and can lead to significant speed gains or losses if done incorrectly. One can easily lose 1000 times memory bandwidth if incompatible memory layouts are employed.

The largest speed ups are, however, gained on the algorithm level. Using convolutions where possible or approximations where meaningful. The grid size during the decomposition must be properly adjusted to avoid unphysical numerical boundary artifacts (see also the discussion in section 2.4.3). In practice the grid must be large enough to convolve the spatial part of the electron phase space density and the reference single electron emission.

The implementation is in general complicated and in particular due to the parallel and performance optimized nature, intensive and time consuming tests were necessary and performed. These tests are discussed in the next section.

The algorithm is written in modern programming paradigms like object orientated programming and to some degrees test driven development. Some compromises in the design, as this is often the case in high performance computing, had to been made in order to not degraded the performance of the calculation. External libraries like SRW for the calculation of the single electron reference emission E_0 or SLEPc for the diagonalization are well isolated and may be easily replaced by other implementations. An overview of the code structure is given in Fig. 4.4. The most important classes of the current implementation are mentioned in Table. 4.5.

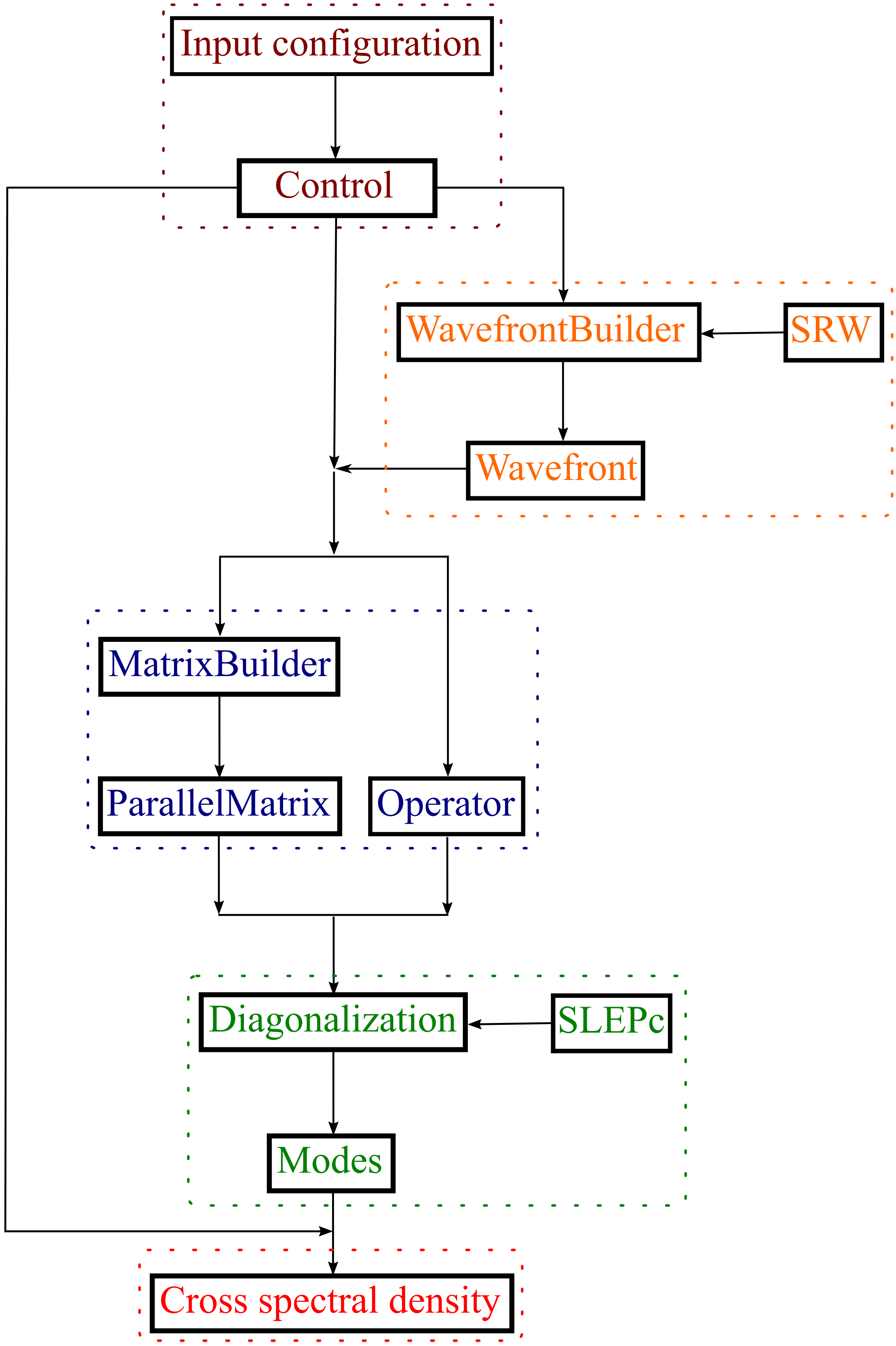

Figure 4.4.: Overview of the code structure. The coloring and its meaning is the same as in Table. 4.5.

Structure	Class name	Purpose
Control	ElectronBram	Models electron beam settings.
	Undulator	Models undulator settings.
	PhaseSpaceDensity	Models the electron phase space density.
	SigmaMatrix	Models the sigma matrix.
	AutocorrelationSimulatorConfiguration	Models all configuration settings for the algorithm: lattice, undulator, grid settings, sampling factor,. . .
	AutocorrelationSimulator	Controls the calculation.
Wavefront	Wavefront	Models a wavefront.
	WavefrontBuilder	Creates a wavefront. Uses SRW and converts its output to a Wavefront.
Calculation	MatrixBuilder	Creates a ParallelMatrix.
	AutocorrelationMatrixBuilderStrategy	Implements the calculation of the representing matrix (matrix method). Choices are convolution or direct integration for finite alpha.
	ParallelVector	Implements a distributed vector.
	ParallelMatrix	Implements a distributed matrix.
	DistributionPlan	Defines how ParallelVector and ParallelMatrix are distributed.
	AutocorrelationOperator	Spatial cross spectral density operator (two-step method).
	DivergenceOperator	Cross spectral density operator (two-step method).
Diagonalization	Eigenmoder	Diagonalizes and creates Twoform.
	EigenmoderStrategy	Implements an eigensolver. By default it is SLEPc.
	EigenmoderSeparation	Diagonalizes for a supposedly separable cross spectral density.
	Twoform	Should be named Modes or TensorProduct. Carries eigenvalues, TwoformVectors and grid settings.
	TwoformVectors	Carries the coherent modes.
Cross spectral density	AutocorrelationFunction	Models the cross spectral density.
	AutocorrelationInfo	Calculation log, used configuration, needed times, used CPUs, . . .
	AutocorrelationFunctionPropagator	Propagates a AutocorrelationFunction along a SRW beamline.

Figure 4.5.: The most important classes of the current implementation.

4.2. Tests of the matrix method

Because of the complexity of the algorithm's implementation intensive tests have been made to guarantee its well functioning. For all our tests we use the corresponding ESRF-EBS settings defined in 2.1.8 and the undulators defined in section 2.3.4. The configuration files to calculate the tests are listed in the appendix.

First we present the verification of the fundamental relation of the brightness convolution theorem Eq. 3.3, i.e. the relation between the initial condition of an electron entering the undulator and the shift of its emission relative to the emission of an electron entering on-axis with velocity vector directed exactly along the longitudinal coordinate. We verify this for all the undulators used throughout this thesis, i.e. the ESRF u18 1m, 2m and 4m long undulators.

A question arises how to judge the equalness of two cross spectral densities and when two decompositions can be considered approximately equal. We will address this question and develop a comparison criteria suited for numerical evaluation in section 4.2.2.

Afterwards we present tests for Dirac delta shaped electron beams and we compare the numerically obtained eigenvalues and coherent modes to the theoretical results for an initial Gaussian wavefront (see section 3.3.3). We test both cases: an electron beam at the symmetry point and an electron beam with finite alpha.

To show the numerical agreement with the theory we used grid settings deceived from real application that will be discussed in chapter 5. A discussion about convergence in dependence of the grid and convergence tests can be found there.

The numerical results of all our test agree to a high precision to the theoretical predictions.

4.2.1. Verification of the relation between the initial electron condition and the radiation shift

In this section we verify numerically one of the fundamental proposition of the brightness convolution theorem and therefore of our algorithm: the relation between initial conditions of a single electron at the virtual source and its produced field relative to a reference electric field, i.e. Eq. 3.3.

Computer codes like pySRU[25] or SRW[24] allow us to specify the initial conditions of an electron entering an undulator and to calculate its emission. We performed all the calculations with pySRU and SRW and got basically identical results. The results presented here are based on calculations performed with pySRU. We verify Eq. 3.3 for realistic spatial offsets $\boldsymbol{r}_i$ and angles $\boldsymbol{\theta}_i$ of the ESRF-EBS lattice as defined in section 2.1.8. The offsets are chosen to cover three standard deviations of the spatial electron beam distribution and angular beam distribution, respectively.

Like always in this thesis we use the ESRF u18 undulator settings defined in section 2.3.4 with undulators of 1m, 2m and 4m length. The calculations are performed at their resonance energy likewise given in section 2.3.4.

From the theory we expect that the emission E_i shifts by an offset $\boldsymbol{r}_i$ with respect to a reference emission if the electron enters the undulator with an offset $\boldsymbol{r}_i$ with respect to the reference electron in the virtual source plane, i.e. we expect $E_i(\boldsymbol{r}) \propto E_0(\boldsymbol{r} - \boldsymbol{r}_i)$ (see Fig. 3.3 top).

For everything that follows we extract the relative shift Δ between the emission from the reference electron E_0 and the emission from the shifted electron E_i with the help of the correlation function:

$$C(\boldsymbol{h}) = |E_0(\boldsymbol{r})| \, |E_i(\boldsymbol{r} + \boldsymbol{h})| \, . \tag{4.7}$$

We looked for the peak of the correlation function C, i.e. we looked for that $\boldsymbol{h}_{max}$ that maximizes C. The so found $\boldsymbol{h}_{max}$ is then considered as our shift Δ.

Since the results produce plots that just give the same ideal straight line for all undulators

Undulator length [m]	Distance screen [m]	Horizontal fit [m]	Vertical fit [m]
1	3.5	4.57	4.57
1	4.5	5.58	5.58
1	5.5	6.58	6.57
1	6.5	7.58	7.58
2	4.0	6.09	6.08
2	5.0	7.09	7.08
2	6.0	8.09	8.08
2	7.0	9.09	9.08
4	5.0	9.09	9.06
4	6.0	10.09	10.06
4	7.0	11.09	11.05
4	8.0	12.08	12.05

Table 4.1.: Fitted slopes for the shifts depicted in Fig. 4.6.

and all screen distances we spare the plots and conclude that numerical simulations confirm the one to one relation between spatial shift in the virtual source plane and the shift of the emitted emission.

For initial electron angles $\boldsymbol{\theta}_i$ we theoretically assume that the emission is shifted relative to the reference emission by:

$$\Delta = z\boldsymbol{\theta}_i \tag{4.8}$$

where z is the distance between the virtual source plane and the observation screen (see Fig. 3.3 bottom). The plots Fig. 4.6 show very good linear dependence between initial angle and shift. We performed regressions from which we determined z and the distance z is the position of the virtual source.

The slopes taken from the regressions are found in table 4.1. The fitted values agree very well with the prediction and the R^2 value of all regressions takes the maximal possible value of $R = 1$ within numerical precision. We note that pySRU like SRW applies an extra offset before the undulator entrance plane to account for possible fringe fields and for the magnetic field termination, i.e. the field integrals of the undulator should be zero to have no net effects on the electron dynamic and the magnetic field should go to zero smoothly. In pySRU this offset has a size of five period lengths and in SRW it is two period lengths. In our case of the ESRF u18 this gives an extra of 0.09 m. The horizontally and vertically fitted values in Table. 4.1 must therefore be read like:

$$0.09m + u_l + d = z_{fit} \tag{4.9}$$

with $u_l = \{1m, 2m, 4m\} \pm 0.018m$ because the undulators in our calculations have only full periods and d is the distance of the observation screen measured from the undulator exit.

We find a very good agreement with the theoretical assumption and furthermore determine that the **virtual sources lies at the position where the electron initial conditions are applied**. This is in good agreement with the theoretical prediction discussed in 3.1. The agreement is valid for all the undulators used in this thesis and at different screen positions. We conclude that the brightness convolution theorem can be safely applied for the undulators used throughout this thesis and the ESRF-EBS electron beam settings.

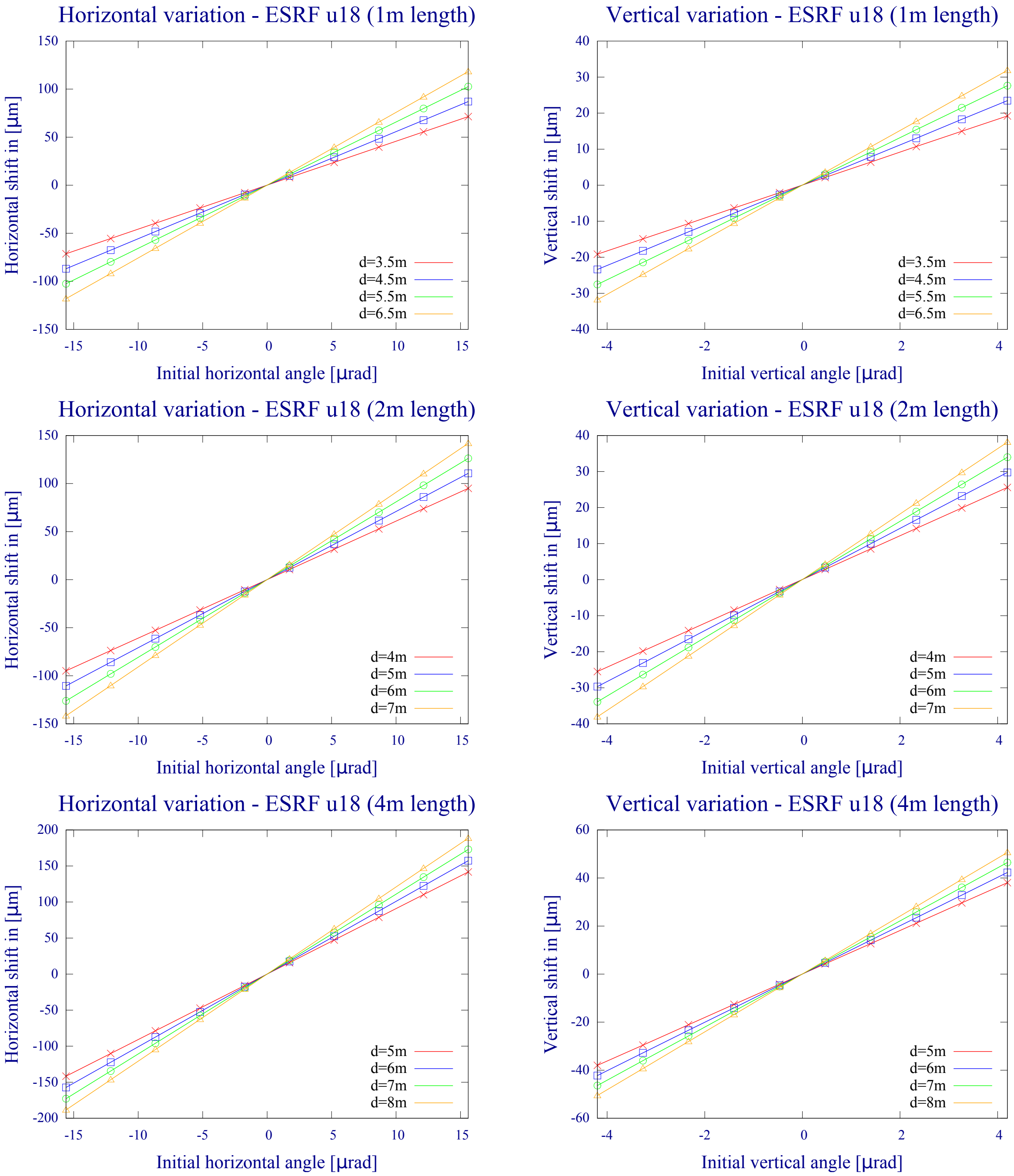

Figure 4.6.: Shifts of the single electron emission as a function of the initial angle of the electron at the undulator entrance plane for all the undulators used in this thesis at their resonance energy (see section 2.3.4). The observation screen is placed in distance d from the exit of undulator.

4.2.2. A criteria for numerical comparison

In order to judge the quality of a result the question naturally arises if two results are equal and if they are not exactly equal how a similarity can be defined.

An easy criteria for equalness would be: two decompositions are equal if they have the same eigenvalue spectrum and the same coherent modes. This could be reformulated as two cross spectral density operators are equal if they have the same eigenvectors and the same diagonal representation in it. This strict definition has a small problem because even orthonormalized eigenvectors are only determined up to a factor of magnitude one. Every eigenvector can be multiplied by a constant of magnitude one and the the set of eigenvectors remains orthonormal. The numerical eigensolver has therefore the freedom to return at each application an eigenvector that differs by a constant of magnitude one. Depending on the used algorithm this happens in practice. Certainly if all the eigenvalues have pairwise relative error smaller than one percent and all the modes have pairwise difference norm of less than one percent the two cross spectral densities will be similar but what does this tell us quantitatively? Using the triangle inequality some quantitative statements may be easily derived but their estimates remain weak and rely on the overlap matrix that may become ill-conditioned for higher modes. Furthermore between two similar but different operators degeneracy leads to different representations of an associated eigenspace. These problems become more severe for higher modes. It can in principle be treated but that takes additional care and computational time. Furthermore, if we compare to a real analytically result we may never completely approach it numerically due to discretization errors. Different coherent modes may change the cross spectral density which is the sum of all its modes but it may be already numerically converged in the sense that for the numerical propagation of the cross spectral density function it is not important to know the exact analytical coherent modes.

In essence we look for a criteria that tells us that for all points of our interest:

$$\forall \boldsymbol{r}_1, \boldsymbol{r}_2 : \left| W(\boldsymbol{r}_1, \boldsymbol{r}_2, \omega) - W'(\boldsymbol{r}_1, \boldsymbol{r}_2, \omega) \right| \leq \mathcal{C} \ll 1 \tag{4.10}$$

i.e., for two different cross spectral densities the pointwise difference between W and W' is smaller than a small constant that is independent of the concrete choice of points. This could be done numerically but depending on the grid size and the number of modes a full comparison for all pairs of points could take very significant numerical resources because for every point the modes must be summed up at that points. For moderate grid sizes of 250 × 100 and a few hundred modes the time needed can be of the order of days.

Suppose we could show that:

$$\left(\int d\boldsymbol{r}'_2 \left| \int d\boldsymbol{r}'_1 (W - W')(\boldsymbol{r}'_1, \boldsymbol{r}'_2) f(\boldsymbol{r}'_1) \right|^2 \right)^{\frac{1}{2}} \leq \mathcal{C} \tag{4.11}$$

for every f with norm one.
Since we are interested in the pointwise difference at $\boldsymbol{r}_1$ and $\boldsymbol{r}_2$ let us test the difference with a constant function f of small finite support centered at $\boldsymbol{r}_1$ in a small environment around $\boldsymbol{r}_1$. The function f shall have norm equal to 1. One example of such a f would be a normalized two-dimensional step function that we typically use in our basis in this thesis. With such a function the inequality becomes:

$$\left(\int d\boldsymbol{r}'_2 \left| (W - W')(\boldsymbol{r}_1, \boldsymbol{r}'_2) \right|^2 \right)^{\frac{1}{2}} \leq \mathcal{C} \tag{4.12}$$

The remaining integral goes over the entire two-dimensional space but we may restrict it to a finite region $B_\delta(\boldsymbol{r}_2)$, like a rectangle, around $\boldsymbol{r}_2$. Since the integrand is positive the inequality still holds because we sum up less:

$$\left(\int_{B_\delta(\boldsymbol{r}_2)} d\boldsymbol{r}_2' \left|(W - W')(\boldsymbol{r}_1, \boldsymbol{r}_2')\right|^2\right)^{\frac{1}{2}} \leq \mathcal{C} \tag{4.13}$$

We may choose the sphere B arbitrary small and therefore probing the difference at the two points $\boldsymbol{r}_1$ and $\boldsymbol{r}_2$ because the integral will approach a typical value of the difference in that sphere times the area of the sphere.

In our numerical setting, in which we want to compare two cross spectral densities on a grid, we may discuss much more practical arguments. Let us chose $B_\delta(\boldsymbol{r}_2)$ to be the same rectangular as we used for our two-dimensional step function centered at $\boldsymbol{r}_2$. If we compare two different grids we chose B_δ to correspond to the finer grid. The implicit approximation of the step function basis set assures that the difference between the two cross spectral densities is constant over the area of B_δ and Eq. 4.13 becomes:

$$\sqrt{h}\left|(W - W')(\boldsymbol{r}_1, \boldsymbol{r}_2)\right| \leq \mathcal{C} \tag{4.14}$$

which is rewritten as:

$$\left|(W - W')(\boldsymbol{r}_1, \boldsymbol{r}_2)\right| \leq \frac{\mathcal{C}}{\sqrt{h}}. \tag{4.15}$$

So, the difference for every pair of points is uniformly bounded by $\mathcal{C}/\sqrt{h}$.

It remains the question to find this $\mathcal{C}$.

Let us define the difference cross spectral density operator D:

$$D = (A_W - A_{W'})[f](\boldsymbol{r}) = \int d\boldsymbol{r}_1 \left[\sum_n \lambda_n \Phi_n^*(\boldsymbol{r}_1)\Phi_n(\boldsymbol{r}) - \sum_m \lambda_m' \Phi_m'^*(\boldsymbol{r}_1)\Phi_m'(\boldsymbol{r})\right] f(\boldsymbol{r}_1). \tag{4.16}$$

It turns out that the largest eigenvalue in magnitude of D is exactly $\mathcal{C}$ because Eq. 4.11 is the L^2 induced operator norm which is equal to the largest eigenvalue in magnitude[50, 51]. This norm is called **operator norm**. Using our infrastructure we may look for that largest eigenvalue quickly. We use a Shell-free implementation that evaluates this operator directly by integrating the modes of the two cross spectral densities. Thus finding small eigenvalues of D defined in Eq. 4.16 implies small pointwise errors between W and W'.

Let us define the notions of errors we want to use in this thesis. An **absolute error** Δx of a quantity x is given by:

$$\Delta x = \|x_{\text{exact}} - x\|. \tag{4.17}$$

With a **relative error** δx of a quantity x we mean:

$$\delta x = \frac{\|x_{\text{exact}} - x\|}{\|x_{\text{exact}}\|} \tag{4.18}$$

where the norm is appropriately chosen. For the cross spectral density operator A_W it is the operator norm, for a coherent mode it is the L^2 norm and for an eigenvalue it is the absolute value.

In summary we want to compare two cross spectral densities and we will use our numerical infrastructure to look for the largest eigenvalue $\mathcal{C}$ of the difference operator D given by Eq. 4.16. This eigenvalue, which can also be called the operator norm, gives a boundary for the pointwise absolute error of the difference between the two cross spectral densities W and W' which is independent of the chosen pair of points. To pass from here to something like a relative error the absolute pointwise difference should be divided by a representative value of W that is independent of the chosen set of points. In this thesis we are not so much interested in the exact quantitative meaning of the operator norm but mainly by its trend when the sampling factor s of our calculations is increased. The operator norm will help us to identify convergence of our calculations. In general we will mainly use relative errors for our comparison purposes which are independent of any normalization.

4.2.3. The test case of a Dirac-delta electron beam

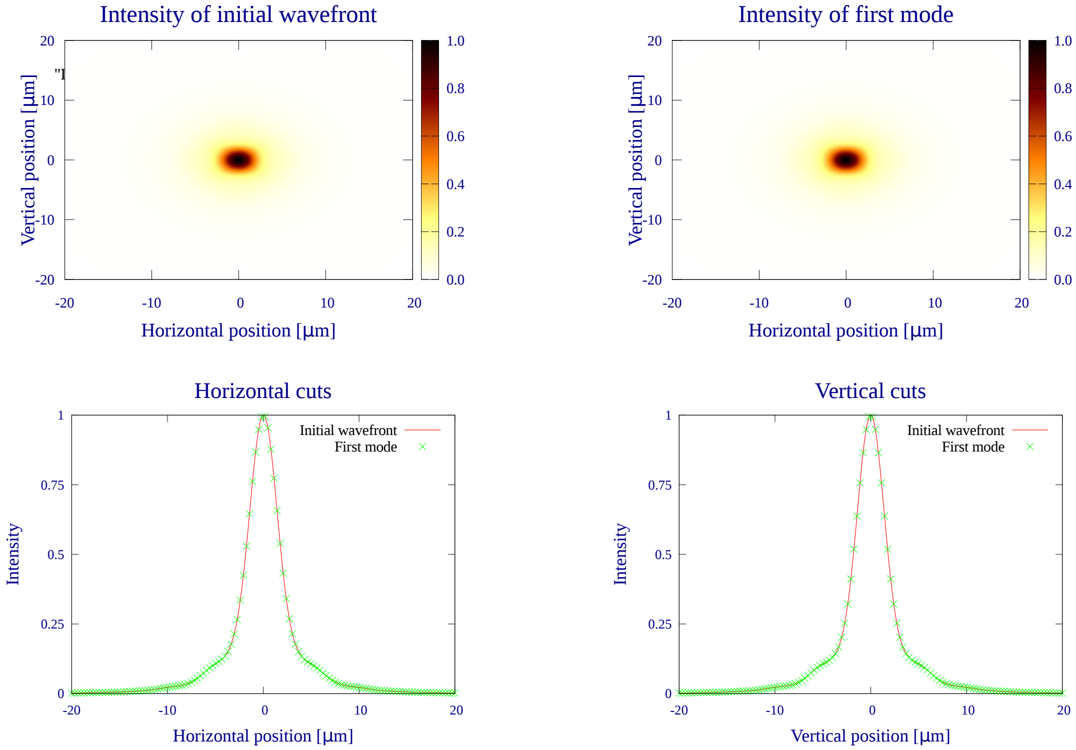

Figure 4.7.: Upper left: normalized intensity of the initial reference single electron emission at the virtual source. Upper right: normalized intensity of the first mode of the decomposition. Bottom left: horizontal cuts of the intensities. Bottom right: vertical cuts of the intensities.

Let us define the five-dimensional electron phase space density to be a delta function

$$\rho_5(\boldsymbol{r},\boldsymbol{\theta},\gamma) = \mathcal{C}\ \delta(\boldsymbol{r})\delta(\boldsymbol{\theta})\delta(\gamma-\gamma_0) \tag{4.19}$$

with a constant $\mathcal{C} > 0$ and the ideal electron energy γ_0. For the sake of readability we use the electron energy γ instead of the electron momentum deviation. They are linearly related by Eq. 2.7 and the substitution in the integration is straightforward. This electron phase space density describes a thin electron beam.

Putting this electron phase space density into the brightness convolution theorem (Eq. 3.15) gives:

$$W(\boldsymbol{r}_1,\boldsymbol{r}_2,\omega) = \widetilde{\mathcal{C}} \cdot E_0{}^*\left(\boldsymbol{r}_1,\omega,\gamma_0\right) E_0\left(\boldsymbol{r}_2,\omega,\gamma_0\right). \tag{4.20}$$

with a constant $\widetilde{\mathcal{C}}$. This is the form of a single moded cross spectral density function. We arrive up to a constant at one coherent mode which is essentially the initial wavefront E_0. We tested this case with our algorithm. The first mode of the decomposition incorporates the spectral density within numerical precision. In agreement with the theoretical prediction the first mode reproduces the initial wavefront (see Fig. 4.7).

4.2.4. The test case of an initial Gaussian wavefront

We tested the matrix method for an initial Gaussian wavefront:

$$E_0(\boldsymbol{r}) = A \exp\left(-\frac{r_x^2}{2s_x^2} - \frac{r_y^2}{2s_y^2}\right) \tag{4.21}$$

with $s_x = s_y = 2.85\mu m$. The values of s_x and s_y were taken from a fit to the emission cone of the first harmonic of the ESRF u18 2m long undulator at the virtual source. We did these calculations because we can compare the numerically obtained eigenvalues and coherent modes against the theoretical result of section 3.3.3. In a real application of the algorithm the initial wavefront E_0 is given by the numerically calculated undulator emission.

We use the electron beam settings defined in section 2.1.8 and the undulator settings given in section 2.3.4.

In the case of the symmetry point the relative errors of the first twenty and some higher order eigenvalues are written in Table. 4.2. The relative error for the eigenvalues is always smaller than $1.0 \cdot 10^{-4}$. The relative error for the coherent modes is at most $3.8 \cdot 10^{-5}$. The relative error in operator norm is $4.1 \cdot 10^{-5}$ for the first 100 modes. Hereby with *for the first 100 modes* we mean that the truncated cross spectral density $W^{(100)}$ that consists only of the first 100 modes defined in Eq. 2.141, was used for the comparison. The truncation is for performance purposes and should not change significantly compared to truncations with more considered modes due to the exponential decrease of the mode spectrum in our calculations, i.e. higher modes become less and less important.

For the finite alpha case, i.e. off the symmetry point, we have the Hermite function based modes and the Gaussian Schell model eigenvalues as we discussed in 3.3.3. The relative errors of the eigenvalues and coherent modes are written in Table. 4.2. The relative error is always smaller than $2.3 \cdot 10^{-4}$ for the eigenvalues. The relative error for the coherent modes is at most $3.8 \cdot 10^{-4}$. The computation of the decomposition with finite alpha is much slower because the cross spectral density has to be calculated without the usage of convolutions. The calculation for the symmetry point case took 40 minutes on 80 CPU cores. The calculation for the finite alpha case took 1 day and 10 minutes on 35 CPU cores, hereby the integration in the finite alpha case was performed with a more coarse grid(sampling factor $s = 1.5$) than the grid of the symmetry point calculation(sampling factor $s = 2.5$). The scaling is essentially to the fourth power with the sampling factor s. To attain higher precision we would have consumed significantly more numerical resources. It is therefore not surprising that the relative errors for the finite alpha case are higher. However we still consider that the result shows very good agreement between the analytical equations and the numerical result. In section 4.4 we present a much more economic algorithm for the decomposition. That method can then calculate the finite alpha case to a higher precision in even less time. The relative error in operator norm is $3.6 \cdot 10^{-4}$ for the first 100 modes.

Overall the algorithm demonstrates high numerical agreement with the theory. Superficially the algorithm performs worse for the finite alpha case but this is probably due to the reduced grid fineness. The agreement is nevertheless clear. We do not show it here, but one can observe the general trend that with an increase in the sampling factor s goes a decrease of the relative errors. But these settings are significantly more computational expensive and we do not see any further clarification given the computational investment.

Symmetry point:

# mode	λ_n	$\delta\lambda$	δmode
1	$6.9 \cdot 10^8$	$2.9 \cdot 10^{-5}$	$1.9 \cdot 10^{-5}$
2	$6.2 \cdot 10^8$	$3.4 \cdot 10^{-5}$	$2.1 \cdot 10^{-5}$
3	$5.5 \cdot 10^8$	$3.9 \cdot 10^{-5}$	$2.5 \cdot 10^{-5}$
4	$4.9 \cdot 10^8$	$4.5 \cdot 10^{-5}$	$2.8 \cdot 10^{-5}$
5	$4.4 \cdot 10^8$	$5.0 \cdot 10^{-5}$	$3.2 \cdot 10^{-5}$
6	$3.9 \cdot 10^8$	$5.5 \cdot 10^{-5}$	$3.5 \cdot 10^{-5}$
7	$3.5 \cdot 10^8$	$6.0 \cdot 10^{-5}$	$3.6 \cdot 10^{-5}$
8	$3.1 \cdot 10^8$	$6.6 \cdot 10^{-5}$	$3.7 \cdot 10^{-5}$
9	$2.8 \cdot 10^8$	$7.1 \cdot 10^{-5}$	$3.7 \cdot 10^{-5}$
10	$2.5 \cdot 10^8$	$7.6 \cdot 10^{-5}$	$3.8 \cdot 10^{-5}$
11	$2.3 \cdot 10^8$	$9.3 \cdot 10^{-5}$	$8.8 \cdot 10^{-6}$
12	$2.2 \cdot 10^8$	$8.1 \cdot 10^{-5}$	$3.7 \cdot 10^{-5}$
13	$2.1 \cdot 10^8$	$9.8 \cdot 10^{-5}$	$9.0 \cdot 10^{-6}$
14	$2.0 \cdot 10^8$	$8.6 \cdot 10^{-5}$	$3.7 \cdot 10^{-5}$
15	$1.9 \cdot 10^8$	$1.0 \cdot 10^{-4}$	$9.6 \cdot 10^{-6}$
16	$1.8 \cdot 10^8$	$9.1 \cdot 10^{-5}$	$3.6 \cdot 10^{-5}$
17	$1.7 \cdot 10^8$	$1.1 \cdot 10^{-4}$	$1.0 \cdot 10^{-5}$
18	$1.6 \cdot 10^8$	$9.6 \cdot 10^{-5}$	$3.5 \cdot 10^{-5}$
19	$1.5 \cdot 10^8$	$1.1 \cdot 10^{-4}$	$1.2 \cdot 10^{-5}$
20	$1.4 \cdot 10^8$	$1.0 \cdot 10^{-4}$	$3.4 \cdot 10^{-5}$
$\vdots$	$\vdots$	$\vdots$	$\vdots$
30	$8.1 \cdot 10^7$	$1.2 \cdot 10^{-4}$	$2.7 \cdot 10^{-5}$
40	$5.5 \cdot 10^7$	$1.7 \cdot 10^{-4}$	$3.4 \cdot 10^{-5}$
50	$3.8 \cdot 10^7$	$1.7 \cdot 10^{-4}$	$4.0 \cdot 10^{-6}$
100	$8.7 \cdot 10^6$	$2.4 \cdot 10^{-4}$	$1.0 \cdot 10^{-6}$

Finite alpha:

# mode	λ_n	$\delta\lambda$	δmode
1	$5.9 \cdot 10^8$	$4.5 \cdot 10^{-5}$	$4.4 \cdot 10^{-4}$
2	$5.3 \cdot 10^8$	$5.4 \cdot 10^{-5}$	$3.9 \cdot 10^{-4}$
3	$4.7 \cdot 10^8$	$6.2 \cdot 10^{-5}$	$3.5 \cdot 10^{-4}$
4	$4.2 \cdot 10^8$	$7.0 \cdot 10^{-5}$	$3.1 \cdot 10^{-4}$
5	$3.8 \cdot 10^8$	$7.8 \cdot 10^{-5}$	$2.8 \cdot 10^{-4}$
6	$3.4 \cdot 10^8$	$8.5 \cdot 10^{-5}$	$2.5 \cdot 10^{-4}$
7	$3.0 \cdot 10^8$	$9.2 \cdot 10^{-5}$	$2.3 \cdot 10^{-4}$
8	$2.7 \cdot 10^8$	$9.9 \cdot 10^{-5}$	$2.0 \cdot 10^{-4}$
9	$2.4 \cdot 10^8$	$1.1 \cdot 10^{-4}$	$1.8 \cdot 10^{-4}$
10	$2.2 \cdot 10^8$	$1.1 \cdot 10^{-4}$	$1.7 \cdot 10^{-4}$
11	$2.1 \cdot 10^8$	$1.3 \cdot 10^{-4}$	$2.2 \cdot 10^{-4}$
12	$1.9 \cdot 10^8$	$1.2 \cdot 10^{-4}$	$1.5 \cdot 10^{-4}$
13	$1.8 \cdot 10^8$	$1.3 \cdot 10^{-4}$	$2.1 \cdot 10^{-4}$
14	$1.7 \cdot 10^8$	$1.2 \cdot 10^{-4}$	$1.3 \cdot 10^{-4}$
15	$1.6 \cdot 10^8$	$1.4 \cdot 10^{-4}$	$1.9 \cdot 10^{-4}$
16	$1.5 \cdot 10^8$	$1.3 \cdot 10^{-4}$	$1.2 \cdot 10^{-4}$
17	$1.5 \cdot 10^8$	$1.5 \cdot 10^{-4}$	$1.6 \cdot 10^{-4}$
18	$1.4 \cdot 10^8$	$1.3 \cdot 10^{-4}$	$1.1 \cdot 10^{-4}$
19	$1.3 \cdot 10^8$	$1.6 \cdot 10^{-4}$	$1.5 \cdot 10^{-4}$
20	$1.3 \cdot 10^8$	$1.4 \cdot 10^{-4}$	$1.0 \cdot 10^{-4}$
$\vdots$	$\vdots$	$\vdots$	$\vdots$
30	$7.2 \cdot 10^7$	$1.6 \cdot 10^{-4}$	$1.2 \cdot 10^{-4}$
40	$5.1 \cdot 10^7$	$1.7 \cdot 10^{-4}$	$5.5 \cdot 10^{-5}$
50	$3.4 \cdot 10^7$	$2.3 \cdot 10^{-4}$	$4.4 \cdot 10^{-5}$
100	$8.2 \cdot 10^6$	$2.3 \cdot 10^{-4}$	$2.0 \cdot 10^{-5}$

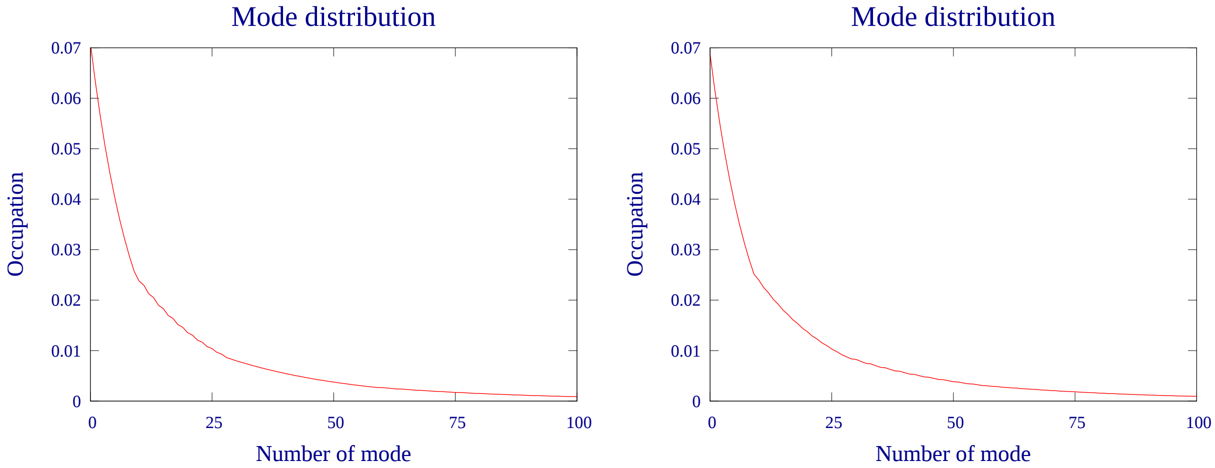

Table 4.2.: Eigenvalues and relative errors between the numerical result and the analytical equations of section 3.3.3 for the eigenvalues and the coherent modes at the symmetry point(left) and for finite alpha(right). Their numerically calculated mode distributions are plotted in the bottom.

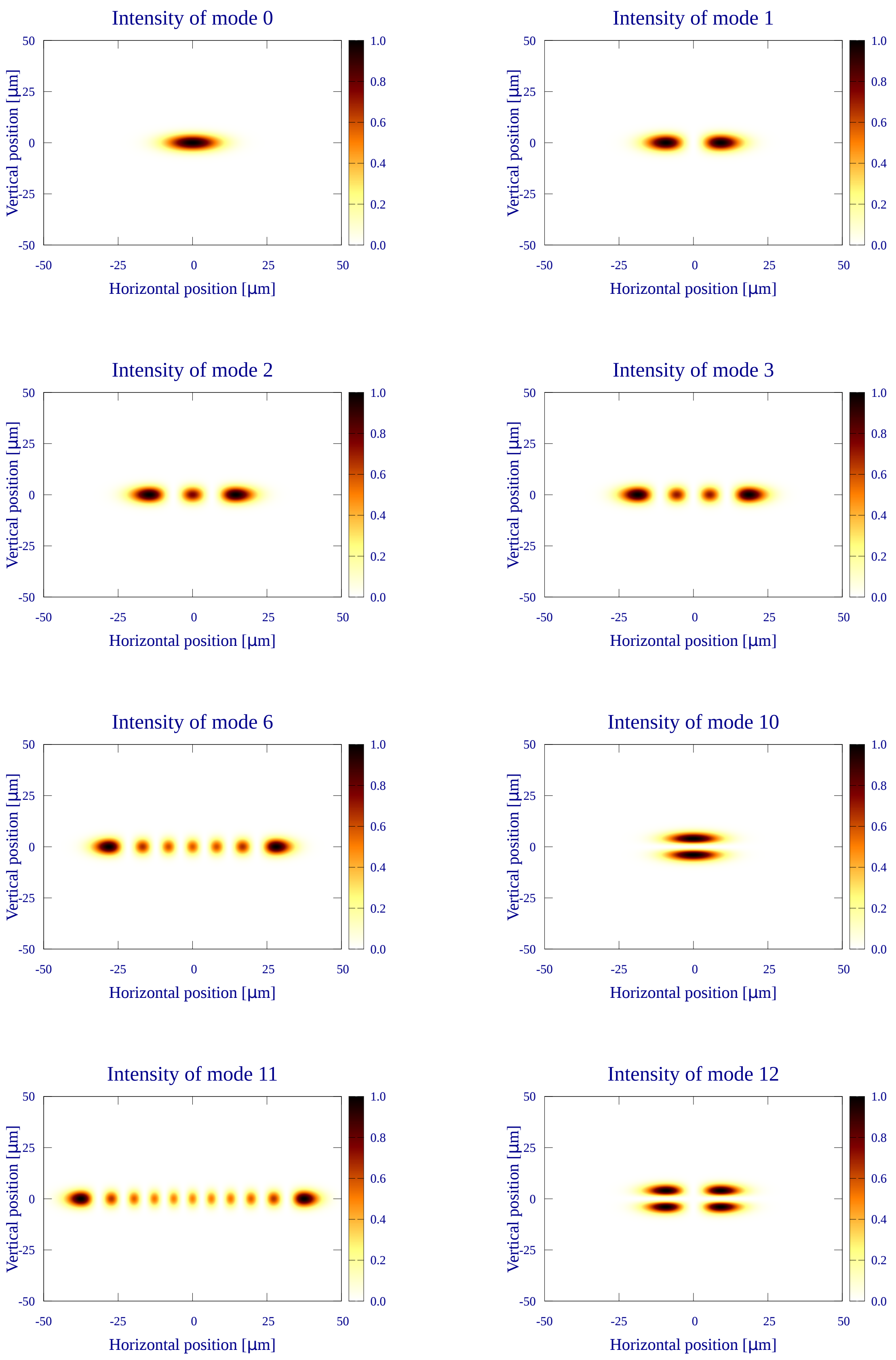

Figure 4.8.: Some coherent modes of the symmetry point test case. The modes are chosen such that the character of the small parameters in the vertical dimension become visible.

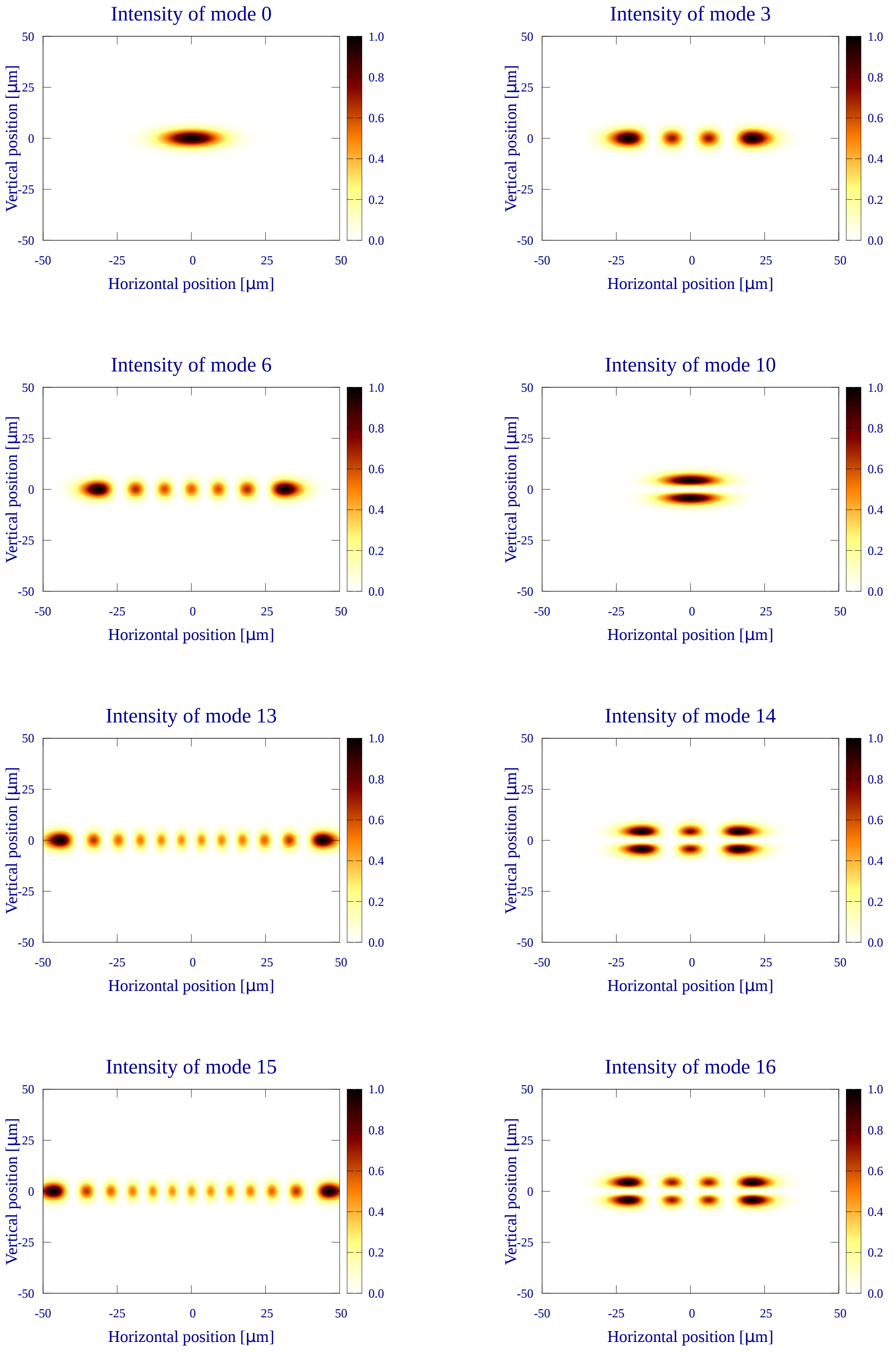

Figure 4.9.: Some coherent modes of the finite alpha test case. The modes are chosen such that the character of the small parameters in the vertical dimension become visible.

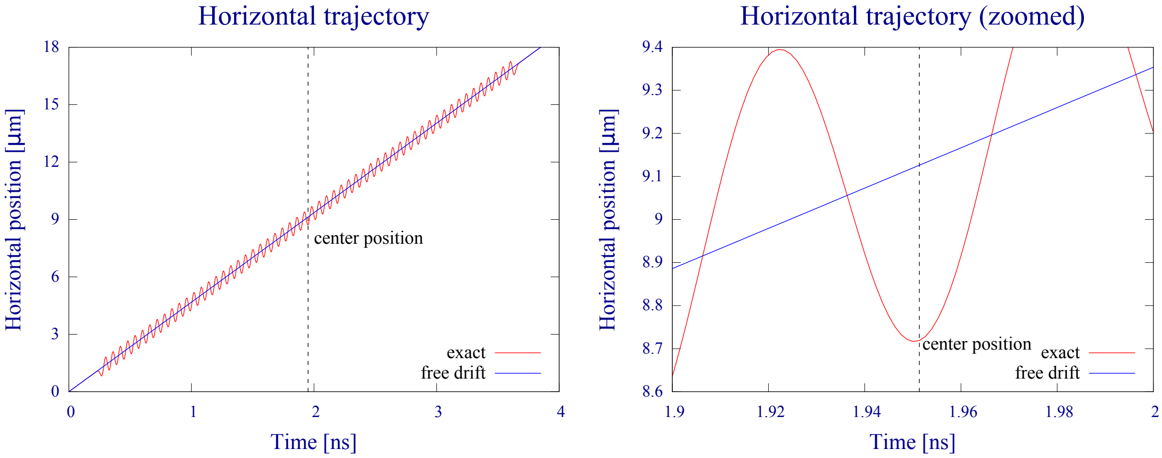

Figure 4.10.: Plot of the horizontal trajectory of an electron in a 1m long ESRF u18 undulator. The electrons enters with an initial horizontal angle $\theta_x = 1.56 \cdot 10^{-5}$. The total trajectory is depicted left and a zoom around the undulator center is right. The dashed vertical line indicates the center position of the undulator.

4.2.5. Investigation of the assumption that the undulator does not change the electron beam distribution

In this section we investigate numerically the assumption that at the position of the center of the undulator the electron beam phase space distribution is the same for the storage ring with undulator as for the storage ring without the undulator. The considerations of this section concern directly only the electron trajectories.

We calculate numerically with pySRU the spatial coordinates and the velocities of the electron at the center of the undulator. As undulators settings we use all the undulators used in this thesis, i.e. the ESRF u18 undulators of 1m, 2m and 4m length defined in section 2.3.4. The electron initial conditions are varied in a similar way as in section 4.2.1, i.e. the initial conditions are varied over a range of three standard deviations of the spatial and divergence ESRF-EBS beam settings defined in section 2.1.8. The results of the simulations are compared to a free space propagation of an electron:

$$\boldsymbol{r}_{center} = \boldsymbol{r}_0 + \boldsymbol{v}_0 \cdot t_{center} \tag{4.22}$$

where $\boldsymbol{r}_{center}$ is the transverse electron position at the center of the undulator, $\boldsymbol{r}_0$ is the initial position at the undulator entrance, $\boldsymbol{v}_0 = c\boldsymbol{\theta}_0$ is the initial velocity and t_{center} is the time it takes the electron to travel to the center of the undulator. The idea is depicted in Fig. 4.10 for the case of a 1m long ESRF u18 undulator with initial vertical angle and no spatial shift. The undulator magnetic fields are all taken in symmetric configuration, i.e. symmetric to the y-axis.

We find that the maximal deviation between the vertical offsets and the velocities are negligible. They attain at most a fraction of microns which is small compared to typical scales of microns for the spatial coordinate and microns for the velocity in units of the speed of light c (see Table. 4.3). The horizontal offset, however, reaches deviations of $0.4\mu m$ which may be not easily negligible. The horizontal shift is basically independent of the initial condition.

Based on this calculation we come to the conclusion that *the assumption that the undulator does not change the electron beam distribution may be checked from undulator to undulator* and maybe a correction is appropriate if the undulator virtual source is chosen to be in the center of the undulator.

Undulator	Δx [μm]	Δy [μm]	$\Delta x'$ [μrad]	$\Delta y'$ in [μrad]
u18 1m	0.4	$1.6 \cdot 10^{-3}$	$2.0 \cdot 10^{-5}$	$6.3 \cdot 10^{-3}$
u18 2m	0.4	$6.4 \cdot 10^{-3}$	$2.0 \cdot 10^{-5}$	$1.3 \cdot 10^{-2}$
u18 4m	0.4	$2.5 \cdot 10^{-2}$	$2.0 \cdot 10^{-5}$	$2.5 \cdot 10^{-2}$

Table 4.3.: Maximal deviation of the electron phase space coordinates after a free drift and a pySRU simulation for ESRF-EBS initial conditions.

Theoretically one can correct for a fixed spatial shift $\boldsymbol{s}$ of the electron beam phase distribution that is independent of the electron initial condition by shifting the reference emission E_0:

$$\tilde{E_0}(\boldsymbol{r}) = E_0(\boldsymbol{r} - \boldsymbol{s}) \tag{4.23}$$

because Eq. 3.15 takes the form:

$$W(\boldsymbol{r}_1, \boldsymbol{r}_2, \omega) = N_e \int d\delta d\boldsymbol{r} d\boldsymbol{\theta}\ \rho(\boldsymbol{r}, \boldsymbol{\theta}, \delta) e^{ik\Delta \boldsymbol{r}} {E_0}^*(\boldsymbol{r}_1 - \boldsymbol{r} - \boldsymbol{s}, \omega, \delta) E_0(\boldsymbol{r}_2 - \boldsymbol{r} - \boldsymbol{s}, \omega, \delta). \tag{4.24}$$

and the shift of the reference electric field is equivalent to the shift of the spatial dimension of the electron phase space distribution:

$$W(\boldsymbol{r}_1, \boldsymbol{r}_2, \omega) = N_e \int d\delta d\boldsymbol{r} d\boldsymbol{\theta}\ \tilde{\rho}(\boldsymbol{r}, \boldsymbol{\theta}, \delta) e^{ik\Delta \boldsymbol{r}} {E_0}^*(\boldsymbol{r}_1 - \boldsymbol{r}, \omega, \delta) E_0(\boldsymbol{r}_2 - \boldsymbol{r}, \omega, \delta). \tag{4.25}$$

with

$$\tilde{\rho}(\boldsymbol{r}, \boldsymbol{\theta}, \delta) = \rho(\boldsymbol{r} - \boldsymbol{s}, \boldsymbol{\theta}, \delta). \tag{4.26}$$

However, through out this thesis we do not apply this correction and **for our algorithm we will always define the virtual source to be at the undulator entrance plane**.

4.3. Propagation and rediagonalization

In section 2.5.9 we discussed the propagation of the cross spectral density in terms of its coherent modes. The propagation includes free space propagation in vacuum and propagation or transmission through optical elements and apertures. With the algorithm described in the previous chapter we can determine numerically the coherent modes. The coherent modes may now be propagated with any wavefront propagation code available. In this work we mainly used the Synchrotron Radiation Workshop (SRW)[24] for the propagation of the coherent modes. With SRW the Fresnel propagation of a wavefront can be calculated efficiently using FFT based calculations of convolutions. The discussion of chapter 2.4.3 applies to the usage of SRW.

If somewhere in the beamline the modes are subjected to a propagation operator that does not commute with the cross spectral density operator A_W then the new cross spectral density operator will have different eigenvectors, i.e. different coherent modes. This is a result known from quantum mechanics or more generally from operator theory. Apart from this even if two operators A and B commute the composition AB will in general have a different eigenvalue spectrum than A or B, i.e. a propagation operator will in general change the eigenvalue spectrum.

As an example, imagine an ideal one to one imaging beamline set up (see Fig. 4.11). Here the beamline produces a one to one image of the center of the undulator. We subsequently reduce the size of the final aperture which results in a cutting of the undulator center image. In [4] they performed this experiment in the framework of ptychography reconstruction of modes of the cross spectral density. They measure that a reduction of the slit size reduces the number

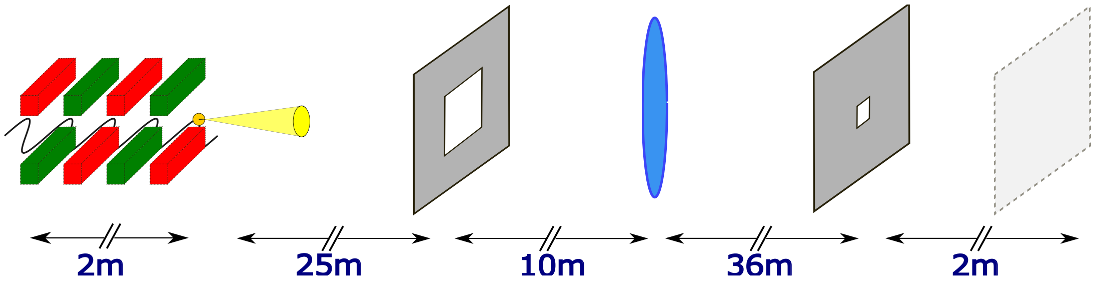

Figure 4.11.: Illustration of an ideal one to one imaging beamline of the center of the undulator with an aperture in the image plane of the lens. The primary slit is widely opened and the vertical and horizontal focal length of the lens is 18 m.

of modes, i.e. that the mode occupations of the first modes become larger and larger while the mode occupations of higher modes decrease. This can also be expected from the theory because the reduction of the aperture size removes *fluctuations* or *cleans the ensemble*. This is illustrated in a very simplified fashion in Fig. 4.12. We expect that the reduction of the aperture size results in a smaller number of relevant coherent modes and an overall reduction of the spectral density. This application will be considered in more detail in chapter 5.

To actually calculate this application we need to rediagonalize the cross spectral density after the propagation. To archive this numerically we propagate the modes to the image plane of the lens where we subject them to the aperture. Now we could, similar to the initial decomposition, create the representing matrix in the stepfunction basis. However, we may also just implement the action of the integral operator directly in terms of the coherent modes:

$$A_W[f](\boldsymbol{r}) = \int d\boldsymbol{r}_1 W(\boldsymbol{r}_1, \boldsymbol{r}_2, \omega) f(\boldsymbol{r}_1) = \sum_n \lambda_n \Phi_n(\boldsymbol{r}) \int d\boldsymbol{r}_1 \Phi_n^*(\boldsymbol{r}_1) f(\boldsymbol{r}_1). \tag{4.27}$$

The number of modes N is usually limited by a few hundreds or a few thousands. If the grid of the mode is large and the number of modes is small, it is much more economic in terms of memory to evaluate Eq. 4.27 directly than to build the representing matrix whose size is the square of the size of the mode grid. For this implementation the numerical eigensolver needs to support user defined matrix-vector operations. The idea to avoid the full calculation of the representing matrix is driven by the aspects of sparse iterative eigensolver techniques, which are often based only on matrix-vector products. Full diagonalization implementations often favor dense matrix-matrix operations that must be optimized differently on today's computers. We use again the solver package SLEPc. It is optimized for sparse eigenvalue problems and offers the possibility to provide user defined matrix-vector multiplications (Schell-free form).

It is clear that we have to face the same index mapping problem due to operator discretization as discussed in the eigendecomposition section 4.1 and we use the same mapping here as we used in that section.

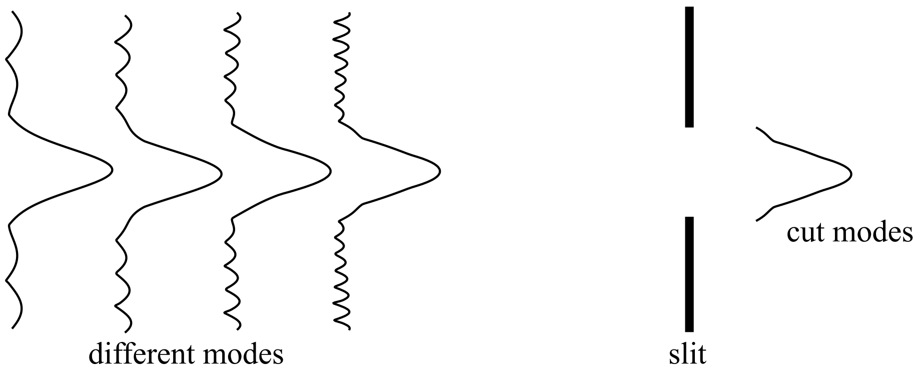

Figure 4.12.: Oversimplified illustration of cutting of different modes. After the slit the cut modes are all similar.

4.4. Numerical eigendecompositon: the two-step method

As it turns out the decomposition method presented so far, while correct and giving correct results, becomes rather quickly impractical due to the unfavorable scaling of the representing matrix with the sampling factor s. For high emittance lattices this method can not be used. A converged result requires many high resolution modes because these modes differ from each other on a small spatial scale compared to the electron beam size. Furthermore, apart from the immense memory demand to construct the representing matrix all the matrix elements have to be calculated. In the case of the symmetry point approximation this may be efficiently done with *a convolution*. For the more general finite alpha case this is not possible and the calculation of the matrix becomes much slower and practically impossible for these dense grids. In summary not many real problems can be calculated with the matrix method.

We present here a method of divide-and-conquer type. It calculates the coherent modes in two steps. First the cross spectral density is calculated as if there was no divergence. This can be made directly with Krylov subspace methods and convergence is usually reached after $2n$ "divergence less" cross spectral density operator actions where n is the number of desired *spatial modes* Φ_n^s. We use the notion spatial because only the spatial part of the electron phase space density contributes to their creation. We underline the fact that the spatial modes must not be very similar to the final coherent modes. This depends strongly on the divergence. Once we have the spatial modes we apply the action of the divergence, again directly by application of Krylov-subspace methods. The discretization and index mapping explained in section 4.1 remains unaltered and is addressed the same way.

We mainly discuss the finite alpha case from which the symmetry point case follows as a special case.

Let us review equation Eq. 3.57 that calculates the cross spectral density for finite alpha. We want to neglect all constants and, for now, the energy spread integration and the exponential outside the integral. The exponential outside the integral depends only on the electron beam's divergences. The integral that is left depends only on the spatial part of the electron beam. We call this part of the cross spectral density the **spatial cross spectral density** W_s because it neglects any effects of electron beam divergence. We can say that the spatial cross spectral density is up to constants the zero divergence limit of the cross spectral density. In this section when we speak of **full cross spectral density** W we mean the cross spectral density W in order to distinguish it from the spatial cross spectral density W_s. The spatial cross spectral density W_s

has all the properties of the full cross spectral density and takes the form:

$$\boxed{W_s(\boldsymbol{r}_1, \boldsymbol{r}_2, \omega) = \int d\boldsymbol{r} h_{\boldsymbol{r}_1}(\boldsymbol{r})\, E_0(\boldsymbol{r}_2 - \boldsymbol{r}, \omega) \exp\left(-ik\boldsymbol{r}_2 \begin{bmatrix} \frac{m_{xx'}}{m_{x'x'}} x \\ \frac{m_{yy'}}{m_{y'y'}} y \end{bmatrix}\right)} \tag{4.28}$$

here

$$\boxed{h_{\boldsymbol{r}_1}(\boldsymbol{r}) = \exp\left(-\frac{N_x x^2}{2} - \frac{N_y y^2}{2}\right) E_0{}^*(\boldsymbol{r}_1 - \boldsymbol{r}, \omega) \exp\left(ik\boldsymbol{r}_1 \begin{bmatrix} \frac{m_{xx'}}{m_{x'x'}} x \\ \frac{m_{yy'}}{m_{y'y'}} y \end{bmatrix}\right)} \tag{4.29}$$

is a function parametrized by $\boldsymbol{r}_1$. For the full notation refer to section 3.3.2.2. This form was intentionally stated in its numerically useful form. It depends only on $\boldsymbol{r}$ and depends parametric on $\boldsymbol{r}_1$. We will shortly discuss why this is of tremendous numerical value.

Let us consider the spatial cross spectral density operator A^s_W in more detail:

$$\begin{aligned} A^s_W[f](\boldsymbol{r}_2) &= \int d\boldsymbol{r}_1\; W_s(\boldsymbol{r}_1, \boldsymbol{r}_2) f(\boldsymbol{r}_1) \\ &= \int d\boldsymbol{r}_1 \int d\boldsymbol{r}\; h_{\boldsymbol{r}_1}(\boldsymbol{r})\, E_0(\boldsymbol{r}_2 - \boldsymbol{r}, \omega) \exp\left(-ik\boldsymbol{r}_2 \begin{bmatrix} \frac{m_{xx'}}{m_{x'x'}} x \\ \frac{m_{yy'}}{m_{y'y'}} y \end{bmatrix}\right) f(\boldsymbol{r}_1) \\ &= \int d\boldsymbol{r}\; E_0(\boldsymbol{r}_2 - \boldsymbol{r}, \omega) \exp\left(-ik\boldsymbol{r}_2 \begin{bmatrix} \frac{m_{xx'}}{m_{x'x'}} x \\ \frac{m_{yy'}}{m_{y'y'}} y \end{bmatrix}\right) \int d\boldsymbol{r}_1 h_{\boldsymbol{r}_1}(\boldsymbol{r})\, f(\boldsymbol{r}_1) \end{aligned} \tag{4.30}$$

here we interchanged the integration order. We may rewrite this as

$$A^s_W[f](\boldsymbol{r}_2) = \int d\boldsymbol{r}\; E_0(\boldsymbol{r}_2 - \boldsymbol{r}, \omega) \exp\left(-ik\boldsymbol{r}_2 \begin{bmatrix} \frac{m_{xx'}}{m_{x'x'}} x \\ \frac{m_{yy'}}{m_{y'y'}} y \end{bmatrix}\right) B[f](\boldsymbol{r}) \tag{4.31}$$

with the operator B

$$B[f](\boldsymbol{r}) = \int d\boldsymbol{r}_1 h_{\boldsymbol{r}_1}(\boldsymbol{r})\, f(\boldsymbol{r}_1). \tag{4.32}$$

Here something noteworthy happened. Because we interchanged the integration order we may actually calculate the action of the spatial cross spectral density operator by the calculation of two times number of grid points two-dimensional integrals. This *is computationally much more favorable* than the case of the full cross spectral density W.

Let us discuss why the full case is numerically less favorable. In the full case there is an extra exponential in front of the spatial cross spectral density W_s. This factor could not be taken out of the integral defining the integral operator B. This implies that the analogue of B from Eq. 4.32 would take the modified form B_{full} in the full case:

$$B_{\text{full}}[f](\boldsymbol{r}, \boldsymbol{r}_2) = \int d\boldsymbol{r}_1 \exp\left(-\frac{k^2(x_2 - x_1)^2}{2m_{x'x'}} - \frac{k^2(y_2 - y_1)^2}{2m_{y'y'}}\right) h_{\boldsymbol{r}_1}(\boldsymbol{r})\, f(\boldsymbol{r}_1). \tag{4.33}$$

This modified B_{full} *depends not only on* $\boldsymbol{r}$ *but also on* $\boldsymbol{r}_2$. In the zero divergence case of the spatial cross spectral density the integral operator B can be calculated and stored in memory, i.e. it can be *reused* for every $\boldsymbol{r}_2$. To understand the dimension of the numerical difference: the full B_{full} depends on two two-dimensional spatial coordinates and for every pair of points $\boldsymbol{r}$, $\boldsymbol{r}_2$ a two-dimensional integral must be calculated. This gives in total number of grid points square two-dimensional integrations. The effort to calculate B_{full} for a given f is therefore of the same order as to calculate the full representing matrix. This is often an practically unsolvable problem and our intention was exactly to avoid the calculation and storage of the full representing matrix. On the other side the operator B in the zero divergence case depends only on $\boldsymbol{r}$. It can be easily stored in memory because it has the same size in memory as a single coherent mode and it requires only number of grid points two-dimensional integrations for a given f.

So far we realized that we can calculate the spatial cross spectral density that neglects any influence of the electron beam divergence. This can be done numerically rather efficient with the help of Krylov-methods. But in general the divergence can not be neglected because its contribution is often very important. We will therefore account for the electron beam divergence in a second step as follows:

Since the spatial cross spectral density has all the properties of a cross spectral density we may perform a coherent mode decomposition. Having the decomposition of the spatial cross spectral density we have spatial eigenvalues λ_n^s and modes Φ_n^s. The *spatial* integral in Eq. 3.57 may be expressed in terms of these eigenvalues and coherent modes, i.e. in its coherent mode representation:

$$\boxed{W(\boldsymbol{r}_1, \boldsymbol{r}_2, \omega) = \mathcal{C} \exp\left(-\frac{k^2 \Delta x^2}{2m_{x'x'}} - \frac{k^2 \Delta y^2}{2m_{y'y'}}\right) \sum_n \lambda_n^s (\Phi_n^s)^*(\boldsymbol{r}_1) \Phi_n^s(\boldsymbol{r}_2).} \tag{4.34}$$

here $\mathcal{C}$ is a constant. The associated cross spectral density operator takes the form:

$$\boxed{A_W[f](\boldsymbol{r}_2) = \mathcal{C} \sum_n \lambda_n^s \Phi_n^s(\boldsymbol{r}_2) \int d\boldsymbol{r}_1 \exp\left(-\frac{k^2 \Delta x^2}{2m_{x'x'}} - \frac{k^2 \Delta y^2}{2m_{y'y'}}\right) (\Phi_n^s)^*(\boldsymbol{r}_1) f(\boldsymbol{r}_1).} \tag{4.35}$$

The integral in Eq. 4.35 is in fact a convolution of a Gaussian with the product of a spatial coherent mode with f. The separability of the Gaussian convolution kernel can be exploited to speed up the numerical calculation. To evaluate the full action of the operator A_W additionally number of coherent modes n convolutions per action have to be performed.

The big advantages of this two-step method is that it basically only needs the memory for the spatial and the final coherent modes. Depending on the grid size this may still be several gigabytes or even a few hundred gigabytes. Software packages like SLEPc distribute the modes across computer nodes so that these problems can be practically calculated on small sized clusters.

We point out that *this method becomes an approximation if the first step does not reproduces the spatial cross spectral density completely*, i.e. if the first step does not calculate sufficient spatial modes. However, **this can be controlled** by the sum of the spatial eigenvalues because the operator is nuclear and the sum of its eigenvalues equals the trace of the operator which can be independently and efficiently calculated using a convolution.

To estimate the calculation effort let us assume we need as many spatial modes to converge the spatial operator as we wish to have coherent modes in the end. Let N_m be this number of requested coherent modes and let N_g be the number of grid points. For the first step the Krylov-subspace based method will perform about $2N_m$ times $2N_g$ two-dimensional integrals giving a total of $4N_mN_g$ two-dimensional integrals. The second step will perform N_m convolutions per action for about $2N_m$ actions so in total $2N_m^2$ convolutions. If we consider a FFT based convolution roughly as N_g two-dimensional integrals we end up with a total of $2N_mN_g(2 + N_m)$ two-dimensional integrals. The full matrix method would need N_g^2 two-dimensional integrals plus N_m matrix-vector products that are effectively a two-dimensional integral, giving a total of $N_g^2 + N_m$ two-dimensional integrals. The scaling with N_g is linear for the two-step method and quadratic for the matrix method. If $N_g \gg N_m$, as in the case of high-emittance lattices where N_g is of the order of a few hundred thousands and N_m is of the order of a few thousands, the two-step methods is not only more memory efficient, and therefore feasible at all, but also performs a lot fewer calculations.

As a final remark we point out that in the special case of the symmetry point the spatial cross spectral operator can be calculated efficiently with the usage of convolutions. The second step which is usually computationally more demanding remains, however, unchanged.

Concerning the level of complexity of the implementation, it is even a bit higher than for the matrix method. Everything we discussed in view of the complexity of the matrix method in section 4.1.3 applies to the two-step method as well. The implementation of the two-step method requires parallel and performance optimized programming. The reason is again the large memory need and the large amount of calculations that can not be handled by a single state of the art computer. Parallel and optimized programming gives more space for implementation errors and the development must be made very careful and tested extensively. While the matrix method has only one step, the two-step method consists of two-steps. The two-step method has therefore more potential for implementation errors and development and testing required more time.

4.5. Tests and comparison of the two-step method

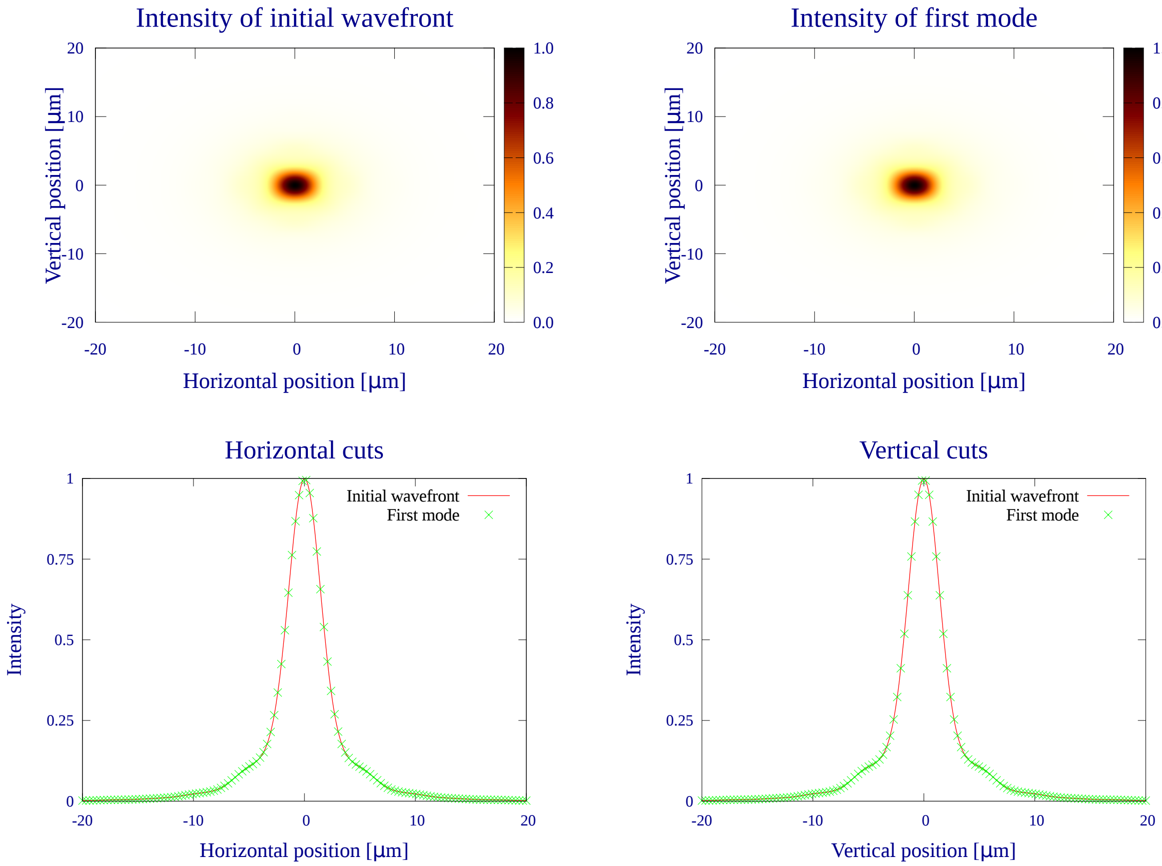

Figure 4.13.: Decomposition using the two-step method algorithm with a delta shaped electron beam. The initial wavefront is recovered from the first mode of the decomposition.

The two-step method is even more complicated to implement than the matrix method. Additionally, it must be guaranteed that the first step is sufficiently converged. While the equations of the two-step method look reasonable the matrix method appears to be more straightforward and therefore more trustworthy. We performed all the tests we did for the matrix method likewise with the two-step method. Additionally, we tested the the two-step methods against the matrix method. The following pages contain therefore a rather long list of test results.

To arrive at a good numerical convergence for the test case of a delta shaped electron beam one requires a more dense sampling than it is needed for the matrix method. Nevertheless the initial wavefront is recovered (see Fig. 4.13). Additionally, we compare the matrix method and the two-step method for ESRF-EBS lattice settings and ESRF u18 2m long and 4m long undulators. We always find high numerical agreement between the two methods and their implementations. This adds extra confidence to both methods because even though the two methods are based on the same physics the implementations and their equations are rather different and offer many possibilities for implementation bugs. Like for the tests of the matrix method in section 4.2 we used grid settings that showed to perform well in real applications. The sampling factor is usually $s = 2.5$. A detailed discussion of convergence issues can be found in the applications chapter 5. We start the discussion with the presentation of the comparison to the analytical results for an initial Gaussian wavefront:

$$E_0(\boldsymbol{r}) = A\exp\left(-\frac{r_x^2}{2s_x^2} - \frac{r_y^2}{2s_y^2}\right) \tag{4.36}$$

with $s_x = s_y = 2.85\mu m$. As in section 4.2 the values of the parameters s_x and s_y are taken from a fit to the central cone of the first harmonic of an 2m long ESRF u18 undulator. For the symmetry point settings the relative errors of the eigenvalues and coherent modes are written in Table. 4.4. The relative error is at most $1.6 \cdot 10^{-5}$ for the eigenvalues and at most $3.2 \cdot 10^{-6}$ for the coherent modes. The relative error in operator norm is $5.8 \cdot 10^{-6}$ for the first 100 modes.

In contrast to the matrix method this method can perform the decomposition in practical times and even to a higher precision for the finite alpha case as well. The calculations here were performed with a sampling factor of $s = 2.5$ whereas the finite alpha tests for the matrix method were performed only with a sampling factor of $s = 1.5$. Although the precision was increased this method took less calculation time and used less memory. The two-step method calculation took 18 hours and 5 minutes on 28 CPU cores whereas the related calculation in the matrix test section 4.2 took 24 hours and 6 minutes on 35 CPU cores. The relative errors of the eigenvalues and coherent modes are written in Table. 4.4. The relative error is at most $1.8 \cdot 10^{-4}$ for the eigenvalues and at most $3.8 \cdot 10^{-4}$ for the coherent modes. The relative error in operator norm is $3.0 \cdot 10^{-4}$ for the first 100 modes.

Let us now compare the two methods directly. For an initial Gaussian wavefront the two methods agree to the theoretical result and they will therefore also agree among each other. It is however theoretically possible that they agree less among each other than to the theoretically result. Our results show that this is not the case, i.e. the agreement between the two methods is very good. All the relative errors are at most $6.2 \cdot 10^{-10}$ (see Table. 4.5). The comparisons is only made for the symmetry point case because in the finite alpha case the calculations were, as already discussed, made at different sampling settings.

We enlarge our test cases to some real applications. We compare numerical results for ESRF-EBS lattice with a 2 meter and a 4 meter long ESRF u18 undulator. The calculations are performed at their first harmonics and the convergence parameter (sampling factor $s = 2.5$) is taken from the application chapter 5.

For the symmetry point the relative errors are written in Table. 4.6. The relative error is at most $4.3 \cdot 10^{-5}$ for the eigenvalues for both undulators and is at most $1.1 \cdot 10^{-6}$ for the coherent modes. The relative error in operator norm is $3.2 \cdot 10^{-6}$ (2m) and $4.9 \cdot 10^{-7}$ (4m) for the first 300 modes.

For the finite alpha case and both undulators the relative error of the eigenvalues is at most

Symmetry point:

# mode	λ_n	$\delta\lambda$	δmode
1	$6.9 \cdot 10^8$	$3.7 \cdot 10^{-6}$	$2.3 \cdot 10^{-6}$
2	$6.2 \cdot 10^8$	$4.3 \cdot 10^{-6}$	$2.0 \cdot 10^{-6}$
3	$5.5 \cdot 10^8$	$5.0 \cdot 10^{-6}$	$1.9 \cdot 10^{-6}$
4	$4.9 \cdot 10^8$	$5.5 \cdot 10^{-6}$	$1.7 \cdot 10^{-6}$
5	$4.4 \cdot 10^8$	$6.1 \cdot 10^{-6}$	$1.7 \cdot 10^{-6}$
6	$3.9 \cdot 10^8$	$6.6 \cdot 10^{-6}$	$1.6 \cdot 10^{-6}$
7	$3.5 \cdot 10^8$	$7.1 \cdot 10^{-6}$	$1.7 \cdot 10^{-6}$
8	$3.1 \cdot 10^8$	$7.6 \cdot 10^{-6}$	$1.9 \cdot 10^{-6}$
9	$2.8 \cdot 10^8$	$8.0 \cdot 10^{-6}$	$2.1 \cdot 10^{-6}$
10	$2.5 \cdot 10^8$	$8.3 \cdot 10^{-6}$	$2.3 \cdot 10^{-6}$
11	$2.3 \cdot 10^8$	$9.9 \cdot 10^{-6}$	$1.4 \cdot 10^{-6}$
12	$2.2 \cdot 10^8$	$8.7 \cdot 10^{-6}$	$2.4 \cdot 10^{-6}$
13	$2.1 \cdot 10^8$	$1.1 \cdot 10^{-5}$	$1.2 \cdot 10^{-6}$
14	$2.0 \cdot 10^8$	$9.0 \cdot 10^{-6}$	$2.6 \cdot 10^{-6}$
15	$1.9 \cdot 10^8$	$1.1 \cdot 10^{-5}$	$1.1 \cdot 10^{-6}$
16	$1.8 \cdot 10^8$	$9.3 \cdot 10^{-6}$	$2.8 \cdot 10^{-6}$
17	$1.7 \cdot 10^8$	$1.2 \cdot 10^{-5}$	$1.0 \cdot 10^{-6}$
18	$1.6 \cdot 10^8$	$9.5 \cdot 10^{-6}$	$2.9 \cdot 10^{-6}$
19	$1.5 \cdot 10^8$	$1.2 \cdot 10^{-5}$	$9.1 \cdot 10^{-7}$
20	$1.4 \cdot 10^8$	$9.7 \cdot 10^{-6}$	$3.0 \cdot 10^{-6}$
⋮	⋮	⋮	⋮
30	$8.1 \cdot 10^7$	$1.0 \cdot 10^{-5}$	$3.2 \cdot 10^{-6}$
40	$5.5 \cdot 10^7$	$1.1 \cdot 10^{-5}$	$8.4 \cdot 10^{-7}$
50	$3.8 \cdot 10^7$	$1.6 \cdot 10^{-5}$	$1.1 \cdot 10^{-6}$
100	$8.7 \cdot 10^6$	$1.5 \cdot 10^{-5}$	$5.0 \cdot 10^{-5}$

Finite alpha:

# mode	λ_n	$\delta\lambda$	δmode
1	$6.2 \cdot 10^8$	$2.5 \cdot 10^{-5}$	$3.8 \cdot 10^{-4}$
2	$5.6 \cdot 10^8$	$3.0 \cdot 10^{-5}$	$3.4 \cdot 10^{-4}$
3	$5.0 \cdot 10^8$	$3.5 \cdot 10^{-5}$	$3.1 \cdot 10^{-4}$
4	$4.5 \cdot 10^8$	$4.0 \cdot 10^{-5}$	$2.8 \cdot 10^{-4}$
5	$4.1 \cdot 10^8$	$4.5 \cdot 10^{-5}$	$2.5 \cdot 10^{-4}$
6	$3.7 \cdot 10^8$	$5.0 \cdot 10^{-5}$	$2.2 \cdot 10^{-4}$
7	$3.3 \cdot 10^8$	$5.5 \cdot 10^{-5}$	$2.0 \cdot 10^{-4}$
8	$3.0 \cdot 10^8$	$5.9 \cdot 10^{-5}$	$1.8 \cdot 10^{-4}$
9	$2.7 \cdot 10^8$	$6.4 \cdot 10^{-5}$	$1.7 \cdot 10^{-4}$
10	$2.4 \cdot 10^8$	$6.9 \cdot 10^{-5}$	$1.5 \cdot 10^{-4}$
11	$2.3 \cdot 10^8$	$7.5 \cdot 10^{-5}$	$2.1 \cdot 10^{-4}$
12	$2.2 \cdot 10^8$	$7.4 \cdot 10^{-5}$	$1.3 \cdot 10^{-4}$
13	$2.1 \cdot 10^8$	$8.0 \cdot 10^{-5}$	$1.9 \cdot 10^{-4}$
14	$1.9 \cdot 10^8$	$7.8 \cdot 10^{-5}$	$1.2 \cdot 10^{-4}$
15	$1.9 \cdot 10^8$	$8.5 \cdot 10^{-5}$	$1.7 \cdot 10^{-4}$
16	$1.7 \cdot 10^8$	$8.3 \cdot 10^{-5}$	$1.1 \cdot 10^{-4}$
17	$1.7 \cdot 10^8$	$9.0 \cdot 10^{-5}$	$1.5 \cdot 10^{-4}$
18	$1.6 \cdot 10^8$	$8.7 \cdot 10^{-5}$	$1.0 \cdot 10^{-4}$
19	$1.5 \cdot 10^8$	$9.5 \cdot 10^{-5}$	$1.4 \cdot 10^{-4}$
20	$1.4 \cdot 10^8$	$9.2 \cdot 10^{-5}$	$9.0 \cdot 10^{-5}$
⋮	⋮	⋮	⋮
30	$8.5 \cdot 10^7$	$1.2 \cdot 10^{-4}$	$1.9 \cdot 10^{-4}$
40	$5.9 \cdot 10^7$	$1.3 \cdot 10^{-4}$	$4.4 \cdot 10^{-5}$
50	$4.2 \cdot 10^7$	$1.5 \cdot 10^{-4}$	$3.9 \cdot 10^{-5}$
100	$1.1 \cdot 10^7$	$1.8 \cdot 10^{-4}$	$1.2 \cdot 10^{-5}$

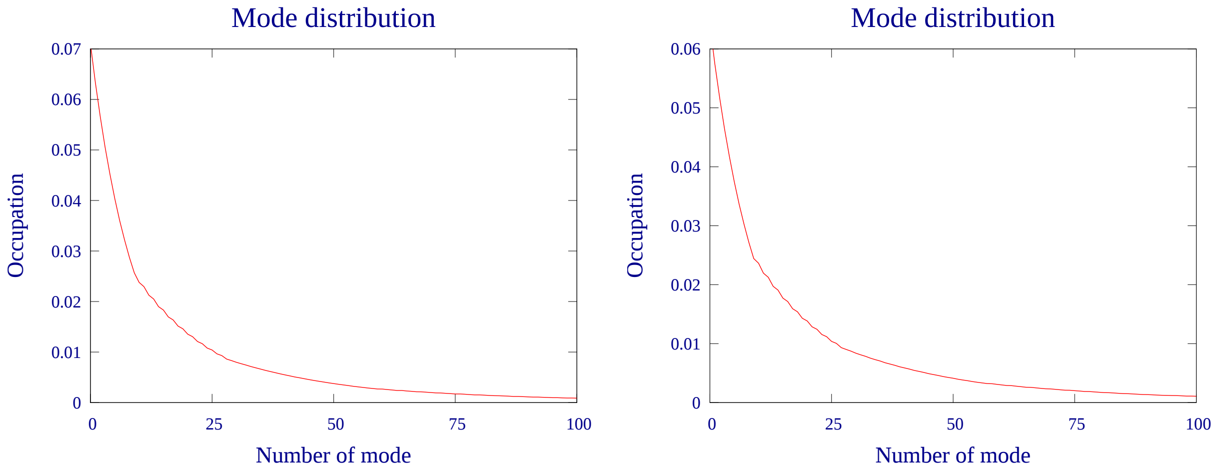

Table 4.4.: Relative errors between the analytical and numerical result for the eigenvalues and coherent modes with an initial Gaussian wavefront using the two-step method at the symmetry point(left) or with finite alpha(right) and their mode distributions(bottom).

# mode	$\delta\lambda$	δmode
1	$6.2 \cdot 10^{-15}$	$8.5 \cdot 10^{-14}$
2	$1.8 \cdot 10^{-14}$	$6.0 \cdot 10^{-14}$
3	$4.3 \cdot 10^{-15}$	$2.3 \cdot 10^{-13}$
4	$3.4 \cdot 10^{-14}$	$1.6 \cdot 10^{-13}$
5	$6.2 \cdot 10^{-14}$	$3.3 \cdot 10^{-13}$
6	$1.2 \cdot 10^{-13}$	$5.7 \cdot 10^{-13}$
7	$2.5 \cdot 10^{-13}$	$1.1 \cdot 10^{-12}$
8	$5.3 \cdot 10^{-13}$	$2.0 \cdot 10^{-12}$
9	$1.1 \cdot 10^{-12}$	$3.2 \cdot 10^{-12}$
10	$2.0 \cdot 10^{-12}$	$5.5 \cdot 10^{-12}$
11	$9.0 \cdot 10^{-16}$	$5.1 \cdot 10^{-14}$
12	$3.6 \cdot 10^{-12}$	$8.3 \cdot 10^{-12}$
13	$3.3 \cdot 10^{-14}$	$8.6 \cdot 10^{-14}$
14	$6.4 \cdot 10^{-12}$	$1.3 \cdot 10^{-11}$
15	$8.9 \cdot 10^{-14}$	$2.2 \cdot 10^{-13}$
16	$1.1 \cdot 10^{-11}$	$1.9 \cdot 10^{-11}$
17	$2.4 \cdot 10^{-13}$	$5.6 \cdot 10^{-13}$
18	$1.8 \cdot 10^{-11}$	$2.8 \cdot 10^{-11}$
19	$6.2 \cdot 10^{-13}$	$1.2 \cdot 10^{-12}$
20	$2.9 \cdot 10^{-11}$	$3.8 \cdot 10^{-11}$
$\vdots$	$\vdots$	$\vdots$
30	$2.5 \cdot 10^{-10}$	$1.8 \cdot 10^{-10}$
40	$2.3 \cdot 10^{-12}$	$1.7 \cdot 10^{-12}$
50	$6.2 \cdot 10^{-10}$	$2.1 \cdot 10^{-10}$
100	$9.5 \cdot 10^{-12}$	$1.9 \cdot 10^{-12}$

Table 4.5.: Relative errors for the eigenvalues and the coherent mode between the matrix and the two step method for a Gaussian wavefront.

$3.6 \cdot 10^{-5}$ for the eigenvalues and it is at most $9.9 \cdot 10^{-7}$ for the coherent modes (see Table. 4.6). The relative error in operator norm is $2.8 \cdot 10^{-6}$ (2m) and $6.9 \cdot 10^{-7}$ (4m) for the first 300 modes.

The results of the two methods are in very good agreement. The results could be even further improved if higher sampling factors s were used. But we do not consider this necessary given the extra consumption of computational resources. We may conclude that both methods are identical in the limits of numerical precision.

ESRF u18 2m:

# mode	$\delta\lambda$	δmode
1	$4.3 \cdot 10^{-8}$	$8.9 \cdot 10^{-8}$
2	$5.2 \cdot 10^{-8}$	$1.2 \cdot 10^{-7}$
3	$8.3 \cdot 10^{-8}$	$1.6 \cdot 10^{-7}$
4	$1.2 \cdot 10^{-7}$	$2.1 \cdot 10^{-7}$
5	$1.5 \cdot 10^{-7}$	$2.1 \cdot 10^{-7}$
6	$1.9 \cdot 10^{-7}$	$2.2 \cdot 10^{-7}$
7	$2.3 \cdot 10^{-7}$	$2.3 \cdot 10^{-7}$
8	$2.8 \cdot 10^{-7}$	$2.4 \cdot 10^{-7}$
9	$3.4 \cdot 10^{-7}$	$2.8 \cdot 10^{-7}$
10	$4.1 \cdot 10^{-7}$	$2.8 \cdot 10^{-7}$
11	$2.7 \cdot 10^{-7}$	$1.5 \cdot 10^{-7}$
12	$5.2 \cdot 10^{-7}$	$3.4 \cdot 10^{-7}$
13	$3.6 \cdot 10^{-7}$	$2.3 \cdot 10^{-7}$
14	$6.2 \cdot 10^{-7}$	$3.4 \cdot 10^{-7}$
15	$5.0 \cdot 10^{-7}$	$2.4 \cdot 10^{-7}$
16	$7.6 \cdot 10^{-7}$	$3.7 \cdot 10^{-7}$
17	$6.6 \cdot 10^{-7}$	$2.6 \cdot 10^{-7}$
18	$9.2 \cdot 10^{-7}$	$4.1 \cdot 10^{-7}$
19	$8.4 \cdot 10^{-7}$	$2.8 \cdot 10^{-7}$
20	$1.1 \cdot 10^{-6}$	$4.1 \cdot 10^{-7}$
⋮	⋮	⋮
30	$2.5 \cdot 10^{-6}$	$4.8 \cdot 10^{-7}$
40	$3.5 \cdot 10^{-6}$	$7.8 \cdot 10^{-7}$
50	$8.1 \cdot 10^{-6}$	$6.5 \cdot 10^{-7}$
100	$4.3 \cdot 10^{-5}$	$1.1 \cdot 10^{-6}$

ESRF u18 4m:

# mode	$\delta\lambda$	δmode
1	$4.9 \cdot 10^{-9}$	$1.1 \cdot 10^{-7}$
2	$4.4 \cdot 10^{-8}$	$5.3 \cdot 10^{-8}$
3	$3.9 \cdot 10^{-8}$	$1.6 \cdot 10^{-7}$
4	$2.7 \cdot 10^{-8}$	$4.8 \cdot 10^{-8}$
5	$2.3 \cdot 10^{-8}$	$4.4 \cdot 10^{-8}$
6	$3.5 \cdot 10^{-8}$	$5.0 \cdot 10^{-8}$
7	$6.1 \cdot 10^{-8}$	$1.0 \cdot 10^{-7}$
8	$9.4 \cdot 10^{-8}$	$9.1 \cdot 10^{-8}$
9	$1.4 \cdot 10^{-7}$	$1.0 \cdot 10^{-7}$
10	$1.7 \cdot 10^{-7}$	$1.1 \cdot 10^{-7}$
11	$1.2 \cdot 10^{-7}$	$5.6 \cdot 10^{-8}$
12	$2.0 \cdot 10^{-7}$	$1.0 \cdot 10^{-7}$
13	$1.9 \cdot 10^{-7}$	$5.0 \cdot 10^{-8}$
14	$2.4 \cdot 10^{-7}$	$9.3 \cdot 10^{-8}$
15	$2.7 \cdot 10^{-7}$	$9.0 \cdot 10^{-8}$
16	$2.2 \cdot 10^{-7}$	$5.5 \cdot 10^{-8}$
17	$2.9 \cdot 10^{-7}$	$7.6 \cdot 10^{-8}$
18	$2.6 \cdot 10^{-7}$	$8.9 \cdot 10^{-8}$
19	$3.2 \cdot 10^{-7}$	$7.2 \cdot 10^{-8}$
20	$3.1 \cdot 10^{-7}$	$6.3 \cdot 10^{-8}$
⋮	⋮	⋮
30	$8.7 \cdot 10^{-7}$	$8.7 \cdot 10^{-8}$
40	$1.6 \cdot 10^{-6}$	$1.2 \cdot 10^{-7}$
50	$2.6 \cdot 10^{-6}$	$1.3 \cdot 10^{-7}$
100	$7.6 \cdot 10^{-6}$	$1.1 \cdot 10^{-7}$

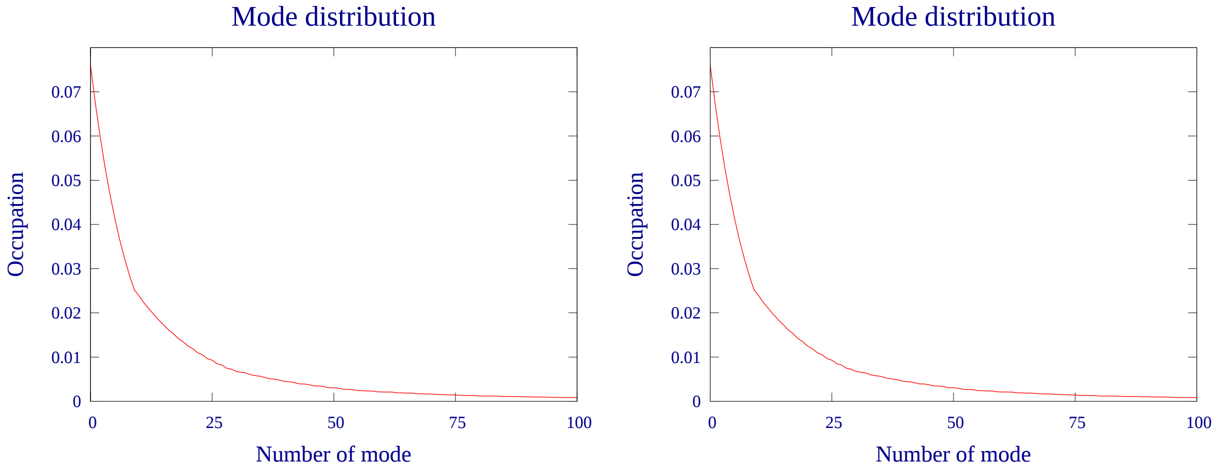

Table 4.6.: Relative errors of the eigenvalues and the coherent modes between the matrix and the two-step method for the ESRF-EBS lattice at a symmetry point and an ESRF u18 undulator of 2m length(left) or 4m length(right) and their mode distributions (bottom).

ESRF u18 2m:

# mode	$\delta\lambda$	δmode
1	$2.4 \cdot 10^{-8}$	$1.3 \cdot 10^{-7}$
2	$4.5 \cdot 10^{-8}$	$1.3 \cdot 10^{-7}$
3	$5.8 \cdot 10^{-8}$	$1.4 \cdot 10^{-7}$
4	$7.7 \cdot 10^{-8}$	$1.6 \cdot 10^{-7}$
5	$1.1 \cdot 10^{-7}$	$2.0 \cdot 10^{-7}$
6	$1.4 \cdot 10^{-7}$	$2.3 \cdot 10^{-7}$
7	$1.9 \cdot 10^{-7}$	$2.7 \cdot 10^{-7}$
8	$2.3 \cdot 10^{-7}$	$2.7 \cdot 10^{-7}$
9	$2.9 \cdot 10^{-7}$	$2.9 \cdot 10^{-7}$
10	$3.6 \cdot 10^{-7}$	$2.9 \cdot 10^{-7}$
11	$2.3 \cdot 10^{-7}$	$2.8 \cdot 10^{-7}$
12	$4.3 \cdot 10^{-7}$	$3.1 \cdot 10^{-7}$
13	$3.1 \cdot 10^{-7}$	$3.6 \cdot 10^{-7}$
14	$5.2 \cdot 10^{-7}$	$3.5 \cdot 10^{-7}$
15	$4.0 \cdot 10^{-7}$	$2.4 \cdot 10^{-7}$
16	$6.2 \cdot 10^{-7}$	$3.5 \cdot 10^{-7}$
17	$5.1 \cdot 10^{-7}$	$2.7 \cdot 10^{-7}$
18	$7.6 \cdot 10^{-7}$	$3.6 \cdot 10^{-7}$
19	$6.5 \cdot 10^{-7}$	$3.5 \cdot 10^{-7}$
20	$9.1 \cdot 10^{-7}$	$3.8 \cdot 10^{-7}$
⋮	⋮	⋮
30	$2.1 \cdot 10^{-6}$	$4.5 \cdot 10^{-7}$
40	$2.7 \cdot 10^{-6}$	$7.8 \cdot 10^{-7}$
50	$6.2 \cdot 10^{-6}$	$5.5 \cdot 10^{-7}$
100	$3.6 \cdot 10^{-5}$	$9.9 \cdot 10^{-7}$

ESRF u18 4m:

# mode	$\delta\lambda$	δmode
1	$1.4 \cdot 10^{-8}$	$4.1 \cdot 10^{-8}$
2	$2.0 \cdot 10^{-8}$	$4.8 \cdot 10^{-8}$
3	$2.8 \cdot 10^{-8}$	$7.1 \cdot 10^{-8}$
4	$3.6 \cdot 10^{-8}$	$5.0 \cdot 10^{-8}$
5	$4.4 \cdot 10^{-8}$	$4.9 \cdot 10^{-8}$
6	$5.4 \cdot 10^{-8}$	$5.0 \cdot 10^{-8}$
7	$6.8 \cdot 10^{-8}$	$5.4 \cdot 10^{-8}$
8	$8.4 \cdot 10^{-8}$	$6.2 \cdot 10^{-8}$
9	$1.1 \cdot 10^{-7}$	$6.8 \cdot 10^{-8}$
10	$1.3 \cdot 10^{-7}$	$7.0 \cdot 10^{-8}$
11	$1.7 \cdot 10^{-7}$	$7.8 \cdot 10^{-8}$
12	$1.3 \cdot 10^{-7}$	$7.2 \cdot 10^{-8}$
13	$2.0 \cdot 10^{-7}$	$7.9 \cdot 10^{-8}$
14	$2.1 \cdot 10^{-7}$	$1.6 \cdot 10^{-7}$
15	$2.5 \cdot 10^{-7}$	$8.1 \cdot 10^{-8}$
16	$2.4 \cdot 10^{-7}$	$8.1 \cdot 10^{-8}$
17	$3.0 \cdot 10^{-7}$	$9.1 \cdot 10^{-8}$
18	$2.8 \cdot 10^{-7}$	$7.5 \cdot 10^{-8}$
19	$3.6 \cdot 10^{-7}$	$8.4 \cdot 10^{-8}$
20	$3.3 \cdot 10^{-7}$	$7.5 \cdot 10^{-8}$
⋮	⋮	⋮
30	$8.4 \cdot 10^{-7}$	$1.1 \cdot 10^{-7}$
40	$1.4 \cdot 10^{-6}$	$1.3 \cdot 10^{-7}$
50	$2.3 \cdot 10^{-6}$	$1.4 \cdot 10^{-7}$
100	$9.9 \cdot 10^{-6}$	$2.0 \cdot 10^{-7}$

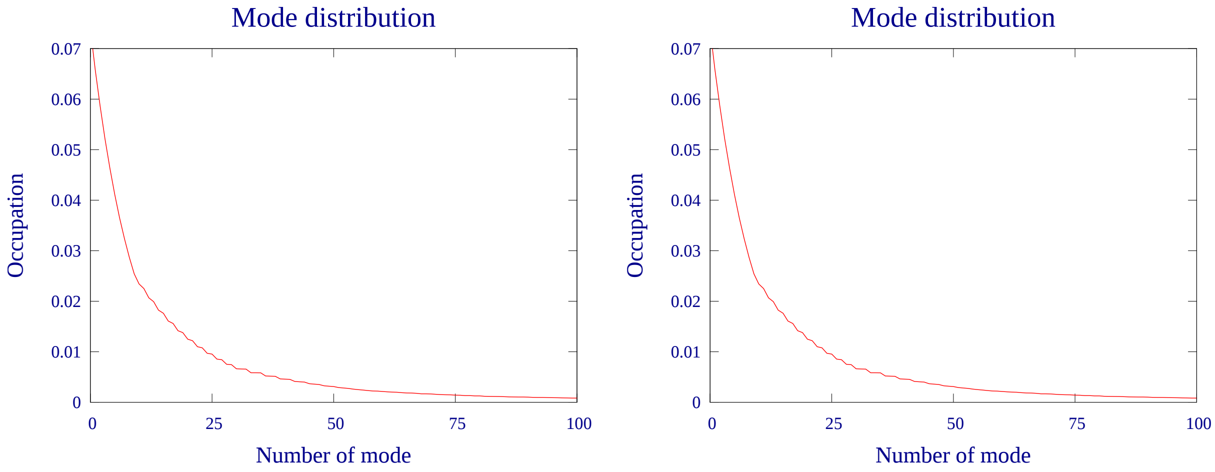

Table 4.7.: Relative errors of the eigenvalues and the coherent modes between the matrix and the two-step method for the ESRF-EBS lattice with finite alpha for the ESRF u18 undulator of 2m length(left) and 4m length(right) and their mode distributions (bottom).

4.6. Addition of energy spread

Until now the presented implementations only calculated the cross spectral density for the ideal electron energy. In reality the electron beam consists of electrons with different energies. This circumstance is called energy spread. If we calculate the cross spectral density at the resonance frequency of the ideal electron the electric field produced by the electrons with different energies will be off resonance but will still contribute. To account for this effect we have to sum the contributions of electrons with different energies weighted by their statistical appearance. Let $W_\gamma(\boldsymbol{r}_1, \boldsymbol{r}_2, \omega)$ be the cross spectral density for an electron energy γ. From Eq. 3.15 or from Eq. 3.50 combined with a linear substitution (see Eq. 2.7) we find the cross spectral density with energy spread:

$$W(\boldsymbol{r}_1, \boldsymbol{r}_2, \omega) = \int d\gamma \; \rho_\gamma(\gamma) W_\gamma(\boldsymbol{r}_1, \boldsymbol{r}_2, \omega) \tag{4.37}$$

where ρ_γ is the probability distribution that an electron has energy γ. In our implementation this integral is replaced by a sum:

$$W(\boldsymbol{r}_1, \boldsymbol{r}_2, \omega) \approx \sum_i h \; \rho_\gamma(\gamma_i) W_{\gamma_i}(\boldsymbol{r}_1, \boldsymbol{r}_2, \omega) \tag{4.38}$$

where h is the constant integration step width. The weight can be put into the initial electric field used in Eq. 3.50.

$$\widetilde{E_0}(\gamma_i) = \sqrt{\rho_\gamma(\gamma_i)} E_0(\gamma_i). \tag{4.39}$$

With this implementation the energy spread case is reduced to the sum of several weighted ordinary cases:

$$\boxed{W(\boldsymbol{r}_1, \boldsymbol{r}_2, \omega) \approx h \sum_i \widetilde{W_{\gamma_i}}(\boldsymbol{r}_1, \boldsymbol{r}_2, \omega).} \tag{4.40}$$

The algorithm samples energies over a range of three standard deviations of the energy spread σ_δ. The energy point sampling to discretize the integral is equidistant and the number of energy points used have to be configured in the configuration file of the calculation. We do not set a fixed value here.

For this implementation of the energy spread only minor adjustments to the algorithm are necessary. Extensive tests can be avoided because the energy spread calculation builds on the well tested algorithm for the calculation without energy spread. The matrix method that calculates the full representing matrix is basically unchanged because it works on the new full matrix, which just takes longer to calculate. The two-step method calculates the action of the total cross spectral density operator A_W (see Eq. 4.35) for all weighted fields directly. In both cases the effort for the calculations scales linearly with the number of energy integration points.

4.6.1. Tests of the eigendecomposition with energy spread

We have not developed an analytical test case for the energy spread calculations. But we may at least do consistency checks between the matrix method and the two-step method. If both methods agree implementation errors become less likely.

With both methods we performed calculations for ESRF-EBS lattice settings as defined in section 2.1.8 with energy spread at the symmetry point for the 2m and 4m long ESRF u18 undulators as defined in 2.3.4. The algorithm samples always over three standard deviations of the energy spread σ_δ and in these tests we used 61 energy sampling points.

The sampling factor $s = 2.5$ was again taken from convergence considerations presented in the application chapter 5. The relative errors of the eigenvalues and coherent modes are written in

Table. 4.8. For both undulators the relative error for the eigenvalues is at most $3.8 \cdot 10^{-5}$. The relative error for the modes is at most $2.2 \cdot 10^{-6}$. The relative error in operator norm is $2.2 \cdot 10^{-5}$ (2m) and $3.3 \cdot 10^{-6}$ (4m) for the first 300 modes. The first sixteen coherent modes of the ESRF u18 2m long undulator with ESRF-EBS lattice settings are depicted in Fig. 4.14 and Fig. 4.15. The purpose of this section is only to test the algorithm. The consequence of the variation of the energy spread will be discussed in chapter 5.

We conclude that both implementations are identical within numerical precision.

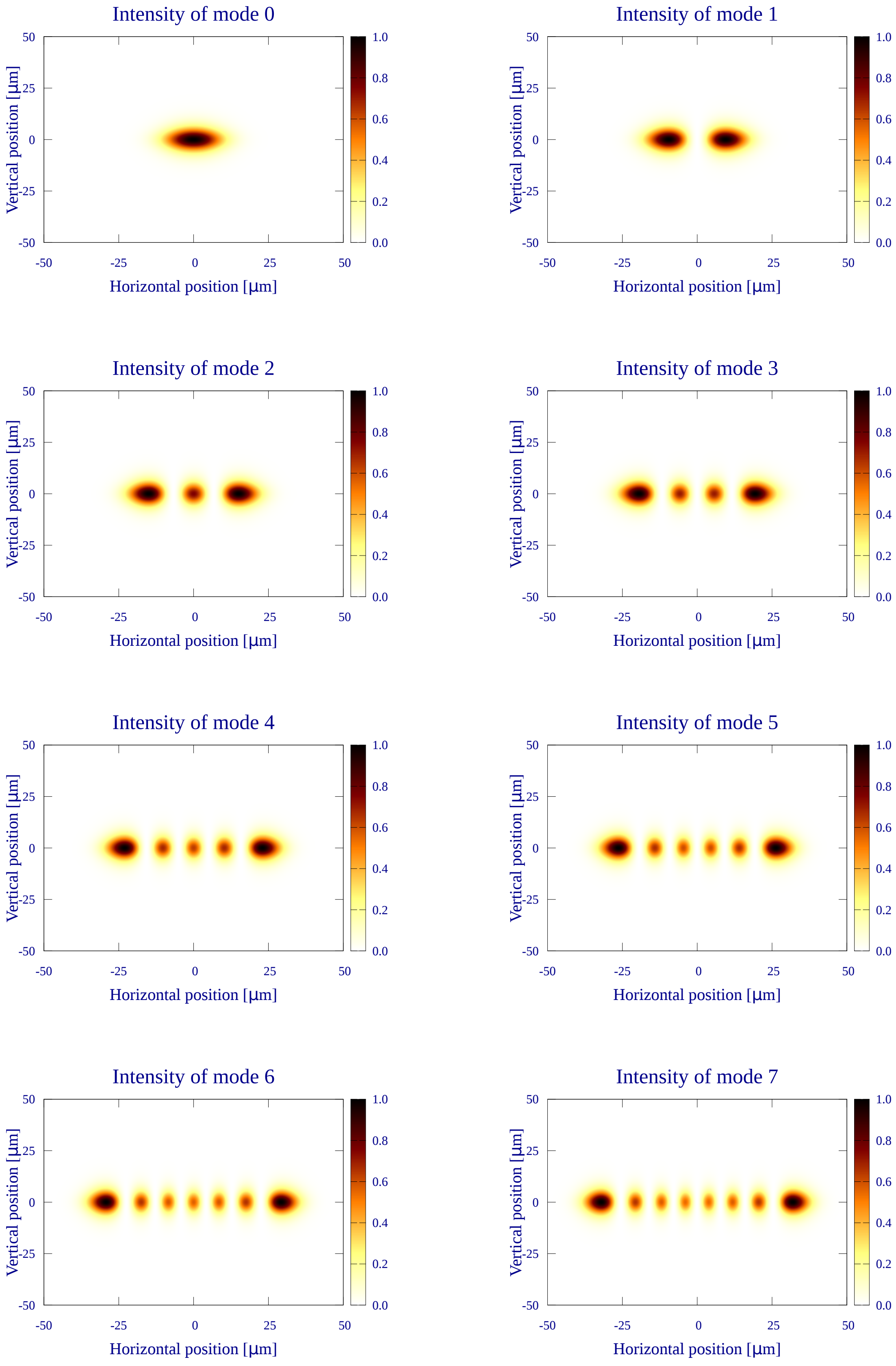

Figure 4.14.: The normalized intensities of the first eight coherent modes of the ESRF u18 2m long undulator with ESRF-EBS lattice settings at the symmetry point with energy spread.

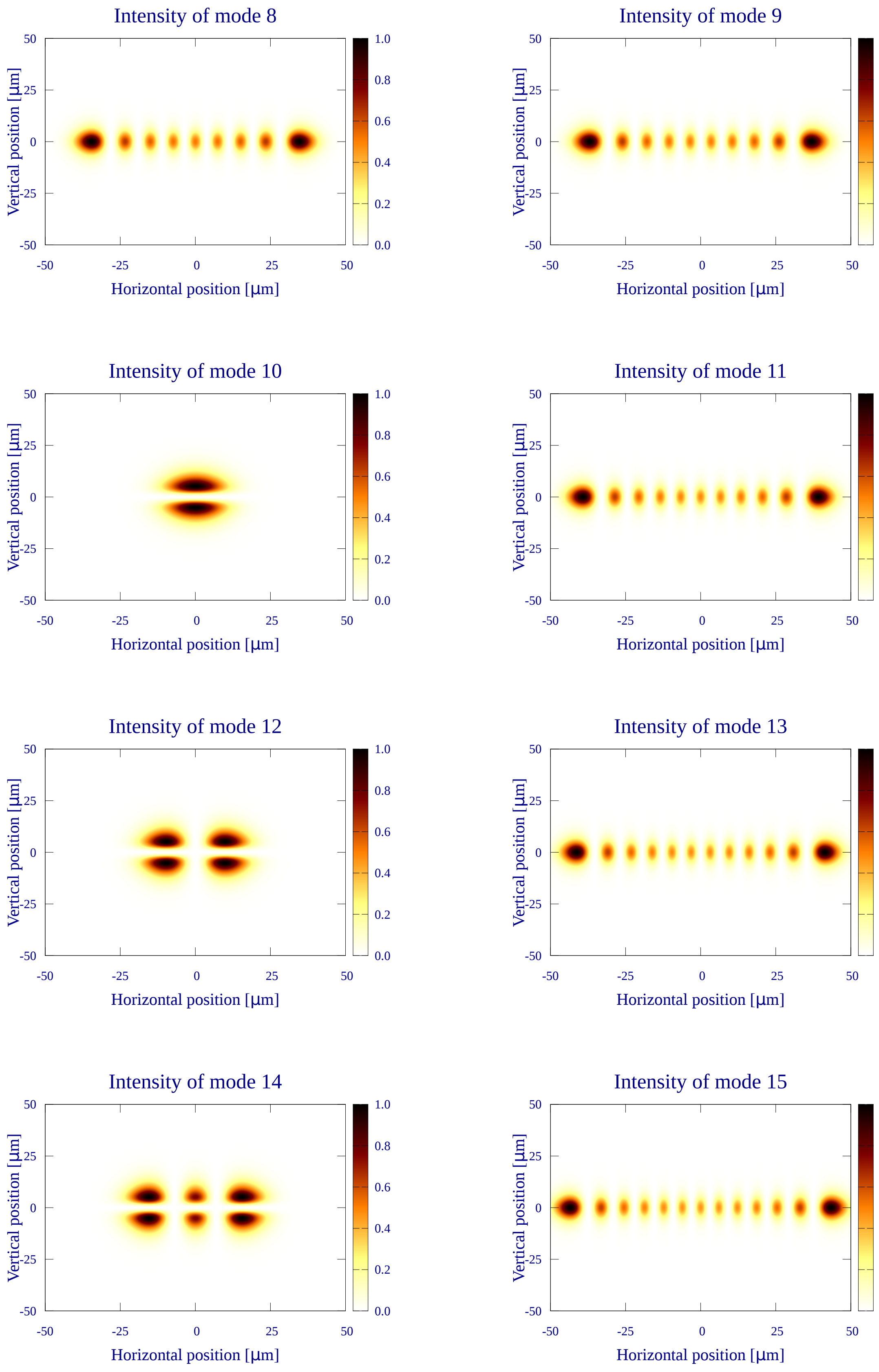

Figure 4.15.: Continuation of the normalized intensities of the coherent modes starting from the ninth mode for the ESRF u18 2m long undulator with ESRF-EBS lattice settings at the symmetry point with energy spread.

ESRF u18 2m:

# mode	$\delta\lambda$	δmode
1	$5.4 \cdot 10^{-9}$	$1.4 \cdot 10^{-7}$
2	$2.2 \cdot 10^{-9}$	$1.5 \cdot 10^{-7}$
3	$9.2 \cdot 10^{-9}$	$4.5 \cdot 10^{-7}$
4	$1.7 \cdot 10^{-8}$	$2.4 \cdot 10^{-7}$
5	$2.4 \cdot 10^{-8}$	$2.4 \cdot 10^{-7}$
6	$3.1 \cdot 10^{-8}$	$2.5 \cdot 10^{-7}$
7	$3.9 \cdot 10^{-8}$	$2.9 \cdot 10^{-7}$
8	$5.1 \cdot 10^{-8}$	$3.1 \cdot 10^{-7}$
9	$6.9 \cdot 10^{-8}$	$3.6 \cdot 10^{-7}$
10	$9.5 \cdot 10^{-8}$	$3.9 \cdot 10^{-7}$
11	$6.2 \cdot 10^{-8}$	$2.2 \cdot 10^{-7}$
12	$1.3 \cdot 10^{-7}$	$4.4 \cdot 10^{-7}$
13	$9.8 \cdot 10^{-8}$	$5.6 \cdot 10^{-7}$
14	$1.8 \cdot 10^{-7}$	$5.1 \cdot 10^{-7}$
15	$1.6 \cdot 10^{-7}$	$3.7 \cdot 10^{-7}$
16	$2.4 \cdot 10^{-7}$	$5.5 \cdot 10^{-7}$
17	$2.4 \cdot 10^{-7}$	$4.2 \cdot 10^{-7}$
18	$3.2 \cdot 10^{-7}$	$5.9 \cdot 10^{-7}$
19	$3.5 \cdot 10^{-7}$	$6.1 \cdot 10^{-7}$
20	$4.1 \cdot 10^{-7}$	$6.4 \cdot 10^{-7}$
$\vdots$	$\vdots$	$\vdots$
30	$2.6 \cdot 10^{-7}$	$3.0 \cdot 10^{-7}$
40	$3.1 \cdot 10^{-6}$	$1.2 \cdot 10^{-6}$
50	$3.0 \cdot 10^{-6}$	$9.8 \cdot 10^{-7}$
100	$3.8 \cdot 10^{-5}$	$2.2 \cdot 10^{-6}$

ESRF u18 4m:

# mode	$\delta\lambda$	δmode
1	$5.7 \cdot 10^{-9}$	$8.0 \cdot 10^{-8}$
2	$1.0 \cdot 10^{-8}$	$7.5 \cdot 10^{-8}$
3	$1.6 \cdot 10^{-8}$	$2.7 \cdot 10^{-7}$
4	$2.2 \cdot 10^{-8}$	$1.2 \cdot 10^{-7}$
5	$3.0 \cdot 10^{-8}$	$1.4 \cdot 10^{-7}$
6	$4.1 \cdot 10^{-8}$	$1.6 \cdot 10^{-7}$
7	$5.5 \cdot 10^{-8}$	$1.8 \cdot 10^{-7}$
8	$7.4 \cdot 10^{-8}$	$2.0 \cdot 10^{-7}$
9	$9.9 \cdot 10^{-8}$	$2.3 \cdot 10^{-7}$
10	$1.3 \cdot 10^{-7}$	$2.5 \cdot 10^{-7}$
11	$1.0 \cdot 10^{-7}$	$1.9 \cdot 10^{-7}$
12	$1.7 \cdot 10^{-7}$	$2.7 \cdot 10^{-7}$
13	$1.7 \cdot 10^{-7}$	$1.7 \cdot 10^{-7}$
14	$2.1 \cdot 10^{-7}$	$2.9 \cdot 10^{-7}$
15	$2.5 \cdot 10^{-7}$	$2.0 \cdot 10^{-7}$
16	$2.7 \cdot 10^{-7}$	$3.1 \cdot 10^{-7}$
17	$3.6 \cdot 10^{-7}$	$4.1 \cdot 10^{-7}$
18	$3.4 \cdot 10^{-7}$	$3.4 \cdot 10^{-7}$
19	$5.0 \cdot 10^{-7}$	$3.2 \cdot 10^{-7}$
20	$4.3 \cdot 10^{-7}$	$3.7 \cdot 10^{-7}$
$\vdots$	$\vdots$	$\vdots$
30	$1.0 \cdot 10^{-6}$	$4.8 \cdot 10^{-7}$
40	$2.4 \cdot 10^{-6}$	$4.7 \cdot 10^{-7}$
50	$2.9 \cdot 10^{-6}$	$3.4 \cdot 10^{-7}$
100	$2.7 \cdot 10^{-5}$	$9.3 \cdot 10^{-7}$

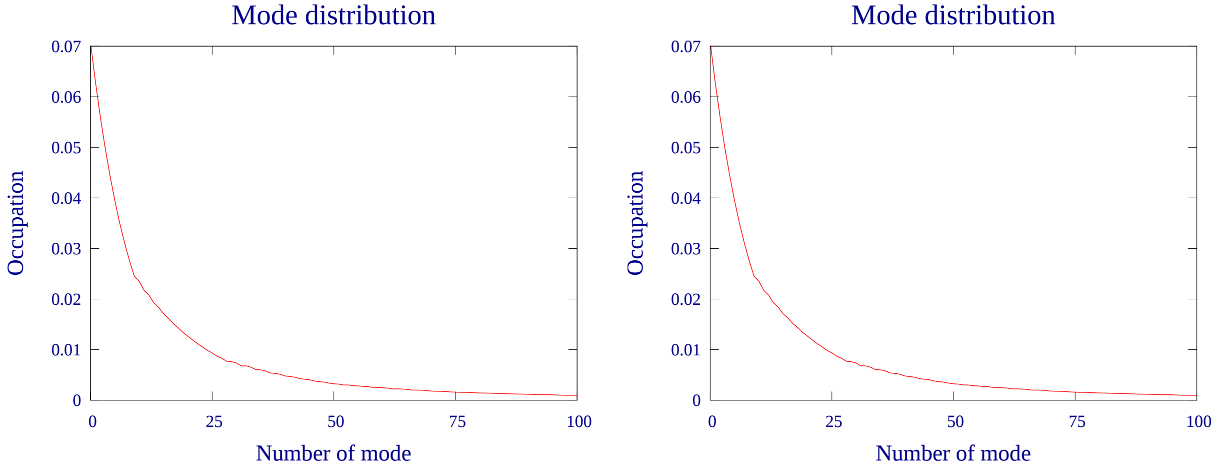

Table 4.8.: Relative errors for the eigenvalues and coherent modes between the matrix and the two-step method for the ESRF-EBS lattice with energy spread for an ESRF u18 undulator of 2m length(left) or 4m length(right).

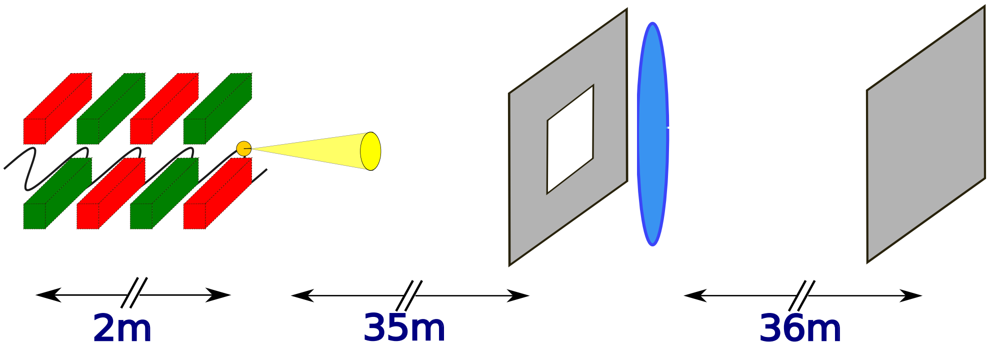

Figure 4.16.: Simple 1:1 imaging beamline of the undulator center with an ideal lens. The primary slit is widely opened. The vertical and horizontal focal lengths are 18m.

4.7. Comparison to SRW

We close this chapter with the demonstration of the propagation of the modes calculated with the two-step method. To simulate statistical phenomena, like partial coherence, SRW offers a multielectron calculation. The initial conditions of an electron entering the undulator are sampled according to a Gaussian electron phase space distribution. The emission of each electron is averaged. This method can calculate the spectral density or selected points of the cross spectral density. The full cross spectral density would be too big for practical usage of this method. One drawback of this method is, that like any other Monte Carlo method, one never knows when the result is finally converged. On the other hand memory consumption is rather low, parallelization over each electron is straightforward and unlike the brightness convolution theorem, no requirements to the undulator magnetic field are necessary.

Since our expertise in modelling beamlines with FFT based techniques is limited we opted for a simple beamline. For our comparison we choose the simple beamline depicted in Fig. 4.16.

The spectral density is once calculated from the propagated coherent modes and once calculated with the SRW multielectron sampling. For this spectral density comparison we used the 2m and 4m ESRF u18 undulators and the ESRF-EBS settings at the symmetry point, with finite alpha or with energy spread. Some comparisons are plotted in Fig. 4.17.

To compare the FWHM of the spectral densities a fit on a finer grid was made. We remark that the SRW multielectron method is a Monte Carlo approach and that small fluctuations around the exact value are therefore always possible. The FWHM of the vertical and horizontal cut coincide within the error range (see Table. 4.9). We choose the error range to be the step width of the grid of the SRW sampling. The SRW sampling were performed on coarser grids than the coherent mode decomposition and mode propagation. The reason for the reduced step width was the saving of computational resources. At least with the settings we used for SRW and since we wanted to have some certainty that the results were converged, the SRW calculations took already several days. If we had set the same grid settings for the SRW calculation we used for the decomposition we would have needed several weeks for the calculations. The grid sizes $(H \times V)$ of the wavefront at the final observation plane were of the order 180×60 for SRW and 1764×294 for the coherent modes.

The spectral degree of coherence for a horizontal and a vertical cut calculated from the propagated coherent modes and calculated by the SRW multielectron sampling is plotted in Fig. 4.18. If SRW performs a spectral degree of coherence calculation it creates either a vertical cut or a horizontal cut of the four-dimensional spectral degree of coherence. In a vertical cut the horizontal coordinates of $\boldsymbol{r}_1$ and $\boldsymbol{r}_2$ are fixed to zero and only the vertical coordinates are varied. This results in a two-dimensional set of values. In a horizontal cut the vertical coordinates of $\boldsymbol{r}_1$

ESRF u18 2m:

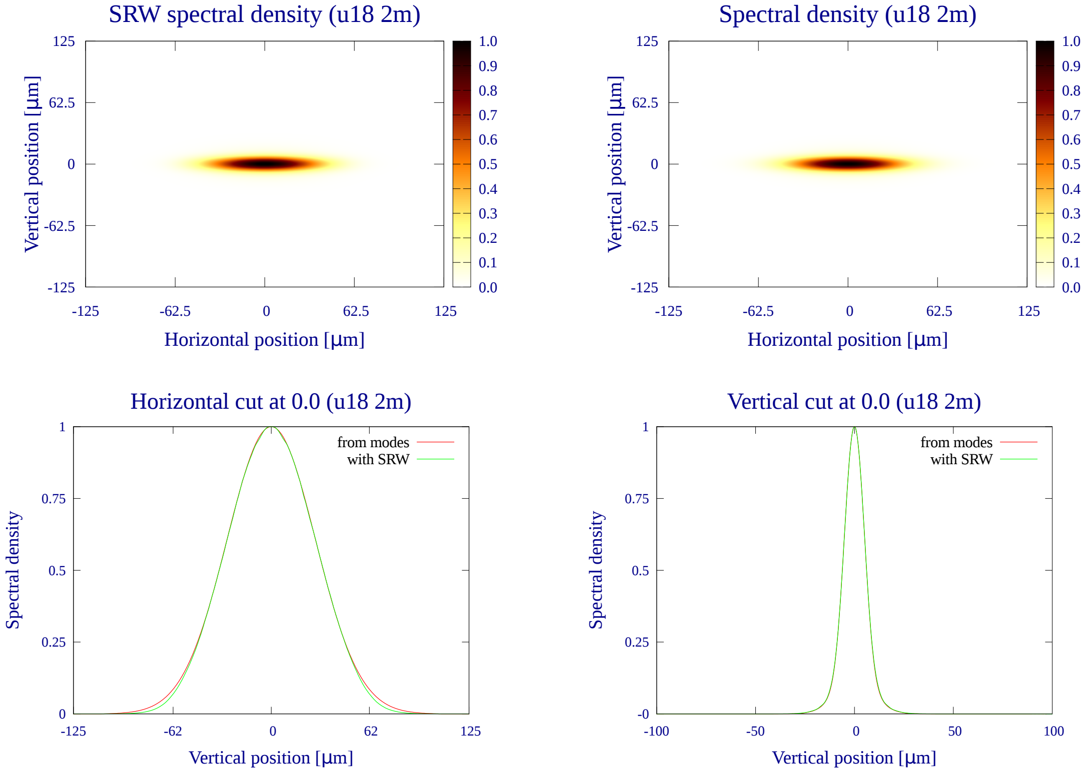

ESRF u18 4m:

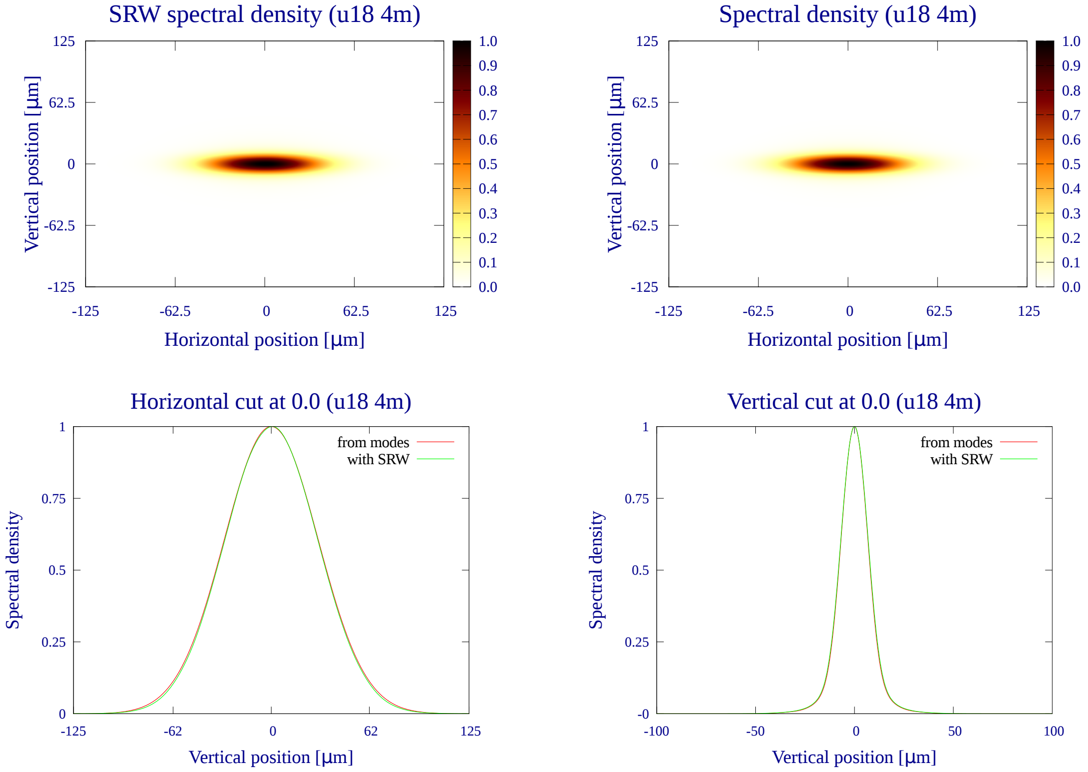

Figure 4.17.: Normalized spectral density from propagated modes (left) and from SRW multielectron sampling (right) at the image plane of the beamline Fig. 4.16 for ESRF-EBS settings at a symmetry point with the 2m (top) and the 4m (bottom) ESRF u18 undulator at the first harmonic.

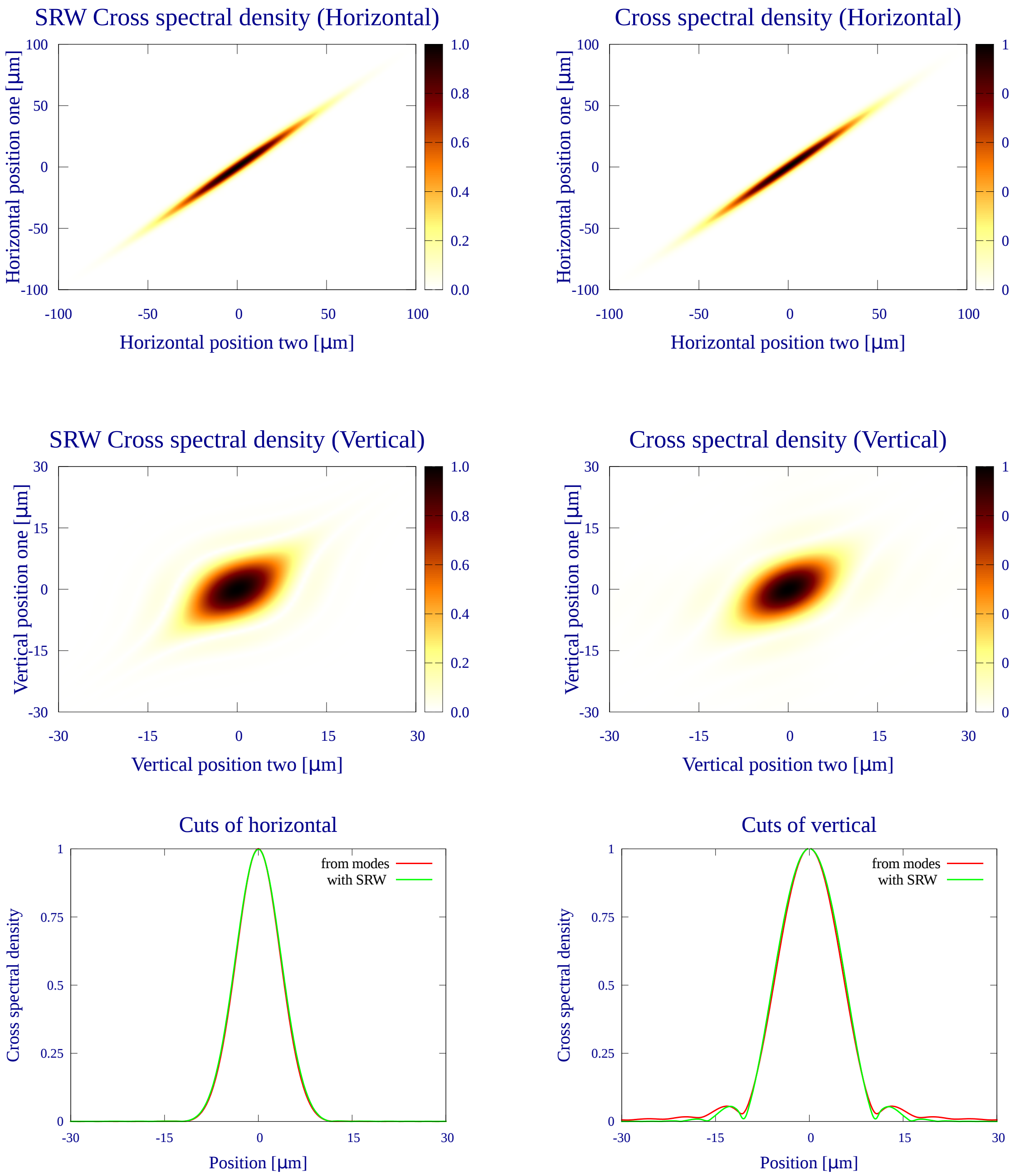

Figure 4.18.: Vertical and horizontal cuts of the normalized cross spectral density at the image plane of the beamline Fig. 4.16 with SRW Monte Carlo sampling(left) and from coherent modes(right) for ESRF-EBS settings and the 2m u18 ESRF undulator at the first harmonic.

Symmetry point:

	Vertical [μm]		Horizontal [μm]	
Undulator	from modes	SRW	from modes	SRW
2m	12.49 ± 0.6	12.49 ± 1.6	66.07 ± 0.6	65.94 ± 1.6
4m	16.13 ± 0.7	16.27 ± 2.2	69.72 ± 0.7	69.06 ± 2.2

Finite alpha:

	Vertical [μm]		Horizontal [μm]	
Undulator	from modes	SRW	from modes	SRW
2m	11.97 ± 0.7	11.97 ± 1.6	72.58 ± 0.7	72.45 ± 1.6
4m	15.62 ± 0.7	15.88 ± 1.7	74.40 ± 0.7	73.75 ± 2.2

Symmetry point with finite energy spread:

	Vertical [μm]		Horizontal [μm]	
Undulator	from modes	SRW	from modes	SRW
2m	12.23 ± 0.7	12.10 ± 2.2	66.07 ± 0.7	66.07 ± 1.5
4m	15.35 ± 0.7	15.62 ± 1.7	69.97 ± 0.7	69.06 ± 1.7

Table 4.9.: FWHM of the propagated spectral density for a simple beamline (Fig. 4.16) using coherent modes and SRW multielectron sampling with the 2m or 4m long ESRF u18 undulators with ESRF-EBS settings at a symmetry point, with finite alpha or at a symmetry point with energy spread.

and $\boldsymbol{r}_2$ are set to zero and only the horizontal coordinates are varied. In order to not introduce further possible sources of errors or an additional approximation we compare these cuts directly to the cuts of our cross spectral density in coherent mode representation. For this comparison the SRW multielectron calculation was performed with doubled resolution for several weeks. The horizontal cuts agree very well for the SRW method and the coherent mode decomposition. The vertical cuts agree essentially as well. Minor difference are though visible. The origin of the slight difference could be the underlying approximations of the brightness convolution theorem or statistical fluctuations of the SRW Monte Carlo based sampling.

4.8. Summary

In this chapter we present two algorithms for a numerical coherent mode decomposition of the cross spectral density for undulator storage ring emission. We restrict ourselves to the symmetry point and the finite alpha positions in the straight section defined in section 2.1.6. For the creation of the single electron emission and the propagation to the virtual source we use SRW.

We start with the *matrix method* that discretizes the cross spectral density operator A_W in a step function basis set (Eq. 4.4). We introduced the *sampling factor* as a measure for the density of numerical grid points in section 4.1.1.

The discretization is followed by an iterative diagonalization. We use SLEPc[46] for this purpose. The implementation of the algorithms is called *Coherent Modes for Synchrotron Light (comsyl)*. It is open source and available at [9]. A brief overview of the structure of the code is depicted in Fig. 4.4. The most important classes are mentioned in Table. 4.5. The implementations are parallel and performance optimized. This implies a rather high complexity of the implementations that had to be tested intensively. We present tests for a Dirac delta shaped electron beam and for a reference Gaussian wavefront, whose result can be calculated analytically. The agreement with the theoretical predictions is very good. Additionally we test in section 4.2.1 that the undulators we use in this thesis follow the fundamental relation of the brightness convolution theorem between the initial condition of the electron entering the undulator and the shift of its emission given by Eq. 3.3. In section 4.2.5 we discuss for the undulators used in this thesis if they change the electron beam phase space density at their center. We find that they introduce a constant spatial shift of the density at the undulator center. For our algorithm this has no consequences because we define the virtual source to lie always at the undulator entrance plane.

In section 4.3 we discuss that the propagation of the cross spectral density may change its spectrum and its coherent modes. With Eq. 4.27 we show how a cross spectral density that is represented in modes can be decomposed directly in terms of these modes, i.e. how to avoid the construction of the full representing matrix.

The drawback of the matrix method is that it requires a lot of memory and computational resources. It scales essentially with $N_x^2 N_y^2$ where N_x, N_y are the numbers of grid points in the x and y dimension, respectively. Typical sizes for N_x and N_y can easily reach a few hundred up to a few thousand. In the latter case the memory requirements would reach several thousand terabytes. To reduce the memory requirements of the matrix method we present the *two-step method* that first performs a coherent mode decomposition for a zero divergence electron beam and based on this decomposition performs a second decomposition that takes the divergence into account. The memory requirement for our undulator applications is drastically reduced to about $4N_xN_yN_m$ where N_m is the number of requested coherent modes. This allows the calculation of higher harmonics or higher emittance rings where $N_xN_y \gg N_m$. Just like the matrix method we test the two-step method for a delta shaped electron beam and a reference Gaussian wavefront. In section 4.6 we add the contributions from the electron beam energy spread.

Finally in section 4.7 we compare the decomposition to some results obtained by SRW multi-electron Monte Carlo sampling for the spectral density and for some selected points of the cross spectral density because SRW can neither calculate the full spectral density nor the mode spectrum or the coherent modes. All the tests show very good agreement given the fact that different methods and approximations are used for the calculations.

5. Applications

In this chapter we present some applications of the decomposition algorithm and a propagation of the cross spectral density.

First we discuss the influence of the undulator harmonic number and the undulator length on the number of coherent modes, coherence length and the required computational time. In this chapter we use the the notion of **coherence length** for the FWHM of the spectral degree of coherence μ where $\boldsymbol{r}_1$ is fixed at the origin and $\boldsymbol{r}_2$ is varied. This discussion may support design decisions whether a certain undulator is useful for a given beamline that exploits coherence. The discussion is accompanied with a detailed convergence test.

Afterwards we present a virtual experiment similar to the experiment performed in [4] for the current ESRF and the future ESRF-EBS lattice settings with an ESRF u18 undulator of 2m length.

Then the changes of the mode spectrum for a variation of energy spread settings, the effect of finite alpha and the effect of a scaling of all electron beam settings are presented. These kind of calculations are suitable to support storage ring design decisions.

As a final application we compare some exact numerical decompositions to other approximations: the *Gaussian Schell-model approximation*, a *separation approximation* and an *analytical approximation* proposed by Geloni *et al.*[8]. Similar or other approximations have been discussed in [59, 60, 61, 62]. These approximations are much faster than the coupled exact calculation and thus finding suitable approximation could be of great value for practical calculations.

The presented results are based on more than one thousand calculations to ensure convergence. Throughout this chapter only the two-step method is used for the numerical decomposition. The lattice settings are given in section 2.1.8 and the undulator settings are found in section 2.3.4.

5.1. Dependence of the mode spectrum on undulator length and number of harmonic

In this section we investigate the convergence for all the different undulators used in this thesis and at different harmonics as well as at some photon energies for maximum flux. As lattice we use the ESRF-EBS settings without energy spread. Energy spread is turned off to save computation time. The coherent mode decompositions are performed at the undulator entrance plane.

We converge the calculations by increasing the sampling factor s (see its definition in section 4.1.1). The total number of grid points scales quadratically with the sampling factor. The factor $s = 1$ refers to the sampling factor 1.0 of the SRW calculation of the single electron reference emission E_0. In chapter 4 we compared numerical coherent mode decompositions on the same numerical grid. Here during the convergence test an extra difficulty arises in the comparison of two calculations. The different sampling factors define different numerical grids. In order to calculate the error in the operator norm (see section 4.2.2) we interpolate the higher resolution to the coarser resolution and we compare these two calculations. This reduction may introduce an extra error and the so obtained error in operator norm may be overestimated. Our discussion focuses therefore on the trend of convergence with increasing sampling factor rather than its quantitative value. One consequence is however strictly deducible: if the error in operator norm is small then in any case the two calculations are close.

The plots in Fig. 5.1(left) show the general convergence trend in operator norm. We plot the mean of the relative error of the first 150 eigenvalues $\overline{\delta\lambda} = (1/150)\sum_{n=0}^{149} \delta\lambda_n$ in Fig. 5.1(right) as well. The eigenvalues converge very fast. Basically $s = 1.0$ is already sufficient. For the operator norm and the first harmonic there is a jump between the sampling factor 1.0 and 1.5 but overall the relative error of less than $1.5 \cdot 10^{-4}$ is very small. For the third harmonic the jump is between 1.5 and 2.0 and for the fifth it is between 1.0 and 1.2. In general *higher harmonics are more difficult to converge*.

A larger number of coherent modes is needed for incorporating 95% of the spectral density for shorter undulator and for higher harmonics. The mode spectrum broadens with decreasing undulator length and increasing harmonic number (see Table. 5.1). In this sample the lowest number of modes for taking 95% of the spectral density into accounting is 131 for the first harmonic of the 4m undulator and the largest number is about 5000 for the fifth harmonic of the 1m undulator. It looks like the smaller cone of the single electron emission leads to an increase of the number of coherent modes. It could be that in the case where all the information of the single electron emission are encoded on a smaller length scale fluctuations of the electron beam that were negligible for a larger single electron emission cone become more significant. This could in consequence lead to a degradation of coherence.

With L being the undulator length and $\lambda\!\!\!^{-} = \lambda/2\pi$ being the reduced wavelength Geloni *et al.*[8] define at the middle of the undulator $\sqrt{\lambda\!\!\!^{-}/L}$ as the radiation diffraction angle and $\sqrt{\lambda\!\!\!^{-} L}$ as the radiation diffraction size. The characteristic transverse range in the far field is then given in units of the radiation diffraction angle. Likewise the characteristic transverse range at the virtual source placed at the *middle* of the undulator is given in units of the radiation diffraction size (see also [23, 52] for similar definitions). Furthermore Geloni *et al.* express the characteristic scales of the electron beam size and divergence in these units:

$$\begin{aligned} N_i &= \frac{\sigma_i^2}{\lambda\!\!\!^{-} L} \\ D_i &= \frac{\sigma_{i'}^2}{\lambda\!\!\!^{-}/L} \end{aligned} \tag{5.1}$$

where $i \in \{x, y\}$. Large values of N_i and D_i imply that the electron beam properties dominate

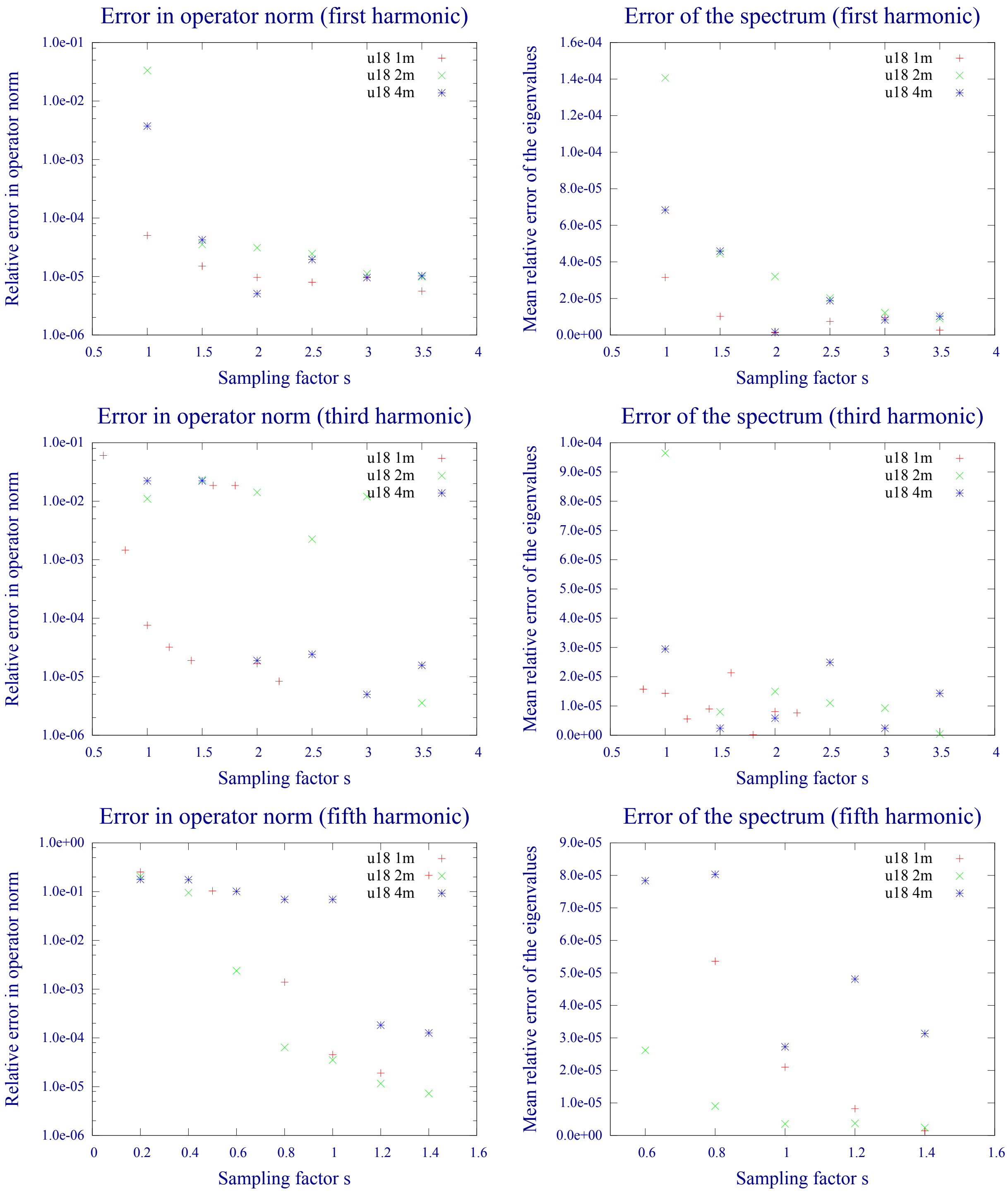

Figure 5.1.: Behavior of the operator error norm (left) and the mean relative error of the first 150 eigenvalues (right) for harmonics 1, 3, 5 for the ESRF u18 undulators (1m, 2m, 4m) at ESRF-EBS lattice settings.

Number of modes:

Undulator	1.harmonic	3.harmonic	5.harmonic	1.flux max	3.flux max
1m	260	2406	5080	228	1845
2m	154	490	1550	193	605
4m	141	461	908	260	729

FWHM horizontal spectral degree of coherence in μm:

Undulator	1.harmonic	3.harmonic	5.harmonic	1.flux max	3.flux max
1m	6.5	3.0	2.0	5.3	2.7
2m	7.8	3.3	2.1	5.1	2.7
4m	9.0	3.5	2.1	5.0	2.7

FWHM vertical spectral degree of coherence in μm:

Undulator	1.harmonic	3.harmonic	5.harmonic	1.flux max	3.flux max
1m	11.1	5.1	3.6	8.4	4.1
2m	21.0	7.2	4.8	11.0	4.8
4m	30.0	9.5	6.0	11.0	5.3

Table 5.1.: Number of modes to cover 95% of the spectral denisty and horizontal and vertical FWHM of the spectral degree of coherence.

over the single electron emission. On the contrary small values of N_i and D_i indicate that single electron emission features become more dominant. In Table. 5.2 the D and N numbers for the used undulators and photon energies at ESRF-EBS settings are listed. The numbers increase with increasing photon energy, i.e. electron beam properties become more dominant.

We can also see from Table. 5.1 that at the resonances a higher number of coherent modes is accompanied with a decrease of the coherence length. Moreover for the 2m and 4m long undulator at photon energies of the first and third flux maximum the number of coherent modes is higher than for the associated resonant case and accordingly the coherence lengths are reduced. Surprisingly, for the 1m undulator the number of coherent modes is smaller for the energies of the flux maxima than for the resonance cases while the coherence length is still smaller than in the resonant case.

Depending on the undulator length and the photon energy the FWHM of the spectral density of our calculations are between $64 - 74\mu m$ in the horizontal direction and between $10 - 22\mu m$ in the vertical direction. We can conclude from Table. 5.1 that at least for the first harmonic the undulator emission is not quasi-homogeneous because the spectral density varies in both directions over the coherence length. Consequently the requirements of the (generalized) van Cittert-Zernike theorem[15, 42] are not fulfilled and the theorem can not be used to describe the cross spectral density in the limit we are mainly interested in, i.e. the limit of rather high coherence. For higher photon energies the coherence lengths decrease while the spectral density stays rather constant and possibly for high enough photon energies the emission becomes quasi-homogeneous but coherence properties will be poor for these energies.

The convergence of the 1m long undulator was practically more difficult than the convergence of 2m or 4m long undulators. Because of the large number of involved coherent modes the calculations were rather long (several days). And if the settings were not sufficiently tight the calculations had to be remade. A method to estimate a priori the needed number of coherent modes has not yet been developed. It can therefore take some tries to find good initial settings

		N		D	
Undulator	Energy	Horizontal	Vertical	Horizontal	Vertical
1m	E_{0max}	$3.0 \cdot 10^1$	$4.7 \cdot 10^{-1}$	$1.1 \cdot 10^0$	$7.8 \cdot 10^{-2}$
	E_0	$3.0 \cdot 10^1$	$4.7 \cdot 10^{-1}$	$1.1 \cdot 10^0$	$7.8 \cdot 10^{-2}$
	E_{2max}	$9.0 \cdot 10^1$	$1.4 \cdot 10^0$	$3.2 \cdot 10^0$	$2.3 \cdot 10^{-1}$
	E_2	$9.1 \cdot 10^1$	$1.4 \cdot 10^0$	$3.2 \cdot 10^0$	$2.4 \cdot 10^{-1}$
	E_4	$1.5 \cdot 10^2$	$2.4 \cdot 10^0$	$5.4 \cdot 10^0$	$3.9 \cdot 10^{-1}$
2m	E_{0max}	$1.5 \cdot 10^1$	$2.3 \cdot 10^{-1}$	$2.2 \cdot 10^0$	$1.6 \cdot 10^{-1}$
	E_0	$1.5 \cdot 10^1$	$2.3 \cdot 10^{-1}$	$2.2 \cdot 10^0$	$1.6 \cdot 10^{-1}$
	E_{2max}	$4.5 \cdot 10^1$	$7.0 \cdot 10^{-1}$	$6.5 \cdot 10^0$	$4.7 \cdot 10^{-1}$
	E_2	$4.5 \cdot 10^1$	$7.0 \cdot 10^{-1}$	$6.6 \cdot 10^0$	$4.8 \cdot 10^{-1}$
	E_4	$7.5 \cdot 10^1$	$1.2 \cdot 10^0$	$1.1 \cdot 10^1$	$7.9 \cdot 10^{-1}$
4m	E_{0max}	$7.4 \cdot 10^0$	$1.2 \cdot 10^{-1}$	$4.3 \cdot 10^0$	$3.1 \cdot 10^{-1}$
	E_0	$7.5 \cdot 10^0$	$1.2 \cdot 10^{-1}$	$4.4 \cdot 10^0$	$3.2 \cdot 10^{-1}$
	E_{2max}	$2.2 \cdot 10^1$	$3.5 \cdot 10^{-1}$	$1.3 \cdot 10^1$	$9.5 \cdot 10^{-1}$
	E_2	$2.2 \cdot 10^1$	$3.5 \cdot 10^{-1}$	$1.3 \cdot 10^1$	$9.5 \cdot 10^{-1}$
	E_4	$3.7 \cdot 10^1$	$5.9 \cdot 10^{-1}$	$2.2 \cdot 10^1$	$1.6 \cdot 10^0$

Table 5.2.: N and D numbers (see Eq. 5.1) for the used undulators and photon energies at ESRF-EBS lattice settings.

which then have to be converged by increasing the sampling factor s. The modes of the spatial cross spectral density of the first step of the two-step method was targeted to cover more than 99.5% of the spatial spectral density. With a fixed mode number the coverage of the spatial cross spectral density decreased slightly while the sampling factor s was increased. For the higher harmonics of the 1m long undulator and the highest used sampling factor the coverage is more about 99.0% of the spatial spectral density. Furthermore, for the higher harmonic cases of the 1m long undulator that result in a larger number of coherent modes, the number of modes to incorporate 95% of the spectral density is more sensitive to the sampling factor than for the cases with fewer coherent modes. This is due to the fact that the mode spectra have an exponential shape. Additionally, for the cases of a large number of coherent modes the coverage of the spatial spectral density in the first step of the two-step method becomes more important for the final number of coherent modes to incorporate 95% of the spectral density due to propagation of error. On the other side the coherence length should not be affected strongly by the tails of the mode spectra of the spatial cross spectral density or the tails of the mode spectra of the cross spectral density because their contributions to the spectral degree of coherence μ are small.

It is also interesting to see the calculation times for the different undulators and harmonics Table. 5.3. We see the same relation as for the number of coherent modes. Shorter undulators and higher harmonics need more computational time. This is explained by the increasing number of needed modes. The shortest calculation took 13 CPU hours and the longest took 9888 CPU hours.

Undulator	1.harmonic	3.harmonic	5.harmonic	1.flux max	3.flux max
1m	367	2688	9888	228	2649
2m	38	85	2550	13	42
4m	41	91	330	13	49

Table 5.3.: Calculation times in CPU core hours to produce the spectra for Table. 5.1.

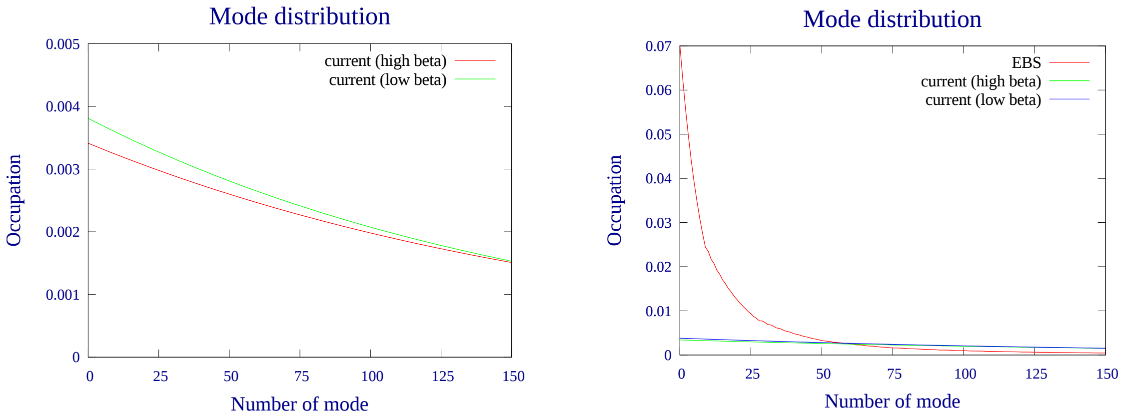

Figure 5.2.: Mode distribution for the 2m ESRF u18 undulator at its first harmonic for ESRF-EBS and current ESRF lattice parameters at the undulator entrance plane.

5.2. Comparison of the current lattice and the ESRF-EBS lattice

In this section we compare the current lattice to the future ESRF-EBS lattice. The calculations for the current lattice are rather expensive because the emittance of the current lattice is orders of magnitude larger than for the new lattice (see section 2.1.7). This requires a larger grid. The scaling is essentially linear with the grid size. A single calculation for the current lattice (both low and high beta) takes about 2 days on 4 nodes of the ESRF oar cluster. We restrict our discussion therefore to one case only: the ESRF u18 2m undulator at its first harmonic. We discuss simulations at the virtual source, i.e. the undulator entrance plane, and after propagation through a 1:1 imaging beamline consisting of an ideal lens followed by an aperture that is varied in size (see Fig. 4.11).

Lattice	N_x	N_y	D_x	D_y
ESRF-EBS	$1.5 \cdot 10^1$	$2.3 \cdot 10^{-1}$	2.2	$1.6 \cdot 10^{-1}$
High beta	$3.0 \cdot 10^3$	$2.5 \cdot 10^{-1}$	8.6	$1.2 \cdot 10^{-1}$
Low beta	$2.8 \cdot 10^1$	$2.5 \cdot 10^{-1}$	$9.2 \cdot 10^2$	$1.2 \cdot 10^{-1}$

Table 5.4.: N and D numbers (see Eq. 5.1) for the used lattice settings and the 2m long u18 undulator at the first harmonic.

5.2.1. At the virtual entrance plane

Lattice	Number of modes
EBS	165
high beta	3164
low beta	2724

Table 5.5.: Number of modes to cover 95% of the spectral density.

With the virtual source positioned at the entrance plane of the undulator we find the mode spectra of Fig. 5.2. In Table. 5.5 the number of coherent modes necessary to cover 95% of the spectral density is listed. We see that the new lattice needs 15 times less modes than the

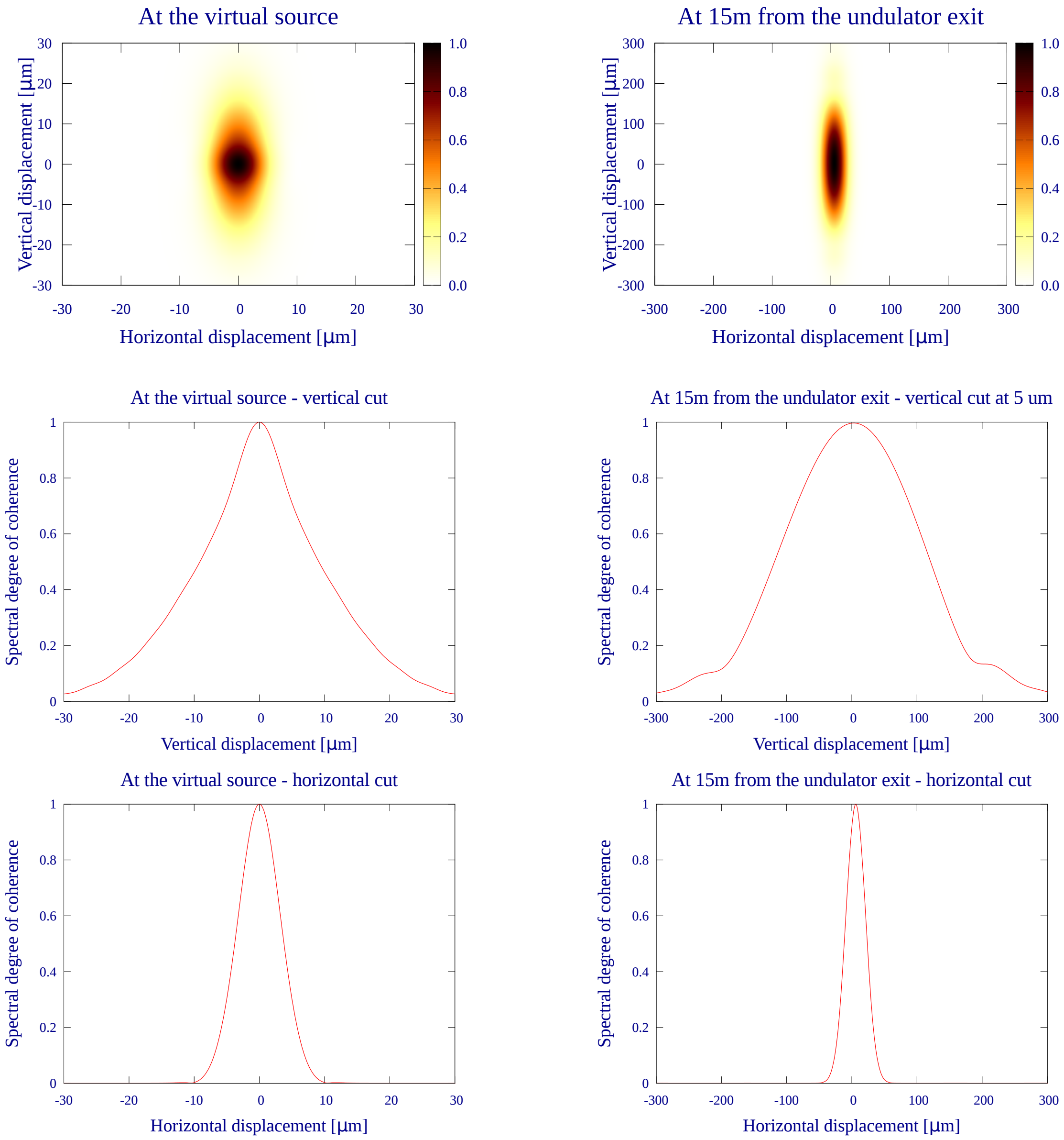

At the virtual source

At 15m from the undulator exit

At the virtual source - vertical cut

At 15m from the undulator exit - vertical cut at 5 um

At the virtual source - horizontal cut

At 15m from the undulator exit - horizontal cut

Figure 5.3.: Change of the spectral degree of coherence and the increase of the coherence length (FWHM of the vertical and horizontal cuts) due to propagation in free space from the undulator entrance(left) to 15m from the undulator exit(right). Note the change of scale.

current lattice. We expect these numbers to be undulator and photon energy dependent. For the high beta case the occupation of the first mode d_0 is $3.8 \cdot 10^{-3}$, for low beta it is slightly lower: $3.4 \cdot 10^{-3}$ and for the ESRF-EBS settings it is an order of magnitude larger: $7.0 \cdot 10^{-2}$. The number of numerical grid points of these calculations at the virtual source in the horizontal and vertical direction are: 3651×145 (high beta), 1367×597 (low beta) and 491×327 (ESRF-EBS). As already mentioned, all the calculations were performed with the two-step method. To do the same calculations with the matrix method one would need 4 terabytes of RAM just for the representing matrix plus all the memory that is needed by the eigensolver and the coherent modes. The two-step method on the other hand used in total only about 150 gigabytes.

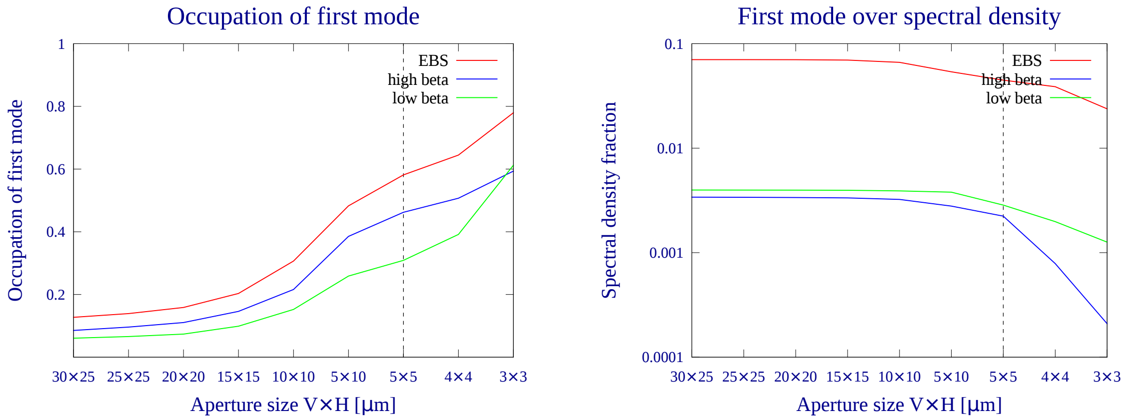

Figure 5.4.: Occupation (left) and spectral density fraction(right) of the first mode for a given slit size (VxH in μm) after additional 2m propagation. The fraction is calculated with respect to the spectral density at the undulator virtual source. Values for slit sizes smaller than 5×5 should be viewed with care.

5.2.2. Propagation and rediagonalization

With the 1:1 imaging beamline (see Fig. 4.11) we image the center of the 2m long u18 undulator for the first harmonic with ESRF-EBS lattice settings and with the current high beta and low beta lattice settings. The primary slit is opened widely and should basically accept all the radiation.

Let us first see how the coherence length changes by free space propagation. At 15 meters from the undulator exit, i.e. before the primary slit, the change of the spectral degree of coherence by free space propagation is depicted in Fig. 5.3. The coherence length at the undulator entrance plane and at 15 m, 20 m and 25 m distance measured from the undulator exit are listed in Table. 5.6. The changes of the coherence length from 15m to 25m appear to be linearly related.

Position	Horizontal [μm]	Vertical [μm]
Source	7.5	18.0
15m	36.0	240.0
20m	46.0	316.0
25m	56.0	390.0

Table 5.6.: Change of the coherence length due to free space propagation. Listed are the lengths at the virtual source and at 15m, 20m and 25m measured from the undulator exit.

Let us now come to the end of the beamline. The final slit of the beamline in Fig. 4.11 is placed close to the lens focus and is varied in size. It is followed by another short free space propagation that is the final position of the beamline. At this position we perform another coherent mode decomposition. We see that the spectral density at this position concentrates into fewer modes, i.e. the first mode occupation increases (Fig. 5.4 left).

However, with this concentration into fewer modes the intensity of the first mode, i.e. its eigenvalue, is reduced. This is seen from Fig. 5.4(right) where the ratio of the first mode intensity to the spectral density at the virtual source is depicted. We trade statistical purity or coherence for spectral density. The ESRF-EBS lattice performs best. It has the largest first mode occupation and the largest fraction of the first mode intensity ot the spectral density at the virtual source. The high beta lattice has a larger occupation of the first mode than the low beta lattice but a smaller fraction of the spectral density in its first mode. This is probably due to the fact that

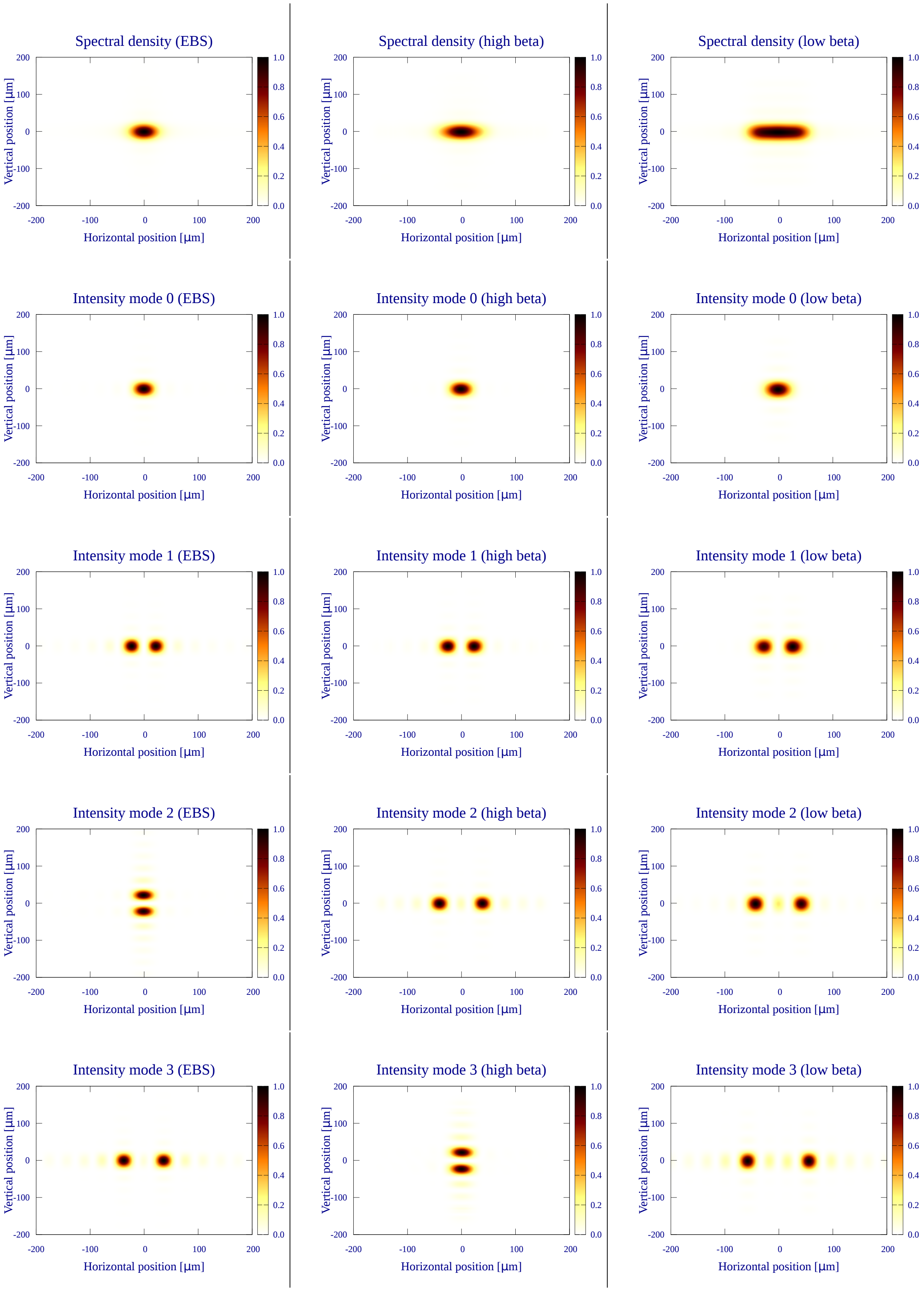

Figure 5.5.: Normalized spectral density(top) and the first four coherent modes propagated by 2m after a $5\mu m \times 5\mu m$ sized final slit for ESRF-EBS(left column), ESRF high beta (center column) and ESRF low beta (right column) lattice settings.

the final aperture cuts more of the emission in the high beta case than in the low beta case.

A technical limitation arises for slits smaller than $5\mu m \times 5\mu m$ and their results should be considered with care. For slit sizes smaller than $5\mu m \times 5\mu m$ the resulting modes can no longer be propagated with SRW because we have too few grid points left. Theoretically one could redo the calculation with a finer resolution but the propagation of the modes through the beamline becomes impossible. SRW is not parallelized over a single wavefront propagation and at some positions in the beamline our modes are in this resolution already at the edge of the currently possible because of single CPU memory limitation (about 10gb). This is in particular true for higher order coherent modes that have large spatial extend. One could think of interpolating the propagated modes in the final slit but this would need a lot of careful studies of the probable form of the mode in the slit and we did not follow this route to avoid biased results.

In Fig. 5.5 we show the propagated modes after the slits, i.e. at the final position of the beamline.

5.3. Effects of the energy spread on the mode spectrum

In this section we are interested in the consequences of the energy spread on the width of the mode spectrum. We use ESRF-EBS lattice settings and the usual ESRF u18 undulator of 1, 2 or 4 meter lengths at their first harmonic.

The ESRF-EBS energy spread is varied according to:

$$(\sigma_\delta)' = \sigma_\delta \cdot s \tag{5.2}$$

with

$$s \in \{0.0, 0.2, 0.4, \ldots, 1.0, \ldots, 1.8, 2.0\} \tag{5.3}$$

whereas the transverse beam parameters are kept fixed. The energy integration was performed with 27 points.

We observe that the total number of coherent modes to incorporate 95% of the spectral density as well as the occupation of the first mode d_0 for the 1m long undulator is barely changed whereas for the 4m long undulator there are relatively large changes. The mode occupation varies barely for the 1m long undulator and becomes slightly less compact with increasing energy spread for the 4m long undulator (see Fig. 5.6).

Length 4m:

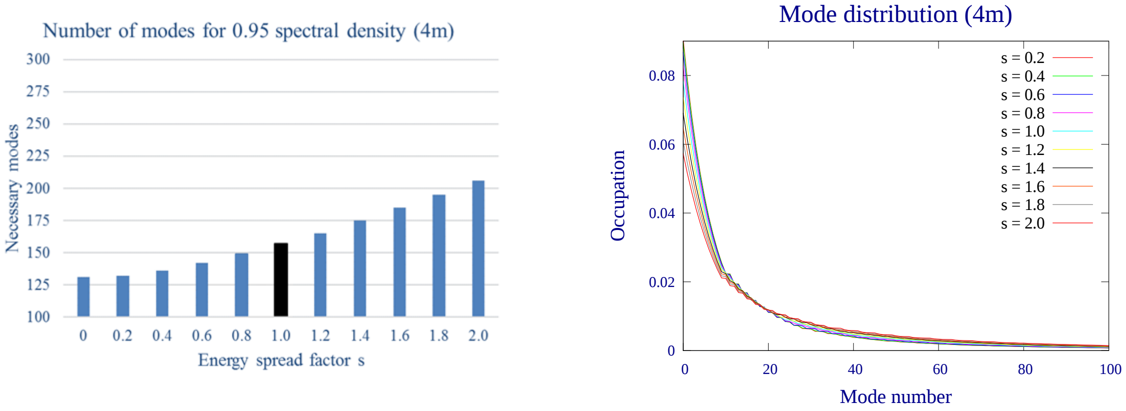

Length 2m:

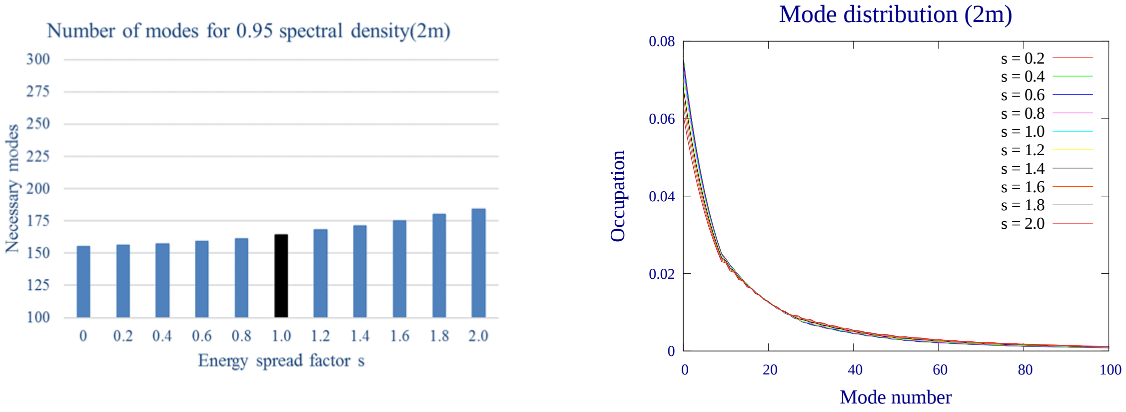

Length 1m:

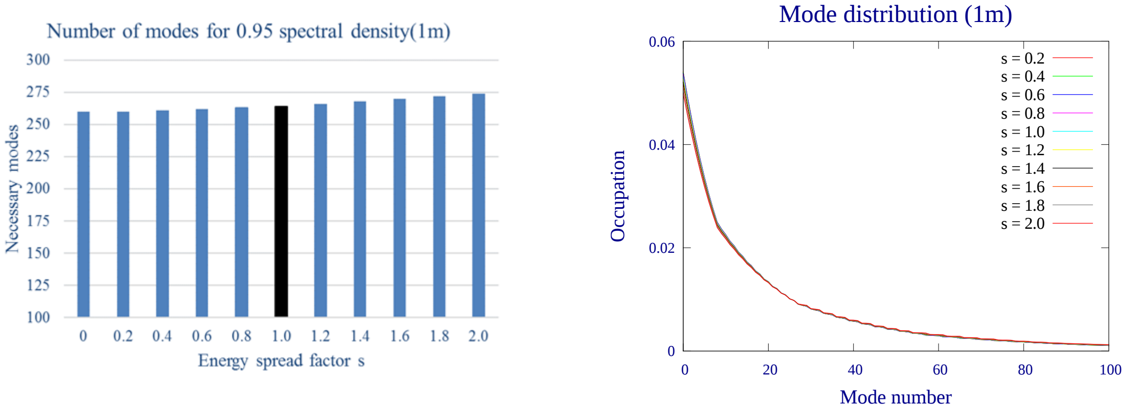

Figure 5.6.: Number of modes for 95% of the spectral density(left) and mode distribution(right) for a linear variation of the energy spread with ESRF u18 undulators (1m, 2m, 4m) and ESRF-EBS lattice settings($s = 1.0$).

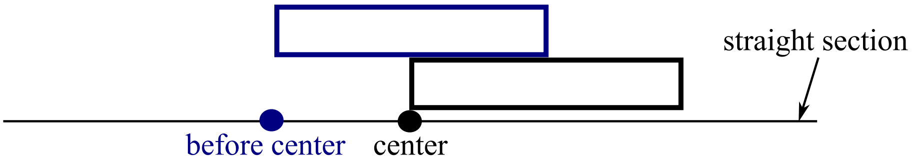

Figure 5.7.: Illustration of the different placements of the undulators in the straight section. One undulator is placed with its entrance at the center (black) and the other is placed with its entrance at a position with finite alpha (blue).

5.4. Consequences of finite alpha on the mode distribution

In this section we compare an ESRF u18 2m long undulator with its entrance placed at different positions in the storage ring. We use the ESRF-EBS lattice settings. One calculation is performed with the entrance of the undulator at the symmetry point and one calculation is performed with the entrance of the undulator 1m before the symmetry point (see Fig. 5.7).

We find that the total number of coherent modes to incorporate 95% of the spectral density and the coherence lengths are barely changed Table. 5.7. This is also true for the shape of the spectra Fig. 5.8 at the virtual source and after a propagation through the ideal one to one imaging beamline Fig. 4.16.

Undulator entrance at	Number modes	Coherence length [μm]	
		Horizontal	Vertical
symmetry point	154	7.8	20.6
1m before symmetry point	163	8.6	21.3

Table 5.7.: Comparison of the number of coherent modes to incorporate 95% of the spectral density for ESRF-EBS lattice settings with an ESRF u18 undulator of 2m length.

We discuss only the 2m long undulator because finite alpha calculations are about 10 times slower than those performed at the symmetry point. The reason for the increase of calculation time is that convolutions can no longer be used for the calculation of the coherent modes.

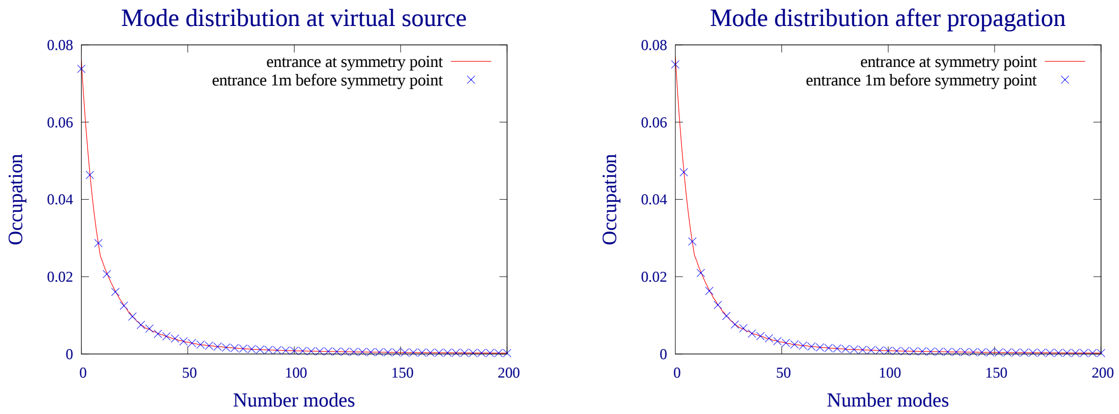

Figure 5.8.: Comparison of the mode spectrum for the ESRF u18 2m long undulator with entrance slits placed at waist and 1m before the waist at the virtual source(left) and after propagation through the beamline Fig. 4.11 (right).

5.5. Variation of electron beam parameters

In this section we investigate the influence of the variation of the electron beam parameters on the coherent mode spectrum. For this we use again the first harmonic of the ESRF u18 2m long undulator. Starting from the transverse electron beam settings and roughly[1] the energy spread of the new ESRF-EBS lattice we multiply each of these parameters by a scalar proportional to M with $0.1 < M < 28$. More precisely we use the electron beam settings $(\sigma_i)'$ with:

$$\text{for } i \in \{x, x', y, y', \delta\} : (\sigma_i)' = \frac{M}{20}\sigma_i. \tag{5.4}$$

That means that the parameters are changed homogeneously by $M/20$. In particular $M = 20$ corresponds transverse to the ESRF-EBS settings and the energy spread is its initial value $\sigma_\delta = 0.89 \cdot 10^{-3}$. The choice of parameters was based on the idea to find the onset from a single mode to several modes. Additionally, we performed a similar variation were we followed basically the same schema but kept the energy spread σ_δ constant and varied only the transverse beam settings. The energy integration was performed with 27 points. The results for both variations are illustrated in Fig. 5.9.

One can see from these simulations that a homogeneous reduction by 0.01/20 leads basically to a single mode in this approximation. Mind however that for beam parameters of that size other physical effects that were neglected in our approximations could become significant (e.g. electron-electron-interactions). From the difference between the two series we can see that the energy spread is not very dominant but it cannot be neglected.

In the case in which all parameters are varied we arrive at a single coherent mode. On the other hand in the case where only the transverse beam settings are reduced and the energy spread is kept fixed the first mode intensity still carries at most only 93% of the spectral density. This is consistent with section 3.4 because the electron phase space density does not approach a delta function in the electron energy dimension.

---

[1] Accidentally the ESRF-EBS energy spread was assumed to be $\sigma_\delta = 0.89 \cdot 10^{-3}$ instead of $\sigma_\delta = 0.95 \cdot 10^{-3}$. In view of the computational resources invested into all the calculations and its convergence tests and given the small difference and the fact that we are mainly interested in very small electron beam settings, we decided to accept this small difference.

Homogeneous scaling:

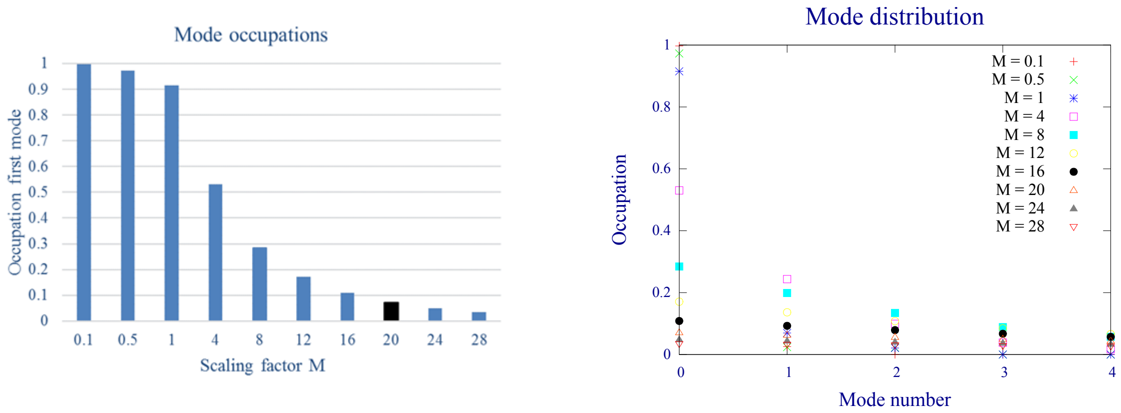

Homogeneous scaling with fixed energy spread $\sigma_\delta = 0.89^{-3}$:

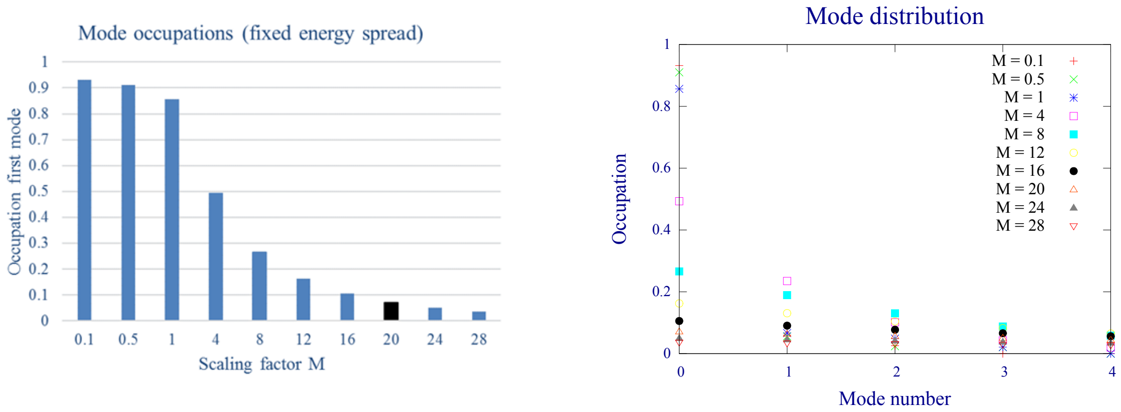

Figure 5.9.: First coherent mode occupation (left) and mode distribution (right) for varying electron beam parameters (see Eq. 5.4) and the ESRF u18 2m long undulator. The series *20* corresponds to ESRF-EBS settings.

5.6. Comparison to some approximations

In this section we compare some exact numerical calculations to some approximations. The approximations are the Gaussian Schell-model (GSM), an analytical approximation that exploits the large emittance of third generation synchrotrons proposed by Geloni *et al.*[8] as well as what we will call *the separation approximation*. All approximations have in common that they separate the horizontal and vertical dimensions which reduces the numerical complexity enormously. Because of this separation the computational cost in these approximations is drastically reduced. We present first the theory of the Gaussian Schell-model approximation and the theory of the separation approximation. We will then present the results of their application. Afterwards we introduce the equations of the analytical approximation which are followed by the results of its application.

5.6.1. The Gaussian Schell-model approximation

A Gaussian Schell-model (Eq. 2.170) is defined by the three free parameters A, σ_s and σ_g. The normalization constant A can be determined from the value at the origin:

$$W(0,0) = A^2. \tag{5.5}$$

A fit to the trace can be used to determine the spectral width σ_s:

$$W(x,x) = A^2 \exp\left(-\frac{x^2}{2\sigma_s^2}\right). \tag{5.6}$$

Knowing the spectral width σ_s a fit to the other diagonal determines the correlation width σ_g:

$$W(x,-x) = A^2 \exp\left(-\frac{x^2}{2\sigma_s^2}\right) \exp\left(-\frac{(2x)^2}{2\sigma_g^2}\right). \tag{5.7}$$

We mind that the Gaussian Schell model is always real and its spectral density must be Gaussian. For a Gaussian Schell model it is necessary that the cross spectral density W separates into a horizontal and a vertical part. If this is not the case then the cross spectral density can not be described in terms of a Gaussian Schell-model.

5.6.2. The separation approximation

Here we present a separation approximation that is universal in the sense that if the cross spectral density is separable into a purely vertical and a purely horizontal part then it is reproduced by the following approximation. We will therefore call this approximation **the separation approximation**.

We will call a *cut* of a function along a dimension the values of that function along that dimension whereas the variables of the other dimension are constant.

For any function[1] of four parameters $W(x_1, y_1, x_2, y_2)$ that can be separated into the product of two functions of two parameters f, g:

$$W(x_1, y_1, x_2, y_2) = f(x_1, x_2) g(y_1, y_2) \tag{5.8}$$

we show that f and g can up to constant be recovered from cuts along the horizontal and vertical dimension and that the product of these cuts reproduce W.

---

[1] which is not zero everywhere on its horizontal or vertical cut,

Setting $x_1 = x_2 = 0$ or $y_1 = y_2 = 0$ we derive three equations:

$$\begin{aligned} &a)\ W(0, y_1, 0, y_2) = f(0,0)g(y_1, y_2) \\ &b)\ W(x_1, 0, x_2, 0) = f(x_1, x_2)g(0,0) \\ &c)\ W(0,0,0,0) = f(0,0)g(0,0) \end{aligned} \tag{5.9}$$

The first two equations determine f and g up to a constant. It remains only to find these constants.

To find these constants we note that the equation c) establishes a relation between the product of the two constants. Solving equation a) and b) for f and g[1], respectively, and multiplication of f and g yields:

$$W(x_1, y_1, x_2, y_2) = \frac{W(0, y_1, 0, y_2)W(x_1, 0, x_2, 0)}{f(0,0)g(0,0)} = \frac{W(0, y_1, 0, y_2)W(x_1, 0, x_2, 0)}{W(0,0,0,0)} \tag{5.10}$$

in the last line we used equation c).

Summarizing the product of the cuts divided by W at zero reproduce W.

Because f and g are independent(separated) the coherent modes of W are the product of the coherent modes of f and g:

$$f_n(x, y) = f_{I_f(n)}(x)g_{I_g(n)}(y) \tag{5.11}$$

and the eigenvalues are:

$$\lambda_n = \lambda_{I_f(n)}\lambda_{I_g(n)} \tag{5.12}$$

here $I_f(n)$ and $I_g(n)$ are index functions that order the product of the eigenvalues of f and g in descending order a function of n.

5.6.3. Results for the Gaussian Schell-model approximation and the separation approximation

We determine f and g (Eq. 5.8) from two-dimensional cuts of the exact cross spectral density W. Afterwards we perform coherent mode decompositions for f and g and build from the product of their modes the coherent modes, i.e. we perform the separation approximation.

We tested this process with a Gaussian wavefront reference electric field at the symmetry point and at the finite alpha position 1m away from it and we could to good numerical precision recover the theoretically predicted Gaussian Schell-model (see section 3.3.3). The relative errors for the eigenvalues and modes were of the order 10^{-6}. The relative errors in operator norm for the first 150 modes, i.e. $W = W^{(150)}$ (Eq. 2.141), were of the order of 10^{-6}. The restriction to 150 modes was made purely for performance reasons. The small errors show that the idea of the separation approximation works.

We apply the separation approximation to the EBS and current lattice calculations made with an 2m long u18 undulator at the first harmonic. We test the constructed W from the separation approximation on its horizontal and vertical cuts against the exact calculation and we get high numerically agreement. The relative error in operator norm between the exact calculation and the separation approximation increase with the number of considered modes m (see $W^{(m)}$ (Eq. 2.141)). The error lies at about 0.05 for EBS and between $0.05 - 0.35$ for high and low beta (see Fig. 5.10). While the relative error is smaller for the ESRF-EBS lattice its absolute error is larger. The relative error of the eigenvalues lies between $10^{-2} - 10^{-1}$ (EBS), $10^{-5} - 10^{-3}$ (high beta) and at about $5 \cdot 10^{-3}$ (low beta). The trend of increasing errors with increasing mode

---

[1] $f(0,0)$ and $g(0,0)$ can not be zero unless the entire cut is zero.

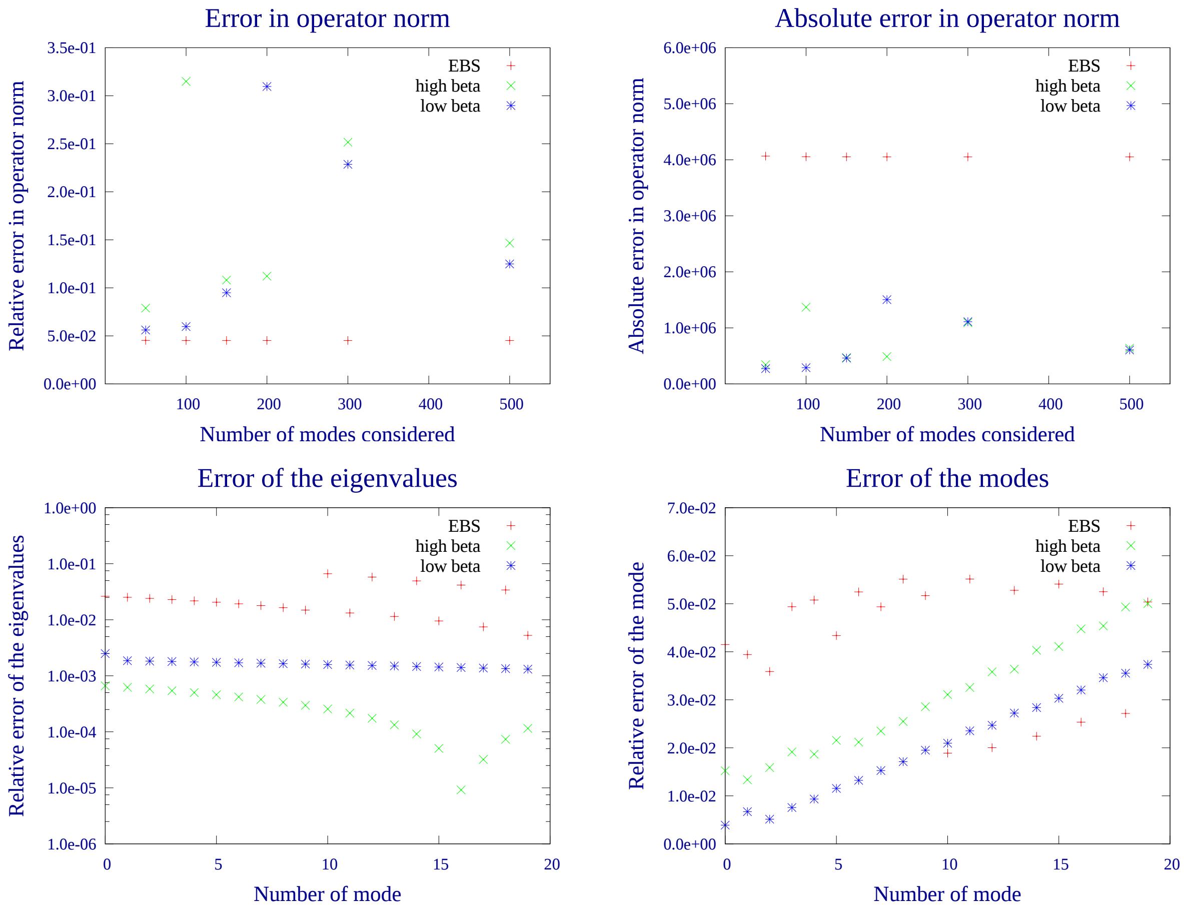

Figure 5.10.: Relative error in operator norm(top left), absolute error in operator norm(top right), relative error of the eigenvalues (bottom left) and relative error of the coherent modes(bottom right) for the separation approximation applied to the ESRF-EBS and the current ESRF lattice settings with a 2m long u18 undulator at the first harmonic.

number is also true for the relative errors of the coherent modes for the high and low beta cases. For the ESRF-EBS settings the error alternates. It takes values between $2 \cdot 10^{-2} - 6 \cdot 10^{-2}$ (EBS), $1 \cdot 10^{-2} - 5 \cdot 10^{-2}$ (high beta) and $5 \cdot 10^{-3} - 4 \cdot 10^{-2}$ (low beta). In general we can observe that the lowest order modes are not badly approximated but higher order modes are approximated worse. Some selected modes, partially of even higher order than 20, are depicted in Fig. 5.12. In particular higher order modes may change shape and are no longer orthogonal to the exact coherent modes. It is not difficult to find points, that do not lie on one of the cuts, with a relative error above 1. For the ESRF-EBS settings the situation is similar and maybe even slightly worse. The differences start larger and increases faster.

We equally apply the Gaussian Schell-model (GSM) approximation, i.e. we fit the Gaussian Schell-model parameters as described in section 5.6.1 to numerically calculated values of the cross spectral density. The GSM approximation used in this thesis is therefore from its nature a fit and not a modelling of the cross spectral density. The relative error in operator norm lies between 2 to 3 for the current ESRF lattice and at about 0.3 for the ESRF-EBS lattice. The relative error of the coherent modes varies mainly between 0.2 and 0.6 for the first 20 modes. For the current ESRF lattice the relative error of the eigenvalues is rather constant over the first 20 modes and

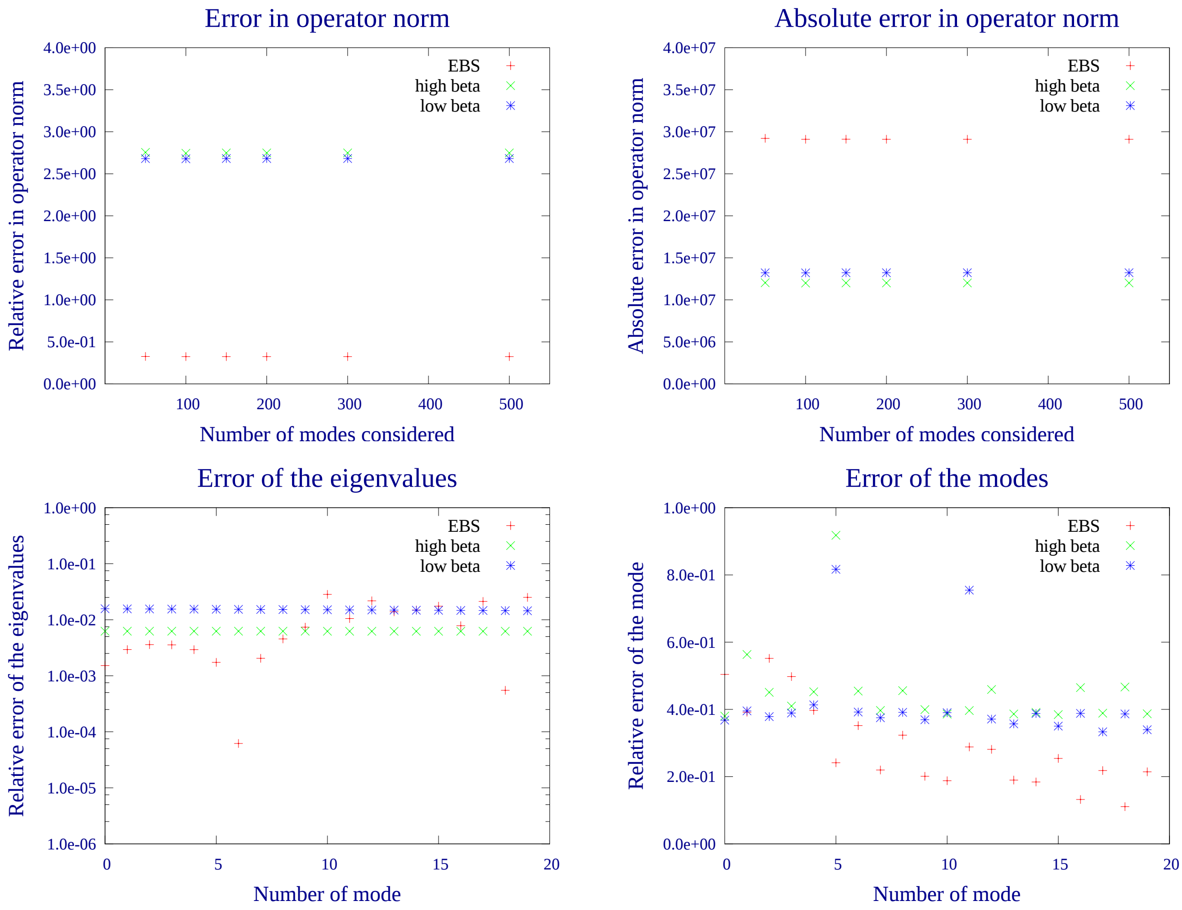
Error in operator norm

Absolute error in operator norm

Error of the eigenvalues

Error of the modes

Figure 5.11.: Relative error in operator norm(top left), absolute error in operator norm(top right), relative error of the eigenvalues (bottom left) and relative error of the coherent modes(bottom right) for the Gaussian Schell-model approximation applied to the ESRF-EBS and the current ESRF lattice settings with a 2m long u18 undulator at the first harmonic.

about 0.006(high beta) and and 0.02(low beta). For ESRF-EBS settings the relative error is mainly between 0.003 and 0.05. The error in operator norm is worse for the Gaussian Schell-model approximation than for the separation approximation. For the eigenvalues the errors are similar for high and low beta but the Gaussian Schell-model approximation performs better for EBS settings. The relative error of the coherent modes is an order of magnitude worse for the Gaussian Schell-model approximation.

In conclusion we find that the separation approximation leads to (significant) differences for the current as well as for the future ESRF-EBS lattice. On the other hand, however, we find that even for the ESRF-EBS lattice with and without energy spread at the first and third harmonic the cross spectral density on selected cuts (one hole fixed at origin ($\boldsymbol{r}_1 = 0$, $\boldsymbol{r}_2 = \boldsymbol{r}$), symmetric displacement ($\boldsymbol{r}_1 = \boldsymbol{r}_2$)) are very well approximated by the separation approximation (see Figures 5.14, 5.15, 5.16, 5.17, 5.18). The notion *hole* is chosen in analogy to Young's experiment where the mutual coherence function is probed with pinholes. The cuts are chosen to see if the cross spectral density is translation invariant. At least on these two cuts the results indicate translation invariance. This remains essentially true also for the propagated cross spectral density (see Fig. 5.19). The spectral density is equally approximated very well (see Fig. 5.21). Surprisingly

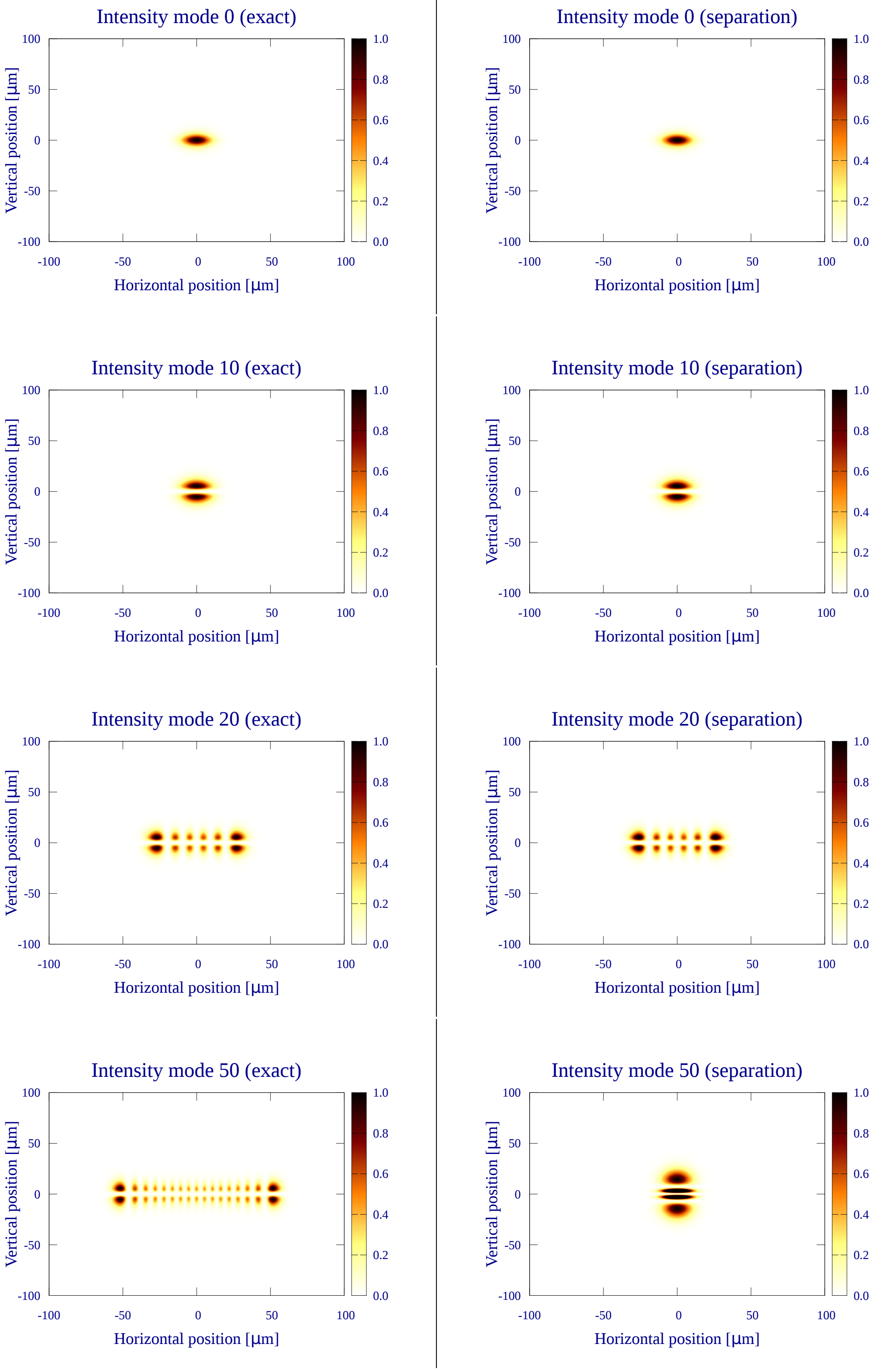

Figure 5.12.: Comparison of the intensity of the exact coherent modes (left) with the intensity of modes from separation(right).

First harmonic:

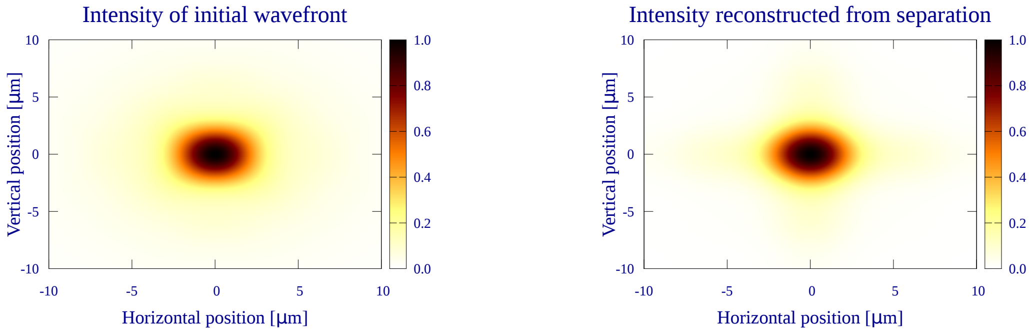

First flux maximum:

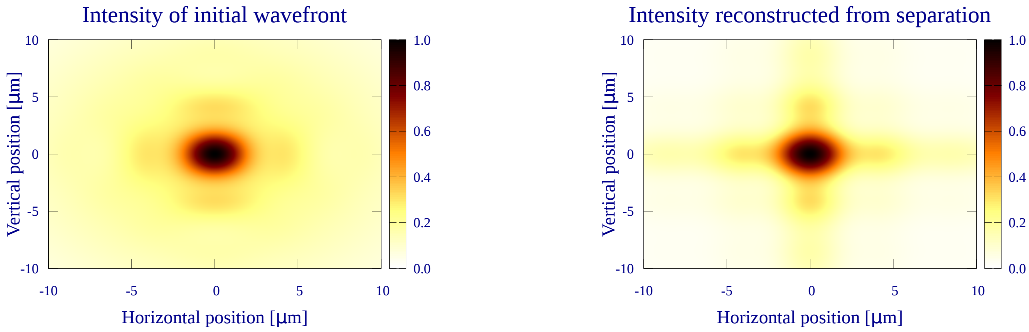

Figure 5.13.: **Separation of the initial wavefront** at the virtual source, i.e. the undulator entrance plane, for the first harmonic(top) and first flux maximum(bottom)

even for very low electron beam parameter configurations such as for a homogeneous scaling of all ESRF-EBS beam parameters by $M/20$ with $M = 1$ (see Eq. 5.4) the separation approximation performs equally well (see Fig. 5.20).

The Gaussian Schell-model approximation works well for the horizontal dimension but underestimates the vertical cut at the first harmonic. The situation becomes worse for the highest flux photon energy or the reduced emittance case (see Figures 5.20, 5.22, 5.23). In these cases the separation approximation still performs very well but the shape deviates from a Gaussian and the Gaussian Schell-model becomes inadequate

Similar to the separation of cross spectral density we can separate the reference single electron undulator emission E_0 used in the calculation of the cross spectral density (Eq. 3.51) or (Eq. 3.54). At the *virtual source* the separation of the single electron emission intensity is quite good for the first harmonic as well as for the flux maximum (see Fig. 5.13). This could explain the good agreement of the separation approximation because a separable single electron emission allows the separation of the cross spectral density as can be see from Eq. 3.51 or Eq. 3.54. This good agreement of the separation approximation may change for electron beams that have coupling between the horizontal and vertical dimension.

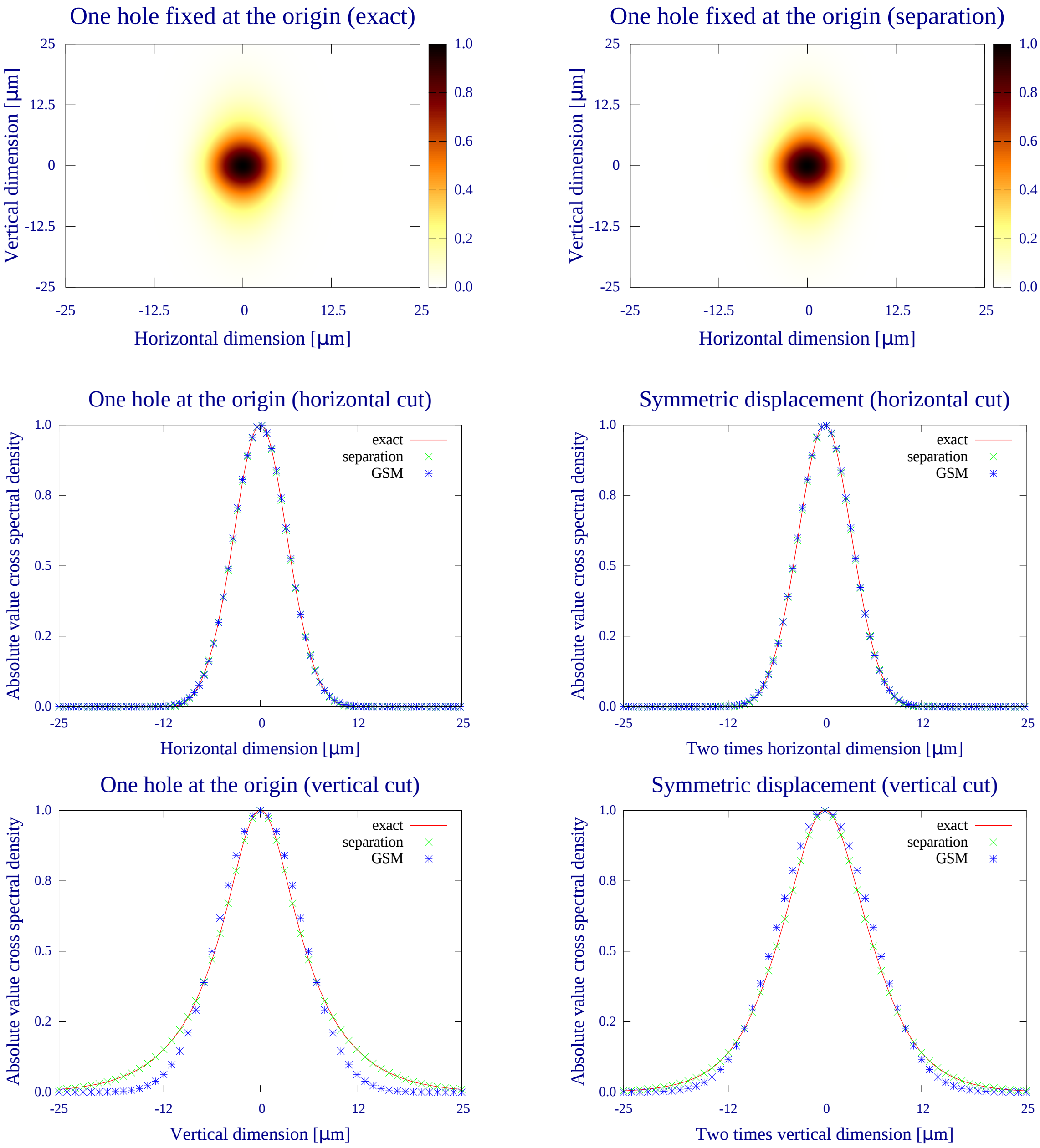

Figure 5.14.: Comparison of the normalized cross spectral density in Gaussian Schell-model and separation approximation for the ESRF **2m** u18 at the **1.harmonic**.

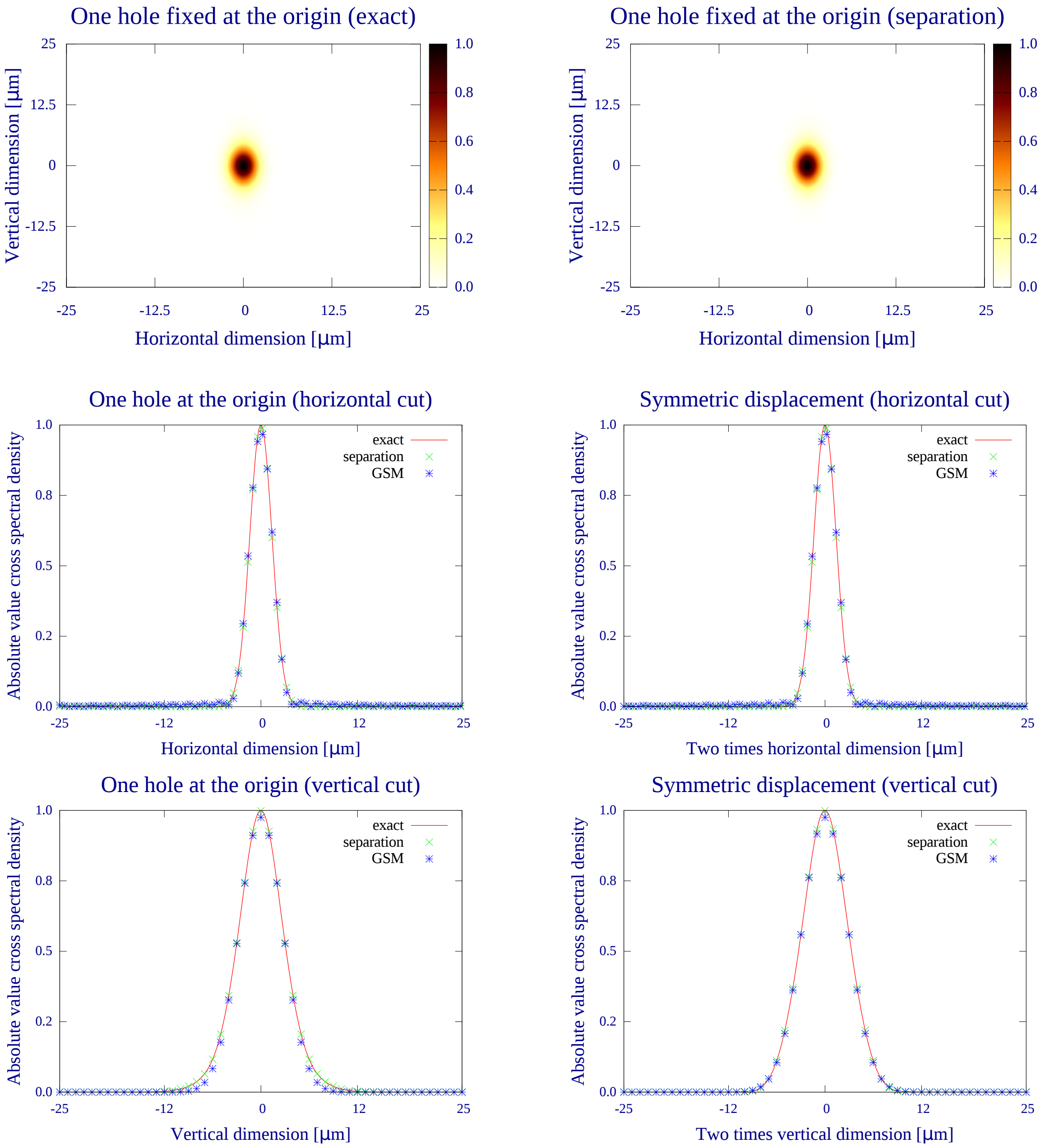

Figure 5.15.: Comparison of the normalized cross spectral density in Gaussian Schell-model and separation approximation for the ESRF **2m** u18 at the **3.harmonic**.

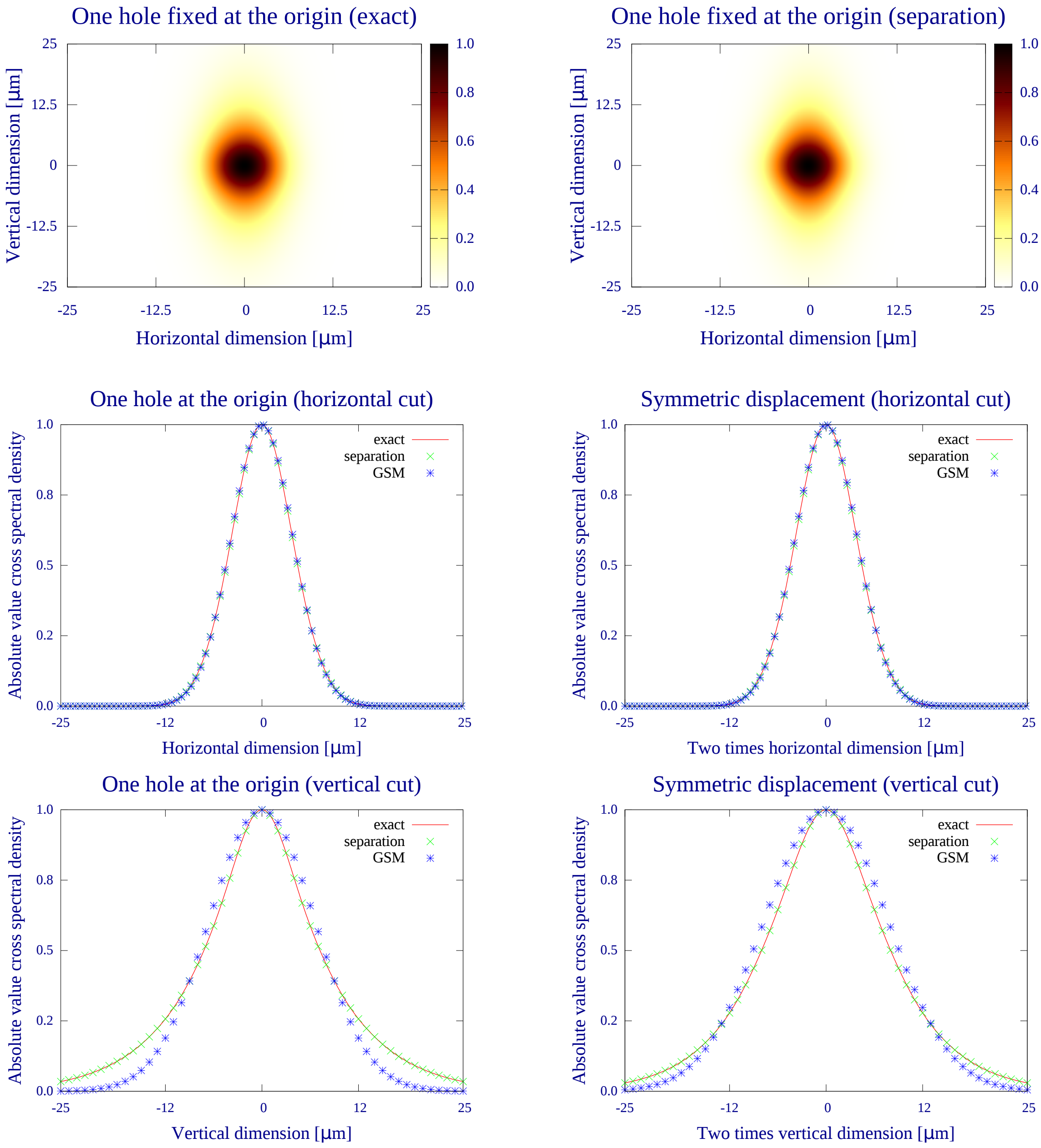

Figure 5.16.: Comparison of the normalized cross spectral density in Gaussian Schell-model and separation approximation for the ESRF **4m** u18 at the **1.harmonic**.

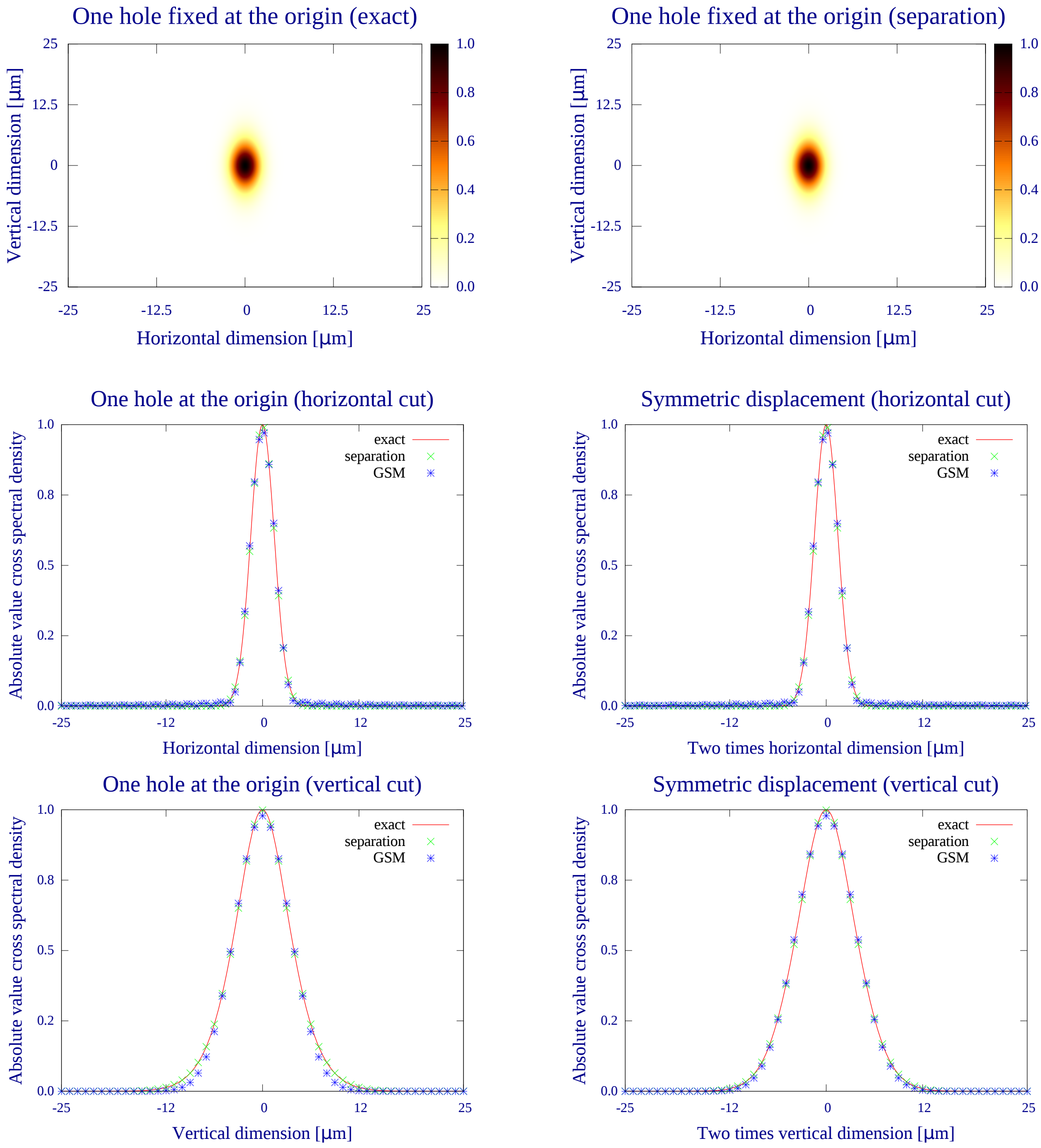

Figure 5.17.: Comparison of the normalized cross spectral density in Gaussian Schell-model and separation approximation for the ESRF **4m** u18 at the **3.harmonic**.

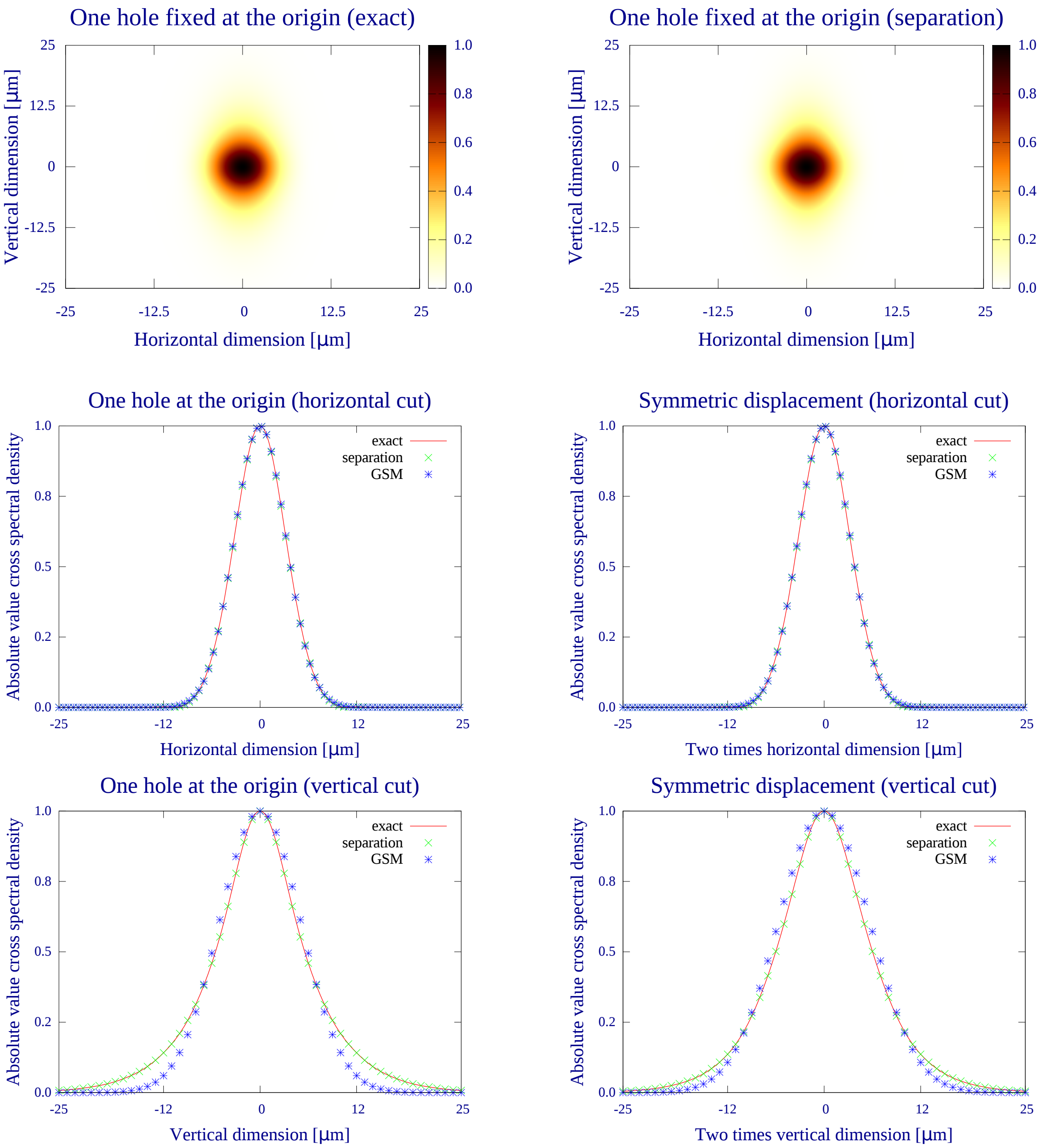

Figure 5.18.: Comparison of the normalized cross spectral density in Gaussian Schell-model and separation approximation for the ESRF **2m** u18 at the **1.harmonic** with **energy spread**.

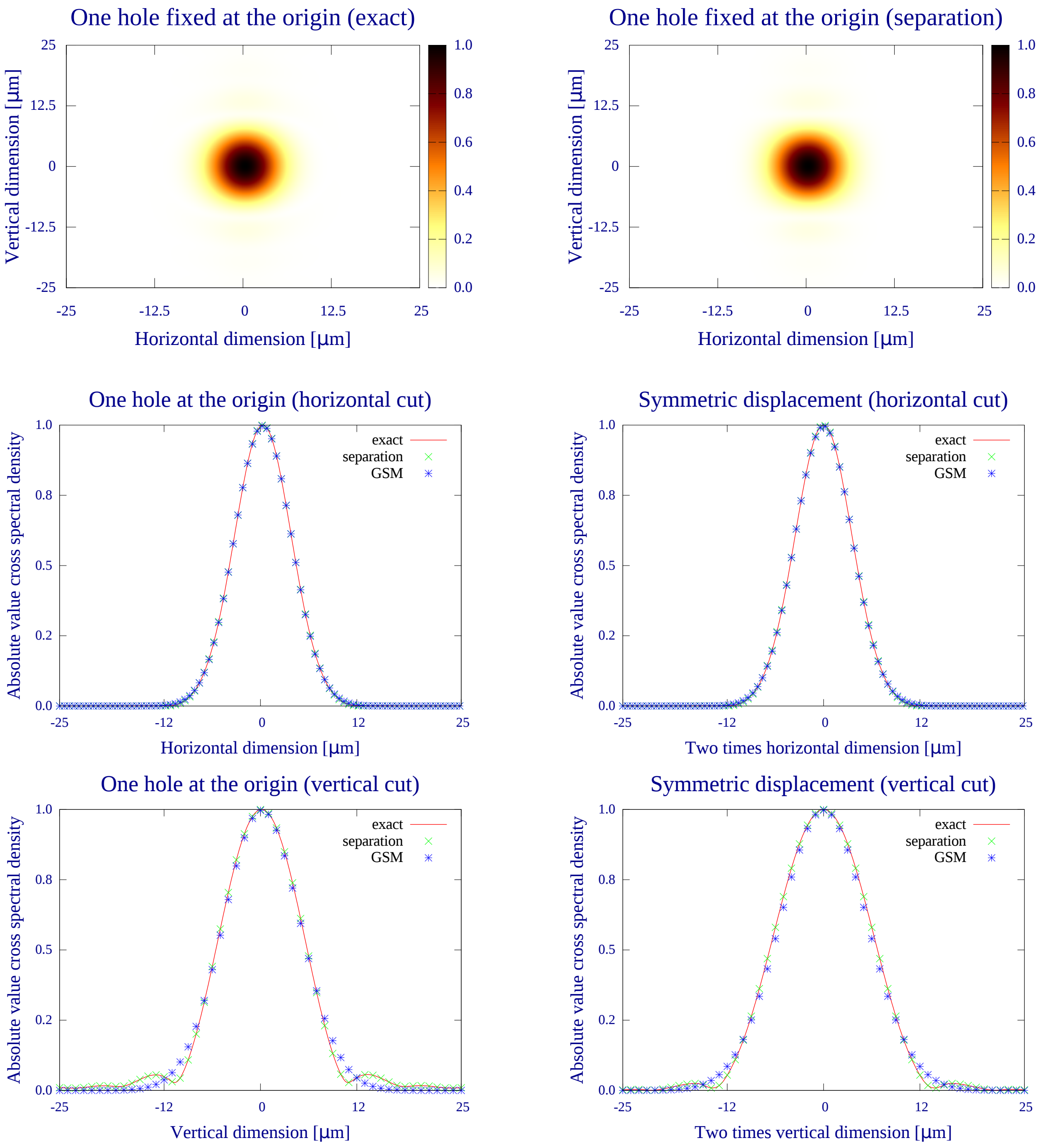

Figure 5.19.: Comparison of the normalized **propagated** cross spectral density in Gaussian Schell-model and separation approximation for the ESRF **2m** u18 at the **1.harmonic**.

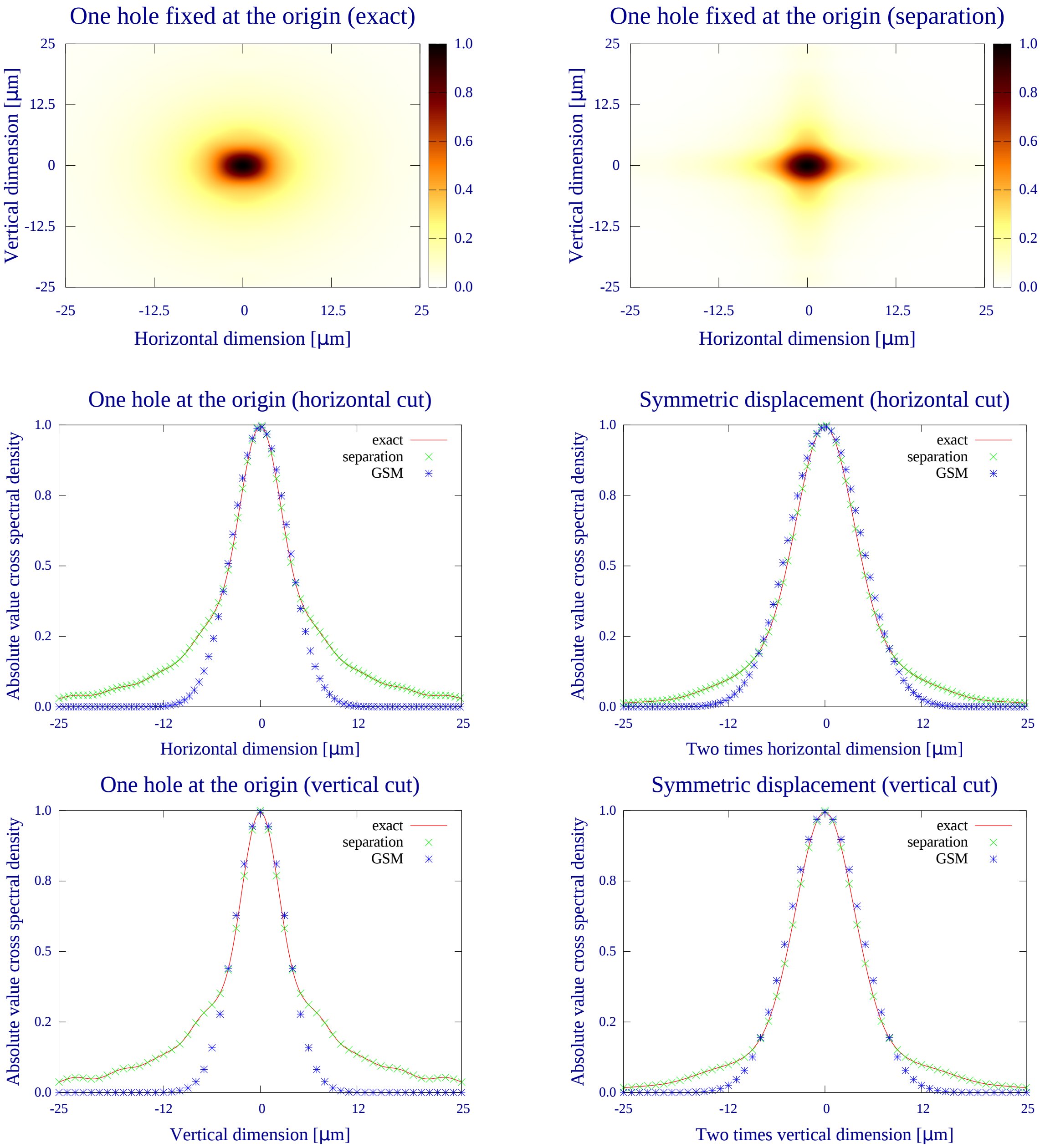

Figure 5.20.: Comparison of the normalized cross spectral density in Gaussian Schell-model and separation approximation for the ESRF **2m** u18 at the **1.harmonic for very low emittance** settings (homogeneous scaling of all ESRF-EBS beam parameters by $M/20$ with $M = 1$ as in Eq. 5.4).

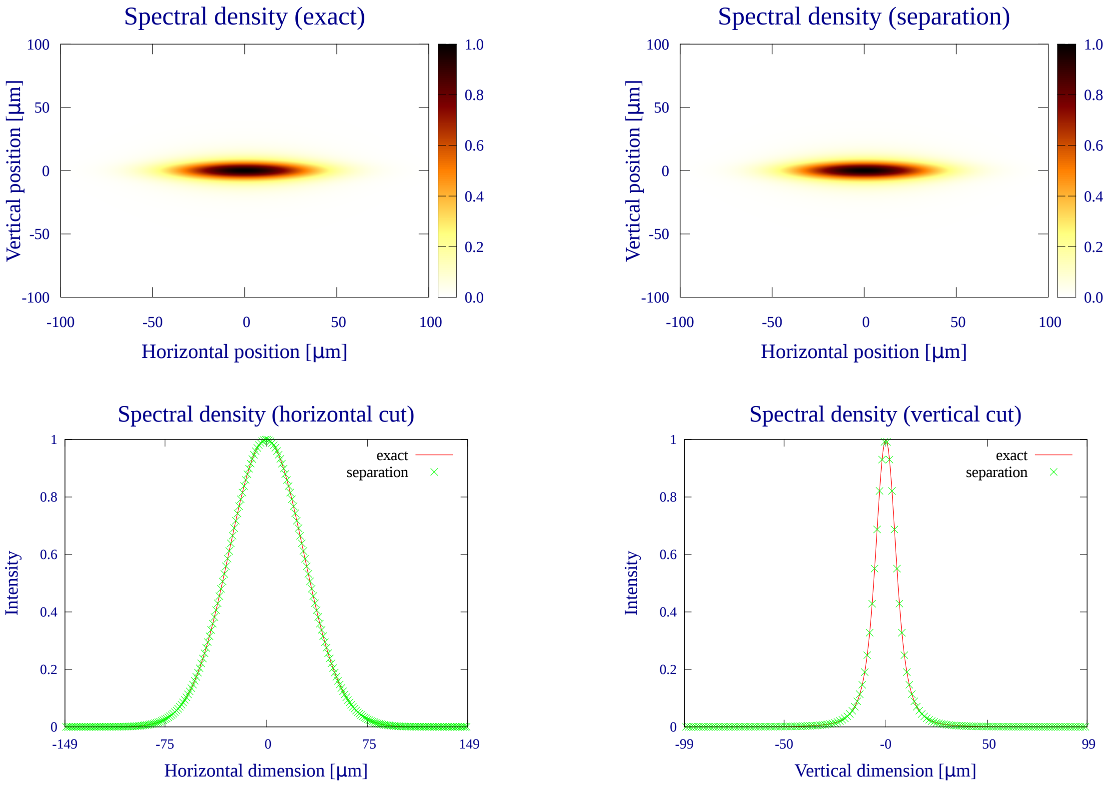

Figure 5.21.: Comparison of the **spectral density** for the ESRF-EBS lattice and the separation approximation.

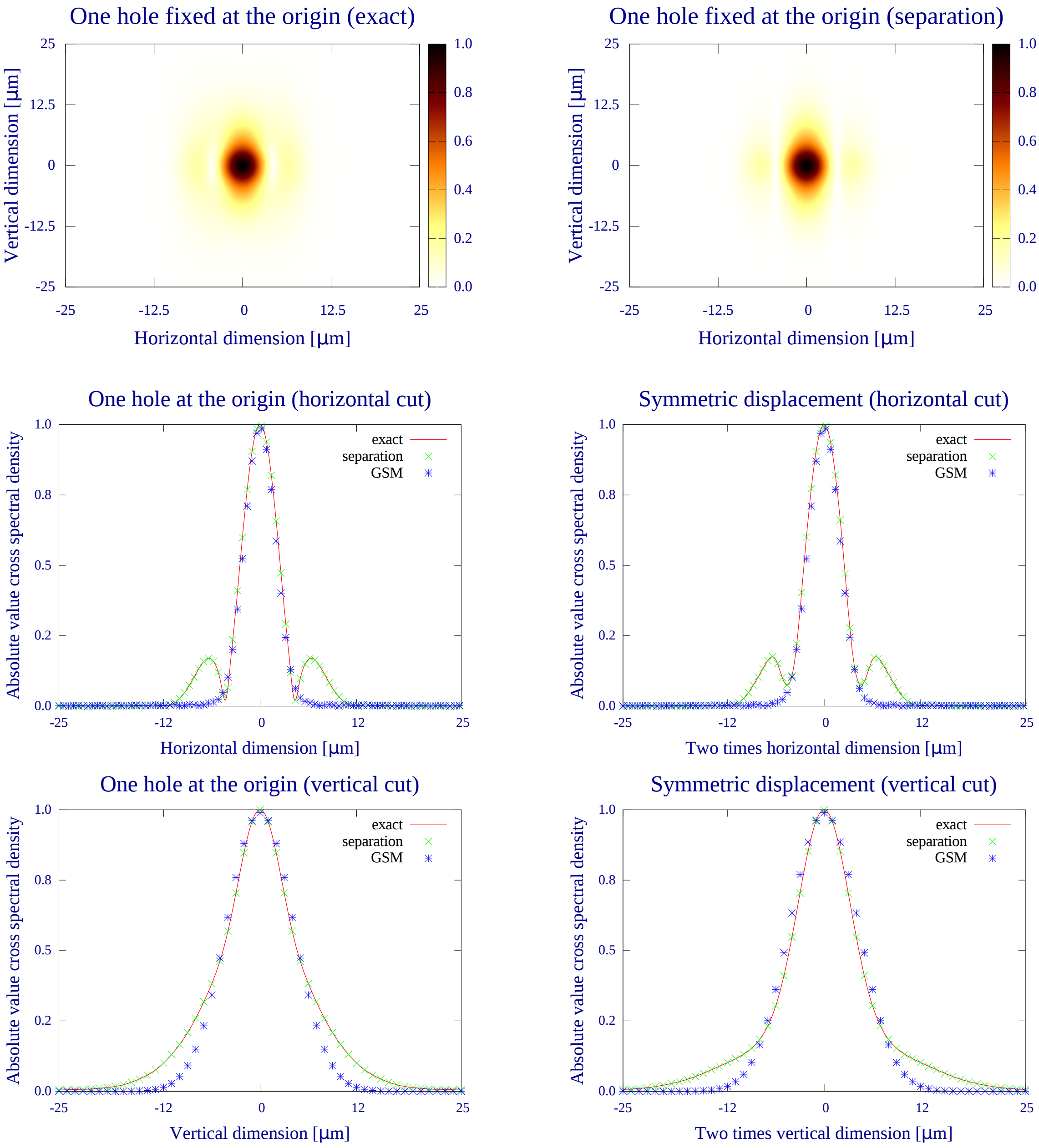

Figure 5.22.: Comparison of the normalized cross spectral density in Gaussian Schell-model and separation approximation for the ESRF **2m** u18 at the **first spectral maximum**.

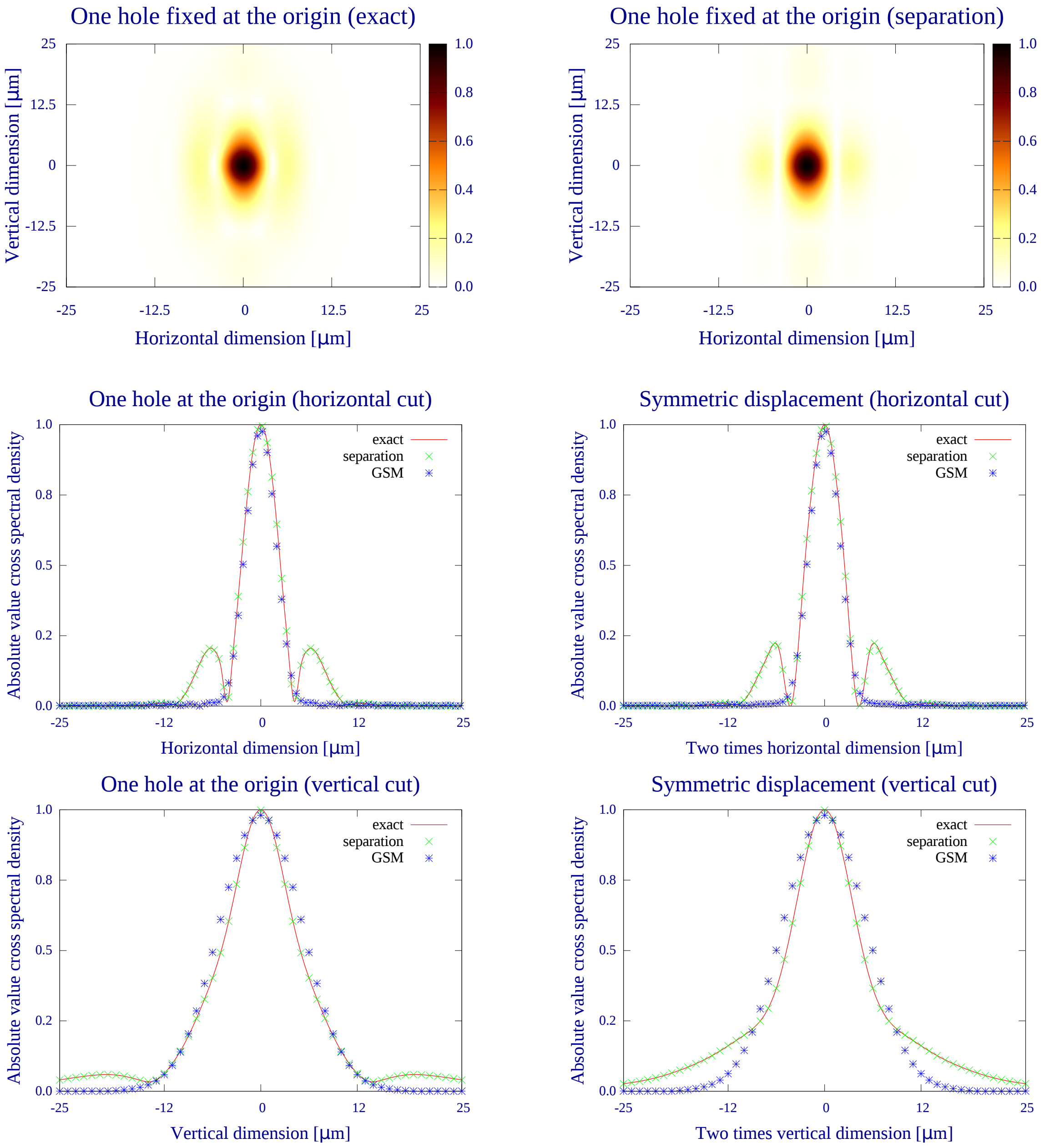

Figure 5.23.: Comparison of the normalized cross spectral density in Gaussian Schell-model and separation approximation for the ESRF **4m** u18 at the **first spectral maximum**.

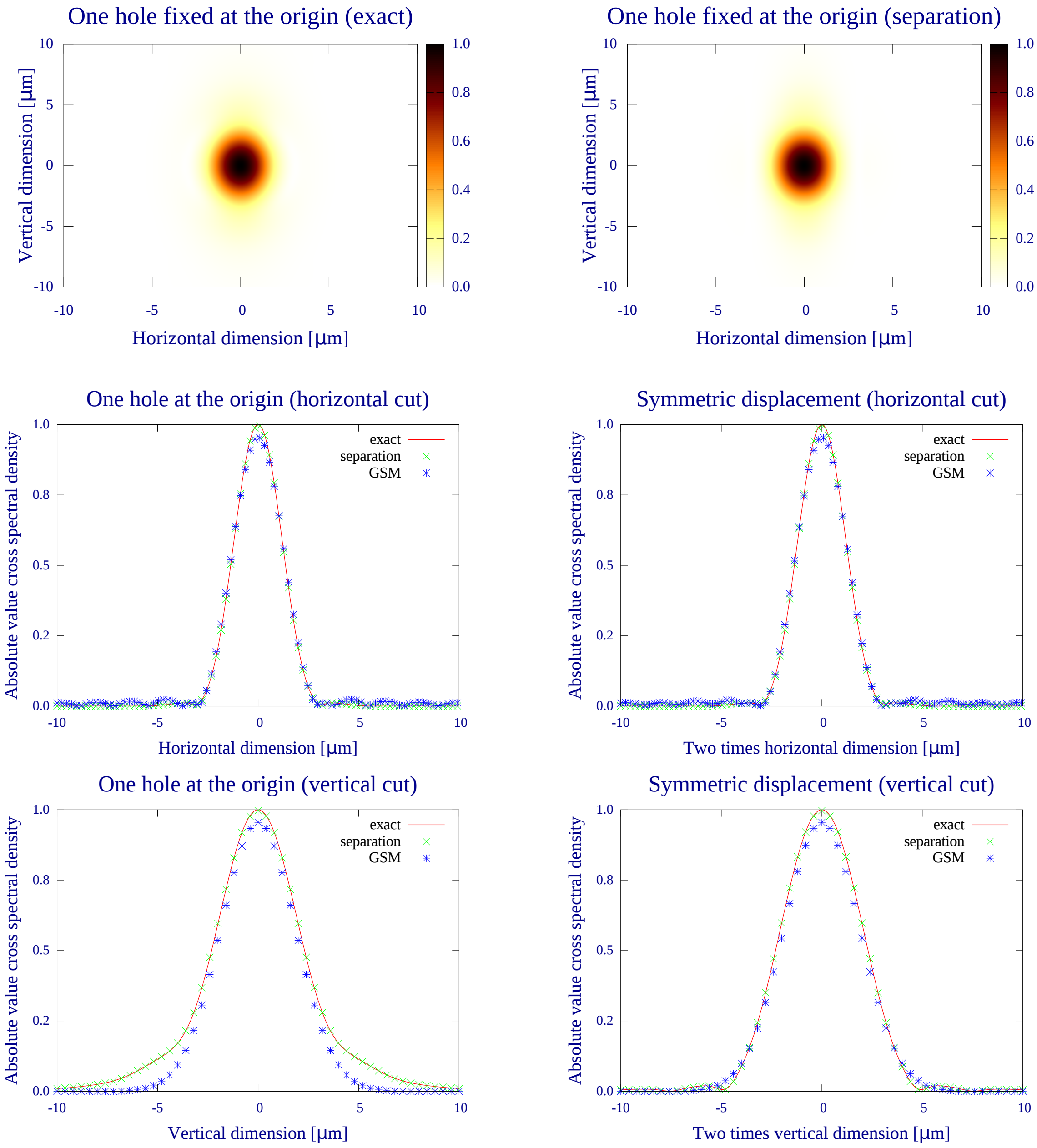

Figure 5.24.: Comparison of the normalized cross spectral density in Gaussian Schell-model and separation approximation for the ESRF **2m** u18 at the **third spectral maximum**.

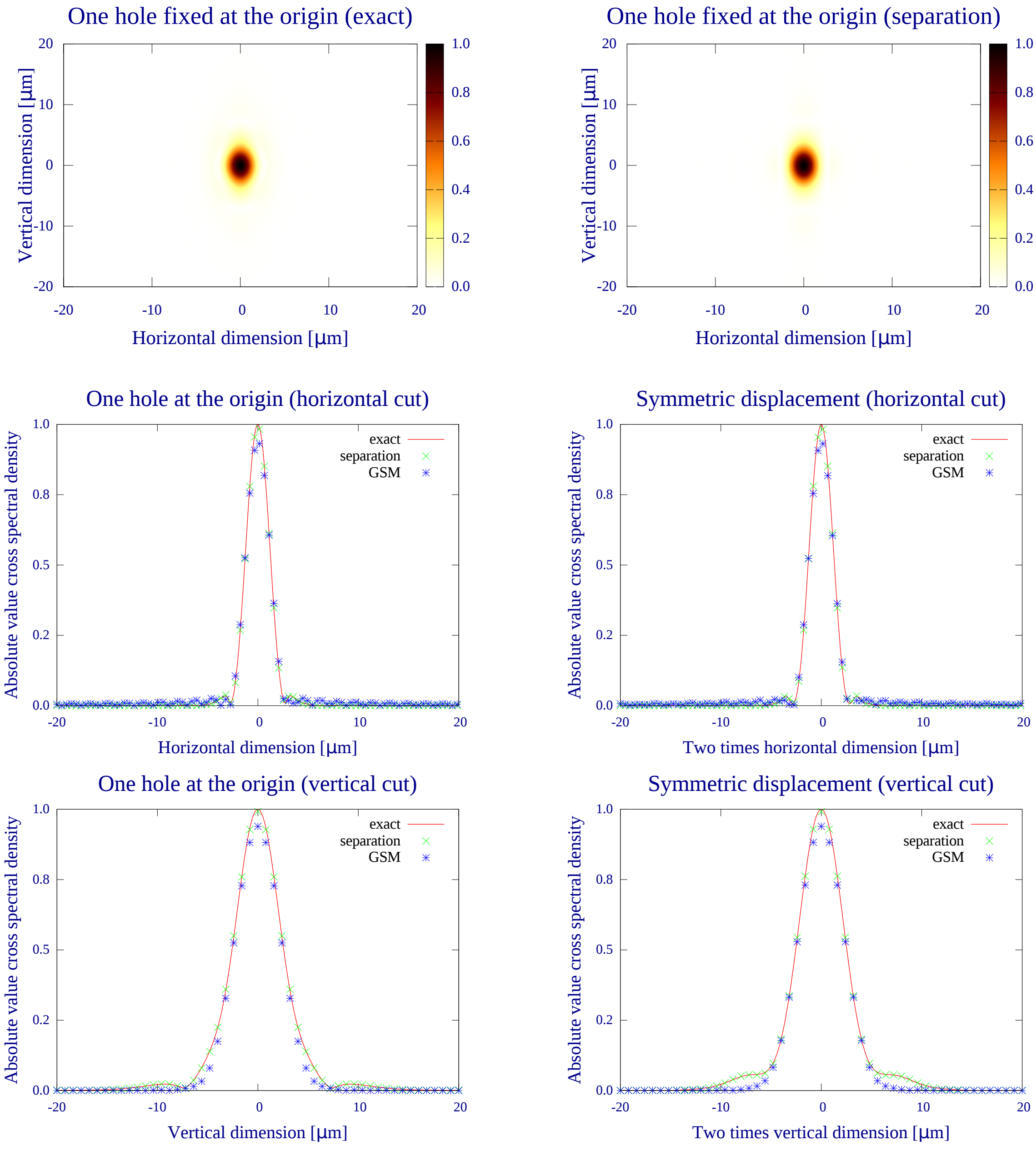

Figure 5.25.: Comparison of the normalized cross spectral density in Gaussian Schell-model and separation approximation for the ESRF **4m** u18 at the **third spectral maximum**.

5.6.4. The analytical separation approximation

In [8] Geloni *et al.* proposed an analytical approximation of the cross spectral density (equations 56-58 in the original paper). The description decouples the horizontal and vertical degrees of freedom for third generation synchrotrons. The underlying idea is to exploit the horizontal emittance that is large compared to the size of the singe electron emission at the virtual source. The *approximation assumes the virtual source* to be at the middle of the undulator. The middle of the undulator itself is supposed to lie at the symmetry point of the straight section. This allows the application of the resonance approximation for the single electron undulator emission and the symmetry point approximation for the electron beam phase space density.

They define:

$$A_{JJ} = J_0\left(\frac{K^2}{4+2K^2}\right) - J_1\left(\frac{K^2}{4+2K^2}\right) \tag{5.13}$$

and for $i \in \{x, y\}$:

$$\begin{aligned}\bar{i} &= \frac{i_1 + i_2}{2} \\ \Delta i &= i_1 - i_2\end{aligned} \tag{5.14}$$

where K is the undulator K value, J_0 and J_1 are the Bessel functions of the first kind of order 0 and 1, respectively.

The approximated cross spectral density takes the form:

$$W(\boldsymbol{r}_1, \boldsymbol{r}_2, \omega) = \left(\frac{K\omega e A_{JJ}}{2c^2\gamma}\right)^2 W_x(\bar{x}, \Delta x, \omega) W_y(\bar{y}, \Delta y, \omega) \tag{5.15}$$

with the horizontal cross spectral density:

$$\hat{W}_x(\bar{x}, \Delta x, \omega) = \sqrt{\frac{\pi}{N_x}} \exp\left(-\frac{(\Delta x)^2 D_x}{2}\right) \exp\left(-\frac{\bar{x}^2}{2N_x}\right) \tag{5.16}$$

and the vertical cross spectral density:

$$\begin{aligned}\hat{W}_y(\bar{y}, \Delta y, \omega) =& \frac{1}{2}\sqrt{\frac{\pi}{N_y}} \exp\left(-\frac{(\Delta y)^2 D_y}{2}\right) \\ & \times \int d\boldsymbol{\theta} \exp\left(-\frac{(\theta_y + \bar{y})^2}{2N_y}\right) \Psi_0\left(\left\|\boldsymbol{\theta} + \begin{bmatrix} 0 \\ \frac{\Delta y}{2}\end{bmatrix}\right\|\right) \Psi_0\left(\left\|\boldsymbol{\theta} - \begin{bmatrix} 0 \\ \frac{\Delta y}{2}\end{bmatrix}\right\|\right)\end{aligned} \tag{5.17}$$

with

$$\Psi_0(\alpha) = \frac{1}{\pi}\left(\pi - 2\int_0^{\alpha^2} dt \frac{\sin(t)}{t}\right) \tag{5.18}$$

and D_i, N_i are defined in Eq. 5.1.

5.6.5. Results for the comparison with the analytical approximation

The analytical approximation assumes the virtual source to lie in the middle of the undulator. Our algorithm performs the decomposition with the virtual source at the entrance of the undulator. In order to compare the two descriptions we propagate our decomposition to the center of the undulator. For our algorithm we use ESRF-EBS finite alpha electron beam settings that are 1m away from the symmetry point. Thus at the center of the undulator the electron beam

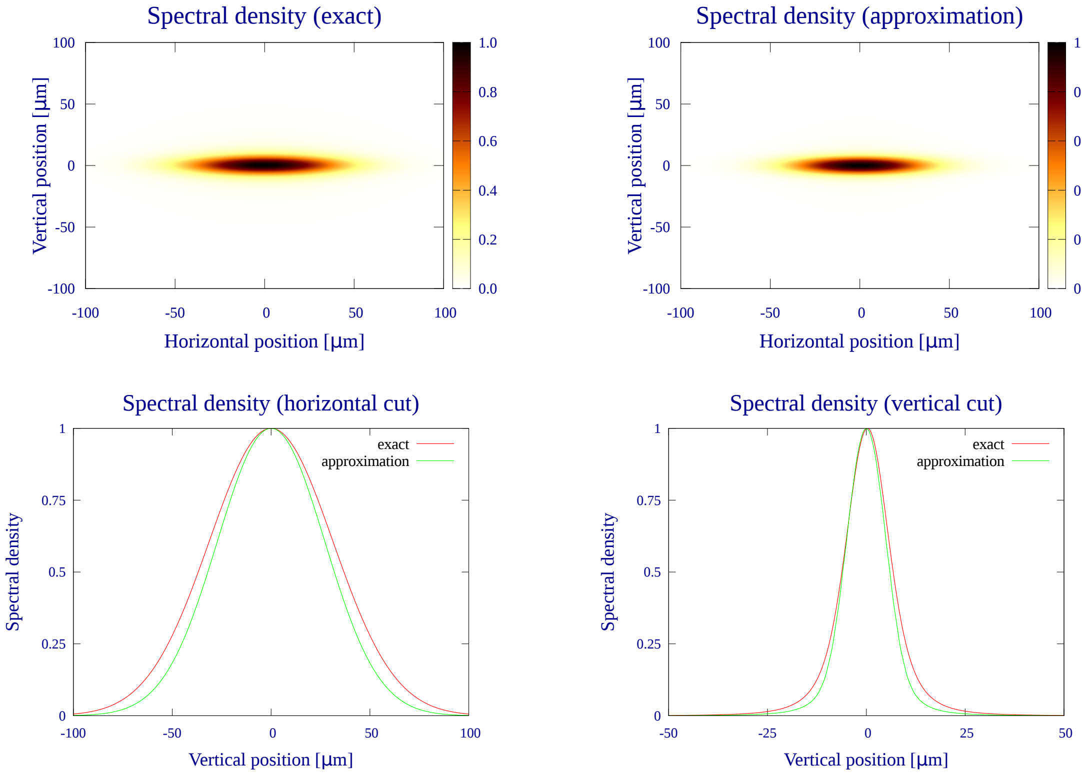

Figure 5.26.: Normalized spectral density of the exact calculation and the analytical approximation for a 2m u18 ESRF undulator.

follows ESRF-EBS symmetry point settings. It should be noted, however, that for finite alpha settings at the undulator entrance the electron beam distribution at the center of the undulator is *horizontally spatially shifted* as discussed in section 4.2.5. This shift might have a influence on the quantitative result. We compare only the ESRF u18 2m long undulator because the only finite alpha settings we use in this thesis are 1m away from the symmetry point.

We built the cross spectral density from the Eq. 5.15 and performed numerically a coherent mode decomposition. In what follows we present the results of the comparison with the exact calculation.

The description of the horizontal part of the separated cross spectral density in analytical approximation is a Gaussian Schell-model. We discussed this approximation already in the previous section. In this section the approximation performs slightly worse than in the previous section. In the previous section the parameters of the Gaussian Schell-model were determined by a fit to the exact calculation. In this section they are calculated directly from analytical expressions. The shift of the electron beam distribution at the center of the undulator that we discussed in the previous paragraph, might be related to this.

In the vertical dimension the analytical approximation shows extra oscillations which are absent in the exact calculation (see Fig. 5.27). The occupation of the first mode is overestimated by the analytical approximation by about 20% (Fig. 5.28) and the extend of the total distribution is smaller than in the exact calculation.

The comparisons of the spectral degree of coherence show again extra oscillations which are consequences of the extra oscillations of the cross spectral density (see Fig. 5.29). The support of the analytical results is a bit smaller than that of the exact calculations but they are of the

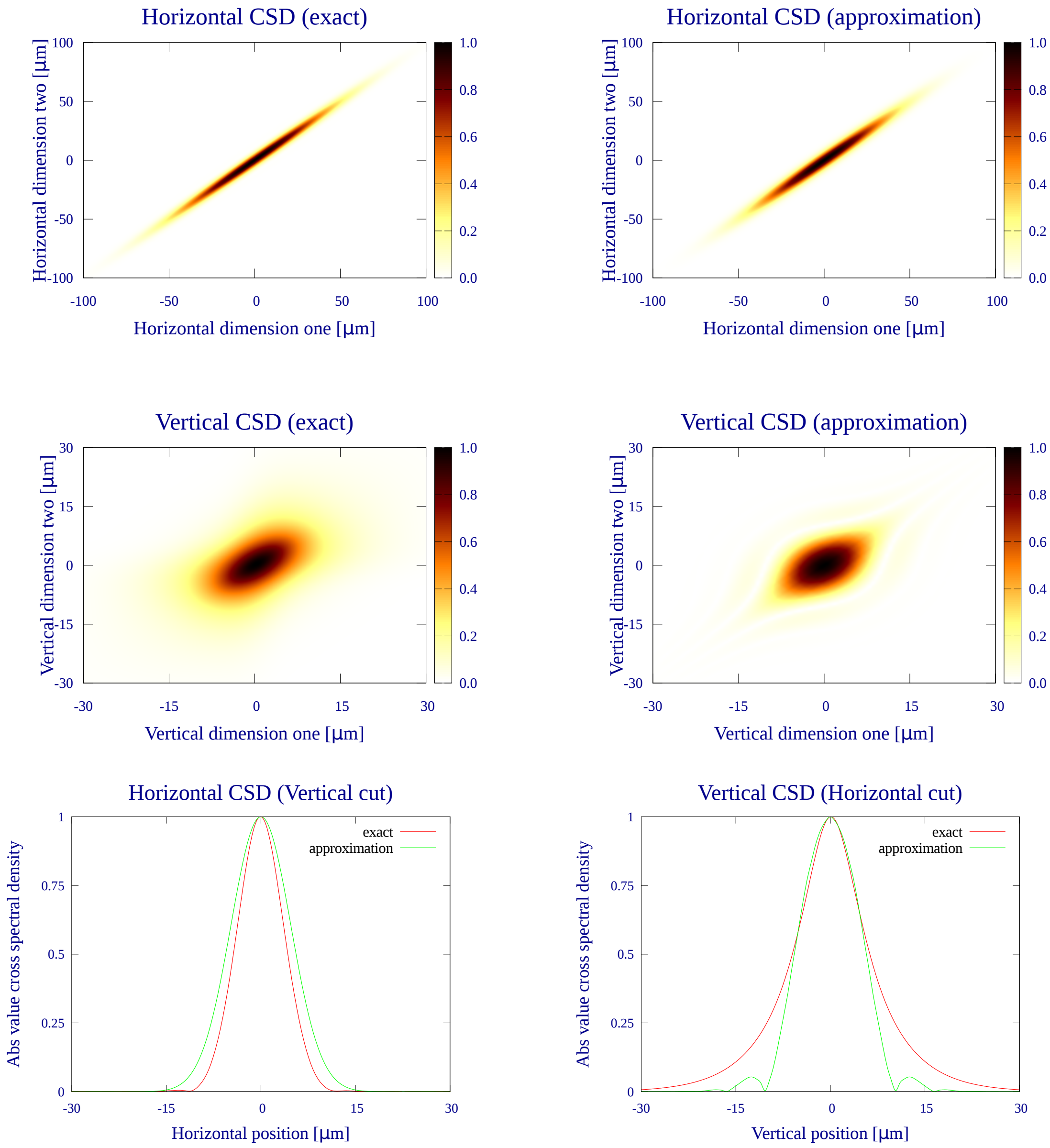

Figure 5.27.: Comparison for the normalized cross spectral density with the analytical approximation for a 2m u18 ESRF undulator for the mode spectrum and the normalized cross spectral density.

same order of magnitude.

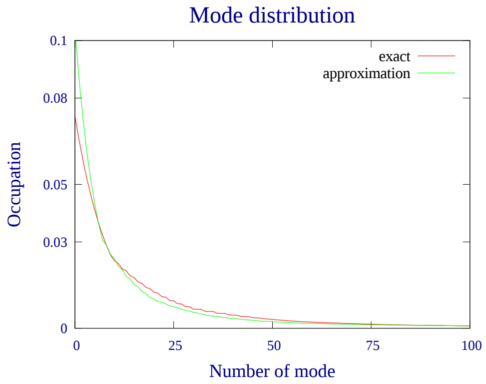

Figure 5.28.: Mode distribution of the exact calculation and the analytical approximation for a 2m u18 ESRF undulator.

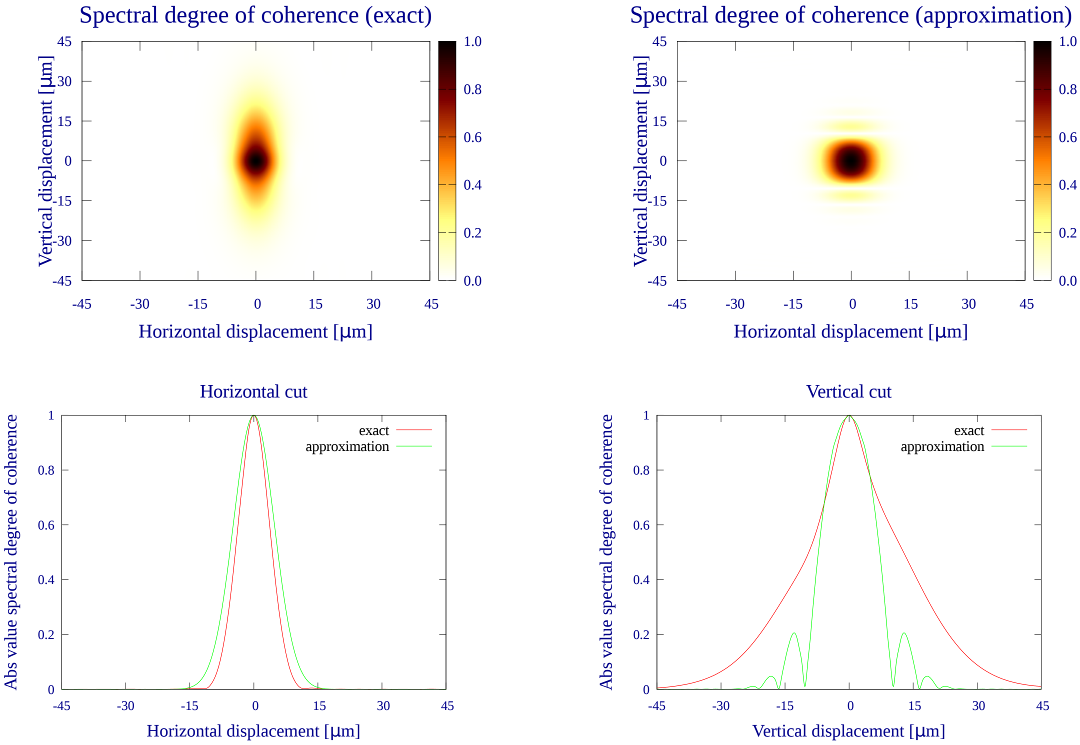

Figure 5.29.: Comparison of the normalized spectral degree of coherence with the analytical approximation for a 2m u18 ESRF undulator for the absolute value of the spectral degree of coherence.

5.7. Summary

In this chapter we apply the coherent mode decomposition algorithm to some applications.

We investigate how the mode spectrum and the coherence length changes as a function of the undulator length and the photon energy. We define the *coherence length* as the FWHM of the spectral degree of coherence μ where $\boldsymbol{r}_1$ is fixed to the origin and $\boldsymbol{r}_2$ is varied. We find that the number of coherent modes decreases and the coherence length increases for longer undulators and that the mode number increases and the coherence length decreases with higher harmonics. The calculations at photon energies corresponding to the maximum flux give smaller coherence length than the calculations at the resonance.

We imitate and idealize an experiment given in [4] where a one to one image of the undulator center is subjected to an aperture. The aperture size is reduced and the mode spectrum is investigated. Closing the aperture reduces the spectral density but narrows the mode spectrum and increases the coherence.

We investigate the effect of a variation of the energy spread. For this we keep the transverse electron beam settings fixed and vary only the energy spread of the ESRF-EBS settings. We find that a reduction of the energy spread does not change the mode spectrum of the ESRF u18 1m long undulator at the first harmonic much but that the changes for the 2m and 4m long ESRF u18 undulators become more relevant.

The effect of a finite Twiss alpha is investigated for a 2m long ESRF u18 undulator. The undulator is once placed with its entrance plane 1m before the symmetry point and once at the symmetry point. The finite alpha calculation are at least ten times slower than the symmetry point calculation because no convolutions can be used in their calculations. Because of the big computation requirements we only inspect the 2m long undulator. There is a change in the mode spectrum and in the coherence lengths but it is not large.

We calculate the change of the mode spectrum for a variation of transverse electron beam settings with fixed energy spread and with decreasing energy spread. We see that the mode spectrum collapses to a single mode if both the transverse electron beam settings and the energy spread is drastically reduced. If the energy spread is kept fixed and only the transverse electron beam settings are decreased then the occupation of the first mode reaches at most only 93%. This is in agreement with the results of section 3.4 because the energy dimension of the electron phase space distribution does not approach a $\delta-$function.

We compared the exactly calculated coherent modes to a Gaussian Schell-model (GSM) approximation, the separation approximation and an analytical approximation given by Geloni *et al.* [8]. A fit to a Gaussian Schell-model shows large errors in the operator norm and in the coherent modes. The error for eigenvalues is fair. Selected cuts of the Gaussian Schell-model fitted cross spectral density show differences to the exact calculation. The errors become worse for smaller electron beam parameters. For the separation approximation the situation is better. The relative error in operator norm is still about 0.05 for ESRF-EBS lattice settings and the modes from the separation approximation are different from the coherent modes. The eigenvalues are approximated worse by the separation approximation than by the Gaussian Schell-model approximation. However, all the quantities we were interested in: spectral density, vertical and horizontal cuts of the cross spectral density for one hole fixed ($\boldsymbol{r}_1 = 0$, $\boldsymbol{r}_2 = \boldsymbol{r}$) and symmetric displacement ($\boldsymbol{r}_1 = \boldsymbol{r}_2$) show very good agreement with the exact calculation. The analytical approximation performs qualitatively good but the cross spectral density has extra oscillations in the vertical direction that are absent in the exact calculation.

The separation approximation seems to be a good and quick numerical approximation for beamline design purposes and should be executable even on ordinary computers.

6. Possible future research and developments

In the this chapter we briefly present some possible ideas for future research and further development of the algorithm or its implementation.

Sampling of the cross spectral density

The cross spectral density W could be calculated numerically with Monte Carlo techniques. The electrons of a bunch are sampled and the ensemble average is approximated numerically:

$$W(\boldsymbol{r}_1, \boldsymbol{r}_2, \omega) = \langle \boldsymbol{E}^*(\boldsymbol{r}_1, \omega) \boldsymbol{E}(\boldsymbol{r}_2, \omega) \rangle_{ens} . \tag{6.1}$$

Afterwards the cross spectral density can be passed to the decomposition algorithm. The so obtained cross spectral density would be subjected to the same memory limitations as the matrix method discussed in section 4.1. The brightness convolution theorem would be circumvented and this allows the calculation of magnetic structures that have a varying magnetic field over the dimension of the electron beam size. A disadvantage however would be the non deterministic nature, i.e. one does not know when the calculation is converged.

Effects of the alignment of undulators

It would be interesting to model and investigate the emission that is produced by two undulators. Does a variation of the gap between the undulators change the coherence properties? Is there a optimal gap?

Additionally, one can inspect the consequences of the undulator alignment, i.e. what is the effect on the mode distribution and the coherence length if the undulator entrance plane is spatially shifted or tilted.

Furthermore in real life there are fluctuations in the power supply of the magnets causing magnetic field fluctuations and there are vibrations of the optical elements in a beamline. The influence of these fluctuations on the radiation could be investigated.

Extension for polarized electric fields

The brightness theorem is only formulated for one polarization. A deterministic field can be described with a well defined field vector and in free space the two dimensions of vibration can be decomposed into a parallel and perpendicular coordinate system. The situation changes in the statistical case in which random phasors are added and the direction of the field vector becomes itself a random function. To describe this kind of phenomenas for quasi monochromatic light the mutual intensity function J is no longer a scalar function but a matrix the so called 2x2 equal time coherence matrix:

$$J(\boldsymbol{r}_1, \boldsymbol{r}_2, \tau) = \begin{bmatrix} \langle E_x^* E_x \rangle_{ens} & \langle E_x^* E_y \rangle_{ens} \\ \langle E_y^* E_x \rangle_{ens} & \langle E_y^* E_y \rangle_{ens} \end{bmatrix} . \tag{6.2}$$

Furthermore one can define a degree of polarization P:

$$P = \sqrt{\left[1 - \frac{4 \det J}{(\mathrm{tr}(J))^2}\right]} \tag{6.3}$$

where $P = 0$ means completely unpolarized(natural light) and $P = 1$ means total polarization.

As discussed in section 3.2 under the given conditions the cross spectral density is the uncoupled sum of single electron emission cross spectral densities. It follows directly the knowledge of the diagonal elements of the frequency representation of the coherency matrix. It remains only to think of the off-diagonal elements. Very likely, they can be calculated analogous with the brightness convolution theorem Eq. 3.15 where one of the reference fields is replaced by the σ-polarization of the reference field and the other reference field is replaced by the π-polarization:

$$W_{\sigma\pi}(\boldsymbol{r}_1, \boldsymbol{r}_2, \omega) = N_e \int d\gamma d\boldsymbol{r} d\boldsymbol{\theta}\ \rho(\boldsymbol{r}, \boldsymbol{\theta}, \gamma) e^{ik\boldsymbol{\theta}(\boldsymbol{r}_2 - \boldsymbol{r}_1)} E_{0\sigma}^*(\boldsymbol{r}_1 - \boldsymbol{r}, \omega, \gamma) E_{0\pi}(\boldsymbol{r}_2 - \boldsymbol{r}, \omega, \gamma). \tag{6.4}$$

But this should be discussed more thoughtfully.

Automatic detection of tuning or precision parameters

A pure technical improvement of the algorithm could be the detection of suitable configuration parameters. In the current implementation suitable grid sizes for the reference single electron emission and the cross spectral density at the virtual source must be manually specified. For the well functioning of the algorithm it is crucial to calculate completely the single electron emission, i.e. all its important features. This means that the grid of the reference single electron emission must be sufficiently large. In the current implementation this is named the exit slit wavefront[1]. Additionally, the virtual source grid must be specified. The grid must be large enough to allow the application of a FFT based numerical convolution of the electron phase space density with the single electron emission that was back-propagated to the virtual source. In the current implementation this parameter is called source wavefront.

During the choice of these parameters it is *important* to avoid artificial boundary effects from the numerical convolution. Until this stage we wanted to have full supervision of the configuration settings to avoid unnecessary error sources. It should however be rather straightforward to implement an algorithm to adjust safe grid settings. Furthermore in the current implementation one has to adjust the number of demanded coherent modes before the start of the calculation. Given the fair agreement for the eigenvalues of the Gaussian Schell-model approximation one could estimate roughly the number of coherent modes on the basis of a Gaussian Schell-model approximation prediction (see Eq. 2.168). On top of this the calculations must be converged. It is probably more subtle to do this automatically. One could investigate if there are some criteria that can guess a priori a converged sampling factor s. The guess would be dependent on the wavelength of the emission and the parameters of the electron beam. These parameters are dominant in the definition of two rather independent grids that must simultaneously converge.

Extension to take into account further electron beam coupling

The thesis and the implementation of the algorithm are restricted to the symmetry point case and the finite alpha case. Other couplings are neglected (see section 2.1.6). The extension to

---

[1] strictly, it is the wavefront a few meters away from the undulator exit slit.

these cases does not pose any theoretical problem as long as the coupling of the longitudinal electron position to the other beam parameters is sufficiently weak. This is already discussed in chapter 3. The extension of the algorithm to more general cases should not be too difficult. During development we intentionally kept the complexity of the algorithm as low as possible and focused on the most easy applications first. Now, it would be a good time to advance to more general applications.

In a first step Eq. 3.50 could be applied to the case where there is no coupling of the electron energy to any other random variable. The finite alpha case can be extended to this case. The implementation would then need to calculate:

$$\exp\left(ik\boldsymbol{\Delta r}M_{P'}^{-1}S_{P'}\boldsymbol{r}\right) \tag{6.5}$$

for matrices $M_{P'}^{-1}$, $S_{P'}$ that may now have finite off-diagonal elements. The presence of off-diagonal elements couple the x-component of $\boldsymbol{\Delta r}$ to the y-component of $\boldsymbol{r}$. The implementation can be adapted to this case with no significant performance loss. However, the complexity increases because the possible values of the complex exponential are stored in memory for performance reasons. In this adaption more exponentials would need to be stored.

Afterwards one could implement Eq. 3.50 in its most general form. In that case additionally $\boldsymbol{s}_{P'\delta}$ and $\boldsymbol{s}_{P'\delta r}$ may be not zero. This leads to an extra electron energy dependent exponential factor in the integration:

$$\exp\left(\langle \boldsymbol{a}(\boldsymbol{s}_{P'\delta}, \boldsymbol{s}_{P'\delta r}, \delta), \boldsymbol{r}\rangle\right) \tag{6.6}$$

with a vector values function $\boldsymbol{a}(\boldsymbol{s}_{P'\delta}, \boldsymbol{s}_{P'\delta r}, \delta)$. The performance and the memory requirements should not be significantly impacted by this enhancement. Possibly, the separation approximation may perform worse for a fully coupled beam.

Another related topic that could be researched are the consequences of non Gaussian shaped electron beams on the X-ray emission properties.

Perturbation theory

We have seen in section 5.6.2 that the separation approach performs surprisingly well. Improvements may still be possible or even necessary depending on the application. One can hope that the perturbation to the exact solution is small. A possible route to improve the result would be the application of standard perturbation theory from quantum mechanics[53]. In terms of the associated cross spectral density operators, we may define:

$$V = A_W^{\text{exact}} - A_W^{\text{sep}} \tag{6.7}$$

as a supposedly small perturbation. The first order corrections to the n-th eigenvalue is then

$$\lambda_n^{(1)} = \langle \Phi_n, V\Phi_n\rangle. \tag{6.8}$$

A quick test of the application of the Rayleigh-Schrödinger perturbation theory to the results of the separation approximation show that at least the eigenvalues are in even better agreement (see Fig. 6.1 left). We did however not test the eigenfunctions. For the Gaussian Schell-model that was fitted to the exact calculation as described in section 5.6.1, the first order corrections actually increases the relative error (see Fig. 6.1 right).

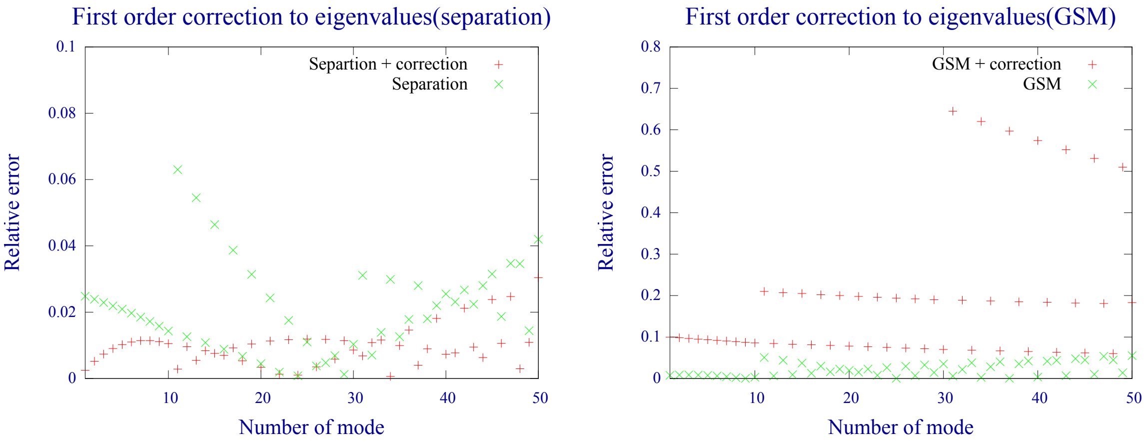

Figure 6.1.: Relative errors of the first order corrections to the eigenvalues for the separation approximation(left) and the fitted Gaussian Schell-model approximation(right). The calculations relate to ESRF-EBS settings without energy spread and an ESRF u18 undulator of 2m length at its first harmonic. While the first order correction improves the eigenvalues in the case of the separation approximation, it worsens the agreement in the fitted Gaussian Schell-model approximation.

Gaussian statistics

In section 3.2 we explained that for frequencies that are relevant to us, i.e. X-ray frequencies, the undulator storage ring emission is a zero mean circularly-symmetric Gaussian random process. In a finite dimensional case its probability density would be described by Eq. 2.174:

$$f_Z(z) = \frac{1}{\pi^n \det(\Sigma)} e^{-z^* \Sigma^{-1} z}. \tag{6.9}$$

The covariance matrix Σ is related to the cross spectral density W:

$$\Sigma = \frac{1}{2} \begin{pmatrix} \mathrm{Re}\ W & -\mathrm{Im}\ W \\ \mathrm{Im}\ W & \mathrm{Re}\ W \end{pmatrix}. \tag{6.10}$$

If a coherent mode representation of W is known the covariance matrix can be expressed in terms of the coherent modes. It would be interesting to clarify the relation of the coherent modes to the eigenfunctions of the integral operator associated to f_Z. Furthermore it would be interesting to look for links and possible input from other physical disciplines like statistical mechanics[54], statistical quantum mechanics[55] or the path integral formalism of quantum mechanics[43] in which the role of the covariance matrix we use in this thesis is usually replaced by the Hamiltonian of the system. An interesting question would be if an analogue of the Boltzmann factor can be defined for a circularly-symmetric Gaussian emission ensemble.

7. Summary

The context of this thesis is the study of the partial coherence in synchrotron beams produced by ultra low emittance storage rings, like the ESRF-EBS ring under construction. As main objectives we had the understanding, application and development of the underlying physics and the implementation of computer tools able to calculate the relevant parameters.

In the first part of this thesis we develop a theory for statistical optics for storage ring radiation. It is based on the brightness convolution theorem by Kim[7] and on the subtle but very important theoretical contributions from Geloni *et al.*[8]. We derive their formulas in a slightly different way or in more a detailed form.

We emphasize the importance of the description of the electron beam stochastic for the coherence properties of storage ring emission. We observe that for weak coupling of the longitudinal electron position to the other beam parameters the bunch length is a free parameter in view of coherence properties.

We build our description of statistical optics around coherent modes. We show that an ensemble is completely coherent if and only if its coherent mode decomposition is a single mode. Geloni *et al.*[8] mentioned that the synchrotron storage ring emission is a Gaussian random process. We add that the process has zero mean and is circularly-symmetric. In consequence we can give the spectral degree of coherence a physical interpretation in terms of Gaussian shaped conditional probability densities.

We developed and implemented an algorithm that calculates the coherent mode decomposition of the cross spectral density for a given wavelength. It can be applied to electron beams with finite Twiss alpha and with energy spread. We implemented two algorithms. The first version solves the Fredholm equation in a two-dimensional step function basis set. Because of its memory requirements high undulator harmonics or current lattices with high emittances can not be calculated. To reduce the memory requirements we developed the two-step method that solves the problem first for an electron beam with zero divergence and adds the effects of the divergence in a second step. The algorithms use the eigensolver library SLEPc. The implementations of the algorithms are open source and can be found at [9].

We present extensive tests of the algorithms. They include a $\delta-$function shaped electron beam, a Gaussian single electron reference electric field, whose results are analytically known, and comparisons to SRW Monte Carlo samplings.

We apply the algorithm to some particular cases. We determine how many modes are necessary to incorporate 95% of the spectral density and how the spectral degree of coherence changes. We find that the energy spread adds extra coherent modes. This effect is negligible for current lattices but for the ESRF-EBS lattice it accounts for a significant fraction of the total modes. Shorter undulators and higher harmonics increase the number of modes. A comparison between an undulator placed at a point with finite alpha and at a symmetry point shows no significant differences. A reduction of the ESRF-EBS beam parameters show a decrease of the mode numbers until they reach a single mode. We simulate a simple 1:1 imaging beamline with an aperture in the image plane. A reduction of the aperture size changes the eigenvalue spectrum to fewer and fewer modes that is paid with a decrease of flux. We present a comparison of the calculated cross spectral density with a Gaussian Schell-model, an analytic approximation and a separation approximation. Although there are not negligible errors between the exact calculation and the separation approximation we come to the conclusions that the separation approximation might be a good and quick approximation that allows the calculation on portable computers.

We end the thesis with some ideas for future research.

Appendices

Configuration files

The configuration files for testing the decomposition methods are located in the configuration subdirectory *compare_methods*. The subdirectorys *waist_resonance* correspond to tests without energy spread, *waist* to tests with energy spread and *alpha* to tests with finite alpha but without energy spread. Configurations with *gaussian* in their file name indicate the usage of a Gaussian as a single electron reference emission E_0.

Some directories for application configurations files are mentioned in Table .1.

Folder	Content
compare_lattice	Comparison between ESRF-EBS and the current ESRF lattice.
compare_undulator	Investigation of different undulator settings (1m, 2m, 4m) for the ESRF-EBS lattice.
compare_energy_spread	Investigation of an energy spread variation.
compare_dream	Investigation of fictive lower emittance lattices.
high_flux	Investigations for photon energies at the flux maxima.

Table .1.: Subdirectories with configuration files.

Summary(short)

In view of the recent raising interest in partially coherent X-ray radiation produced by ultra low emittance storage rings we present a theoretical study and a numerical algorithm for the coherent mode decomposition of undulator emission in storage rings. A numerical description of the undulator cross spectral density in terms of its coherent modes opens a new door for theoretical investigations of coherence properties and for beamline design. The description in coherent modes is much more memory efficient than the naive storage of the cross spectral density. Based on the theoretical work of Kim and Geloni *et al.* we develop a statistical optics theory for synchrotron radiation which is the basis for the algorithm. We highlight the importance of the electron beam parameters for the coherence of the emission. We apply our algorithm to some problems in order to investigate the change of coherence properties as a function of electron beam or undulator parameters.

A. Résumé en français

Dans cette thèse, je discute l'application de l'optique statistique au rayonnement qui est produit aux synchrotrons. Nous nous concentrons sur la cohérence du deuxième ordre. La cohérence du deuxième ordre nous permet de *calculer* les propriétés de la cohérence et l'intensité moyenne.

Le rayonnement synchrotron a connu une croissance énorme au cours des dernières décennies en raison de son applicabilité à la science appliquée multidisciplinaire. L'histoire du rayonnement synchrotron passe par plusieurs générations de sources synchrotron. Dans les années 1960 la première génération du synchrotron a utilisé des anneaux de stockage dédiés à la physique des hautes énergies et a produit le rayonnement synchrotron en mode parasite. Des nombreuses techniques expérimentales ont été développés et cette nouvelle méthode de production de rayonnement est devenu populaire dans la communauté scientifique. L'impact sur la science appliquée a mené la communauté à la construction des anneaux de stockage dédiés exclusivement à la production et l'utilisation du rayonnement synchrotron. C'est la deuxième génération du synchrotron, caractérisée par un haut brillance ou luminosité (puissance émise par unité d'angle et taille de source). Une nouvelle façon d'augmenter la brillance a été implémenté : l'élément d'insertion ou «insertion device». Les éléments d'insertion ont des aimants qui font vibrer fortement les électrons ce qui en conséquence augment leur accélération et alors leur émission. Une autre évolution de la génération de la machine (troisième génération) ont été développé. La troisième génération a des grandes sections droites (straight sections) qui peuvent être utiliser pour l'installation des plusieurs insertion devices. Entre les trois plus grandes sources de troisième génération au monde (ESRF, APS et Spring8), l'ESRF était le premier synchrotron qui a fonctionné. Une haute augmentation de brillance a été fournie en combinant le flux élevé émis par les insertion devices et en réduisant la taille et la divergence de la source, c'est à dire en limitant l'émittance d'électrons. La petite émittance verticale (4pm à l'ESRF) par rapport aux 1000 fois plus grande émittance horizontale a conduit à une cohérence de la radiation relativement élevée. La cohérence de la radiation était à la base de nombreuses techniques expérimentales qui sont standard aujourd'hui. Des exemples de ces techniques sont : X-ray photon correlation spectroscopy (XPCS) [1], coherent diffraction imaging (CDI) [2, 3] et ptychography [4, 5]. La génération actuelle des synchrotrons est maintenant continuée dans deux directions différentes : les X-ray free electron lasers (XFEL), basés sur la technologie d'accélérateur linéaire, et les anneaux de stockage circulaires, dites «diffraction limited storage rings» où l'émittance horizontale des électrons est abaissé à un niveau comparable à l'émittance verticale actuelle. Ces nouvelles installations visent aux expériences qui exploitent la cohérence du faisceau de rayons X, comme X-ray photon correlation spectroscopy, coherent diffraction imaging ou ptychographie. Dans tout les nouvelles synchrotrons ou des mises à jour de celles qui existent déjà, le mot-clé «cohérence» est omniprésent. Nous regardons la mise à jour des installations existantes, comme l'EBS (Extremely Brilliant Source) à l'ESRF. L'EBS vise à créer un anneau de stockage avec une émittance de 150 pm (par rapport au présent de 4 nm) qui stimulera la brillance des rayons X et les propriétés de la cohérence.

Dans le cadre du mettre à jour l'ESRF et la construction d'un nouvel anneau de stockage, il est important d'effectuer des calculs précis et des évaluations quantitatives des paramètres liés à la cohérence des rayons X. Ces paramètres peuvent être extraits de la densité spectrale (cross spectral density). La densité spectral est une fonction complexe dont l'évaluation est coûteuse. Par contre la densité spectral contient la plupart des informations sur la cohérence dont nous avons besoin. Il n'est pas seulement nécessaire d'évaluer cette fonction pour la position de la source, mais de la propager le long des éléments optiques de la ligne de faisceau. Cette thèse propose une nouvelle façon pratique et faisable pour le calcul de la densité spectrale et de la propager le long de la ligne de faisceau. Pour la propagation nous utilisons des méthodes optiques standard. Notre point clé est la décomposition de la densité spectral dans ses modes cohérents. Bien que l'idée soit bien connue dans la domaine de l'optique statistique, cette thèse montre comment effectuer ce calcul numériquement pour les sources de synchrotron. Une fois que la densité spectrale est décomposée, on peut propager chaque mode cohérent comme n'importe quel champ cohérent le long de la ligne de faisceau et on peut construire la densité spectrale à n'importe quel point de la ligne de faisceau. Avec cette densité spectrale, on peut déterminer les paramètres habituels comme les longueurs de cohérence, le degré spectral de cohérence, l'intensité moyenne en représentation de fréquence, etc. Mais on peut faire même plus : la décomposition en modes cohérents donne des informations plus pratiques qui ne sont pas directement visibles dans la densité spectrale. La décomposition permet le calcul précis du spectre des modes, ou comment le rayonnement est distribué dans les différents modes cohérents. De cette façon, il sera démontré qu'une source entièrement cohérente ne contient qu'un seul mode, une source assez cohérente, comme l'EBS, a la plupart de ses rayonnements répartis sur quelques modes (peut-être quelques centaines) et une source assez incohérente aura généralement un spectre de mode presque uniforme. L'étude de la façon dont le spectre de mode est modifié par la ligne de faisceau est fondamentale pour la conception de nouvelles lignes de faisceau. Par exemple, nous montons quantitativement comment la cohérence augmente lors de la fermeture d'une ouverture, une méthode bien connue pour améliorer les caractéristiques du faisceau dans les expériences qui exploitent la cohérence. La maximisation de la fraction d'intensité portée par le premier mode cohérent, à l'aide d'éléments optiques, est la tâche principale du concepteur d'une ligne de faisceau pour des applications cohérentes. La méthode présentée ici permettra des études pratiques quantitatives qui pourraient avoir un impact sur la conception et les constructions de lignes de faisceau plus efficaces. En outre, la description numérique de la densité spectrale de l'ondulateur en termes de ses modes cohérents ouvre une nouvelle porte pour des recherches théoriques et pratiques. Un exemple serait comment les faisceaux de rayons X cohérents partiels interagissent avec les échantillons.

Le but principal de cette thèse est le développement d'un algorithme pratique pour calculer et propager la densité spectrale. De plus, nous voulons souligner l'influence des paramètres du faisceau d'électrons qui entrent dans les calculs des émissions de rayons X. Pour les ordinateurs d'aujourd'hui, le stockage de la densité spectrale d'une manière naïve est très exigeant en mémoire car il s'agit d'une fonction à quatre dimensions. Les exigences de mémoire peuvent facilement atteindre plusieurs téraoctets, ce qui nécessite en conséquence un grand cluster informatique. C'est pour cette raison que j'ai décidé d'effectuer une décomposition en mode cohérent qui aboutit à une représentation de la densité spectral avec relativement peu de modes cohérents. Ces modes peuvent être sauvegardés et diffusés beaucoup plus efficacement. L'hypothèse selon laquelle un petit nombre de modes est suffisant pour calculer avec précision toutes les propriétés de cohérence a été motivée par l'approximation du modèle Gaussian Schell.

La thèse est accompagnée par un logiciel *Coherent Modes for Synchrotron Light (comsyl)* [9] qui est source ouvert.

Dans ce qui suit, nous présentons un bref résumé de chaque chapitre.

Dans le chapitre 2, nous discutons la théorie nécessaire pour cette thèse.

Nous présentons les concepts fondamentaux de l'optique statistique. Ces phénomènes statistiques sont basés sur la physique de l'optique et nous présentons les concepts nécessaires pour la compréhension de cette thèse. En outre, nous présentons un peu de la physique des accélérateurs et un peu de la théorie des éléments d'insertions. Ce sont les fluctuations statistiques des électrons dans l'anneau de stockage synchrotron qui déterminent les propriétés de cohérence du rayonnement X.

Nous expliquons le principe de fonctionnement des anneaux de stockage d'électrons. Les électrons sont accélérés aux vitesses ultra-relativistes et conservés dans l'anneau de stockage. Les structures magnétiques comme aimants dipolaires et quadruples guident les électrons le long des anneaux de stockage. Les électrons perdent énergie due à l'émission de rayonnement synchrotron. L'énergie perdue est rechargée par des cavités HF. L'émission du rayonnement synchrotron est un phénomène statistique et conduit par conséquent à des statistiques d'électrons dans l'anneau de stockage. Ces statistiques électroniques peuvent être décrites par une densité de probabilité gaussienne dans l'espace de phase (Eq. 2.10) avec la matrice de covariance Σ. La matrice de covariance peut être calculée numériquement avec un logiciels dédiée à la physique des accélérateurs. Dans les calculs de cette thèse, nous sommes principalement intéressés par *les éléments* m_{ij} de l'inverse de la matrice de covariance M comme nous les définissons dans Eq. 2.14. Dans la section 2.1.6, nous présentons les deux positions dans la section droite (straight section) auxquelles nous effectuons les calculs dans cette thèse : Le ≪*symmetry point*≫ et la position ≪*finite alpha*≫. Nous définissons le *paramètres de faisceau d'électrons* utilisé dans cette thèse dans la section 2.1.8.

Nous discutons des caractéristiques générales du rayonnement synchrotron et des dispositifs spéciaux pour la production de rayons X intenses, les ≪insertion devices≫, dans la section 2.2 et 2.3. Dans cette thèse, nous n'utilisons que des insertion devices de type d'ondulateur. Un ondulateur planaire est une structure magnétique qui crée approximativement un champ magnétique sinusoïdal dans un plan. Un électron qui entre dans un ondulateur planaire effectue une trajectoire sinusoïdale dans un plan perpendiculaire au plan du champ magnétique. Le rayonnement qui est crée est plutôt intense et collimaté. Nous décrivons comment l'émission peut être calculée à partir de la trajectoire des électrons qui est liée à la champ magnétique précis du insertion device. Dans cette thèse, nous calculons l'émission d'ondulateurs numériquement avec SRW [24]. Nous définissons les notions de *énergie de résonance*, *flux maximum* ainsi que les paramètres d'ondulateur que nous utilisons dans cette thèse dans la section 2.3.4.

Nous présentons la théorie de l'optique physique en vue des applications de synchrotron dans section 2.4. Nous dérivons la formule de diffraction de Fresnel, l'équation de Helmholtz et nous discutons comment les éléments optiques dans l'approximation des éléments minces (thin element approximation) affectent le champ électrique. Dans la section 2.4.3, nous mentionnons comment le propagateur de Fresnel peut être implémenté numériquement en termes de convolutions basés sur la transformation de Fourier rapide (FFT) et certaines difficultés reliées à ce type des implémentations. Nous introduisons la notion de *front d'onde* qui est utilisé par SRW et qui signifie le champ électrique dans un plan le long ou avant de la ligne de faisceau.

Dans la section 2.5, nous présentons la cohérence du deuxième ordre ce qui est un concept de la théorie d'optique statistique. Nous soulignons que les fluctuations de source sont *fundamental* pour les propriétés de la cohérence de l'émission. Nous définissons plusieurs quantités importants de la théorie de la cohérence du deuxième ordre. Un résumé de ces quantités est donné dans Fig. 2.22. Pour cette thèse, les quantités les plus importants sont : la *densité spectrale (cross spectral density)*W (Eq. 2.107), *l'opérateur de densité spectrale* A_W (Eq. 2.139), le *degré spectral de cohérence* μ (Eq. 2.151) et la *densité spectrale de puissance* S (Eq. 2.108). Nous introduisons la décomposition en modes cohérents de la densité spectrale dans Eq. 2.137 qui donne une représentation de la densité spectrale en termes de *valeurs propres* λ_n et *modes cohérents* Φ_n. La décomposition en modes cohérents est la base théorique de l'algorithme que nous présentons dans le chapitre 4. Nous définissons le *spectre de mode* de la densité spectrale comme l'ensemble de ses valeurs propres ; le *occupation des modes* d_n dans Eq. 2.150 comme le n-ème valeur propre normalisée par le somme de toutes les valeurs propres ; *distribution des modes* comme l'ensemble des occupations de tous les modes et le *l'intensité du mode* comme l'intensité d'un mode cohérent. Dans la section 2.5.6, nous montrons qu'il n'y a aucune représentation de la densité spectrale de dimension finie qui incorpore plus de densité spectrale de puissance que la représentation en modes cohérents avec la même dimension finie. Dans la section 2.5.7 nous discutons que l'émission est complètement cohérente si et seulement si la densité spectrale se decompose d'un seul mode. Nous mentionnons comment la densité spectrale peut être propagée le long d'une ligne de faisceau d'un synchrotron. Compte tenu d'un noyau de propagation h, la propagation de la densité spectrale peut être décrite par Eq. 2.119 ou en termes de ses modes cohérents (Eq. 2.157). Nous présentons le *modèle Gaussian Schell* dans Eq. 2.170 qui possède une décomposition analytique en modes cohérents et nous discutons les propriétés de son spectre de mode. Le modèle Gaussien Schell sert de cas de test importants pour notre algorithme qui est décrit dans le chapitre 4.

Nous discutons dans la section 2.5.12 que pour un processus aléatoire gaussien avec une symétrie circulaire le degré spectral de cohérence μ peut être interprété comme un facteur échelle quadratique de l'écart-type de la probabilité conditionnelle.

Nous dérivons dans chapitre 3 les résultats théoriques fondamentaux pour l'optique statistique appliquée au rayonnement synchrotron. Ce sont le théorème de la convolution de la brillance, qui a été développé par Kim [7], et la théorie développée par Geloni *et al.* [8]. Notre dérivation est légèrement différente des originaux et plus détaillée. Nous mettons particulièrement l'accent sur l'explication des idées physiques sous-jacentes dans les formules. Cela conduit à une discussion concernant la position de la section droite à laquelle la convolution de la brillance peut être effectuée et aux exigences du faisceau d'électrons et de l'ondulateur.

Nous commençons par le *brightness convolution theorem* développé par Kim [7]. Nous dérivons le théorème d'une manière différente et ajoutons des commentaires supplémentaires. Le fondement du théorème est la relation entre les conditions initiales des électrons à la *source virtuelle* et les changements de leur émission produite par rapport à une émission de référence E_0. La source virtuelle est un plan virtuel dans ou avant l'ondulateur qui reproduit l'émission réelle d'électrons en dehors de l'ondulateur si le champ électrique est propagé à une position dehors l'ondulateur. À la source virtuelle, la relation entre les conditions d'électrons initiales et le changement d'émission est donnée par Eq. 3.3. Nous identifions le *position naturelle de la source virtuelle étant le plan d'entrée de l'ondulateur*. En outre, le théorème exige l'indépendance statistique des électrons qui est naturellement donné dans un anneau de stockage et que la modification du champ magnétique du insertion device est négligeable.

Dans la dérivation du théorème de la convolution de la brillance, on effectue une sommation sur toutes les corrélations possibles de deuxième ordre des émissions d'électrons dans Eq. 3.14. Dans [8] Geloni *et al.* ont consacré une étude détaillée à cette sommation. Entre autres paramètres, leur dérivation exploite la résolution du monochromateur afin de conclure que la densité spectrale est stationnaire au sens faible. Dans l'original, il est supposé que le temps d'arrivée des électrons et les autres paramètres du faisceau d'électrons étaient indépendants. Dans la section 3.2, nous améliorons légèrement leur discussion et nous montons que pour les couplages faibles entre la position longitudinale d'électron s et les autres paramètres du faisceau d'électrons, le résultat de Geloni *et al.* reste valide. Aussi dans [8], il est mentionné que l'émission de l'anneau de stockage est un processus aléatoire gaussien. Nous ajoutons que le processus a une symétrie circulaire. En conséquence les résultats de section 2.5.12 peuvent être appliqués à l'émission de l'anneau de stockage, c'est-à-dire que le degré spectral de cohérence μ peut être interprété comme un facteur échelle quadratique de l'écart-type de la probabilité conditionnelle entre deux positions spatiales.

Dans la section 3.3, nous dérivons du théorème de convolution de la brillance avec la densité spatiale en cinq dimensions des électrons ρ_5 (voir Eq. 2.17) et avec l'hypothèse de couplages faibles à la position d'électron longitudinale s l'équation générale pour le calcul de la densité spectrale de l'émission de l'anneau de stockage Eq. 3.50) dans l'approximation du théorème de la convolution de la brillance. Nous appliquons cette formule aux cas spéciaux du symmetry point (Eq. 3.51) et à la position finite alpha (Eq. 3.54). Dans la section 3.3.3, nous appliquons ces formules à une émission de référence gaussienne E_0 et nous arrivons à une source Gaussian Schell. Ces cas sont de cas de test importants pour l'algorithme développé dans le chapitre 4.

Dans la section 3.4, nous mentionnons que dans l'approximation du théorème de la convolution de la brillance, l'émission est complètement cohérente si et seulement si la densité de probabilité ρ_6 dans l'espace des phases est une fonction de Dirac.

Après avoir établi la description théorique, nous présentons au chapitre 4 un algorithme pour déterminer numériquement la densité spectrale sous des hypothèses qui ne sont pas trop restrictives. Plusieurs applications des decompositions en modes cohérents pour les ondulateurs d'un synchrotron sont réalisées. Pour les paramètres d'ESRF-EBS les décompositions entraînent un nombre de modes cohérents relativement petit. La mémoire totale requise est réduite à quelques gigaoctets. Enfin, ces modes sont propagés à l'aide de méthodes de propagation standard.

Nous présentons deux algorithmes numériques pour la décomposition en modes cohérents de la densité spectrale pour l'émission de l'anneau de stockage de l'ondulateur. Nous nous limitons aux deux positions de la section droite : le symmetry point et la position finite Twiss-alpha qui sont définis dans la section 2.1.6. Nous utilisons SRW pour la création de l'émission d'un seul électron et pour la propagation de son champ électrique vers la source virtuelle.

Nous commençons par la méthode ≪*matrix*≫ qui discrétise l'opérateur de densité spectrale A_W dans une base des fonctions constantes par morceaux (Eq. 4.4). Dans la section 4.1.1 nous introduisons le *factor d'échantillonnage* comme mesure de la densité des points de la grille numérique.

La discrétisation est suivie d'une diagonalisation itérative. Pour cela nous utilisons SLEPc [46]. L'implémentation des algorithmes s'appelle *Coherent Modes for Synchrotron Light (comsyl).* Il est source ouvert et disponible sur [9]. Un bref aperçu de la structure du code est donné dans Fig. 4.4. Les classes les plus importantes sont mentionnées dans Table. 4.5. Les implémentations sont parallèles et optimisées. Cela implique une complexité des implémentations assez élevée qui doivent être testées de manière intensive. Nous présentons des tests pour un faisceau d'électrons en forme de fonction delta de Dirac et pour un champ électrique de référence qui est gaussien. Dans le deuxième cas les résultats numériques peuvent être comparés à des résultants analytiques. L'accord avec les prédictions théoriques est très bon. En outre, nous testons dans la section 4.2.1 que les ondulateurs que nous utilisons dans cette thèse obéirent la relation fondamentale du théorème de convolution de la brillance entre l'état initial de l'électron entrant dans l'ondulateur et le décalage de son émission donné par Eq. 3.3. Dans la section 4.2.5, nous discutons pour tous les ondulateurs utilisés dans cette thèse si elles modifient la densité de l'espace des phases du faisceau d'électrons à leurs centres. Nous constatons que les ondulateurs introduisent un déplacement spatial constant de la densité à leurs centres. Pour notre algorithme, cela n'a pas de conséquences parce que nous définissons toujours que la source virtuelle est sur le plan d'entrée de l'ondulateur.

Dans la section 4.3, nous discutons que la propagation de la densité spectrale peut changer son spectre et ses modes cohérents. Avec Eq. 4.27, nous montons comment une densité spectrale qui est représentée dans ses modes peut être décomposée directement en termes de ces modes, c'est-à-dire comment éviter la construction de la matrice complète qui représente l'opérateur de la densité spectrale dans la base de dimension finie.

L'inconvénient de la méthode matrix est qu'il nécessite beaucoup de mémoire et de ressources informatiques. Il est essentiellement égal à $N_x^2 N_y^2$ alors que N_x, N_y sont les nombres de points de grille dans la dimension x et y. Les tailles typiques pour N_x et N_y peuvent facilement atteindre quelques centaines jusqu'à quelques milliers. Dans ce dernier cas, les besoins en mémoire atteindraient plusieurs milliers de téraoctets. Pour réduire les besoins en mémoire de la méthode matrix, nous présentons la méthode *en deux pas* qui effectue d'abord une décomposition en modes cohérents pour un faisceau d'électrons avec une divergence égal à zéro et, sur la base de cette décomposition, effectue une seconde décomposition qui prend en compte la divergence. L'exigence de mémoire pour nos applications est considérablement réduite à environ $4N_xN_yN_m$ alors que N_m soit le nombre de modes cohérents demandés. Cela permet de calculer des harmoniques supérieures ou des anneaux avec des émittances plus élevés. Tout comme la méthode matrix, nous testons la méthode en deux pas pour un faisceau d'électrons en forme de fonction delta de Dirac et pour un champ électrique de référence en forme de gaussien. Dans la section 4.6, nous ajoutons les contributions de la dispersion d'énergie du faisceau d'électrons.

Enfin, dans la section 4.7, nous comparons la décomposition à certains résultats obtenus par SRW multielectron Monte Carlo échantillonnage pour la densité spectrale de puissance et pour certains points sélectionnés de la densité spectrale parce que SRW ne peut ni calculer la densité spectrale complète ni le spectre des modes ou les modes cohérents. Tous les tests montrent un très bon accord étant donné que différentes méthodes et approximations sont utilisées pour les calculs.

Dans le chapitre 5, nous appliquons l'algorithme de décomposition en modes cohérents à quelques applications. Nous étudions comment le spectre de mode et la longueur de cohérence changent en fonction de la longueur de l'ondulateur et de l'énergie du photon. Nous définissons la *longueur de cohérence* comme la largeur à mi-hauteur du degré spectral de cohérence μ alors que $\boldsymbol{r}_1$ soit fixé à l'origine et $\boldsymbol{r}_2$ soit varié. Nous constatons que le nombre de modes cohérents diminue et que la longueur de cohérence augmente pour les ondulateurs plus longs. En plus le nombre de mode augmente et la longueur de cohérence diminue avec les harmoniques supérieures. Les calculs font avec les énergies de photons correspondant au flux maximal donnent une plus petite longueur de cohérence que les calculs à l'énergie de résonance.

Nous imitons et idéalisons une expérience donnée dans [4] où une image du centre de l'ondulateur est soumise à une ouverture. La taille de l'ouverture est réduite et le spectre du mode est étudié. La fermeture de l'ouverture réduit la densité spectrale de puissance, mais en même temps réduit le spectre de mode et augmente la cohérence.

Nous étudions l'effet d'une variation de la dispersion d'énergie du faisceau d'électrons. Pour cela, nous maintenons les paramètres transversaux du faisceau d'électrons fixés et ne modifions que la dispersion d'énergie de l'ESRF-EBS. Nous constatons qu'une réduction de la dispersion d'énergie ne modifie pas gravement le spectre de mode de l'ESRF u18 1m ondulateur pour le premier harmonique. Cela change pour les ondulateurs ESRF u18 de 2m et 4m où le spectre de mode change plus fort.

L'effet d'un Twiss alpha fini est étudié pour un ondulateur ESRF u18 2m. L'ondulateur est placé soit avec son plan d'entrée 1 m avant le point de symétrie ou au point de symétrie. Le calcul aven un alpha fini est au moins dix fois plus lent que le calcul au point de symétrie car aucune convolution ne peut pas être utilisée dans leurs calculs. En raison des grandes exigences des ressources informatique, nous inspectons seulement l'ondulateur avec une longueur de 2 m. Il y a un changement dans le spectre des modes et dans les longueurs de cohérence, mais il n'est pas important.

Nous calculons la variation du spectre de mode pour une variation des paramètres transversaux du faisceau d'électrons avec une dispersion d'énergie fixe ou une diminution de la dispersion d'énergie. Nous voyons que le spectre de mode s'effondre en un seul mode si les paramètres du faisceau d'électrons transversaux et la dispersion d'énergie sont considérablement réduits. L'occupation du premier mode atteint au maximum seulement 93 % si la dispersion d'énergie est maintenue fixée au valeur de l'EBS et seuls les paramètres transversaux du faisceau d'électrons sont réduits. Ceci est en accord avec les résultats de la section 3.4 car la dimension de la dispersion d'énergie de la distribution d'espace des phases n'est pas une fonction delta de Dirac.

Nous comparons les modes cohérents exactement calculés à un modèle Gaussian Schell (GSM), à l'approximation de séparation et à une approximation analytique donnée par Geloni *et al.* [8]. Une comparaison avec un modèle Gaussian Schell montre de grandes erreurs dans la norme de l'opérateur et dans les modes cohérents. L'erreur de valeurs propres n'est pas grande. Les erreurs deviennent pires pour des paramètres de faisceau d'électrons plus petits. Pour l'approximation de séparation l'erreur relative dans la norme de l'opérateur est encore d'environ 0.05 pour les paramètres de l'ESRF-EBS. Les modes de l'approximation de séparation sont différents des modes cohérents exacts. Les valeurs propres sont approximativement pires que les valeurs propres obtenues avec l'approximation du modèle Gaussian Schell. Cependant, tous les quantités qui nous intéressent : densité spectrale de puissance, coupure verticale et horizontale de la densité spectrale pour quelques points spéciaux montrent un très bon accord avec le calcul exact. L'approximation analytique produit des résultat qualitativement correct, mais la densité spectrale présente des oscillations supplémentaires dans la direction verticale qui sont absentes dans le calcul exact.

L'approximation de séparation semble être une bonne et rapide approximation numérique. Cela peut être utile pour la conception de la ligne de faisceau et devrait être exécutable même sur les ordinateurs ordinaires.

Au chapitre 6, nous présentons quelques idées pour des recherches futures et des développements ultérieurs. La première idée est l'échantillonnage de la densité spectrale avec les méthodes de Monte Carlo. Évidemment, cela ne peut être fait que pour des cas simples en raison de l'immense consommation de mémoire. Par contre, les exigences du théorème de convolution de la brillance sont évitées. La densité spectrale pourrait ensuite être décomposée en modes cohérents et l'analyse spectrale pourrait être appliquée.

Une autre idée est l'étude des effets de l'alignement de l'ondulateur. Comment sont les propriétés du faisceau de photons et surtout les propriétés de cohérence changés si l'ondulateur est mal aligné. Un désalignement pourrait être une petite inclinaison ou un petit décalage de l'entrée de l'ondulateur par rapport à sa position de conception idéale. En outre, il serait intéressant d'étudier l'effet de deux ondulateurs dans une section droite. S'il y a deux ondulateurs, il y a un écart particulier entre les deux. Est-ce qu'il y a peut-être un écart optimal ?

Dans cette thèse, notre discussion se limite à un faisceau de photons parfaitement polarisé horizontalement. Dans la réalité, le faisceau de photons est polarisé et certaines expériences exploitent la polarisation du rayonnement et modifient la polarisation. Il serait intéressant de modéliser les lignes de faisceau de ces expériences. Dans ce cas-là, le composant horizontal de la densité spectrale n'est pas suffisante et il faut calculer la matrice de cohérence (Eq. 6.2).

La mise en oeuvre actuelle de l'algorithme nécessite une configuration manuelle de plusieurs paramètres d'entrée et de précision. Le logiciel serait plus facile à utiliser si quelques paramètres pourraient être détectés ou réglés automatiquement.

La mise en oeuvre actuelle considère uniquement le couplage de Twiss-alpha finis de faisceau d'électrons et suppose aucun autre couplage entre tous les autres paramètres de faisceau. En particulier on suppose que les dimensions horizontale et verticale sont découplées. Une théorie plus générale est développée dans cette thèse mais n'est pas encore mise en oeuvre dans le logiciel. Tout d'abord, nous voulions une mise en oeuvre qui couvre les cas les plus importants et soit le plus simple possible. D'autres couplages augmenteront la complexité de la mise en oeuvre et réduiront la vitesse. Cependant, ce serait un bon moment pour ajouter des couplages supplémentaires.

Nous voyons qu'au moins pour un faisceau d'électrons horizontalement et verticalement découplé, l'approximation de séparation peut conduire à de bons résultats approximatifs (voir la section 5.6.2). Peut-être que la théorie standard de perturbation de la mécanique quantique pourrait encore améliorer l'approximation. Un test (voir la section 6) montre que au moins les valeurs propres deviennent meilleures.

En tant que dernière idée, nous proposons d'étudier les liens vers d'autres disciplines de la physique statistique. Nous avons discuté dans cette thèse que le rayonnement de l'anneau de stockage du synchrotron suit les statistiques gaussiennes. D'autres théories physiques sont également basés sur les statistiques gaussiennes. Il serait intéressant de voir si des quantités physiques d'autres théories ont un pendentif dans notre théorie. Par exemple, une question pourrait être : existe-t-il un ≪facteur de Boltzmann≫ dans notre théorie ?

Nous finissons avec un bref résumé qui dit :

> Le contexte de cette thèse est l'étude de la cohérence partielle dans les faisceaux synchrotron produits par les anneaux de stockage de basse émittance, comme l'ESRF-EBS. L'objectif principal est la compréhension et l'application de la physique sous-jacente pour l'implémentation et le développement d'outils de calcul. Nous développons d'abord une théorie de l'optique-statistique pour les radiations émisses par des anneaux de stockage qui est basée sur le théorème de Kim et sur les contributions de Geloni *e*t al. Nous utilisons ces formules d'une manière détaillée et légèrement différente. Nous insistons sur l'importance des paramètres stochastiques des faisceaux d'électrons pour décrire les propriétés de cohérence. Nous observerons que la longueur du paquet des électrons n'affecte pas les propriétés de la cohérence s'il y a un couplage faible entre la position longitudinal de l'électron et ses autres paramètres. Nous avons construit une description de l'optique statistique pour l'émission synchrotron liée aux modes cohérents. Nous voyons qu'un ensemble est complètement cohérent si et seulement si ses modes cohérents se réduisent a un seul mode. Geloni et al. mentionnent que l'émission d'un synchrotron est un processus stochastique gaussien. Nous ajoutons qu'il a une moyenne nulle et il est symétrique circulaire. En conséquence nous pouvons donner une interprétation physique au degré de cohérence spectrale en termes de densité de probabilité conditionnée de forme gaussienne. Nous avons développé et implémenté un algorithme qui calcule la décomposition de la densité spectrale en modes cohérents. Il peut être appliqué à un faisceau d'électrons avec un paramètre Twiss-alpha fini et une dispersion d'énergie. Nous avons implémenté deux versions de l'algorithme. La première résout l'équation de Fredholm dans une base de fonctions constantes par morceaux. Les calculs pour les hautes harmoniques d'un ondulateur et pour des émittances relativement larges demandent une trop grande mémoire pour être calculées. Pour réduire la mémoire requise, nous avons développé une méthode en deux pas. On résout d'abord l'équation pour un faisceau d'électron de divergence nulle, puis on ajoute les effets de la divergence dans un second temps. Nous présentons des tests approfondis qui incluent une distribution des électrons du type fonction delta de Dirac, des champs électriques gaussiens dont les résultats analytiques sont connus, ainsi qu'une comparaison avec des résultats Monte Carlo produits par SRW. Nous appliquons cet algorithme sur un nombre de cas particuliers. Nous déterminons combien de modes sont nécessaires pour inclure 95% de la densité spectrale et comment le degré de cohérence spectrale change. Nous trouvons que la dispersion d'énergie ajoute des modes cohérents. Cet effet est négligeable pour des anneaux courants mais pour l'ESRF-EBS elle ajoute des nouveaux modes. Des ondulateurs plus courts et des plus hautes harmoniques augmentent le nombre de modes. Une comparaison entre un ondulateur placée dans un point avec alpha fini et dans un point symétrique ne montre pas de différences significative. Une réduction artificielle de l'émittance du anneau ESRF-EBS montre un décroit du nombre de mode jusqu'à arriver à un seul mode. Nous avons simulé une ligne de lumière simplifiée focalisant 1 : 1. Une réduction de la taille de l'ouverture change les valeurs propres du spectre vers des modes de plus en plus petits ce qui entraine aussi une réduction du flux. Nous présentons une comparaison entre la densité spectrale calculée avec l'approximation Gauss-Shell, l'approximation analytique et l'approximation de la séparation. Bien qu'il n'y a pas d'erreurs négligeables entre le calcul exact et l'approximation de la séparation, nous concluons que cette dernière peut être une bonne et rapide solution permettant des calculs sur des ordinateur portables. Nous terminons cette thèse par des idées sur de futures recherches.

Bibliography

[1] G. Gruebel and F. Zontone. Correlation spectroscopy with coherent x-rays. *Journal of Alloys and Compounds*, 2004. Proceedings of the Sixth International School and Symposium on Synchrotron Radiation in Natural Science (ISSRNS).

[2] P. Cloetens, R. Barrett, J. Baruchel, J.-P. Guigay, and M. Schlenker. Phase objects in synchrotron radiation hard x-ray imaging. *Journal of Physics D: Applied Physics*, 1996.

[3] R. Robinson, I.and Harder. Coherent x-ray diffraction imaging of strain at the nanoscale. *Nat Mater*, Apr 2009.

[4] P.M. Pelz, M. Guizar-Sicairos, P. Thibault, I. Johnson, M. Holler, and A. Menzel. On-the-fly scans for x-ray ptychography. *Applied Physics Letters*, 2014.

[5] P. Thibault and A. Menzel. Reconstructing state mixtures from diffraction measurements. *Nature*, Feb 2013.

[6] R. Dimper, H. Reichert, P. Raimondi, L. Sanchez Ortiz, F. Sette, and J. Susini. *ESRF Upragde programme phase II.* ESRF, 2014.

[7] K.-J. Kim. A new formulation of synchrotron radiation optics using the wigner distribution. *Proc. SPIE 0582, Insertion Devices for Synchrotron Sources, 2*, 1986.

[8] G. Geloni, E. Saldin, E. Schneidmiller, and M. Yurkov. Transverse coherence properties of x-ray beams in third-generation synchrotron radiation sources. *Nuclear Instruments and Methods in Physics Research Section A: Accelerators, Spectrometers, Detectors and Associated Equipment*, 2008.

[9] M. Glass. Coherent modes for synchrotron light (comsyl). https://www.github.com/mark-glass/comsyl.

[10] Accelerator toolkit. http://atcollab.sourceforge.net/.

[11] Strategic accelerator design. http://acc-physics.kek.jp/SAD/.

[12] K. Ohmi, K. Hirata, and K. Oide. From the beam-envelope matrix to synchrotron-radiation integrals. *Phys. Rev. E*, Jan 1994.

[13] B. Nash. *Analytical approach to eigen-emittance evolution in storage rings.* PhD thesis, Stanford, 2006.

[14] D. Einfeld and M. Plesko. Design of a diffraction-limited light source, 1993.

[15] L. Mandel and E. Wolf. *Optical Coherence and Quantum Optics.* Cambridge University Press, 1995.

[16] G. Geloni, V. Kocharyan, and E. Saldin. Brightness of synchrotron radiation from undulators and bending magnets. *Journal of Synchrotron Radiation*, 2015.

[17] J.D. Jackson. *Classical electrodynamics.* Wiley, 1975.

[18] E.M. Rowe. Facilities in the united states. *Physics Today*, 1981.

[19] G.A. Schott. *Electromagnetic Radiation and the Mechanical Reactions Arising from it.* Cambridge University Press, 1912.

[20] A. A. Sokolov and I. M. Ternov. *Synchrotron Radiation.* Berlin, Akademie-Verlag, Pergamon Press, 1968.

[21] G. K. Green. Spectra and optics of synchrotron radiation. Technical report, Upton, New York, Brookhaven National Laboratory, 1975.

[22] D. Attwood. *Soft X-Rays and Extreme Ultraviolet Radiation: Principles and Applications.* Cambridge University Press, 2007.

[23] H. Onuki and P. Elleaume. *Undulators, Wigglers and Their Applications.* CRC Press, 2003.

[24] O. Chubar and P. Elleaume. Accurate and efficient computation of synchrotron radiation in the near field region. *proc. of the EPAC98 Conference*, pages 1177–1179, 1998.

[25] S. Thery, M. Glass, and M. Sanchez del Rio. pysru. https://github.com/SophieTh/und_Sophie_2016.

[26] J. Baruchel, J.-L. Hodeau, M.S. Lehmann, J.R. Regnard, and C. Schlenker. *Neutron and synchrotron radiation for condensed matter studies: Theory, instruments and methods.* Neutron and Synchrotron Radiation for Condensed Matter Studies. Springer-Verlag, 1993.

[27] H. Wiedemann. *Particle Accelerator Physics.* SpringerLink: Springer e-Books. Springer Berlin Heidelberg, 2007.

[28] J.W. Cooley and J.W. Tukey. An algorithm for the machine calculation of complex Fourier series. *Mathematics of Computation*, 1965.

[29] O. Chubar. Wavefront calculations, 2001.

[30] G. Geloni, E. Saldin, E. Schneidmiller, and M. Yurkov. Fourier treatment of near-field synchrotron radiation theory. *Optics Communications*, 2007.

[31] S. Kshevetskii, P. Wojda, and V. Maximov. A high-accuracy complex-phase method of simulating X-ray propagation through a multi-lens system. *Journal of Synchrotron Radiation*, 2016.

[32] O. Chubar, P. Elleaume, and A. Snigirev. Phase analysis and focusing of synchrotron radiation. *Nuclear Instruments and Methods in Physics Research Section A: Accelerators, Spectrometers, Detectors and Associated Equipment*, 1999.

[33] J. R. Fienup and C. C. Wackerman. Phase-retrieval stagnation problems and solutions. *J. Opt. Soc. Am. A*, (11), 1986.

[34] B.E.A. Saleh and M.C. Teich. *Fundamentals of Photonics.* Wiley Series in Pure and Applied Optics. Wiley, 2007.

[35] M. Born, E. Wolf, and A.B. Bhatia. *Principles of Optics: Electromagnetic Theory of Propagation, Interference and Diffraction of Light.* Cambridge University Press, 1999.

[36] E.L. O'Neill. *Introduction to Statistical Optics.* Dover books on physics. Dover Publications, 2004.

[37] A. Berlinet and C. Thomas-Agnan. *Reproducing Kernel Hilbert Spaces in Probability and Statistics.* Springer US, 2011.

[38] A. Starikov and E. Wolf. Coherent-mode representation of gaussian schell-model sources and of their radiation fields. *J. Opt. Soc. Am.*, 1982.

[39] F. Gori. Collett-wolf sources and multimode lasers. *Optics Communications*, 1980.

[40] R.G. Gallager. *Stochastic Processes: Theory for Applications.* Cambridge University Press, 2014.

[41] R.R. Lindberg and K.J. Kim. Compact representations of partially coherent undulator radiation suitable for wave propagation. *Phys. Rev. ST Accel. Beams*, Sep 2015.

[42] J.W. Goodman. *Statistical Optics.* A Wiley-Interscience publication. Wiley, 1985.

[43] A. Altland and B. Simons. *Condensed Matter Field Theory.* Cambridge University Press, 2010.

[44] V. Hernandez, J. E. Roman, and V. Vidal. SLEPc: Scalable Library for Eigenvalue Problem Computations. *Lect. Notes Comput. Sci.*, 2003.

[45] V. Hernandez, J. E. Roman, and V. Vidal. SLEPc: A scalable and flexible toolkit for the solution of eigenvalue problems. *ACM Trans. Math. Software*, 2005.

[46] J. E. Roman, C. Campos, E. Romero, and A. Tomas. SLEPc users manual. Technical report, D. Sistemes Informàtics i Computació, Universitat Politècnica de València, 2016.

[47] S Balay, S Abhyankar, M.F. Adams, J Brown, P. Brune, K. Buschelman, L. Dalcin, V. Eijkhout, W. D. Gropp, D Kaushik, M.-G. Knepley, L.C. McInnes, K. Rupp, B.-F. Smith, S. Zampini, H. Zhang, and H. Zhang. PETSc Web page. `http://www.mcs.anl.gov/petsc`, 2016.

[48] S Balay, S Abhyankar, M.F. Adams, J Brown, P. Brune, K. Buschelman, L. Dalcin, V. Eijkhout, W. D. Gropp, D Kaushik, M.-G. Knepley, L.C. McInnes, K. Rupp, B.-F. Smith, S. Zampini, H. Zhang, and H. Zhang. PETSc users manual. Technical Report ANL-95/11 - Revision 3.7, Argonne National Laboratory, 2016.

[49] S. Balay, W.D. Gropp, L.C. McInnes, and B.S. Smith. Efficient management of parallelism in object oriented numerical software libraries. In E. Arge, A. M. Bruaset, and H. P. Langtangen, editors, *Modern Software Tools in Scientific Computing.* Birkhäuser Press, 1997.

[50] W. Rudin. *Functional Analysis.* International series in pure and applied mathematics. McGraw-Hill, 1991.

[51] D. Werner. *Funktionalanalysis.* Springer-Lehrbuch. Springer Berlin Heidelberg, 2007.

[52] J. Kirz, D. Attwood, B. Henke, M. Howells, K Kennedy, K.-J. Kim, J. Kortright, R. Perera, P. Pianetta, J. Riordan, J. Scofield, A. Thompson, J. Underwood, D. Vaughan, G. Williams, and H. Winick. *X-ray Data Booklet.* Lawrence Berkeley Laboratory, 1986.

[53] J.J. Sakurai and J. Napolitano. *Modern Quantum Mechanics.* Addison-Wesley, 2011.

[54] F. Reif. *Fundamentals of Statistical and Thermal Physics:*. Waveland Press, 2009.

[55] F. Schwabl and W.D. Brewer. *Statistical Mechanics*. Advanced Texts in Physics. Springer Berlin Heidelberg, 2006.

[56] M. R. Howells and B. M. Kincaid. *The Properties of Undulator Radiation*. Springer Netherlands, Dordrecht, 1994.

[57] A.M. Zysk, P.S. Carney, and J.C. Schotland. Eikonal method for calculation of coherence functions. *Phys. Rev. Lett.*, Jul 2005.

[58] P. Vahimaa and J. Turunen. Finite-elementary-source model for partially coherent radiation. *Opt. Express*.

[59] A. Singer and I.A. Vartanyants. Modelling of partially coherent radiation based on the coherent mode decomposition, 2011.

[60] I.A. Vartanyants and A. Singer. Coherence properties of hard x-ray synchrotron sources and x-ray free-electron lasers. *New Journal of Physics*, 2010.

[61] T. Tanaka. Numerical methods for characterization of synchrotron radiation based on the wigner function method. *Phys. Rev. ST Accel. Beams*, 2014.

[62] S. Flewett, H.M. Quiney, C.Q. Tran, and K.A. Nugent. Extracting coherent modes from partially coherent wavefields. *Opt. Lett.*, 2009.

[63] T. Tanaka and H. Kitamura. Universal function for the brilliance of undulator radiation considering the energy spread effect. *Journal of Synchrotron Radiation*, 2009.

[64] E. Hecht. *Optics*. Pearson Education, 2012.

[65] M Sands. The physics of electron storage rings: an introduction, 1971.

[66] G. Gbur and T.D. Visser. Chapter 5 - the structure of partially coherent fields. In Emil Wolf, editor, *Progress in Optics (vol 55)*, Progress in Optics. Elsevier, 2010.

[67] G. Santin and R. Schaback. Approximation of eigenfunctions in kernel-based spaces. *Advances in Computational Mathematics*, 2016.

[68] K.-J. Kim. Characteristics of synchrotron radiation. *AIP Conference Proceedings*, 1989.

[69] V.I. Paulsen and M. Raghupathi. *An Introduction to the Theory of Reproducing Kernel Hilbert Spaces*. Cambridge Studies in Advanced Mathematics. Cambridge University Press, 2016.

[70] A.E. Siegman. *An introduction to lasers and masers*. McGraw-Hill series in the fundamentals of electronic science. McGraw-Hill, 1971.

[71] K. Ohmi, K. Hirata, and K. Oide. From the beam-envelope matrix to synchrotron-radiation integrals. *Phys. Rev. E*, 1994.

[72] D. Einfeld. Multi-bend achromat lattices for storage ring light sources. *Synchrotron Radiation News*, 2014.

[73] L. Mandel. Concept of cross-spectral purity in coherence theory. *J. Opt. Soc. Am.*, 1961.

[74] W.H. Zachariasen. *Theory of X-ray diffraction in crystals.* Dover books on physics and mathematical physics. J. Wiley & sons, inc., 1945.

[75] M.V. Klein and T.E. Furtak. *Optics.* Wiley series in pure and applied optics. Wiley, 1986.

[76] A. Torre. *Linear Ray and Wave Optics in Phase Space: Bridging Ray and Wave Optics via the Wigner Phase-Space Picture.* Elsevier Science, 2005.

[77] W.H. Press, S.A. Teukolsky, W.T. Vetterling, and B.P. Flannery. *Numerical Recipes in C (2nd Edition): The Art of Scientific Computing.* Cambridge University Press, New York, NY, USA, 1992.

[78] E. Gamma, R. Helm, R. Johnson, and J. Vlissides. *Design Patterns: Elements of Reusable Object-oriented Software.* Addison-Wesley Longman Publishing Co., Inc., Boston, MA, USA, 1995.

[79] W. H. Brown, R.C. Malveau, H.W. McCormick, and T.J. Mowbray. *AntiPatterns: Refactoring Software, Architectures, and Projects in Crisis.* John Wiley & Sons, Inc., New York, NY, USA, 1st edition, 1998.

[80] A. Klenke. *Wahrscheinlichkeitstheorie.* Springer-Lehrbuch Masterclass. Springer Berlin Heidelberg, 2008.